DOCTORAL THESIS

Numerical simulation concepts for moisture transport in wood and wood-based products, below and above the fiber saturation point, to predict moisture-induced failure mechanisms

submitted in satisfaction of the requirements for the degree of
Doctor of Science in Civil Engineering
of TU Wien, Faculty of Civil Engineering

DISSERTATION

Numerische Simulationskonzepte für den Feuchtetransport in Holz und Holzwerkstoffen, unterhalb und oberhalb des Fasersättigungspunktes, zur Vorhersage feuchteinduzierter Versagensmechanismen

ausgeführt zum Zwecke der Erlangung des akademischen Grades eines
Doktors der technischen Wissenschaften
eingereicht an der Technischen Universität Wien, Fakultät für Bauingenieurwesen
von

Dipl.-Ing. **Maximilian Autengruber**, BSc
Matr.Nr.: 1126464

Betreuer:
Dipl.-Ing. Dr.techn. **Markus Lukacevic**
Associate Prof. Dipl.-Ing. Dr.techn. **Josef Füssl**
Univ.-Prof. Dipl.-Ing. Dr.techn. Dr.h.c.mult. **Josef Eberhardsteiner**
Institut für Mechanik der Werkstoffe und Strukturen
Technische Universität Wien

Gutachterin:
Dr. **Stefania Fortino**
ProperTune ICME Integration
VTT, Finland

Gutachter:
Univ.-Prof. Dr. **Erik Serrano**
Structural Mechanics
Department of Construction Sciences
Lund University, Sweden

Wien, im März 2021

.....

Die approbierte gedruckte Originalversion dieser Dissertation ist an der TU Wien Bibliothek verfügbar.
The approved original version of this doctoral thesis is available in print at TU Wien Bibliothek.

Die approbierte gedruckte Originalversion dieser Dissertation ist an der TU Wien Bibliothek verfügbar.
The approved original version of this doctoral thesis is available in print at TU Wien Bibliothek.

Acknowledgements

The following work is the scientific result of my work as a research assistant at the Institute for Mechanics of Materials and Structures at TU Wien from July, 2016, to March, 2021. This work was part of the project "H2O – H20 Opportunity", which was realized to improve the design of wood composite formwork beams in cooperation with Doka GmbH for the optimization of wood composite formwork beams. This thesis would not have been possible without the contribution of the following people.

At this point I would like to thank Dr. Markus Lukacevic, Prof. Josef Füssl and Prof. Josef Eberhardsteiner for the excellent support. They always took a lot of time for questions and assistance at any time of the day and sometimes until midnight. With their new ideas and approaches during discussions, they gave me new motivation to push forward and overcome my limits.

Dr. Stefania Fortino (VTT, Finland) and Univ.-Prof. Dr. Erik Serrano (Lund University, Sweden) are gratefully acknowledged for being examiners of this work.

I would also like to thank the partners in this project on behalf of Doka GmbH DI (FH) Gregor Wenighofer, Dr. Raimund Mauritz, Ing. Andreas Neuhauser as well as DI Alexander Glebe for the valuable and constructive cooperation. With their knowledge and experience it was possible to get a deeper insight into the complex beam resistance tests. Without these inputs, the results of this thesis could not have been reproduced in such a realistic way.

I also want to thank all other members of the Institute, first of all our head Prof. Christian Hellmich, for the pleasant and appreciative atmosphere and always being available for questions, as well as Mag. (FH) Martina Pöll, Gabriele Ostrowski and Astrid Schuh for their help in administrative issues as well as our IT administrators David Kaufmann and Jan Vales.

Special appreciation also goes to my roommates Dr. Thomas Kiefer, DI Raphael Suda, Vitezslav Stembera, PhD, and Dr. Mingjing Li as well as DI Sebastian Pech, Dr. Michael Schweigler, Dr. Georg Hochreiner, Dr. Giuseppe Balduzzi, DI Thomas Buchner, Dr. Luis Zelaya-Lainez, Nabor Jimenez Segura, MSc, and Dr. Robert Plachy for their on- and off-topic discussions during our lunch breaks.

Furthermore, I have to thank Florian Brandstätter, Thomas Raimer and Christof Gröstlinger for their motivation during the cooperation in the context of their master's theses.

I would also like to thank my colleagues who accompanied me during my previous studies and, thus, laid my foundation for my interest in scientific work, especially Dr. Christian Schranz, who initiated my interest in this dissertation.

Also without my family and friends this work would not have been possible. Therefore, I would like to especially thank my wife Bianca, as well as my parents Uschi and Norbert, my brother Nikolaus and my grandparents Ria, Ernst and Sissy.

Die approbierte gedruckte Originalversion dieser Dissertation ist an der TU Wien Bibliothek verfügbar.
The approved original version of this doctoral thesis is available in print at TU Wien Bibliothek.
TU Bibliothek Your knowledge hub WIEN

Die approbierte gedruckte Originalversion dieser Dissertation ist an der TU Wien Bibliothek verfügbar.
The approved original version of this doctoral thesis is available in print at TU Wien Bibliothek.

Abstract

Wood and wood-based products exhibit a strongly moisture-dependent behavior. In addition to the influence on certain material properties, the direction-dependent expansion behavior makes moisture in wood an important factor to consider when developing a timber structure or wood product. Dimensional changes of wooden construction elements due to variations in the surrounding climate lead to moisture-induced stresses, which, depending on their magnitude, can lead to cracking, making moisture one of the main reasons for damage and, in the worst case, failure in timber structures. Wood is also used on a large scale and in different types (e.g. as solid wood or particle board) and can subsequently be combined with other materials such as aluminum.

During use but also when stored on the construction site, formwork beams are often exposed to liquid water, e.g. from rain, which can currently not taken into account with existing multi-Fickian transport models, which are only applied for conditions below the so-called fiber saturation point (FSP). Other approaches, developed for kiln drying, also account for free water, but are simplified in the range below the FSP. A unified model combining these two approaches is currently missing. So does a more accurate description of moisture-induced stresses and cracks, which are currently only considered with modification factors depending on the surrounding climate in the European standard for timber structures (Eurocode 5). Since the determination of these stresses, especially when different materials interact, is quite complex, the load-bearing capacity and serviceability of formwork beams are determined with an extensive test program.

In this dissertation, the approaches below and above the FSP are linked with reasonable coupling mechanisms and implemented in Abaqus within the framework of a three-dimensional user element subroutine. This numerically stable and reliable computational model is then used to simulate moisture content (MC) fields of 18 different sized cross-sections in a real climate at Linz, Austria. Based on these simulated moisture fields, a method for predicting such fields for larger cross sections solely based on relative humidity is developed. This allows moisture-induced stresses and changes in material properties due to climatic changes to be easily taken into account in a structural analysis. In a further step, moisture-induced stresses are calculated based on the simulated MC fields and evaluated with a multisurface failure criterion to determine the potential of cracking during the studied time span from November 1, 2014, to January 1, 2016. Simulations are performed at specific points in time using the extended finite element method and the resulting crack lengths are compared to the assumptions of Eurocode 5. The moisture transport model, in combination with advanced material models for brittle and ductile failure of wood, is also used to investigate the behavior of complex wood-aluminum composite beams in different moisture states during the resistance tests of EN 13377 and to predict the load-deformation behavior as well as the maximum bearing capacity.

The in this work presented newly developed tools and methods are intended to lay a basis for improving existing design concepts, subsequently reducing the amount of moisture related damage in timber constructions and wood products.

Die approbierte gedruckte Originalversion dieser Dissertation ist an der TU Wien Bibliothek verfügbar.
The approved original version of this doctoral thesis is available in print at TU Wien Bibliothek.
TU Bibliothek Your knowledge hub WIEN

Die approbierte gedruckte Originalversion dieser Dissertation ist an der TU Wien Bibliothek verfügbar.
The approved original version of this doctoral thesis is available in print at TU Wien Bibliothek.

Kurzfassung

Holz und Holzwerkstoffe weisen ein stark feuchteabhängiges Verhalten auf. Neben dem Einfluss auf bestimmte Materialeigenschaften macht das richtungsabhängige Ausdehnungsverhalten die Holzfeuchtigkeit im Holz zu einem wichtigen Faktor, der bei der Entwicklung einer Holzkonstruktion oder eines Holzproduktes zu berücksichtigen ist. Dimensionsänderungen von Holzbauteilen aufgrund von Schwankungen des Umgebungsklimas führen zu feuchteinduzierten Spannungen, die je nach Ausmaß zu Rissen führen können, so dass Feuchtigkeit eine der Hauptursachen für Schäden und im schlimmsten Fall für das Versagen von Holzkonstruktionen ist. Holz wird sowohl in der ursprünglichen Form als auch in verschiedenen Ausführungen (z.B. als Massivholz oder Spanplatte) eingesetzt und mit anderen Materialien wie Aluminium kombiniert werden.

Im Einsatz auf der Baustelle oder während der Lagerung sind Schalungsträger häufig Wasser ausgesetzt, beispielsweise von Regen. Dies kann mit bestehenden multi-Fickschen Transportmodellen, die nur für Bedingungen unterhalb des sogenannten Fasersättigungspunktes (FSP) entwickelt wurden, derzeit nicht berücksichtigt werden. Andere Ansätze, die für die Holztrocknung entwickelt wurden, berücksichtigen zwar Wasser, sind aber im Bereich unterhalb des FSP vereinfacht. Ein einheitliches Modell, das diese beiden Ansätze kombiniert, fehlt bisher. Ebenso eine genauere Beschreibung der feuchteinduzierten Spannungen und Risse, die in der europäischen Norm für Holzkonstruktionen (Eurocode 5) derzeit nur mit Modifikationsbeiwerten in Abhängigkeit vom Umgebungsklima berücksichtigt werden. Da die Ermittlung dieser Spannungen, insbesondere bei der Interaktion verschiedener Materialien, komplex ist, werden Tragfähigkeit und Gebrauchstauglichkeit von Schalungsträgern mit einem aufwendigem Versuchsprogramm ermittelt.

In dieser Dissertation werden die Ansätze unter- und oberhalb des FSP erstmals mit entwickelten Kopplungstermen verknüpft und in Abaqus mit einer 3D Benutzerelement-Subroutine implementiert. Dieses numerisch stabile Berechnungsmodell wird anschließend verwendet, um Holzfeuchtigkeitsfelder von 18 verschiedenen Querschnitten im Klima des Standortes Linz, Österreich, zu simulieren. Mit diesen Simulationen wird eine Methode zur Vorhersage von Holzfeuchtigkeitsfeldern für größere Querschnitte allein mit der relativen Luftfeuchtigkeit entwickelt. Damit können feuchteinduzierte Spannungen und Änderungen der Materialeigenschaften einfach in einer statischen Berechnung berücksichtigt werden. In einem weiteren Schritt werden auf Basis der simulierten Holzfeuchtigkeitsfelder feuchteinduzierte Spannungen berechnet und mit einem Mehrflächen-Versagenskriterium bewertet, um das Potenzial von Rissen während der untersuchten Zeitspanne vom 1.11.2014 bis zum 1.1.2016 zu ermitteln. Zu bestimmten Zeitpunkten werden Simulationen mit der erweiterten Finite-Elemente-Methode durchgeführt und die resultierenden Risslängen mit den Annahmen des Eurocodes 5 verglichen. Das Feuchtetransportmodell, in Kombination mit hochentwickelten Materialmodellen für sprödes und duktiles Versagen von Holz, wird auch verwendet, um das Verhalten von komplexen Holz-Aluminium-Verbundträgern in verschiedenen Feuchtezuständen während der Widerstandsprüfungen von EN 13377 zu untersuchen und um das Last-Verformungsverhalten sowie die maximale Tragfähigkeit vorherzusagen.

Die in dieser Arbeit neu entwickelten Methoden sollen eine Grundlage für die Verbesserung bestehender Bemessungskonzepte legen, um in der Folge das Ausmaß feuchtebedingter Schäden in Holzkonstruktionen und Holzprodukten zu reduzieren.

Die approbierte gedruckte Originalversion dieser Dissertation ist an der TU Wien Bibliothek verfügbar.
The approved original version of this doctoral thesis is available in print at TU Wien Bibliothek.
TU Bibliothek Your knowledge hub WIEN

Die approbierte gedruckte Originalversion dieser Dissertation ist an der TU Wien Bibliothek verfügbar.
The approved original version of this doctoral thesis is available in print at TU Wien Bibliothek.

Contents

Introduction **1**
Motivation and Outline 1
Research Objectives and Methodology 3
Contribution by the author 5

1 Finite-element-based moisture transport model for wood including free water above the fiber saturation point [3] **9**
1.1 Introduction 10
1.2 Materials and Methods 12
1.2.1 Moisture transport in wood 12
1.2.2 Mathematical model 14
1.3 Model validation 32
1.3.1 Simulation Frandsen [10] 34
1.3.2 Simulation Perré [22] 37
1.3.3 Experiment Eriksson et al. [38] 38
1.3.4 Experiment Sandoval et al. [41] 40
1.3.5 Experiment Gezici-Koç et al. [43] – drying 41
1.3.6 Experiment Gezici-Koç et al. [43] – infiltration 43
1.3.7 Experiment Krabbenhoft and Damkilde [42] 45
1.4 Parameter studies 46
1.4.1 Mesh study 46
1.4.2 Parameters for reaction function H_{wv} 49
1.4.3 Residual free water evaporation time t_{wv} 51
1.4.4 Maximum time increment size 52
1.5 Discussion 53
1.6 Conclusion & Outlook 55

Die approbierte gedruckte Originalversion dieser Dissertation ist an der TU Wien Bibliothek verfügbar.
The approved original version of this doctoral thesis is available in print at TU Wien Bibliothek.
TU Bibliothek Your knowledge hub WIEN

2 Numerical assessment of wood moisture content-based assignments to service classes in EC 5 and a prediction concept for moisture-induced stresses solely using relative humidity data [4] 57
2.1 Introduction . . . 58
2.2 Materials and Methods . . . 59
2.2.1 Mathematical model for moisture transport in wood . . . 60
2.2.2 Geometries . . . 61
2.3 Results . . . 62
2.3.1 MC distributions over the simulation time . . . 63
2.3.2 MC distributions at specific events . . . 63
2.4 Discussion . . . 65
2.4.1 Service Class . . . 65
2.4.2 Comparison of envelope curves . . . 68
2.4.3 Determination of MC values at the boundary based on relative humidities . . . 70
2.4.4 MC distributions along a path . . . 72
2.4.5 2D MC distributions within the GLT 20x40 cross section . . . 72
2.5 Conclusion & Outlook . . . 74

3 Finite-element-based prediction of moisture-induced crack patterns for cross sections of solid wood and glued laminated timber exposed to a realistic climate condition [5] 77
3.1 Introduction . . . 78
3.2 Materials and Methods . . . 80
3.2.1 Mathematical model for moisture transport in wood . . . 80
3.2.2 Finite-element-based model for fracture in wood . . . 82
3.2.3 Geometries . . . 84
3.2.4 Climate data . . . 86
3.3 Results . . . 86
3.3.1 Moisture fields . . . 87
3.3.2 Critical points in time . . . 88
3.3.3 Crack patterns at critical points in time . . . 89
3.4 Discussion . . . 94
3.5 Conclusion & Outlook . . . 97
Appendices . . . 99
3.A Constitutive equations and material parameters for heat and moisture transport . . . 99
3.B Interaction between bound water and water vapor . . . 100
3.C Elasticity tensor for spruce . . . 101

Die approbierte gedruckte Originalversion dieser Dissertation ist an der TU Wien Bibliothek verfügbar.
The approved original version of this doctoral thesis is available in print at TU Wien Bibliothek.
TU Bibliothek Your knowledge hub WIEN

4 Finite-element-based concept to predict stiffness, strength, and failure of wood composite I-joist beams under various loads and climatic conditions [6] 103
4.1 Introduction . . . 104
4.2 Materials and Methods . . . 105
4.2.1 Cross sections . . . 105
4.2.2 Moisture transport simulations . . . 105
4.2.3 Resistance tests . . . 109
4.3 Results . . . 115
4.3.1 Sensitivity analysis . . . 115
4.3.2 Moisture fields . . . 116
4.3.3 Test for bending resistance . . . 117
4.3.4 Test for shear resistance . . . 123
4.3.5 Test for bearing resistance . . . 130
4.4 Discussion . . . 137
4.5 Conclusion & Outlook . . . 139
Appendix . . . 140
4.A Constitutive equations and material parameters . . . 140

Conclusions and Outlook 141
Key Findings . . . 141
Perspectives and Future Research Studies . . . 142

Bibliography 145

Publications and Conference Contributions 153

Curriculum Vitae 157

Die approbierte gedruckte Originalversion dieser Dissertation ist an der TU Wien Bibliothek verfügbar.
The approved original version of this doctoral thesis is available in print at TU Wien Bibliothek.
TU Bibliothek Your knowledge hub WIEN

Die approbierte gedruckte Originalversion dieser Dissertation ist an der TU Wien Bibliothek verfügbar.
The approved original version of this doctoral thesis is available in print at TU Wien Bibliothek.

Die approbierte gedruckte Originalversion dieser Dissertation ist an der TU Wien Bibliothek verfügbar.
The approved original version of this doctoral thesis is available in print at TU Wien Bibliothek.

Introduction

Motivation and Outline

Wood is one of the oldest and most traditional building materials, which is currently experiencing a major upswing. While in man-made materials it is possible to improve certain material properties during the production process, for example by adding boron to steel alloys or different additives to concrete, this is not easily possible in the case of wood, because it is a naturally grown material. Therefore, efficiency improvements in wood products and structures can be achieved either by homogenizing the raw material, as in the case of wood-based materials such as glued laminated timber (GLT) or particleboards, or by a more precise description of the material's behavior though advanced computational tools.

One reason for the potential to describe the material behavior more precisely lies in the complexity of the material behavior itself, which results on one hand from the natural growth process and inhomogeneities such as fiber deviations and knots, and on the other hand from the pronounced moisture behavior. It is hardly possible to take this complexity appropriately into account with conventional (often manual) calculation concepts. Thus, the development of computational methods and concepts is required. Although inhomogeneities can be reduced by homogenization during the production of wood-based materials, the moisture behavior as well as partly the direction-dependent material behavior remain in the final products, e.g. in the case of particleboards. The moisture content (MC) reacts to the surrounding climate and causes changes in the cell wall properties, which also affect material parameters such as stiffness, diffusivities, thermal conductivities as well as strength. Dimensional changes also occur, with wood samples expanding when MC increases (swelling) and shrinking when it decreases. These volumetric changes are non-uniform in the three characteristic dimensions (longitudinal, radial and tangential), which is a result of the tube-shaped, cellular structure of wood. In this context, the MC of wood is referred to as the ratio of the mass of water to the mass of oven-dried wood.

The MC of wood and its changes are responsible for many cases of damage in wooden structures [1]. In addition to the changes in material parameters, moisture-induced stresses occur, which can lead to cracking if the tensile strength is exceeded. The current description of the influence of MC according to the standard Eurocode 5 is based on modification factors and, therefore, does not take into account transient MC fields, which arise in particular during the reaction of the timber component to the surrounding climate after installation at the construction site. Thus, the corresponding

deformations cannot be sufficiently predicted when designing advanced wood products or structural members, such as formwork beams, without extensive testing to ensure load bearing capacities and serviceability limits.

Not only do changes in relative humidity cause the MC to vary, but also contact with water through leaking pipes, tile joints or rain. The latter also affects formwork beams, which are often unprotected when used on the construction site or during storage. In general, water can occur in three different types in wood: as water vapor and free water in the lumen of the cell as well as bound water in the cell wall. Free water only exists when the cell wall is already saturated, which, thus, corresponds to a MC above the fiber saturation point (FSP).

The moisture transport mechanisms below the fiber saturation point can be described mathematically with the multi-Fickian approach. Two diffusion equations for water vapor and bound water are considered in-parallel, which are coupled by the sorption rate. Other models developed in the context of wood-drying from green state include free water transport mechanisms, but are simplified in the range below the FSP. Thus, a combination of both models to include the free water transport in the multi-Fickian framework has not yet been developed.

The key points of this work can be summarized as follows:

- The existing multi-Fickian approach to describe moisture transport in wood below the FSP is combined with a free water transport equation, resulting in a unified moisture transport model to describe all possible MCs below and above the FSP. With reasonable coupling terms, possible states that occur when wood gets into contact with water from, e.g. rain or condensation, can be simulated in 3D. This is shown in **Publication 1**.

- Based on the developed model from **Publication 1**, 18 different cross sections of solid wood (ST) and GLT are simulated in a realistic climate of the location Linz, Austria, to determine the influence of surrounding conditions on the 2D MC fields of the different sized cross sections in a time span of 14 months. In **Publication 2**, emphasis is placed on moisture behavior, comparing maximum and minimum events during the time span. A procedure is defined to describe 2D MC fields solely based on the relative humidities of the surrounding climate.

- In **Publication 3**, the simulated moisture fields of the 18 different cross sections are combined with a mechanical analysis. The resulting stresses are evaluated with a multisurface failure criterion to determine possible critical crack zones in time that show a large number of integration points with the crack criterion fulfilled. Simulations are performed at these critical points in time using the extended finite element method to determine crack lengths. These are then compared to the linear assumption between the crack length and the width of the cross section from Eurocode 5.

- Finally, in **Publication 4**, the moisture transport model is applied to complex 3D wood composite I-joist beams used for formwork support structures. The mechanical analysis includes advanced brittle and ductile failure mechanisms to evaluate

Die approbierte gedruckte Originalversion dieser Dissertation ist an der TU Wien Bibliothek verfügbar.
The approved original version of this doctoral thesis is available in print at TU Wien Bibliothek.
TU Bibliothek Your knowledge hub WIEN

the load-deflection behavior of formwork beams under dry, moist and wet conditions in bending, bearing and shear resistance tests of EN 13377. These extensive tests are necessary to ensure the maximum load-bearing capacity of formwork beams.

The new models and methods proposed in this work make it possible to:

- model all possible moisture states below and above the FSP during drying or infiltration of wood,
- assign cross sections to service classes taking into account their dimensions and their moisture-dependent stiffness properties,
- estimate two-dimensional moisture content fields for large cross sections solely based on the relative humidity of the surrounding conditions,
- determine critical points in times at which critical moisture states can lead to cracking, and
- compute complex wood composite I-joist beams under various climatic conditions in bending, bearing, and shear resistance tests.

The proposed methods can be used to improve the moisture-related design of timber structures as well as wood products by allowing for a deep insight into 3D moisture fields and the resulting mechanical behavior.

Research Objectives and Methodology

The research objectives of the four publications are briefly described below, along with the methods used.

Publication 1 is related to moisture transport in wood. The multi-Fickian approach below the FSP is combined with a free water transport equation. The three-dimensional user element is based on hexahedral elements with linear interpolation functions and is implemented in the software Abaqus. The coupling between the free water transport equation and the rest of the model is done with a time-dependent evaporation/ condensation rate, which allowed a numerically stable connection. In addition, numerical methods such as mass lumping, the mixed formulation of Richards equation and the upstreaming technique were used to overcome numerical difficulties. The model is then validated by means of various experiments and simulation results from literature. A mesh study and an examination of the newly defined parameters are also included.

In **Publication 2**, the model presented in Publication 1 is evaluated for 18 different cross sections with a real climate as a boundary condition during a 14-month time span using the finite element software Abaqus. The resulting 2D MC fields are then further analyzed at specific maximum and minimum events. A method for assigning the service class based on the cross-sectional dimensions is proposed, which can also be used to

Die approbierte gedruckte Originalversion dieser Dissertation ist an der TU Wien Bibliothek verfügbar.
The approved original version of this doctoral thesis is available in print at TU Wien Bibliothek.
TU Bibliothek Your knowledge hub WIEN

obtain the minimum and maximum stiffness values averaged over the cross section during the time span. An approach to estimate 2D MC fields for larger cross sections solely based on the relative humidity is also proposed.

Publication 3 investigates possible cracking due to the 2D MC fields obtained in Publication 2. In a first step, these 2D MC fields are combined with a linear elastic mechanical analysis to obtain stress and strain values. This analysis also evaluates a multisurface failure criterion in the integration points, representative for a specific volume portion of an element. The sum of these volumes of the entire model is then referred to as the "crack-prone volume". In a second step, at two specific points in time which are at the maximum amount of this volume during the wetting period (MC at the boundary greater than MC at the center) and during the drying period (MC at the boundary less than MC at the center), a simulation is performed using the extended finite element method, which accounts for brittle failure based on a multisurface failure criterion developed by [2]. The resulting cracks are then analyzed in terms of length and compared to the Eurocode 5.

In **Publication 4**, complex wood composite I-joist beams are investigated in resistance tests of EN 13377. Mechanical analyses are performed following the 3D MC field simulation. For the 3D MC fields, due to the combination of different materials within these beams, it was necessary to develop an additional multi-point constraints subroutine to define their interactions. To apply the 3D MC field to the mechanical analysis, both models must have the same node numbers and element definitions. For the resistance tests following the MC simulations, the boundary conditions were modified to apply the mechanical loads to the beams using a transmission construction. For the aluminum profile in the flange the isotropic elastic material behavior is followed by plastic failure defined by von Mises plasticity based on experimental data. The particle board in the web uses an orthotropic elasticity tensor, also followed by plastic failure defined by a von Mises criterion adjusted to experimental results. For the spruce solid timber (ST), the failure following the elastic regime is either brittle or ductile, both considered with a multisurface failure criterion developed by [2]. With the material definitions used, the simulations were able to predict the maximum load-bearing capacities and failure mechanisms.

In the next chapters, Publications 1-4 are presented followed by a summary of the key findings as well as an outlook to future research studies.

Die approbierte gedruckte Originalversion dieser Dissertation ist an der TU Wien Bibliothek verfügbar.
The approved original version of this doctoral thesis is available in print at TU Wien Bibliothek.
TU Bibliothek Your knowledge hub WIEN

Contribution by the author

This thesis consists of four publications (either submitted or already published) in peer-reviewed scientific journals. The author's contributions to the respective publications are as follows:

- **Publication 1:** *Finite-element-based moisture transport model for wood including free water above the fiber saturation point [3]*: The author greatly contributed to the development and validated the transport model, performed all computations and prepared most of the manuscript.
- **Publication 2:** *Numerical assessment of wood moisture content-based assignments to service classes in EC 5 and a prediction concept for moisture-induced stresses solely using relative humidity data [4]*: The author greatly contributed to the development of the concept, performed most computations and prepared most of the manuscript.
- **Publication 3:** *Finite-element-based prediction of moisture-induced crack patterns for cross sections of solid wood and glued laminated timber exposed to a realistic climate condition [5]*: The author co-developed the concept, performed most computations and prepared most of the manuscript.
- **Publication 4:** *Finite-element-based concept to predict stiffness, strength, and failure of wood composite I-joist beams under various loads and climatic conditions [6]*: The author co-developed the numerical concept, performed all computations and prepared most of the manuscript.

Die approbierte gedruckte Originalversion dieser Dissertation ist an der TU Wien Bibliothek verfügbar.
The approved original version of this doctoral thesis is available in print at TU Wien Bibliothek.
TU Bibliothek Your knowledge hub WIEN

Die approbierte gedruckte Originalversion dieser Dissertation ist an der TU Wien Bibliothek verfügbar.
The approved original version of this doctoral thesis is available in print at TU Wien Bibliothek.

List of symbols

$\boldsymbol{\xi}$	.....	reduction factor tensor due to the cellular structure of wood ( )
$\boldsymbol{C}$	.....	elasticity tensor ($\mathrm{N\,mm^{-2}}$)
$\boldsymbol{D_b}$	.....	diffusion tensor for bound water ($\mathrm{m^2\,s^{-1}}$)
$\boldsymbol{D_v}$	.....	diffusion tensor for water vapor ($\mathrm{m^2\,s^{-1}}$)
$\boldsymbol{D_{bT}}$	.....	diffusion tensor for bound water (Soret effect) ($\mathrm{kg\,m^{-1}\,s^{-1}\,K^{-1}}$)
$\boldsymbol{f}$	.....	heat flux ($\mathrm{W\,m^{-2}}$)
$\boldsymbol{J_b}$	.....	bound water flux ($\mathrm{kg\,m^{-2}\,s^{-1}}$)
$\boldsymbol{J_v}$	.....	water vapor flux ($\mathrm{kg\,m^{-2}\,s^{-1}}$)
$\boldsymbol{J_w}$	.....	free water flux ($\mathrm{kg\,m^{-2}\,s^{-1}}$)
$\boldsymbol{K_0}$	.....	directional coefficient tensor for conductivity ( )
$\boldsymbol{K_r}$	.....	relative permeability tensor ( )
$\boldsymbol{K_w}$	.....	absolute permeability tensor ($\mathrm{m^2}$)
$\boldsymbol{K}$	.....	conductivity tensor ($\mathrm{W\,m^{-1}\,K^{-1}}$)
$\dot{c}_{bv}$	.....	sorption rate bound water - water vapor ($\mathrm{kg\,m^{-3}\,s^{-1}}$)
$\dot{c}_{wb}$	.....	sorption rate free water - bound water ($\mathrm{kg\,m^{-3}\,s^{-1}}$)
$\dot{c}_{wv}$	.....	evaporation/condensation rate free water - water vapor ($\mathrm{kg\,m^{-3}\,s^{-1}}$)
$\frac{\partial}{\partial \boldsymbol{x}}$	.....	gradient w.r.t. directions ($\mathrm{m^{-1}}$)
μ_w	.....	dynamic viscosity of water ($\mathrm{Pa\,s}$)
$\overline{h}_b$	.....	average enthalpy of bound water ($\mathrm{J\,kg^{-1}}$))
ϕ_T	.....	boundary heat flux ($\mathrm{W\,m^{-2}}$)
ϕ_v	.....	boundary flux of water vapor ($\mathrm{kg\,m^{-2}\,s^{-1}}$)
ϕ_w	.....	boundary flux of free water ($\mathrm{kg\,m^{-2}\,s^{-1}}$)
ρ_a	.....	density of dry air ($\mathrm{kg\,m^{-3}}$)
ρ_d	.....	density of dry wood ($\mathrm{kg\,m^{-3}}$)
ρ_{cwm}	.....	density of dry cell wall material ($\mathrm{kg\,m^{-3}}$)
ρ_{H_2O}	.....	density of water ($\mathrm{kg\,m^{-3}}$)
φ	.....	relative humidity ( )
c_b	.....	bound water concentration ($\mathrm{kg\,m^{-3}}$)
c_v	.....	water vapor concentration ($\mathrm{kg\,m^{-3}}$)
c_w	.....	free water concentration ($\mathrm{kg\,m^{-3}}$)
c_{p_a}	.....	specific isobaric heat capacity of dry air ($\mathrm{J\,kg^{-1}\,K^{-1}}$)
c_{p_s}	.....	specific isobaric heat capacity of solid material matrix ($\mathrm{J\,kg^{-1}\,K^{-1}}$)
c_{p_w}	.....	specific isobaric heat capacity of water ($\mathrm{J\,kg^{-1}\,K^{-1}}$)
$c_{v,0}$	.....	surrounding water vapor concentration ($\mathrm{kg\,m^{-3}}$)
$c_{v_{sat}}$	.....	saturated water vapor concentration ($\mathrm{kg\,m^{-3}}$)
$c_{w,0}$	.....	surrounding free water concentration ($\mathrm{kg\,m^{-3}}$)
E_b	.....	activation energy of bound water ($\mathrm{J\,mol^{-1}}$)

Die approbierte gedruckte Originalversion dieser Dissertation ist an der TU Wien Bibliothek verfügbar.
The approved original version of this doctoral thesis is available in print at TU Wien Bibliothek.
TU Bibliothek Your knowledge hub WIEN

$f_{lum_{gas}}$ ..... volume fraction of gaseous part of the lumen ( )
f_{lum} ..... volume fraction of the lumen ( )
h_b ..... enthalpy of bound water ($\mathrm{J\,kg^{-1}}$)
h_v ..... enthalpy of water vapor ($\mathrm{J\,kg^{-1}}$)
h_w ..... enthalpy of water ($\mathrm{J\,kg^{-1}}$)
k_T ..... heat transfer coefficient ($\mathrm{W\,m^{-2}\,K^{-1}}$)
k_{c_v} ..... mass transfer coefficient for water vapor ($\mathrm{m\,s^{-1}}$)
k_{c_w} ..... mass transfer coefficient for free water ($\mathrm{m\,s^{-1}}$)
M_{H_2O} ..... molar mass of water ($\mathrm{g\,mol^{-1}}$)
p_{atm} ..... atmospheric air pressure (Pa)
P_c ..... capillary pressure (Pa)
P_g ..... pressure of gas phase (Pa)
$p_{v_{air}}$ ..... water vapor pressure (Pa)
R ..... universal gas constant ($\mathrm{J\,mol^{-1}\,K^{-1}}$)
R_{air} ..... specific gas constant for dry air ($\mathrm{J\,kg^{-1}\,K^{-1}}$)
S_w ..... saturation of lumen ( )
T ..... temperature (K)
t ..... time (s)
T_0 ..... surrounding temperature (K)
t_{wv} ..... residual free water evaporation time (s)
$X_{b,eq}$ ..... equilibrium moisture content ( )
EC 5 ..... Eurocode 5 [7]
EMC ..... equilibrium moisture content
FSP ..... fiber saturation point
GLT ..... glued laminated timber
MC ..... moisture content
NMR ..... nuclear magnetic resonance
RVE ..... representative volume element
ST ..... solid timber
XFEM ..... extended finite element method

Die approbierte gedruckte Originalversion dieser Dissertation ist an der TU Wien Bibliothek verfügbar.
The approved original version of this doctoral thesis is available in print at TU Wien Bibliothek.
TU Bibliothek Your knowledge hub WIEN

Die approbierte gedruckte Originalversion dieser Dissertation ist an der TU Wien Bibliothek verfügbar.
The approved original version of this doctoral thesis is available in print at TU Wien Bibliothek.

Publication 1

Finite-element-based moisture transport model for wood including free water above the fiber saturation point [3]

Authored by Maximilian Autengruber, Markus Lukacevic and Josef Füssl

Published in *International Journal of Heat and Mass Transfer*, 161 (2020), 120228

Abstract: Timber constructions and engineered wood products exhibit a strong moisture-dependent behavior, which needs to be sufficiently describable by models to avoid critical designs. For wood, several models exist, able to describe the specific heat and moisture transfer mechanisms under normal service conditions as well as for particular situations during the production process, like the kiln drying of sawn timber. However, a unified model combining free water transport with the multi-Fickian approach below the fiber saturation point and the corresponding stable numerical implementation able to handle several possible states of water (bound water, water vapor and free water) and applicable to both drying and infiltration problems, is still missing.

In this work, we link models for all those transport processes by reasonable coupling mechanisms. Numerical difficulties occurring at transition between different states of water are handled appropriately, leading to a stable and reliable simulation tool, which is implemented through a three-dimensional Abaqus user element. Thus, this contribution extends the applicability of heat and moisture simulation tools for wood to more critical service conditions, where wooden components might get into direct contact with free water. This may happen due to insufficient supervision during construction or in the production process of new types of wood composites. We anticipate that with the developed tool potentially critical designs can be identified by simulation instead of by time-consuming experiments or experience. This is of importance because the presence of free water and the resulting reduction in stiffness and strength is associated with a

higher risk of local failure. This would allow more targeted designs of engineered wood products and efficient optimization strategies, especially with respect to the moisture behavior.

1.1 Introduction

Wood is a naturally grown building material with highly moisture-dependent material properties that differ in three characteristic directions, namely longitudinal, radial and tangential. Additionally, a change in wood moisture content (MC) also leads to a dimensional change, which is also dependent on the material direction. These dimensional changes are called swelling (MC increases, infiltration) and shrinking (MC decreases, drying). Cross-sectional dimension changes are for instance much larger than longitudinal ones. Due to this non-uniform expansion, cracks can be caused by the resulting stresses. In general, water can be present in three different states in wood: free water and water vapor can be found in the lumen and bound water in the cell wall. These three phases of water are interacting with each other. Bound water in the cell wall and water vapor as well as free water in the lumen try to reach an equilibrium state, the equilibrium moisture content (EMC). The MC is defined as the mass of bound water and free water by the oven dry mass of wood, since the water vapor concentration is negligible as it is much smaller than the other contributions [8]. In this paper, the MC is also distinguished between free water MC and bound water MC. The amount of water which is held in the cell wall is limited by the so-called fiber saturation point (FSP). Since dimensional changes are linked to changes in bound water concentration, usually only mechanisms below this point without consideration of free water are studied. These so-called multi-Fickian transport processes below the FSP are well described and have been implemented into several numerical models [8–14] and should be considered in cases with specimen thicker than a few millimeters and also at higher relative humidity levels [8], which occur during the drying process.

Under normal service conditions wood is prevented from getting in contact with water by coatings or appropriate design of construction details. However, in some situations wood might be directly exposed to water. One such case is the use of wood as a scaffold material for concrete constructions. Also during outdoor storage, wood products might be subjected to rainfall or even end up lying in puddles. Other cases could be the leakage of water in bath rooms, which can affect wooden parts of a building or the construction process of a timber-concrete-composite floor, when fresh concrete is poured on a cross-laminated timber plate. In all these cases, MCs significantly higher than the FSP can occur. In general, free water in previously dried wood can only occur due to contact with free water or condensation of water vapor in the course of temperature drops.

Hygrothermal processes in porous media have also been investigated in many other research areas, e.g. in concrete [15–17], bricks [18] and are also in food processing [19–21]. In contrast to wood, a bound water phase with water transport in the solid matrix does not seem to be taken into account for these material types. As explained in [15], unlike concrete for wood, the bound water is separated from the free water, since wood is highly hygroscopic. In [17], chemically bound water is considered part

Die approbierte gedruckte Originalversion dieser Dissertation ist an der TU Wien Bibliothek verfügbar.
The approved original version of this doctoral thesis is available in print at TU Wien Bibliothek.
TU Bibliothek Your knowledge hub WIEN

of the solid skeleton that can be released when heated. In [16], bound water transport was combined with free water together in one phase so that bound water is present for the whole range of water contents and free water is present when the upper limit of the hygroscopic range (which would correspond to the FSP) is exceeded. This approach could also be applied in the context of wood drying, but since the phases are combined, a switch would have to be made when the transport mechanisms change from conditions below the hygroscopic range to conditions above and also the instant equilibrium, which sets the bound water content of the cell wall equal to the FSP, once free water is present, would cause numerical problems and could also be questionable from a physical point of view. Since the bound water content is a function of capillary pressure, this leads to the assumption that, it is not defined as an independent degree of freedom (DOF). Also the models for wood drying described in [15, 22–24] assume an instant equilibrium between the bound water in the cell wall and the water vapor in the lumen during the drying process below the FSP, in contrast to the multi-Fickian approach.

To connect the free water phase to the water vapor phase, two different approaches can be found in literature [25], which are the equilibrium approach, where a sharp moving evaporation front between zones of free water and zones without free water exists, and the non-equilibrium approach, where the evaporation occurs over a zone. Based on the chosen parameters, this zone can also be close to the sharp interface. In [15, 16, 24], the equilibrium approach was chosen with the advantage that the DOFs can be reduced and for instance, free water and water vapor can be combined in a single DOF. However, in food processing, often a time-dependent evaporation rate is used [19–21], which reduces the numerical instabilities. As stated in [19] this approach is easier to implement due to the smooth transition zone. However, the necessary material parameters are rarely found.

In the present work, these mathematical models above the FSP are now combined with the multi-Fickian approach below the FSP to describe the moisture transport processes for all possible MC levels more precisely. To deal with the transition from transport mechanisms above the fiber saturation point to those below (and vice versa), several numerical procedures need to be be implemented [26–28]. A time-dependent evaporation rate is also introduced and fitted to describe the interaction of the free water and water vapor phase.

The resulting model (for moisture transport mechanisms in wood) can then easily be combined with other developments in the field of computational wood mechanics [29, 30]. For example, the moisture uptake and distribution in various wood (product) cross sections and their susceptibility to cracking can be studied with wood-specific failure criteria [31–34]. By including the free water contribution in moisture simulations, not only the water uptake but also the possible accumulation of free water in wooden parts, which are in direct contact to water, can be considered. Those might lead to delayed drying in some regions and, therefore, due to locally decreased strength and stiffness properties, cause critical conditions.

Within this work, first, in Section 1.2.1 the mechanisms and characteristics during drying and infiltration of wood, respectively, are revisited, before in Section 1.2.2 the used mathematical model for several transport processes as well as their numerical implementation are presented. The validation of the model is then shown in Section 1.3, by comparing the numerical results to other published models on the one hand and various

Die approbierte gedruckte Originalversion dieser Dissertation ist an der TU Wien Bibliothek verfügbar.
The approved original version of this doctoral thesis is available in print at TU Wien Bibliothek.
TU Bibliothek Your knowledge hub WIEN

drying and infiltration experiments on the other hand. In Section 1.4 parameter studies, to investigate the mesh dependence and time step as well as numerical parameters introduced are compared. Finally, in Section 1.5 the presented model's performance is discussed and in Section 1.6 concluding remarks and a brief outlook are given.

1.2 Materials and Methods

1.2.1 Moisture transport in wood

Wood is a porous material consisting of cells with lumens, which are surrounded by hygroscopic walls. The cells oriented in the axial direction are called tracheids and are connected at their ends with pits. During the state of green wood, where free water exists, these pits are open and provide a flow path.

During drying, pits are getting closed by the capillary forces when the water meniscus moves through the small openings. Earlywood pits are getting aspirated with a much higher rate than latewood ones. This is related to the thicker cell walls [35]. Aspirated pits can deaspirate, if they get in contact with water again. The percentage of deaspiration depends on the time the piece of wood was dried and the time of contact with water [36]. The drying experiments presented in this paper deal with the drying of green wood, thus the pits are assumed to be open, except for one. For the one validation example, where the drying process was studied for previously dried and rehydrated wood, partially closed pits had to be assumed. Since no reliable material properties regarding free water transport are available for such a situation, they were adapted for this case in order to be able to reproduce the tests as well as possible.

If there is an increase of the relative humidity in the ambient air, the moist air gets through open pores into the lumens of the wood sample. A part of the moist air is getting through the, at least partially, open pits into the porous cell structure, while the other part of the moisture is adsorbed into the cell wall and there transported in terms of bound water. In general, water can be present in three different states in wood: (a) bound water in the cell walls and both (b) water vapor and (c) free water in the lumens. These states are interacting with each other, since the bound water concentration tends to reach an equilibrium state with the water vapor concentration. As soon as free water exists, the water vapor concentration is assumed to reach saturated values quickly.

1.2.1.1 Drying of wood

As described in [37, 38], drying of softwood can be divided into three different zones. At the beginning of the drying process from green wood, where often MCs of more than 100 % prevail, to dry conditions, the free water phase is continuous and the movement of water is described by capillary forces towards an exchange surface [39, 40]. The relative humidity is close to 100 % and thus water vapor diffusion is insignificant [37]. Since the bound water content is coupled to the water vapor content via the time-dependent sorption rate, also the bound water distribution is more or less uniform in this zone [38]. This zone with a continuous free water phase is described as the funicular region in [41].

Die approbierte gedruckte Originalversion dieser Dissertation ist an der TU Wien Bibliothek verfügbar.
The approved original version of this doctoral thesis is available in print at TU Wien Bibliothek.
TU Bibliothek Your knowledge hub WIEN

When the free water path is interrupted during the drying process and capillary transport is thus not possible anymore, the point of irreducible saturation (S_{irr}) is reached, which defines the end of this zone.

As pointed out in [37–39], the mechanisms behind the transport in the second zone, which starts right at S_{irr}, are subject of ongoing discussions. While some approaches neglect transport phenomena in this zone, in [37] a diffusion equation was used to simulate the free water transport. Another approach was made in [41], where the transport of free water in this zone is driven by capillary pressure and therefore the expression for the relative permeability was fitted to experimental results. This led to a slight reduction of the exponent of the relative permeability at the point of irreducible saturation S_{irr} from 2 (above S_{irr}) to 1.8 (below S_{irr}). The end of this zone is reached when there is no free water in the lumen, but theoretically the cell wall is still fully saturated with water. This state is characterized by the FSP and therefore the second zone is by definition between S_{irr} and FSP.

If the drying process continues, in the third zone the MC is lower than the FSP and diffusion of water vapor in the lumens and bound water in the cell walls takes place. According to [9, 11], these two phases are not necessarily in local equilibrium and can be coupled via the sorption rate. This approach is called multi-Fickian.

The point of irreducible saturation relates in case of softwood to a saturation of $S_{irr} = 0.07$ [15, 41], which corresponds to an MC of about 40 %. The free water phase starts to be discontinuous at an MC of about 60 % [40], which relates to $S_{irr} = 0.2$ and it is assumed that up to this point the drying process is driven by heat transfer, followed by a transition phase and further a diffusion controlled drying process below the FSP.

1.2.1.2 Infiltration of wood

While the case of drying is well covered in the literature and sufficient agreement between experiments and models exists, that is not the case for infiltration [42], where it is also stated that the parameters for a single continuum model are difficult to find. In general, it is suggested to model the longitudinal infiltration process in two stages. While large vessels are filled quickly (α-phase), the infiltration into the material surrounding the vessels is much slower (β-phase). This can be described by a so-called double porosity model for infiltration in longitudinal direction, as it is done in [42]. In radial direction ray cells could provide a path for the quick infiltration. For the tangential direction the infiltration process is different, since the cells are only connected by pits. The general three-dimensional case can be modeled with a double permeability model (where two coupled transport processes act in parallel) [42]. This model is mathematically similar to the multi-Fickian approach, since also two coupled transport processes act in parallel but with different processes behind the description of the phases. However, the authors investigated the two types of free water phases without the bound water and water vapor phases. In this work, we focus on the influence of the latter two phases from the multi-Fickian model together with a single free water phase. This modeling approach, which neglects the presence of a β-phase, will be investigated during the infiltration process.

Die approbierte gedruckte Originalversion dieser Dissertation ist an der TU Wien Bibliothek verfügbar.
The approved original version of this doctoral thesis is available in print at TU Wien Bibliothek.
TU Bibliothek Your knowledge hub WIEN

1.2.2 Mathematical model

In this work, for the behavior above the FSP the free water transport is modeled using Darcy's law, where the driving force is the gradient of capillary pressure. In the second zone, between S_{irr} and the FSP, free water transport is assumed to take place as in the first zone, for two reasons: first, the relative permeability values given in [41] differ only slightly between the first and second zone and second, neglecting the transport mechanisms below S_{irr} would make the numerical implementation less stable. The evaporation rate is modeled as time-dependent, whereby no immediate equilibrium between water vapor and free water is assumed. However, the expression for the evaporation rate is chosen to quickly approach saturated water vapor conditions, when free water exists. The time-dependent rate is necessary, since a combination of degrees of freedom (DOF) of both free water and water vapor concentration, would not lead to a numerically stable procedure due to the large differences between these two DOFs. For example, the free water concentration can be up to $600\,\mathrm{kg\,m^{-3}}$, whereas the water vapor concentration is only about $100\,\mathrm{g\,m^{-3}}$ (at 323.15 K). In addition, the change in transport mechanisms from conditions below and above the FSP, which is often handled by introducing an approximation to the Heaviside function [24], would intensify the numerical problems when using a combined DOF.

Below the FSP, in the third zone, coupled transport of bound water and water vapor take place simultaneously and are the predominant transport mechanisms. In the presented model, water vapor and bound water transport are also theoretically possible above the FSP, since they are independent DOFs. However, during drying, since the concentration of water vapor reaches saturated conditions quickly, as shown in Section 1.2.2.4, the contribution of these transport mechanisms is small. The bound water concentration is in equilibrium and equal to the FSP during the first stage of drying and, thus, also no bound water transport takes place during the first and second stage of drying. In case of infiltration, again the water vapor concentration reaches saturation quickly. The bound water concentration approaches the FSP, but not as fast as the water vapor concentration reaches saturation. This allows transport processes to take place theoretically.

As shown in [43] for infiltration in tangential direction, in a first step the MC increases up to the level of the FSP. After that, the infiltration increases the MC slowly. In the area close to the boundary of the specimen, where the free water boundary condition is applied, the adsorption process (described in Section 1.2.1.2) into the denser material is neglected.

In [44] a theory of drying for porous media is proposed, where the concept of volume-averaged transport equations with their macroscopic descriptions is used. For wood, the representative volume element (RVE) is defined at the level of many pores relative to the dry volume of wood [10]. Thus, each phase can be treated as a continuum with the corresponding conservation equations [22]. The three different states of water are defined over the following volumes:

- free water concentration c_w is defined over the whole RVE
- bound water concentration c_b is defined over the whole RVE

Die approbierte gedruckte Originalversion dieser Dissertation ist an der TU Wien Bibliothek verfügbar.
The approved original version of this doctoral thesis is available in print at TU Wien Bibliothek.
TU Bibliothek Your knowledge hub WIEN

- water vapor concentration c_v is defined within the volume of the lumen, which is filled with gas (dry air and water vapor)

1.2.2.1 Assumptions

In this work, for the mathematical model the following assumptions are made:

- Basically, the phases water vapor, bound water and free water are considered independently of each other. They are coupled through phase change terms defined by sorption/condensation/evaporation rates.
- All phases, including the free water above the FSP, are continuous [24].
- All phases have the same temperature at a specific point and time – local thermal equilibrium [22, 23].
- The gaseous volume of the lumen is filled with a mixture of dry air and vapor, which acts like an ideal gas [24].
- The influence of the dry air phase can be neglected, since temperatures are below the boiling point and the transversal permeability for the gaseous phase is above $10^{-16}\,\mathrm{m}^2$ [15]. Under these circumstances, the pressure of the gaseous phase can be treated as constant [45].
- Convection is neglected due to moderate temperature levels. The influence of diffusion on the water vapor transport is much larger than convection, especially at temperatures below 323 K [46].
- Kinetic energies of the phases, work done by body forces and viscous dissipation from the fluid, are negligible [24].
- Gravity is neglected due to the, in comparison, much higher capillary pressure within the wood cells.
- Bound water is treated as a separate phase, with no instant equilibrium between bound water and water vapor.
- If free water exists, the water vapor concentration in the lumen (small volume) is quickly approaching the saturated vapor concentration.
- Water density and FSP are assumed to be not temperature dependent.

In Figure 1.1, the different volume-averaged phases of water are shown schematically. Bound water exists in the cell wall, water vapor and free water in the lumen. The coupling mechanisms between the phases are defined over the whole RVE and given as

- sorption rate $\dot{c}_{wb}$ from free water to bound water and
- sorption rate $\dot{c}_{bv}$ from water vapor to bound water, as well as
- evaporation/condensation rate $\dot{c}_{wv}$ between free water and water vapor.

Die approbierte gedruckte Originalversion dieser Dissertation ist an der TU Wien Bibliothek verfügbar.
The approved original version of this doctoral thesis is available in print at TU Wien Bibliothek.
TU Bibliothek Your knowledge hub WIEN

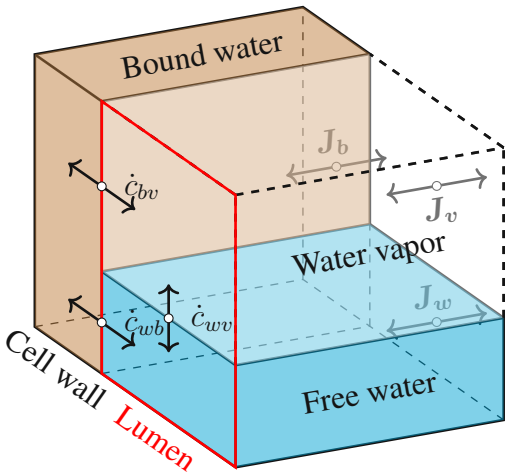

Figure 1.1: Schematic representation of the three different phases of water. Bound water in the cell wall (brown), water vapor and free water in the lumen. The interactions between the phases are characterized by the sorption rates $\dot{c}_{wb}$ from free to bound water, $\dot{c}_{bv}$ from water vapor to bound water and evaporation/condensation rate $\dot{c}_{wv}$ between free water and water vapor. Also depicted are the fluxes of free water $\boldsymbol{J_w}$, bound water $\boldsymbol{J_b}$ and water vapor $\boldsymbol{J_v}$.

While $\dot{c}_{wb}$ acts only within the volume of the free water, $\dot{c}_{bv}$ acts in the rest of the lumen. This is taken into account with the saturation of the lumen S_w.

The fluxes via the boundaries of the RVE are free water flux $\boldsymbol{J_w}$, bound water flux $\boldsymbol{J_b}$ and water vapor flux $\boldsymbol{J_v}$. In addition to the mass conservation equations, a total energy conservation equation with the heat flux $\boldsymbol{f}$, which is described with the process of thermal conduction, is also included. $\frac{\partial}{\partial \boldsymbol{x}}$ denotes the gradient with respect to the directions. The governing equations over the whole RVE follow as:

Conservation of bound water concentration:

$$\frac{\partial c_b}{\partial t} = -\frac{\partial}{\partial \boldsymbol{x}} \cdot \boldsymbol{J_b} + \dot{c}_{bv} + \dot{c}_{wb} \tag{1.1}$$

Conservation of water vapor concentration:

$$\frac{\partial c_v\, f_{lum_{gas}}}{\partial t} = -\frac{\partial}{\partial \boldsymbol{x}} \cdot \boldsymbol{J_v}\, f_{lum_{gas}} - \dot{c}_{bv} + \dot{c}_{wv} \tag{1.2}$$

Conservation of free water concentration:

$$\frac{\partial c_w}{\partial t} = -\frac{\partial}{\partial \boldsymbol{x}} \cdot \boldsymbol{J_w} - \dot{c}_{wb} - \dot{c}_{wv} \tag{1.3}$$

Die approbierte gedruckte Originalversion dieser Dissertation ist an der TU Wien Bibliothek verfügbar.
The approved original version of this doctoral thesis is available in print at TU Wien Bibliothek.
TU Bibliothek Your knowledge hub WIEN

Conservation of energy:

$$\begin{aligned}\frac{\partial \rho\, h}{\partial t} = &- \frac{\partial}{\partial \boldsymbol{x}} \cdot \boldsymbol{f} \\ &- \frac{\partial}{\partial \boldsymbol{x}} \cdot \boldsymbol{J_b}\, \overline{h}_b - \frac{\partial}{\partial \boldsymbol{x}} \cdot \boldsymbol{J_v}\, h_v\, f_{lum_{gas}} - \frac{\partial}{\partial \boldsymbol{x}} \cdot \boldsymbol{J_w}\, h_w \\ &+ \dot{c}_{bv}\,(h_v - h_b) + \dot{c}_{wb}\,(h_w - h_b) + \dot{c}_{wv}\,(h_w - h_v)\end{aligned} \tag{1.4}$$

The terms on the left-hand sides of Equations (1.1) to (1.4) account for the change of concentration/energy over time ∂t, which can be described as accumulation. In (1.4), $\overline{h}_b$ is the averaged enthalpy of bound water and h_b the specific enthalpy of bound water. h_v and h_w are the specific enthalpies of water vapor and free water, respectively. $f_{lum_{gas}}$ takes into account the definition of the water vapor concentration within the gaseous part of the lumen.

1.2.2.2 Description of the transport phenomena and material parameters

1.2.2.2.1 Bound water:

The bound water flux is given in [47] as

$$\boldsymbol{J_b} = -\boldsymbol{D_b} \cdot \frac{\partial c_b}{\partial \boldsymbol{x}} - \boldsymbol{D_{bT}} \cdot \frac{\partial T}{\partial \boldsymbol{x}}, \tag{1.5}$$

where both terms on the right hand side describe diffusion processes. The first term describes the bound water flux in isothermal cases, where it is driven by the gradient of the bound water concentration, the second term accounts for the Soret effect, which describes the bound water driven by a thermal gradient.

The diffusion tensor for bound water $\boldsymbol{D_b}$ is calculated according to [10] as

$$\boldsymbol{D_b} = \boldsymbol{D_0}\, \exp\left(\frac{-E_b}{RT}\right). \tag{1.6}$$

R is the universal gas constant with $8.314\,\mathrm{J\,mol^{-1}\,K^{-1}}$ and E_b the activation energy of bound water according to [35]. Its value decreases with increasing bound water concentration, since the bonding energy at the sorption sites decreases [10]. $\boldsymbol{D_{bT}}$ is defined in [47] using the temperature dependence of the concentration of activated bound water molecules resulting in

$$\boldsymbol{D_{bT}} = \boldsymbol{D_0}\, \frac{c_b\, E_b}{RT^2}\, \exp\left(\frac{-E_b}{RT}\right). \tag{1.7}$$

The activation energy for bound water diffusion is given as

$$E_b = 38500 - 29000\, \frac{c_b}{\rho_d}, \tag{1.8}$$

where ρ_d is the dry density of the wood species.

Die approbierte gedruckte Originalversion dieser Dissertation ist an der TU Wien Bibliothek verfügbar.
The approved original version of this doctoral thesis is available in print at TU Wien Bibliothek.
TU Bibliothek Your knowledge hub WIEN

1.2.2.2.2 Water vapor:

The water vapor flux, which is also a diffusion driven process, is given as

$$\boldsymbol{J_v} = -\boldsymbol{D_v} \cdot \frac{\partial c_v}{\partial \boldsymbol{x}}, \tag{1.9}$$

i.e. it is driven by the gradient of the concentration of water vapor according to Fick's first law. Since the model in this paper is used at moderate temperatures, convective effects are neglected. The expression from [48] for diffusion from vapor in moist air is used and multiplied by the direction-dependent reduction factor $\boldsymbol{\xi}$, taking into account the cellular structure of wood. The diffusion tensor for water vapor $\boldsymbol{D_v}$ is then calculated according to [9, 10] with

$$\boldsymbol{D_v} = \boldsymbol{\xi} \left(2.31 \cdot 10^{-5} \frac{p_{atm}}{p_{atm} + p_{v_{air}}} \left(\frac{T}{273} \right)^{1.81} \right), \tag{1.10}$$

where

$$p_{v_{air}} = c_v \frac{RT}{M_{H_2O}}. \tag{1.11}$$

The atmospheric air pressure p_{atm} depends on the location, whereas the vapor pressure $p_{v_{air}}$ is based on the vapor concentration c_v and converted using the universal gas constant R and the molar mass of water $M_{H_2O} = 18.015\,\mathrm{g\,mol^{-1}}$. The saturated water vapor concentration is defined based on the expression of the saturated vapor pressure from [49, 50] with

$$\begin{aligned} c_{v_{sat}} = & \frac{M_{H_2O}}{RT} 2.2064 \cdot 10^7 \exp\left\{ \frac{647.14}{T} \left(-7.85823 + 1.83991 \cdot \tau^{1.5} \right.\right. \\ & \left.\left. -11.7811 \cdot \tau^3 + 22.6705 \cdot \tau^{3.5} - 15.9393 \cdot \tau^4 + 1.77516 \cdot \tau^{7.5} \right) \right\} \end{aligned} \tag{1.12}$$

where

$$\tau = 1 - \frac{T}{647.14}. \tag{1.13}$$

1.2.2.2.3 Free water:

The flow of free water in wood is modeled according to Darcy's law driven by the gradient of the difference of gaseous pressure P_g and capillary pressure P_c, resulting in

$$\boldsymbol{J_w} = -\rho_{H_2O} \frac{\boldsymbol{K_r} \cdot \boldsymbol{K_w}}{\mu_w} \cdot \frac{\partial P_g - P_c}{\partial \boldsymbol{x}}, \tag{1.14}$$

with absolute $\boldsymbol{K_w}$ and relative permeability $\boldsymbol{K_r}$, respectively. ρ_{H_2O} is the density of water in $\mathrm{kg\,m^{-3}}$.

The equation for the dynamic viscosity of water is given in [51] as

$$\mu_w = 2.414 \cdot 10^{-5} \cdot 10^{\frac{247.8}{T-140}}. \tag{1.15}$$

Die approbierte gedruckte Originalversion dieser Dissertation ist an der TU Wien Bibliothek verfügbar.
The approved original version of this doctoral thesis is available in print at TU Wien Bibliothek.
TU Bibliothek Your knowledge hub WIEN

The expression for the capillary pressure was determined in [52] with

$$P_c = 12400\, S_w^{-0.61}. \tag{1.16}$$

The saturation of the lumen S_w, which is the volume proportion filled with free water c_w, is calculated as

$$S_w = \frac{c_w}{f_{lum}\, \rho_{H_2O}}. \tag{1.17}$$

The volume proportion of the cell lumen f_{lum} is defined according to [53] depending on the bound water concentration c_b, which follows as

$$f_{lum} = 1 - \left(\rho_d \frac{1 + \frac{c_b}{\rho_d}}{1 + 0.84\, c_b} \right) \frac{1}{\rho_{cwm}}, \tag{1.18}$$

where ρ_{cwm} is the density of the pure cell wall material and is about $1530\,\mathrm{kg\,m^{-3}}$, independent of the wood species [11, 35].

The volume proportion of f_{lum} filled with gas (dry air and water vapor) depends on the saturation of free water S_w and results in

$$f_{lum_{gas}} = f_{lum}\,(1 - S_w). \tag{1.19}$$

1.2.2.2.4 Thermal conduction:

Heat transfer is described by conduction $\boldsymbol{f}$ and driven by the gradient of the temperature, reading

$$\boldsymbol{f} = -\boldsymbol{K} \cdot \frac{\partial T}{\partial \boldsymbol{x}}. \tag{1.20}$$

The conduction tensor $\boldsymbol{K}$ is calculated according to [15] as

$$\boldsymbol{K} = \boldsymbol{K_0} \left(0.142 + 0.46\, \frac{c_w + c_b}{\rho_d} \right). \tag{1.21}$$

1.2.2.3 Description of thermodynamic properties

The following equations were used to determine the thermodynamic properties for specific isobaric heat capacities c_p and enthalpies h. The reference state is set to 273.15 K and 101,325 Pa. For free water these values are defined as

$$\begin{aligned} c_{p_w} &= 4.185\,\mathrm{J\,kg^{-1}\,K^{-1}} \text{ and} \\ h_w &= c_{p_w}\,(T - 273.15\,\mathrm{K}). \end{aligned} \tag{1.22}$$

The heat capacity for the cell wall material in $\mathrm{J\,kg^{-1}\,K^{-1}}$ is given by [54] as

$$c_{p_s} = -0.60453 + 0.006714\, T. \tag{1.23}$$

The expression for the enthalpy of water vapor h_v in $\mathrm{J\,kg^{-1}}$ between 273.15 K and 373.15 K is described in [49] as

$$h_v = 2060.5 + 1.3798\, T + 0.84808 \cdot 10^{-4}\, T^2. \tag{1.24}$$

Die approbierte gedruckte Originalversion dieser Dissertation ist an der TU Wien Bibliothek verfügbar.
The approved original version of this doctoral thesis is available in print at TU Wien Bibliothek.
TU Bibliothek Your knowledge hub WIEN

The expression for the specific enthalpy for bound water h_b in $\mathrm{J\,kg^{-1}}$, depending on the wood species, can be found in [55] and includes enthalpy of free water reduced by the differential heat of sorption. For spruce the following expression can be found in [49]:

$$h_b = h_w - 1146.4 \exp\left(-14.48 \frac{c_b}{\rho_d}\right) \tag{1.25}$$

The average enthalpy of bound water $\overline{h}_b$ includes the integral heat of sorption. It is the area under the curve of the differential heat of sorption up to the bound water concentration c_b. The curve has its maximum value at the dry state and is zero at the MC equal to the FSP. According to [23, 24, 49], $\overline{h}_b$ in $\mathrm{J\,kg^{-1}}$ follows as

$$\begin{aligned} \overline{h}_b &= \frac{1}{c_b} \int_0^{c_b} h_b \, dc_b \\ &= -1143.1 + 4.185\,T \\ &\quad - \frac{79.172\,\rho_d \left(1 - \exp\left(-14.48 \frac{c_b}{\rho_d}\right)\right)}{c_b}. \end{aligned} \tag{1.26}$$

The numerator of the term describing the change of the internal energy $\rho\, h$ over time increment Δt can be described as

$$\begin{aligned} (\rho\, h)_{t+\Delta t} - (\rho\, h)_t = {} & \rho_d\, c_{p_s} \left(T_{t+\Delta t} - T_t\right) \\ & + c_{b_{t+\Delta t}}\, \overline{h}_{b_{t+\Delta t}} - c_{b_t}\, \overline{h}_{b_t} \\ & + c_{v_{t+\Delta t}}\, h_{v_{t+\Delta t}}\, f_{lum_{gas_{t+\Delta t}}} - c_{v_t}\, h_{v_t}\, f_{lum_{gas_t}} \\ & + c_{w_{t+\Delta t}}\, h_{w_{t+\Delta t}} - c_{w_t}\, h_{w_t}. \end{aligned} \tag{1.27}$$

1.2.2.4 Interaction between phases

In Figure 1.1 it is shown that the different phases of water in wood are interconnected. Since they might not be in equilibrium, phase changes can occur.

1.2.2.4.1 Bound water and water vapor:

In the presented model the description of [9, 12, 56] for the sorption rate is used, which is briefly described in the following. A certain relative humidity φ is connected to an EMC denoted by $X_{b,eq}$. This connection is defined with a sorption isotherm. Here the definition by [57] for the isotherms is used which is given as

$$X_{b,eq} = \frac{\varphi}{f_1 + f_2\,\varphi + f_3\,\varphi^2}. \tag{1.28}$$

The shape factors f_1, f_2 and f_3 are determined experimentally and described in Section 1.3. The relationship between $X_{b,eq}$ and the corresponding concentration $c_{b,eq}$ as well as the relation c_v to φ are:

$$\begin{aligned} c_{b,eq} &= X_{b,eq}\,\rho_d \\ c_v &= \varphi\, c_{v_{sat}} \end{aligned} \tag{1.29}$$

Die approbierte gedruckte Originalversion dieser Dissertation ist an der TU Wien Bibliothek verfügbar.
The approved original version of this doctoral thesis is available in print at TU Wien Bibliothek.
TU Bibliothek Your knowledge hub WIEN

The sorption rate $\dot{c}_{bv}$, which is the amount of water per time that changes phase, is calculated with the moisture-dependent reaction function H_{bv}, reading

$$\dot{c}_{bv} = H_{bv}\,(c_{b,eq} - c_b). \tag{1.30}$$

Depending on whether there is adsorption or desorption the parameter H_{bv} can be calculated as:

$$H_{bv} = \begin{cases} \text{if } c_b < c_{b,eq} \text{ adsorption:} \\ C_{bv,1}\ \exp\left(-C_{bv,2}\left(\dfrac{c_b}{c_{b,eq}}\right)^{C_{bv,3}}\right) + C_{bv,4} \\ \text{if } c_b > c_{b,eq} \text{ desorption:} \\ C_{bv,1}\ \exp\left(-C_{bv,2}\left(2 - \dfrac{c_b}{c_{b,eq}}\right)^{C_{bv,3}}\right) + C_{bv,4} \end{cases} \tag{1.31}$$

Values for $C_{bv,1}$, $C_{bv,3}$ and $C_{bv,4}$ are constant, whereas $C_{bv,2}$ depends on relative humidity. $C_{bv,2}$ is given as

$$C_{bv,2} = c_{21} \exp\left(c_{22}\,\varphi\right) + c_{23} \exp\left(c_{24}\,\varphi\right), \tag{1.32}$$

with c_{21}, c_{22}, c_{23} and c_{24} being constant.

H_{bv} varies between the maximum value defined by $C_{bv,1} + C_{bv,4}$ and the minimum value $C_{bv,4}$. $C_{bv,2}$ defines the width, where $C_{bv,4}$ is used and $C_{bv,3}$ defines the slope of the smoothing. The values are described in Section 1.3 and were determined by experiments.

Wood under changing climate conditions shows a hysteresis behavior, e.g. during desorption the MC is up to 4 % higher than during adsorption. For problems where both adsorption and desorption occur, a sorption hysteresis has been implemented into the model, which is described in detail in [56, 58] and was also used in [12]. If the hysteresis model used, the material parameters are chosen as given in [56] with d_1 and d_2 as -1.3 and 0.88, respectively and the parameters for the adsorption and desorption isotherm of $f_a, 1 = 1.804$, $f_2 = 13.63$, $f_3 = -12.12$ and $f_1 = 1.886$, $f_2 = 7.884$, $f_3 = -6.526$, respectively. The values for the reaction function H_{bv} are defined according to Section 1.3.

The validation experiments shown in this paper only deal with either adsorption or desorption, thus a sorption hysteresis was not necessary. In addition, for most of the experiments specific isotherms, obtained by fitting to experimental data, were available and should give better results.

1.2.2.4.2 Free water and bound water:

The interaction between free and bound water is considered only in direction from free to bound water since if free water does not exist, water in the lumen is considered as water vapor. When free water exists, the water vapor concentration c_v is assumed to reach quickly the saturated value $c_{v_{sat}}$. In the following this value is used to calculate the sorption rate $\dot{c}_{wb}$ in the same way as described in the previous paragraph.

Die approbierte gedruckte Originalversion dieser Dissertation ist an der TU Wien Bibliothek verfügbar.
The approved original version of this doctoral thesis is available in print at TU Wien Bibliothek.
TU Bibliothek Your knowledge hub WIEN

1.2.2.4.3 Free water and water vapor:

For interaction between free water and water vapor, evaporation from free water to water vapor and condensation from water vapor to free water are modeled. In small volumes, like wooden cells, saturated vapor pressure can be assumed quickly after free water exists. In this paper, the approach to assume a non-instant equilibrium between the two DOF was used, which is easier to implement as stated in [19]. To capture this behavior, an evaporation rate similar to the one previously described between bound water and water vapor is developed.

The evaporation or condensation rate $\dot{c}_{bv}$ is calculated with the water vapor concentration dependent reaction function H_{wv} as

$$\dot{c}_{wv} = H_{wv} \left(c_{v_{sat}} - c_v \right) f_{lum_{gas}}, \tag{1.33}$$

where the volume fraction $f_{lum_{gas}}$ accounts for the definition of the vapor concentration in the gas-filled part of the lumen, whereas $\dot{c}_{wv}$ is defined over the whole RVE. The smoothing of the parameter H_{wv} allows for a better numerical performance, as can be seen in Table 1.3, where a constant value would lead to a higher numerical effort. The evaporation rate $\dot{c}_{wv}$ is limited to the maximum amount of water that can evaporate within a time increment, i.e. $\dot{c}_{wv,max} = c_w/\Delta t$ applies, with c_w as the amount of water at the beginning (for drying) or at the end (for wetting) of the increment and Δt the increment size. So if there is no free water c_w, no evaporation takes place. Since this expression would vary with the size of the time step and thus lead to numerical instabilities, we introduce a so-called residual free water evaporation time t_{wv}, which is subsequently fixed to a value of 36,000 s and which is investigated in a convergence study presented in Section 1.4.3. This means the maximum evaporation rate is now defined as $\dot{c}_{wv,max} = c_w/t_{wv}$.

Depending on whether there is evaporation or condensation the parameter H_{wv} is calculated as follows:

$$H_{wv} = \begin{cases} \text{if } c_v < c_{v_{sat}} \text{ evaporation} \\ C_{wv,1} \exp\left(-C_{wv,2} \left(\dfrac{c_v}{c_{v_{sat}}} \right)^{C_{wv,3}} \right) + C_{wv,4} \\ \text{if } c_v > c_{v_{sat}} \text{ condensation} \\ C_{wv,1} \exp\left(-C_{wv,2} \left(2 - \dfrac{c_v}{c_{v_{sat}}} \right)^{C_{wv,3}} \right) + C_{wv,4} \end{cases} \tag{1.34}$$

Values for $C_{wv,1}$, $C_{wv,2}$, $C_{wv,3}$ and $C_{wv,4}$ are constant. Again, the values for $C_{wv,1}$ and $C_{wv,4}$ define the maximum and minimum value of the reaction function, $C_{wv,2}$ defines the area, where $C_{wv,4}$ is used and the value $C_{wv,3}$ defines the transition between $C_{wv,1}$ and $C_{wv,4}$. The influence of different parameter definitions will be shown in a parameter study in Section 1.4.2.

Die approbierte gedruckte Originalversion dieser Dissertation ist an der TU Wien Bibliothek verfügbar.
The approved original version of this doctoral thesis is available in print at TU Wien Bibliothek.
TU Bibliothek Your knowledge hub WIEN

1.2.2.5 Initial conditions

The initial conditions for the simulations are the initial temperature T_{ini} and the initial water vapor concentration $c_{v,ini}$, which is based on the relative humidity φ_{ini}. In case of initially appearing free water $c_{w,ini} > 0$, the initial water vapor concentration $c_{v,ini}$ is equal to the saturated concentration $c_{v_{sat}}$. The initial bound water concentration $c_{b,ini}$ is chosen to be in equilibrium with the initial water vapor concentration for the later shown validation examples according to the experimental setups, as all samples were equilibrated/treated prior to the experiments.

1.2.2.6 Boundary conditions

All previously described mechanisms, except for the bound water transport, are affected by the climate of the environment, i.e. the bound water flux across the boundary $\phi_b = 0$. Thus, exchange of masses and heat across the boundaries of the sample can take place in terms of heat, free water and water vapor.

In case of infiltration with free water, its flux ϕ_w across the boundary can be determined as

$$\phi_w = k_{c_w} \left(c_w - c_{w,0}\right) f_{lum}, \tag{1.35}$$

where k_{c_w} considers a possible resistance due to e.g. coatings. The boundary condition acts only on the lumen part of the surface, which is considered with f_{lum}, since the structure of wood consists of cellular tubes, i.e. the volume fraction is equal to the surface fraction. $c_{w,0}$ defines the water concentration of the surroundings and its maximum value $c_{w,max}$ is equal to a cell lumen, which is fully saturated with free water:

$$c_{w,max} = f_{lum}\, \rho_{H_2O}. \tag{1.36}$$

As soon as free water exists at the boundary, the water vapor concentration c_v is assumed to quickly approach the saturated concentration. In this case, no boundary condition for water vapor is necessary.

In case of drying or wetting without free water, only a boundary condition for water vapor has to be taken into account, resulting in

$$\begin{aligned} \phi_v &= k_{c_v} \left(c_v - c_{v,0}\right) f_{lum} \text{ and} \\ \phi_w &= 0, \end{aligned} \tag{1.37}$$

where ϕ_v is the water vapor flux across the boundary and k_{c_v} a film boundary coefficient, which considers air flow and convection depending on air speed and surface roughness. $c_{v,0}$ is the water vapor concentration in distant air. Since free water is not present in the mentioned case the gas-filled volume fraction of the lumen is equal to the volume fraction of the total lumen .

In case of drying of samples with free water, the water vapor concentration of the surrounding air is less than the concentration within the lumen, which is equal to the saturated vapor concentration. When the concentrations start to decrease because of the boundary condition, free water in the lumen evaporates and increases the vapor concentration up to the saturated level. Thus, as long as free water exists, only the free

Die approbierte gedruckte Originalversion dieser Dissertation ist an der TU Wien Bibliothek verfügbar.
The approved original version of this doctoral thesis is available in print at TU Wien Bibliothek.
TU Bibliothek Your knowledge hub WIEN

water concentration is decreasing and evaporates directly to the surrounding air. The evaporation process causes a significant drop in temperature due to the phase change process of water.

First, the wet bulb temperature is reached and kept constant as long as free water is present at the boundary. After the free water is evaporated, the water vapor concentration starts to decrease and the temperature starts to increase to the level of the boundary condition. Numerically, if the boundary condition were applied to the water vapor concentration DOF instead of to the free water DOF, the wet-bulb temperature would not be reached because the water vapor concentration of the node at the boundary decreases towards the value of the boundary condition $c_{v,0}$. This would reduce the amount of evaporating water and lead to higher temperatures than the wet-bulb temperature. However, inside the sample, the values stay at the initial level due to the evaporation rate defined in Section 1.2.2.4. The approach from [21], where a boundary condition was applied to the water vapor and free water DOF, respectively, was also not able to reach the theoretical wet-bulb temperature based on the same reason as previously described and led to the following procedure. Thus, a mechanism must be defined that applies the boundary condition to the free water DOF as long as it exists and then switches to the water vapor DOF. Since a Heaviside step function might lead to numerical instabilities, a smoothing function, shown in (1.38), was chosen following the same concept as the previously shown reaction function H_{bv} in Section 1.2.2.4. In Figure 1.2 two examplary functions are shown with two different sets of parameters for $C_{\alpha,1}$ and $C_{\alpha,2}$. To determine an optimal set of parameters, a study with 35 combinations of different values for $C_{\alpha,1}$ and for $C_{\alpha,2}$, varying both from 1e1 to 1e5, was conducted, showing that the influence of $C_{\alpha,1}$ decreases with larger values of $C_{\alpha,2}$. About half of the parameter combinations proved to be unacceptable as they either did not converge or produced results far off the expected wet-bulb temperature. However, the remaining sets provided similar results with differences of less than 0.5 h for the start time of the temperature increase after the removal of free water at the boundary. The parameter combinations, where $C_{\alpha,2}$ was 1e5, yielded the best results, but at the highest numerical costs with 5000 to 8000 increments and 4000 s to 7000 s of CPU time for a simulation of 50 h of drying. In contrast, when using $C_{\alpha,2} = 1e3$, only about 800 increments and 500 s of time were necessary to complete the simulation with almost no loss in accuracy. The parameters were set to $C_{\alpha,1} = 20$ and $C_{\alpha,2} = 1e3$, respectively, and lead to an α_k of less than 1e-8 if free water is zero and 1 if the free water content is larger than $10\,\mathrm{kg\,m^{-3}}$. Thus, this combination is able to predict and hold the wet-bulb temperature as shown in Figure 1.5. Also in case of the other validation examples of the drying processes from Section 1.3.3 to Section 1.3.5 the results can be predicted realistically.

$$\alpha_k = \exp(-C_{\alpha,1}\,(1 - c_w/1000)^{C_{\alpha,2}}). \tag{1.38}$$

The boundary condition ϕ_w defines the evaporation rate within the fraction f_{lum}. The term $(1-\alpha_k)$ is used for the water vapor boundary condition, which has very small values if c_w exists, and is 1 if only water vapor exists. With the consideration of α_k the boundary conditions read as

$$\begin{aligned} \phi_v &= k_{c_v}\,(c_v - c_{v,0})\,f_{lum}\,(1-\alpha_k), \\ \phi_w &= k_{c_v}\,(c_{v_{sat}} - c_{v,0})\,f_{lum}\,\alpha_k. \end{aligned} \tag{1.39}$$

Die approbierte gedruckte Originalversion dieser Dissertation ist an der TU Wien Bibliothek verfügbar.
The approved original version of this doctoral thesis is available in print at TU Wien Bibliothek.
TU Bibliothek Your knowledge hub WIEN

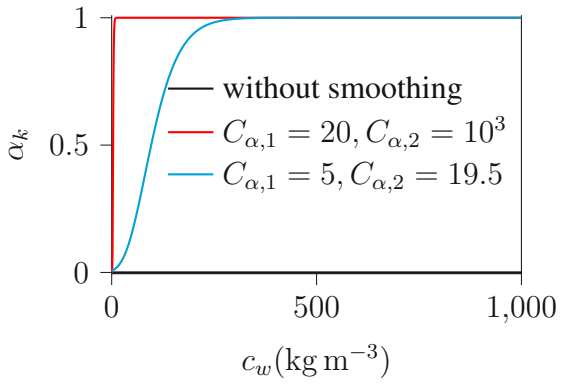

Figure 1.2: Smoothing function for the boundary condition.

As mentioned, it is assumed that the boundary condition for water vapor starts to act if free water is not present any more ($f_{lum_{gas}} = f_{lum}$).

In terms of the energy equation, the previously described processes are taken into account with their enthalpies. As a result, a heat transfer boundary condition must also be applied. Thus, the energy flux across the boundary is defined as

$$\begin{aligned} \phi_T = {} & k_T \left(T - T_0\right) \\ & + k_{c_v} \left(c_v - c_{v,0}\right) f_{lum} \left(1 - \alpha_k\right) h_v \\ & + k_{c_v} \left(c_{v_{sat}} - c_{v,0}\right) f_{lum}\, \alpha_k\, h_v \\ & + k_{c_w} \left(c_w - c_{w,0}\right) f_{lum}\, h_w, \end{aligned} \tag{1.40}$$

where ϕ_T is the heat flux across the boundary, k_T the heat transfer coefficient and T_0 the temperature of the distant air. The boundary term for ϕ_w uses the enthalpy of water vapor h_v since the moisture loss is due to evaporation. The enthalpy relations are defined according to Section 1.2.2.3.

As shown in Section 1.3.2, the process of cooling due to evaporation is limited by the so-called wet bulb temperature. This is the temperature, where the loss of heat due to evaporation at the boundary is equal to the gain of heat due to the convective heat transfer from the boundary condition.

1.2.2.7 Numerical solution

To solve the set of the governing, highly nonlinear partial differential Equations (1.1) to (1.4), the finite element method (FEM) is used. Therefore, the adaptions according to [8, 11] and [59] are made. In the first step the constitutive equations are multiplied with the arbitrary variational fields δc_b, δc_v, $\delta c_w b$, δT and integrated over the arbitrary volume V, reading

$$\int_V \delta c_b \left(\frac{\partial c_b}{\partial t} + \frac{\partial}{\partial \boldsymbol{x}} \cdot \boldsymbol{J_b} - \dot{c}_{bv} - \dot{c}_{wb} \right) dV = 0, \tag{1.41}$$

Die approbierte gedruckte Originalversion dieser Dissertation ist an der TU Wien Bibliothek verfügbar.
The approved original version of this doctoral thesis is available in print at TU Wien Bibliothek.
TU Bibliothek Your knowledge hub WIEN

$$\int_V \delta c_v \left(\frac{\partial c_v \, f_{lum_{gas}}}{\partial t} + \frac{\partial}{\partial \boldsymbol{x}} \cdot \boldsymbol{J_v} \, f_{lum_{gas}} + \dot{c}_{bv} - \dot{c}_{wv} \right) dV = 0, \tag{1.42}$$

$$\int_V \delta c_w \left(\frac{\partial c_w}{\partial t} + \frac{\partial}{\partial \boldsymbol{x}} \cdot \boldsymbol{J_w} + \dot{c}_{wb} + \dot{c}_{wv} \right) dV = 0, \tag{1.43}$$

$$\begin{aligned} \int_V \delta T \Bigg(& \frac{\partial \rho \, h}{\partial t} + \frac{\partial}{\partial \boldsymbol{x}} \cdot \boldsymbol{f} \\ & + \frac{\partial}{\partial \boldsymbol{x}} \cdot \boldsymbol{J_b} \, \overline{h}_b + \frac{\partial}{\partial \boldsymbol{x}} \cdot \boldsymbol{J_v} \, h_v \, f_{lum_{gas}} + \frac{\partial}{\partial \boldsymbol{x}} \cdot \boldsymbol{J_w} \, h_w \\ & - \dot{c}_{bv} \left(h_v - h_b \right) - \dot{c}_{wb} \left(h_w - h_b \right) \\ & - \dot{c}_{wv} \left(h_w - h_v \right) \Bigg) dV = 0. \end{aligned} \tag{1.44}$$

In the next step, the product rule as shown in Equation (1.45) and the divergence theorem as shown in Equation (1.46) for the fluxes as well as their expressions from Section 1.2.2.2 are used.

$$\delta c \frac{\partial}{\partial \boldsymbol{x}} \cdot \boldsymbol{J} = \frac{\partial}{\partial \boldsymbol{x}} \cdot \left(\delta c \, \boldsymbol{J} \right) - \frac{\partial \delta c}{\partial \boldsymbol{x}} \cdot \boldsymbol{J} \tag{1.45}$$

$$\int_V \frac{\partial}{\partial \boldsymbol{x}} \cdot \left(\delta c \, \boldsymbol{J} \right) dV = \int_S \delta c \, \boldsymbol{n} \cdot \boldsymbol{J} dS \tag{1.46}$$

With these adaptions Equations (1.41) to (1.44) can be written as

$$\begin{aligned} & \int_V \delta c_b \frac{\partial c_b}{\partial t} dV \\ & + \int_V \frac{\partial \delta c_b}{\partial \boldsymbol{x}} \cdot \boldsymbol{D_b} \cdot \frac{\partial c_b}{\partial \boldsymbol{x}} dV + \int_V \frac{\partial \delta c_b}{\partial \boldsymbol{x}} \cdot \boldsymbol{D_{bT}} \cdot \frac{\partial T}{\partial \boldsymbol{x}} dV \\ & - \int_V \delta c_b \, \dot{c}_{bv} \, dV - \int_V \delta c_b \, \dot{c}_{wb} \, dV \\ & + \int_S \delta c_b \, \boldsymbol{n} \cdot \boldsymbol{J_b} \, dS = 0, \end{aligned} \tag{1.47}$$

$$\begin{aligned} & \int_V \delta c_v \frac{\partial c_v \, f_{lum_{gas}}}{\partial t} dV + \int_V \frac{\partial \delta c_v}{\partial \boldsymbol{x}} \cdot \boldsymbol{D_v} \cdot \frac{\partial c_v}{\partial \boldsymbol{x}} \, f_{lum_{gas}} \, dV \\ & + \int_V \delta c_v \, \dot{c}_{bv} \, dV - \int_V \delta c_v \, \dot{c}_{wv} \, dV \\ & + \int_S \delta c_v \, \boldsymbol{n} \cdot \boldsymbol{J_v} \, f_{lum_{gas}} \, dS = 0, \end{aligned} \tag{1.48}$$

Die approbierte gedruckte Originalversion dieser Dissertation ist an der TU Wien Bibliothek verfügbar.
The approved original version of this doctoral thesis is available in print at TU Wien Bibliothek.
TU Bibliothek Your knowledge hub WIEN

$$
\begin{aligned}
&\int_V \delta c_w \frac{\partial c_w}{\partial t} dV \\
&+ \int_V \frac{\partial \delta c_w}{\partial \boldsymbol{x}} \cdot \rho_{H_2O} \cdot \frac{\boldsymbol{K_r K_w}}{\mu_w} \cdot \frac{\partial (P_g - P_c)}{\partial \boldsymbol{x}} dV \\
&+ \int_V \delta c_w \, \dot{c}_{wb} \, dV + \int_V \delta c_w \, \dot{c}_{wv} \, dV \\
&+ \int_S \delta c_w \, \boldsymbol{n} \cdot \boldsymbol{J_w} \, dS = 0,
\end{aligned}
\tag{1.49}
$$

$$
\begin{aligned}
&\int_V \delta T \frac{\partial \rho \, h}{\partial t} dV + \int_V \frac{\partial \delta T}{\partial \boldsymbol{x}} \cdot \boldsymbol{K} \cdot \frac{\partial T}{\partial \boldsymbol{x}} dV \\
&+ \int_V \frac{\partial \delta T}{\partial \boldsymbol{x}} \cdot \boldsymbol{D_b} \cdot \frac{\partial c_b}{\partial \boldsymbol{x}} \, \overline{h}_b \, dV \\
&+ \int_V \frac{\partial \delta T}{\partial \boldsymbol{x}} \cdot \boldsymbol{D_{bT}} \cdot \frac{\partial T}{\partial \boldsymbol{x}} \, \overline{h}_b \, dV \\
&+ \int_V \frac{\partial \delta T}{\partial \boldsymbol{x}} \cdot \boldsymbol{D_v} \cdot \frac{\partial c_v}{\partial \boldsymbol{x}} \, h_v \, f_{lum_{gas}} \, dV \\
&+ \int_V \frac{\partial \delta T}{\partial \boldsymbol{x}} \cdot \rho_{H_2O} \cdot \frac{\boldsymbol{K_r K_w}}{\mu_w} \cdot \frac{\partial (P_g - P_c)}{\partial \boldsymbol{x}} \, h_w \, dV \\
&- \int_V \delta T \, \dot{c}_{bv} \, (h_v - h_b) \, dV \\
&- \int_V \delta T \, \dot{c}_{wb} \, (h_w - h_b) \, dV \\
&- \int_V \delta T \, \dot{c}_{wv} \, (h_w - h_v) \, dV \\
&+ \int_S \delta T \, \boldsymbol{n} \cdot \boldsymbol{J_b} \, h_b \, dS + \int_S \delta T \, \boldsymbol{n} \cdot \boldsymbol{J_v} \, h_v \, f_{lum_{gas}} \, dS \\
&+ \int_S \delta T \, \boldsymbol{n} \cdot \boldsymbol{J_w} \, h_w \, dS + \int_S \delta T \, \boldsymbol{n} \cdot \boldsymbol{f} dS = 0.
\end{aligned}
\tag{1.50}
$$

Die approbierte gedruckte Originalversion dieser Dissertation ist an der TU Wien Bibliothek verfügbar.
The approved original version of this doctoral thesis is available in print at TU Wien Bibliothek.
TU Bibliothek Your knowledge hub WIEN

The use of interpolation functions to define the fields of c_b, c_v, c_w and T, only by knowing their nodal values c_b^M, c_v^N, c_w^O and T^P is performed in the next step, as shown in [11]:

$$\begin{aligned}
\delta c_b &= N^M \, \delta c_b^M, \;\; c_b = N^M \, c_b^M \\
\delta c_v &= N^N \, \delta c_v^N, \;\; c_v = N^N \, c_v^N \\
\delta c_w &= N^O \, \delta c_w^O, \;\; c_w = N^O \, c_w^O \\
\delta T &= N^P \, \delta T^P, \;\; T = N^P \, T^P
\end{aligned} \tag{1.51}$$

For the description of the boundary conditions the expressions are defined in [11] as $\boldsymbol{n} \cdot \boldsymbol{J_b} = \phi_b$, $\boldsymbol{n} \cdot \boldsymbol{J_v} \, f_{lum_{gas}} = \phi_v$, $\boldsymbol{n} \cdot \boldsymbol{J_w} = \phi_w$ and $\boldsymbol{n} \cdot \boldsymbol{f} = \phi_T$. In addition, for temporal discretization the backward Euler method is used. This results in

$$\begin{aligned}
F_{c_b}^M = & \frac{1}{\Delta t} \int_V N^M (c_{b,t+\Delta t} - c_{b,t}) \, dV \\
& + \int_V \frac{\partial N^M}{\partial \boldsymbol{x}} \cdot \boldsymbol{D_b} \cdot \frac{\partial c_b}{\partial \boldsymbol{x}} \, dV \\
& + \int_V \frac{\partial N^M}{\partial \boldsymbol{x}} \cdot \boldsymbol{D_{bT}} \cdot \frac{\partial T}{\partial \boldsymbol{x}} \, dV \\
& - \int_V N^M \, \dot{c}_{bv} \, dV - \int_V N^M \, \dot{c}_{wb} \, dV \\
& + \int_S N^M \phi_b \, dS = 0,
\end{aligned} \tag{1.52}$$

$$\begin{aligned}
F_{c_v}^N = & \frac{1}{\Delta t} \int_V N^N (c_{v,t+\Delta t} \, f_{lum_{gas},t+\Delta t} - c_{v,t} \, f_{lum_{gas},t}) \, dV \\
& + \int_V \frac{\partial N^N}{\partial \boldsymbol{x}} \cdot \boldsymbol{D_v} \cdot \frac{\partial c_v}{\partial \boldsymbol{x}} \, f_{lum_{gas},t} \, dV \\
& + \int_V N^N \, \dot{c}_{bv} \, dV - \int_V N^N \, \dot{c}_{wv} \, dV \\
& + \int_S N^N \phi_v \, dS = 0,
\end{aligned} \tag{1.53}$$

Die approbierte gedruckte Originalversion dieser Dissertation ist an der TU Wien Bibliothek verfügbar.
The approved original version of this doctoral thesis is available in print at TU Wien Bibliothek.
TU Bibliothek Your knowledge hub WIEN

$$
\begin{aligned}
F_{c_w}^{O} = & \frac{1}{\Delta t} \int_V N^O (c_{w,t+\Delta t} - c_{w,t})\, dV \\
& + \int_V \frac{\partial N^O}{\partial \boldsymbol{x}} \cdot \rho_{H_2O} \cdot \frac{\boldsymbol{K_r K_w}}{\mu_w} \cdot \frac{\partial (P_g - P_c)}{\partial \boldsymbol{x}}\, dV \\
& + \int_V N^O\, \dot{c}_{wb}\, dV + \int_V N^O\, \dot{c}_{wv}\, dV \\
& + \int_S N^O \phi_w\, dS = 0,
\end{aligned}
\tag{1.54}
$$

Die approbierte gedruckte Originalversion dieser Dissertation ist an der TU Wien Bibliothek verfügbar.
The approved original version of this doctoral thesis is available in print at TU Wien Bibliothek.
TU Bibliothek Your knowledge hub WIEN

$$
\begin{aligned}
F_T^P = & \frac{1}{\Delta t} \int_V N^P \left[(\rho\, h)_{t+\Delta t} - (\rho\, h)_t \right] dV \\
& + \int_V \frac{\partial N^P}{\partial \boldsymbol{x}} \cdot \boldsymbol{K} \cdot \frac{\partial T}{\partial \boldsymbol{x}}\, dV \\
& + \int_V \frac{\partial N^P}{\partial \boldsymbol{x}} \cdot \boldsymbol{D_b} \cdot \frac{\partial c_b}{\partial \boldsymbol{x}}\, \overline{h}_b\, dV \\
& + \int_V \frac{\partial N^P}{\partial \boldsymbol{x}} \cdot \boldsymbol{D_{bT}} \cdot \frac{\partial T}{\partial \boldsymbol{x}}\, \overline{h}_b\, dV \\
& + \int_V \frac{\partial N^P}{\partial \boldsymbol{x}} \cdot \boldsymbol{D_v} \cdot \frac{\partial c_v}{\partial \boldsymbol{x}}\, h_v\, f_{lum_{gas}}\, dV \\
& + \int_V \frac{\partial N^P}{\partial \boldsymbol{x}} \cdot \rho_{H_2O} \cdot \frac{\boldsymbol{K_r K_w}}{\mu_w} \cdot \frac{\partial (P_g - P_c)}{\partial \boldsymbol{x}}\, h_w\, dV \\
& - \int_V N^P\, \dot{c}_{bv}\, (h_v - h_b)\, dV \\
& - \int_V N^P\, \dot{c}_{wb}\, (h_w - h_b)\, dV \\
& - \int_V N^P\, \dot{c}_{wv}\, (h_w - h_v)\, dV \\
& + \int_S N^P \phi_b\, h_b\, dS + \int_S N^P \phi_v\, h_v\, dS \\
& + \int_S N^P \phi_w\, h_w\, dS + \int_S N^P \phi_T\, dS = 0.
\end{aligned}
\tag{1.55}
$$

With the four coupled Equations (1.52) to (1.55) the following system of equations can be established in each integration point:

$$
\begin{bmatrix}
\frac{\partial F^M_{c_b}}{\partial c^Q_b} & \frac{\partial F^M_{c_b}}{\partial c^R_v} & \frac{\partial F^M_{c_b}}{\partial c^S_w} & \frac{\partial F^M_{c_b}}{\partial T^T} \\
\frac{\partial F^N_{c_v}}{\partial c^Q_b} & \frac{\partial F^N_{c_v}}{\partial c^R_v} & \frac{\partial F^N_{c_v}}{\partial c^S_w} & \frac{\partial F^N_{c_v}}{\partial T^T} \\
\frac{\partial F^O_{c_w}}{\partial c^Q_b} & \frac{\partial F^O_{c_w}}{\partial c^R_v} & \frac{\partial F^O_{c_w}}{\partial c^S_w} & \frac{\partial F^O_{c_w}}{\partial T^T} \\
\frac{\partial F^P_T}{\partial c^Q_b} & \frac{\partial F^P_T}{\partial c^R_v} & \frac{\partial F^P_T}{\partial c^S_w} & \frac{\partial F^P_T}{\partial T^T}
\end{bmatrix}
\cdot
\begin{pmatrix} r^Q_{cb} \\ r^R_{cv} \\ r^S_{cw} \\ r^T_T \end{pmatrix}
=
\begin{pmatrix} -F^M_{c_b} \\ -F^N_{c_v} \\ -F^O_{c_w} \\ -F^P_T \end{pmatrix}
\tag{1.56}
$$

Die approbierte gedruckte Originalversion dieser Dissertation ist an der TU Wien Bibliothek verfügbar.
The approved original version of this doctoral thesis is available in print at TU Wien Bibliothek.
TU Bibliothek Your knowledge hub WIEN

The tangent stiffness matrix on the left hand side consists of the derivations of Equations (1.52) to (1.55) with respect to the variables c_b, c_v, c_w and T at the end of the time increment $(t + \Delta t)$. A non-zero value in the off-diagonal entries means a coupling between the corresponding degrees of freedom exists. The vector $\mathbf{r}$ contains the unknown nodal concentrations and temperatures and $\mathbf{F}$ is the incremental load vector. The system of equations is solved by using the modified Newton method in terms of a user element subroutine within the commercial finite element software *Abaqus* [59]. To simulate three-dimensional problems, a hexahedral element with linear shape functions was chosen. Local material directions, arising from the structure of wood can be considered in each integration point. The low order of shape functions is one of the criteria stated in [26] to apply the FEM to this sort of problems.

1.2.2.8 Numerical implementation

During the simulation, free water might not always exist and changes in the equation system occur at the time free water disappears (in case of drying) or appears (in case of infiltration). Thus, numerical problems arise. To deal with these non-linearities the following procedures, as described in [26–28, 60], have to be introduced.

1.2.2.8.1 Upstream weighting:

To avoid oscillating results, upstream weighting for the permeability K_w is used. Since

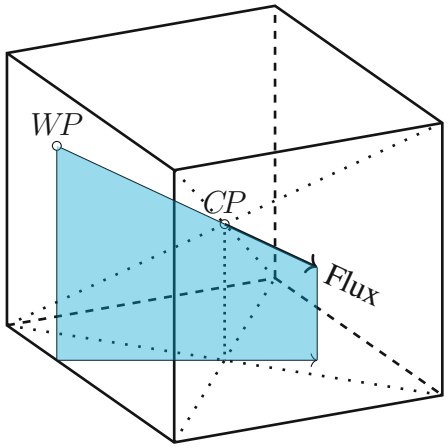

Figure 1.3: Upstream weighting: the weighting point WP is defined at the intersection of the negative flux direction in the central point CP with the element face.

K_w is highly nonlinear and dependent on c_w, huge differences of this value can exist within one element, which can cause oscillations. The position of the weighting point WP is determined as shown in Figure 1.3: in the central point CP the direction of flow of c_w is calculated and in the next step intersected with the boundary of the element. In the resulting weighting point WP, the values of K_w are averaged from the corresponding nodal values. This procedure is described in [60] and [26]. In [27] upstream and central weighting are compared with the conclusion that only upstream weighting is *unconditionally monotone, regardless of mesh or size*.

Die approbierte gedruckte Originalversion dieser Dissertation ist an der TU Wien Bibliothek verfügbar.
The approved original version of this doctoral thesis is available in print at TU Wien Bibliothek.
TU Bibliothek Your knowledge hub WIEN

1.2.2.8.2 Formulation of free water flow:

The free water flow through unsaturated porous media is described with the Richards equation [61], which utilizes the transport description of Darcy's law. This equation can be described in terms of pressure (head), concentration or "mixed", where the pressure gradient and the change in free water concentration over time (or vice versa) are used. The relationship between P_c and c_w is defined via Equation (1.16). The three formulations [26, 28] can be written as

Concentration-based formulation

$$\frac{\partial c_w}{\partial t} = \frac{\partial}{\partial \boldsymbol{x}} \cdot \boldsymbol{D}(c_w) \cdot \frac{\partial c_w}{\partial \boldsymbol{x}}, \tag{1.57}$$

Pressure-based formulation

$$\frac{\partial c_w}{\partial P_c} \frac{\partial P_c}{\partial t} = \frac{\partial}{\partial \boldsymbol{x}} \cdot \boldsymbol{K}(P_c) \cdot \frac{\partial P_c}{\partial \boldsymbol{x}}, \tag{1.58}$$

Mixed formulation

$$\frac{\partial c_w}{\partial t} = \frac{\partial}{\partial \boldsymbol{x}} \cdot \boldsymbol{K}(P_c) \cdot \frac{\partial P_c}{\partial \boldsymbol{x}}. \tag{1.59}$$

[28] states that the pressure-based formulation has significant mass balance errors, since the discretizations of $\frac{\partial c_w}{\partial P_c} \cdot \frac{\partial P_c}{\partial t}$ and $\frac{\partial c_w}{\partial t}$ are not mathematically equivalent, because of the high non-linearity of $\frac{\partial c_w}{\partial P_c}$. Still, the pressure-based formulation is used in general for groundwater problems, since under fully saturated circumstances the concentration-based approach degenerates and material discontinuities generate discontinuous concentration profiles. Further, it is described that the mixed formulation combines mass conservation from the concentration-based approach and the possibility to use it under fully saturated conditions. Thus, the mixed formulation is chosen for the mathematical model.

However, FEM simulations still suffer from oscillations at the moisture front. Therefore, mass lumping is needed as well, which is described in the next paragraph.

1.2.2.8.3 Mass Lumping:

Also in [28], the FEM is compared to the finite difference method. The FEM solution still produced oscillations in the shown examples, which violate the maximum principle. This principle ensures that the maximum value of the solution field is either defined by the initial or the boundary condition. The difference between these two methods is the treatment of the time derivative, which provides a perfect mass balance in case of the FEM. So, when using a diagonalized mass matrix in terms of the FEM, the treatment is the same in both methods and the maximum principle can be fulfilled also with the FEM. The diagonalization of the mass matrix is also called *mass lumping*.

1.3 Model validation

The multi-Fickian approach with the parallel consideration of water vapor and bound water flux below the FSP is well known and validated [9–12, 62]. In this work, the main focus is on the validation of the presented model based on examples including free water above the FSP and the transition from MC values above the FSP to ones below (and vice versa) with the corresponding change of transport mechanisms.

Die approbierte gedruckte Originalversion dieser Dissertation ist an der TU Wien Bibliothek verfügbar.
The approved original version of this doctoral thesis is available in print at TU Wien Bibliothek.
TU Bibliothek Your knowledge hub WIEN

To validate the model, various examples from literature including simulations and experiments were chosen. To avoid extensive individual calibration of the model, a uniform set of material properties (given in Table 1.1) was used, except where were certain parameters were exactly identified/specified. These values are then given in the respective section.

Table 1.1: Diagonal components of the material parameter tensors

Parameter	Component			Ref.
	L	R	T	
$\boldsymbol{K_w}$	$1 \cdot 10^{-12}$	$2 \cdot 10^{-15}$	$1 \cdot 10^{-15}$	[15]
$\boldsymbol{K_r}$	S_w^8	S_w^3	S_w^3	[63]
$\boldsymbol{D_0}$	$2.5 \cdot 7 \cdot 10^{-6}$	$7 \cdot 10^{-6}$	$7 \cdot 10^{-6}$	[12]
$\boldsymbol{\xi}$	0.9	0.11	0.11	[62]
$\boldsymbol{K_0}$	2	2	1	[15]

All considered experiments describe a one-dimensional flow process. In most cases a cylindrical coordinate system was used. In case of drying, the film boundary coefficient for heat transfer k_T is $45\,\mathrm{W\,m^{-2}\,K^{-1}}$ unless otherwise specified in the respective section. The corresponding film boundary coefficient for mass transfer k_{c_v} is calculated using the analogy between heat and mass transfer with the Lewis relation, given as

$$k_{c_v} = \frac{k_T}{\rho_a \, c_{p_a}}, \tag{1.60}$$

where ρ_a is the density of air, R_{air} the specific gas constant of air and c_{p_a} the specific isobaric heat capacity, defined as

$$\begin{aligned} \rho_a &= \frac{p_{atm} - p_v}{R_{air}\, T}, \\ R_{air} &= 287.058\,\mathrm{J\,kg^{-1}\,K^{-1}}, \\ c_{p_a} &= 1009\,\mathrm{J\,kg^{-1}\,K^{-1}}. \end{aligned} \tag{1.61}$$

The atmospheric pressure is set to 101,325 Pa. In most cases, the ad- and/or desorption isotherm was fitted to the given data from the specific experiment.

The values for the sorption rate from free to bound water and water vapor to bound water, respectively, were taken from [62] as $C_{bv,1} = 3.8 \cdot 10^{-4}\,\mathrm{s^{-1}}, C_{bv,3} = 80, C_{bv,4} = 5.94 \cdot 10^{-7}\,\mathrm{s^{-1}}$ and $c_{21} = 3.58, c_{22} = 2.21, c_{23} = 1.59 \cdot 10^{-3}, c_{24} = 14.98$. The initial time increment was selected as 1 s.

In the following, seven different examples from the literature are used to validate the presented model. First, the model is compared with simulations from [8, 10] for conditions below the FSP during a moisture increase. In the second example, the development of temperature and MC for different locations over the simulation time is compared with simulations from [22]. The third example from [38] deals with drying experiments and we compare averaged MCs over time from our model with both experimental values and the model from [38]. Here, the influence of the chosen exponent for the permeability is investigated as well. Validation four is an experiment of a drying process, but in contrast to the previous example, experimental MC profiles are shown along

Die approbierte gedruckte Originalversion dieser Dissertation ist an der TU Wien Bibliothek verfügbar.
The approved original version of this doctoral thesis is available in print at TU Wien Bibliothek.
TU Bibliothek Your knowledge hub WIEN

the specimen and compared with the presented model. Example five from [43] shows profiles during the drying process of previously dried wood, which behaves differently from the other shown drying examples, which started from green wood conditions. The remaining two examples show infiltration processes, once in tangential direction [43] and in longitudinal direction [9].

1.3.1 Simulation Frandsen [10]

To show the accuracy of the presented model below the FSP, we compare our model to results from [10] and [8]. Both simulated a one-dimensional increase in relative humidity from 54 % to 75 % applied to two opposite sides of a sample. Since the air velocity was approximately $3\,\mathrm{m\,s^{-1}}$, the influence of the film boundary layer is negligible and the surface vapor concentration is equal to the air vapor concentration $c_{v,0}$. At the initial state, the bound water concentration is in equilibrium with the water vapor concentration resulting in an initial MC of 8.16 %. The material parameters are chosen as described in Table 1.1, with the exception of the radial and tangential entries for $\boldsymbol{\xi}$, which are set to 0.03. The dry density of wood was $500\,\mathrm{kg\,m^{-3}}$ and the parameters for the sorption isotherm are $f_1 = 2.22$, $f_2 = 15.7$ and $f_3 = -14.0$. In the works of [10] and [8] the sorption rate is defined slightly different based on the vapor pressure p_v, which can be calculated with the relation from Equation (1.11) and is defined as

$$\dot{c}_{bv} = H_{bv}\,(p_v - p_{v,eq}). \tag{1.62}$$

with the reaction function H_{bv} in $\mathrm{kg\,m^{-3}\,Pa^{-1}\,s^{-1}}$ for adsorption

$$H_{bv} = C_{bv,1}\,\exp\left(-C_{bv,2}\left(\frac{p_{v,eq}}{p_v}\right)^{C_{bv,3}}\right) + C_{bv,4}. \tag{1.63}$$

The coefficients are defined according to [10] with $C_{bv,1} = 2.6 \cdot 10^{-6}\,\mathrm{kg\,m^{-3}\,Pa^{-1}\,s^{-1}}$, $C_{bv,3} = 50$, $C_{bv,4} = 8 \cdot 10^{-8}\,\mathrm{kg\,m^{-3}\,Pa^{-1}\,s^{-1}}$ and $c_{21} = 5.22 \cdot 10^{-6}$, $c_{22} = 19$, $c_{23} = 0$, $c_{24} = 0$. Both ways to determine the sorption rate $\dot{c}_{bv}$ are presented in this paper and the results are shown in Figure 1.4. The used finite element model consisted of 1519 nodes and 1080 elements with 6-by-6 elements per cross section and 30 equally distributed elements along the specimen, resulting in an element length of 0.54 mm. 717 increments with a maximum time step of 3600 s were necessary to complete the 29 d of wetting with a total CPU time of 2749 s. Since the experiment is one-dimensional, one element within the cross-section would be sufficient, and by using symmetry conditions, the number of elements could be reduced by a factor of 72, with a corresponding reduction in CPU time. The moisture profiles of all three simulations with the same definition of the sorption rate, stated in Equation (1.62), are depicted in Figure 1.4 and show good agreement. The difference in the models of [8] and [10] is the porosity, which is not taken as constant and the use of a different model for the saturated vapor pressure [8]. Between the model presented in this paper and the model of [8] there are differences in the addition of the energy conservation equation with the corresponding properties as well as the use of upstreaming and lumping procedures. The very small differences in the curves of the presented model and the one from [8] show that the effect of temperature in isothermal conditions below the FSP is negligible. As the energy

Die approbierte gedruckte Originalversion dieser Dissertation ist an der TU Wien Bibliothek verfügbar.
The approved original version of this doctoral thesis is available in print at TU Wien Bibliothek.
TU Bibliothek Your knowledge hub WIEN

conservation equation is included in this paper, a slight temperature increase of 0.04 K after 2 h, when the adsorption process reaches its highest level, as can be seen from the differences between the MC and RH curves, can be observed in Figure 1.4, since the adsorption process acts like a condensation process. The difference in the definition of the sorption rate from Equation (1.30) leads to higher MC values next to the boundary after 2 h. In the center section of the sample and at different points in time, the differences between the two definitions is rather small. In the last shown time steps at 14 d and 29 d, the differences increase slightly to 0.2 % MC due to the different set of used coefficients. The relative humidity profiles of the presented model are compared to other models, showing also in good agreements and similar minor differences as for the MC curves.

Die approbierte gedruckte Originalversion dieser Dissertation ist an der TU Wien Bibliothek verfügbar.
The approved original version of this doctoral thesis is available in print at TU Wien Bibliothek.
TU Bibliothek Your knowledge hub WIEN

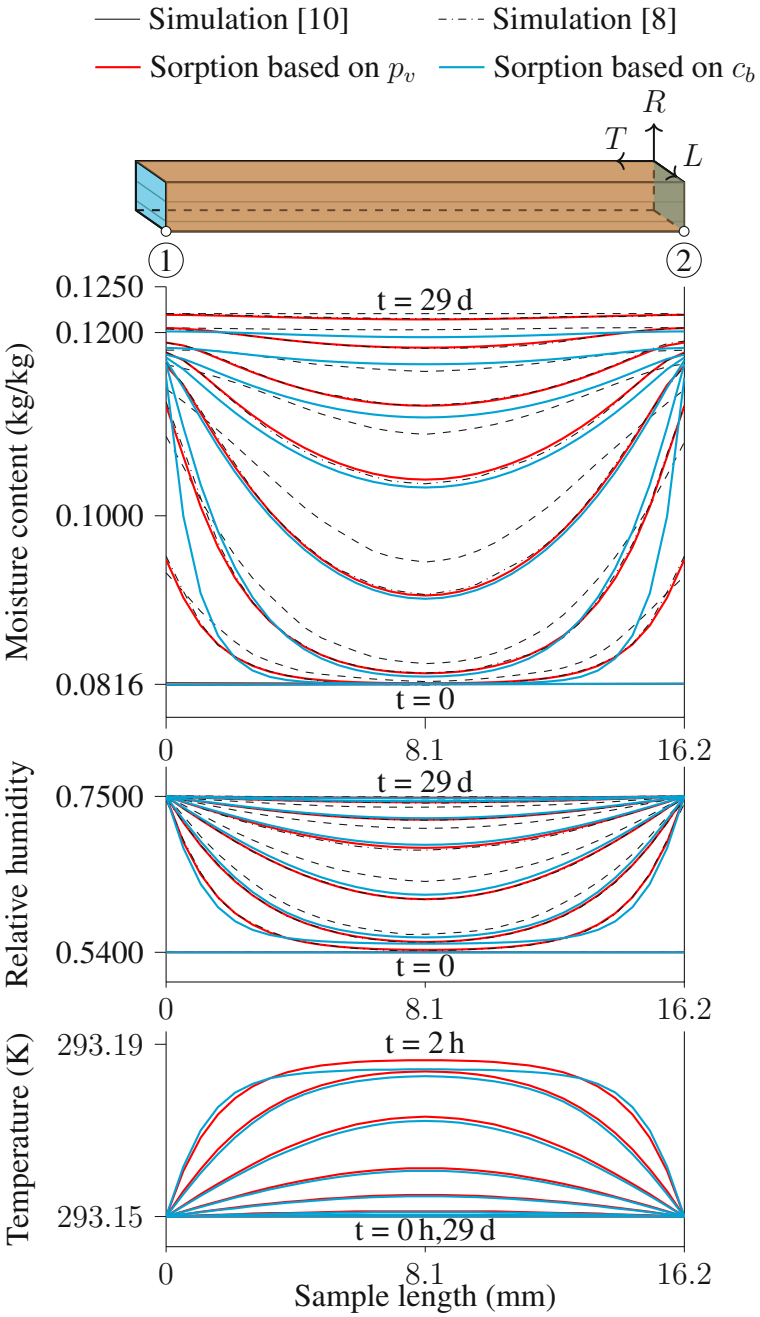

Figure 1.4: Moisture, relative humidity and temperature profiles for one-dimensional increase of relative humidity φ from 54 % to 75 % in tangential direction after 2 h, 10 h, 40 h, 4 d, 7 d, 14 d and 29 d along the path from ① to ②. For the two topmost plots the profiles always increase with each time step, while for the temperature profiles the profiles decrease with each time step after jumping from the marked profiles at 0 h to 2 h. Initial conditions were 8.16 % MC and φ = 54 % at 20 °C. The boundary condition were applied to the left and right surface (blue) with 75 % RH at 20 °C. The boundary conditions are directly applied to the surface due to the high air velocity of 3 $\mathrm{m\,s^{-1}}$. All other surfaces were sealed.

Die approbierte gedruckte Originalversion dieser Dissertation ist an der TU Wien Bibliothek verfügbar.
The approved original version of this doctoral thesis is available in print at TU Wien Bibliothek.
TU Bibliothek Your knowledge hub WIEN

1.3.2 Simulation Perré [22]

In [22] a drying process starting from 100 % MC, meaning the cell walls being fully saturated with the remaining amount of water being present as liquid water within the cell lumens, was simulated with different numerical and analytical models. In contrast to previous models [15, 24] for wood drying, this model does not include high temperature treatment (above the boiling point), i.e. an equation for dry air conservation. Instead the model in [22] was reduced to two degrees of freedom (total MC and temperature T), since only low temperatures were considered. The reference solution with a constant diffusivity (denoted as "Model 1") and with a variable diffusivity (denoted as "Model 2") at a low temperature (below 50 °C) are compared to the model presented in this paper (see Figure 1.5).

The investigated specimen has a thickness of 20 mm and is exposed to one-dimensional convective drying in radial direction. The initial MC is 100 % and the initial temperature is 298.15 K. The film boundary coefficient for heat transfer k_T is 14 $\mathrm{W\,m^{-2}\,K^{-1}}$ and the one for mass transfer k_{c_v} is 0.014 $\mathrm{m\,s^{-1}}$, respectively. The surrounding climate is defined with a temperature of 323.15 K and 32 % relative humidity, which results in an EMC of about 7 %. For the simulations in [22] the diffusivity was set to $D = 10^{-8}\,\mathrm{m^2 s^{-1}}$ for "Model 1" and to $D = 10^{-9}\,\exp(3\,(c_b + c_w)/\rho_d)\,\mathrm{m^2 s^{-1}}$ for "Model 2". The parameters for the sorption isotherm were fitted to the equation in [15] at a temperature of 323.15 K. The resulting values for the Hailwood–Horrobin model [57] are $f_1 = 2.038, f_2 = 11.08, f_3 = -9.689$. The dry density of the material is 500 $\mathrm{kg\,m^{-3}}$ [15].

The exponent for the relative permeability K_w in radial direction is set to S_w^2 instead of S_w^3, as described in Section 1.3.4. The reduction factor $\boldsymbol{\xi}$ for the diffusivity was set to 0.03 in radial direction, as in Section 1.3.1.

The following expression for the capillary pressure from [15] was used

$$P_c = 1.364 \cdot 10^5\,\sigma\,(c_w + 1.2 \cdot 10^{-4})^{-0.61}, \tag{1.64}$$

where σ denotes the surface tension of water. The used finite element model consisted of 40 elements with element lengths along the specimen ranging from 0.2 mm (close to the boundary) to 1 mm, resulting in a total of 164 nodes. 797 increments with a maximum time step of 360 s were necessary to complete the 50 h of drying with a total CPU time of 210 s. It can be seen from Figure 1.5 that the simulation results agree very well, especially for the first 15 h. During that time, the wet bulb temperature is approached first and then kept constant. As soon as the MC at reference point ①, i.e. at the boundary surface, drops below the FSP, the temperature starts to increase to the dry bulb temperature. After 15 h the differences between the simulation can be explained by the different treatment of the three phases of water and their diffusion parameters, which can assumed to be variable or constant. In case of the presented model the factor $\boldsymbol{\xi}$ is responsible for the development of the average MC below the FSP. The increase of the temperature is strongly connected to the loss of heat due to vaporization. Due to the, in comparison to the moisture transport properties, high thermal conductivity, the temperature varies only by a small amount between the reference point ① on the boundary surface and point ② on the end of the sample.

Die approbierte gedruckte Originalversion dieser Dissertation ist an der TU Wien Bibliothek verfügbar.
The approved original version of this doctoral thesis is available in print at TU Wien Bibliothek.
TU Bibliothek Your knowledge hub WIEN

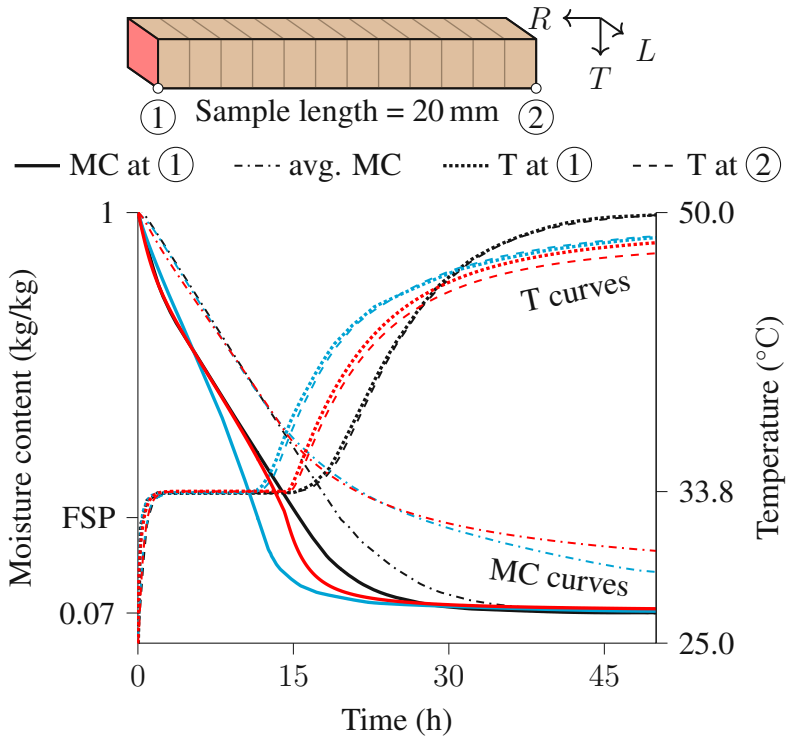

Figure 1.5: Time history of moisture content and temperature during 50 h of one-dimensional drying in radial direction. Comparison of the presented model (——) and of the models from [22] with constant ("Model 1" ——) and variable diffusivity ("Model 2" ——). Initial conditions were 100 % MC and φ = 100 % at 25 °C. Boundary conditions are applied at the red surface on the left end of the sample with φ = 32 % and 50 °C, while all other surfaces were sealed and thermally insulated. Mass transfer coefficient k_{c_v} is 0.014 $\mathrm{m\,s^{-1}}$ and heat transfer coefficient k_T is 14 $\mathrm{W\,m^{-2}\,K^{-1}}$ according to [22]. The relative permeability of free water K_w is set to S_w^2.

1.3.3 Experiment Eriksson et al. [38]

In [38] a mass transport model was developed and used to investigate a drying process under isothermal conditions at low temperatures. In comparison to other models, this one also uses the finite element method. Since the model was considered to be isothermal, heat effects due to vaporization and the connected cooling effect were not taken into account. Below the FSP the bound water and water vapor flux were combined. Above the FSP all phases are combined and assumed to be proportional to the gradient of the over all MC.

For validation of the model in [38], a wood sample was dried from 135 % MC to about 8 %. The cross section of the sample was 42 mm x 31 mm with a length of 205 mm and a dry density of 469 $\mathrm{kg\,m^{-3}}$. The drying took place in radial direction, with a cylindrical coordinate system within the cross section. All surfaces except one were coated with polyurethane glue and aluminum foil. The whole cross section was modeled with 1102 nodes and 504 elements with 18-by-1 elements in the cross section and 28

Die approbierte gedruckte Originalversion dieser Dissertation ist an der TU Wien Bibliothek verfügbar.
The approved original version of this doctoral thesis is available in print at TU Wien Bibliothek.
TU Bibliothek Your knowledge hub WIEN

elements ranging from 0.4 mm at the boundary to 2 mm along the specimen. 1,736 increments with a maximum time step of 3,600 s were necessary to complete the 100 h of drying in 6,235 s CPU time for "Model A". In case of "Model B" 546 increments and 2,161 s of CPU time were necessary.

The boundary conditions were moist air with a relative humidity of 43 % and a temperature of 323.15 K with a speed of about 4 $\mathrm{m\,s^{-1}}$.

To simulate this experiment with the model presented in this paper, the material parameters from Table 1.1 were used. The isotherm for Norway spruce is taken from [62] with $f_1 = 1.36, f_2 = 14.324$ and $f_3 = -11.9$. Two different descriptions for the relative permeability K_w in radial direction were used. "Model A" uses a K_w of S_w^3, whereas "Model B" uses S_w^2. In Figure 1.6 the model proposed in this paper is compared

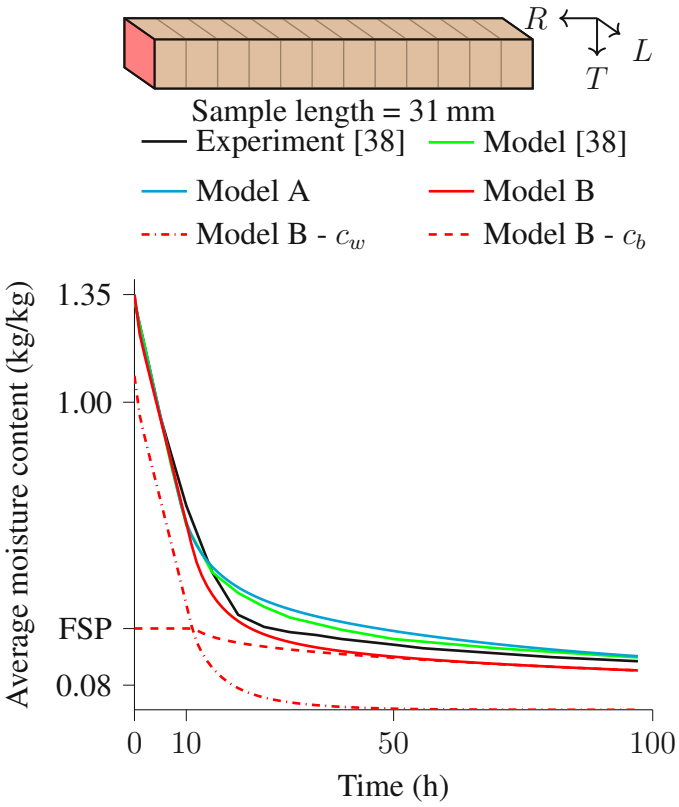

Figure 1.6: Average moisture content for 100 h of drying Norway spruce from 135 % MC (with φ = 100 %) one-dimensional in radial direction. The boundary conditions are relative humidity φ = 43 % and temperature of 50 °C, which are applied to the left (red) surface, while all other surfaces were sealed and thermally insulated. The heat transfer coefficient k_T is 45 $\mathrm{W\,m^{-2}\,K^{-1}}$ and the mass transfer coefficient was calculated with Equation (1.60). "Model A" uses a relative permeability of S_w^3 and "Model B" uses S_w^2.

to the model in [38], where a mass transfer coefficient of $4.7 \cdot 10^{-8}\,\mathrm{m\,s^{-1}}$ and an absolute permeability of $6 \cdot 10^{-15}\,\mathrm{m^2}$ was used, as well as with the experimental result in [38]. For the proposed model, two versions are depicted ("Model A" and "Model B"), since the relative and absolute permeabilities are not exactly known. The experimental curve lies

Die approbierte gedruckte Originalversion dieser Dissertation ist an der TU Wien Bibliothek verfügbar.
The approved original version of this doctoral thesis is available in print at TU Wien Bibliothek.
TU Bibliothek Your knowledge hub WIEN

between the curves of "Model A" and "Model B" after 10 h of drying, when the drying rate decreases and MCs converge to the EMC of 8 %. In addition, the evolution of the phases c_b and c_w are also shown. As long as free water exists everywhere in the model (during the high drying rate at the beginning), there is no change in the bound water concentration and the MC stays at the FSP. As soon as the free water at the boundary is reduced to zero, the water vapor concentration starts to decrease to levels below the saturated concentration and the via sorption connected bound water concentration starts to decrease as well.

1.3.4 Experiment Sandoval et al. [41]

In [41] a model for convective drying of Mexican pine wood is proposed. The results from one-dimensional simulations in radial direction are compared to nuclear magnetic resonance imaging (NMR). The wood samples were 25 cm long, 15 cm wide and 2.54 cm thick and had a dry density of 510 $\mathrm{kg\,m^{-3}}$. The drying was convective with a relative humidity of 25 % and 333.15 K and an air velocity of 2.5 $\mathrm{m\,s^{-1}}$. For the NMR experiment a cylindrical sample with a diameter of 2.54 cm from the same material was used. Initially, the MC was about 90 % and the initial temperature was 298.15 K. The parameters for the sorption isotherm were fitted from the isotherm given in [64] at 333.15 K: $f_1 = 2.276$, $f_2 = 15.36$, $f_3 = -14.26$. In [41] different values for the relative permeability were compared. The experimental results show, that there is a smooth transition in the moisture profiles near the FSP, which would arise with exponents greater than 2 for the relative permeability and the authors concluded that the simulation with a relative permeability of S_w^2 agrees quite well with the experimental results. During the pendular state the relative permeability was set to $S_w^{1.8}$. In our case, a relative permeability of S_w^2 during the funicular (above S_{irr}) and pendular state (between S_{irr} and FSP) gives reasonably good results for all performed experiments, hence, a transport in the pendular region, where the free water phase is not continuous any more, is considered. The value for $\boldsymbol{D_0}$ in radial direction was adjusted from 7E-6 to 2E-4 to better capture the behavior below the FSP.

The model consists of 208 nodes and 51 elements ranging from 0.2 mm at the boundaries to 1 mm in the middle of the specimen one element in the cross section. 453 increments with a maximum time step of 3,600 s were necessary to complete drying simulation with a CPU time of 209 s.

In Figure 1.7, the model proposed in this paper is compared to the experimental results in [41]. The drying process can be described very well, even with the parameter set used in the other simulations and given in Table 1.1, especially above the FSP. The adjustment of the value for $\boldsymbol{D_0}$ leads also to very good results below the FSP.

Die approbierte gedruckte Originalversion dieser Dissertation ist an der TU Wien Bibliothek verfügbar.
The approved original version of this doctoral thesis is available in print at TU Wien Bibliothek.
TU Bibliothek Your knowledge hub WIEN

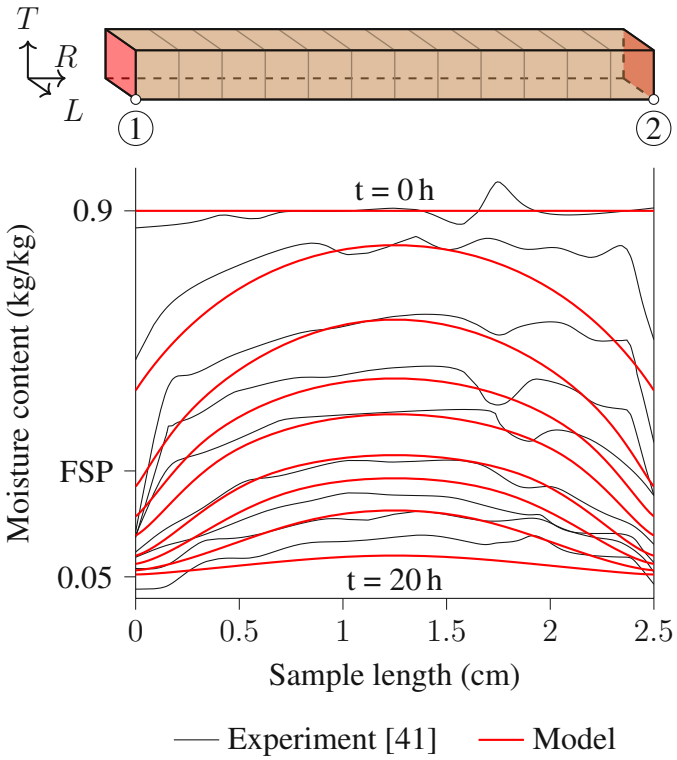

Figure 1.7: Moisture profiles at 0, 1, 2, 3, 4, 6, 8, 12 and 20 h of drying along the path from ① to ②. Initial conditions were 90 % MC and φ = 100 % at 25 °C. Drying was convective and one-dimensional in radial direction with φ = 25 % at 50 °C. The boundary conditions were applied to both ends (red surfaces) of the sample while all other surfaces were insulated. As in the previous example, the heat transfer coefficient k_T was 45 $\mathrm{W\,m^{-2}\,K^{-1}}$ and the mass transfer coefficient was calculated with Equation (1.60). The value for $\boldsymbol{D_0}$ in radial and tangential direction was adjusted from 7E-6 to 2E-4 to better capture the behavior below the FSP.

1.3.5 Experiment Gezici-Koç et al. [43] – drying

In [43], small wood specimens were investigated with NMR imaging. In case of pine sapwood, transport takes place in tangential direction since cylindrical specimens were drilled out of radially cut wooden panels with a thickness of 1 cm. In contrast to the previous examples, the drying test was not performed on green wood. The sample was dried at room conditions with a relative humidity of 40 %. After that, the samples were immersed in distilled water for at least one month, which resulted in a moisture content of about 160 %. Drying was convective with a relative humidity of 25 % and about 295.15 K. The value of 25 % relative humidity of the surrounding air was set according to the final MC at the boundary after 6 days of drying.

The dry density of the sample was 540 $\mathrm{kg\,m^{-3}}$ and the fitted parameters for the sorption isotherm, measured by [43], were: $f_1 = 2.362$, $f_2 = 10.28$, $f_3 = -9.114$.

Die approbierte gedruckte Originalversion dieser Dissertation ist an der TU Wien Bibliothek verfügbar.
The approved original version of this doctoral thesis is available in print at TU Wien Bibliothek.
TU Bibliothek Your knowledge hub WIEN

The simulation was modeled with 968 nodes and 208 elements ranging from 0.02 mm at the boundary to 0.08 mm with one element per cross section. 565 increments with a maximum time step of 3,600 s were necessary to complete the drying simulation with a CPU time of 826 s.

As mentioned, the wood was dried before the drying test took place. It is assumed that the effect of pit aspiration plays a role in this case. This could be a reason why the model was initially not able to predict the drying behavior with the previously described parameters. To capture the drying process the model was fitted by adjusting the permeabilities to an appropriate value.

In case of this drying experiment, the description of the free water flow was changed from the mixed formulation (1.59) to the concentration based formulation (1.57) as it was used in [42] with a diffusivity in tangential direction of

$$D_{c_w} = 3 \cdot 10^{-6} - 5 \cdot 10^{-6}(c_w - 0.2). \tag{1.65}$$

Since the transport takes place only in tangential direction, the diffusivities in the other directions were taken into account in the same way. The moisture profiles shown in Figure 1.8 for every 7 h of drying depict an inwards moving drying front. This front-like behavior can not be predicted with the chosen expression for D_{c_w}, however by including an exponential function with c_w in the exponent such a behavior could be achieved, but with a lower level of agreement overall. Thus, it is assumed that with a better identification of the transport parameters, the prediction accuracy of the simulations could be improved significantly. Within the first seven hours of drying the model agrees quite well with the experimental data. Then, the predicted curves show a different behavior. At 35 h, within the first 2/3 of the sample length the MCs are overestimated by max. 15 % and on the right end of the sample underestimated by max. 30 %. At 70 h there are differences of max. 8 % in the first 2/3 and still about 30 % on the right end. After 98 h the profiles again agree quite well, which is also the case at the end of the experiment after 144 h.

Die approbierte gedruckte Originalversion dieser Dissertation ist an der TU Wien Bibliothek verfügbar.
The approved original version of this doctoral thesis is available in print at TU Wien Bibliothek.
TU Bibliothek Your knowledge hub WIEN

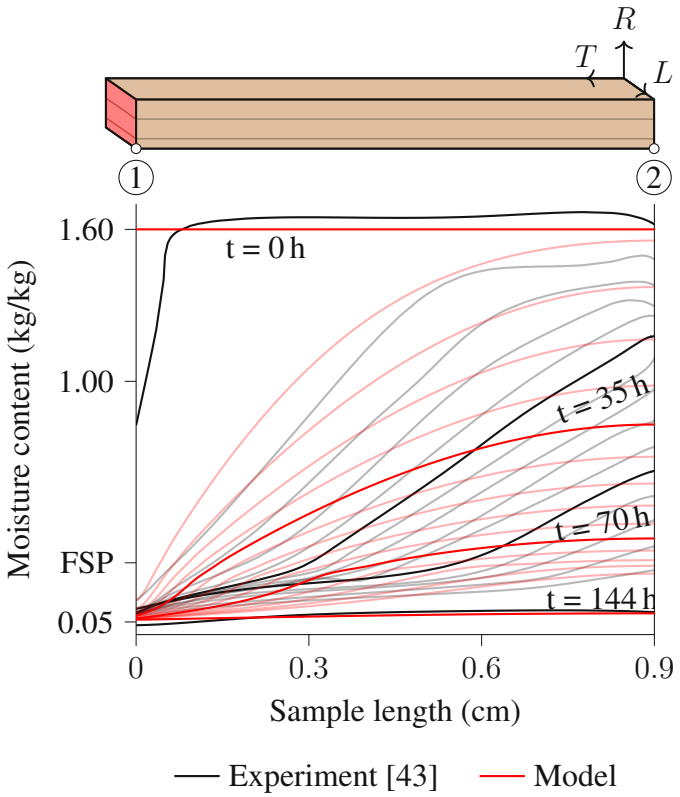

Figure 1.8: Moisture profiles for one-dimensional convective drying in tangential direction for 6 d shown for every 7 h until 98 h and for 144 h along the path from ① to ② (for the sake of clarity only profiles after 0 h, 35 h, 70 h and 144 h are plotted with full opacity). All surfaces except the left, shown in red, were insulated. Initial conditions were 160 % MC and φ = 100 % at 22 °C. Boundary conditions were φ = 40 % at 22 °C. The heat transfer coefficient k_T was 45 $\mathrm{W\,m^{-2}\,K^{-1}}$ and the mass transfer coefficient was calculated with Equation (1.60). In comparison to the other examples the wood was dried and infiltrated prior to the drying experiment.

1.3.6 Experiment Gezici-Koç et al. [43] – infiltration

In [43] also an infiltration experiment was performed. Again, the used material was pine sapwood with a density of 540 $\mathrm{kg\,m^{-3}}$. The samples were dried at φ = 33 % for at least four weeks, which results in an EMC of about 6 %. After that, the samples were exposed to free water at one end surface (see blue surface in Figure 1.9). It can be seen that the MC increases within the first seven days until the FSP at about 30 % MC is reached. Then the MC remains in the range around the FSP. Between seven and 36 days there is only a small increase of MC. To capture this behavior a combination of mass transfer coefficients for free water k_{c_w} and water vapor k_{c_v} were used and fitted to the experimental results. The free water diffusivity was also fitted and chosen to be constant.

Die approbierte gedruckte Originalversion dieser Dissertation ist an der TU Wien Bibliothek verfügbar.
The approved original version of this doctoral thesis is available in print at TU Wien Bibliothek.
TU Bibliothek Your knowledge hub WIEN

$$
\begin{aligned}
D_{c_w} &= 7.76 \cdot 10^{-8}\,\mathrm{m^2\,s^{-1}} \\
k_{c_w} &= 6 \cdot 10^{-8}\,\mathrm{m\,s^{-1}} \\
k_{c_v} &= 0.014\,\mathrm{m\,s^{-1}} \\
k_T &= 25\,\mathrm{W\,m^{-2}\,K^{-1}}
\end{aligned}
\tag{1.66}
$$

The fitted parameters for the adsorption isotherm, which was measured in [43], were: $f_1 = 0.8744, f_2 = 22.79, f_3 = -20.36$. The model is the same as described in the previous drying example with 968 nodes and 208 elements. 451 increments with a maximum time step of 7,200 s were necessary to complete the wetting simulation with a CPU time of 430 s. The moisture profiles shown in Figure 1.9 depict the infiltration

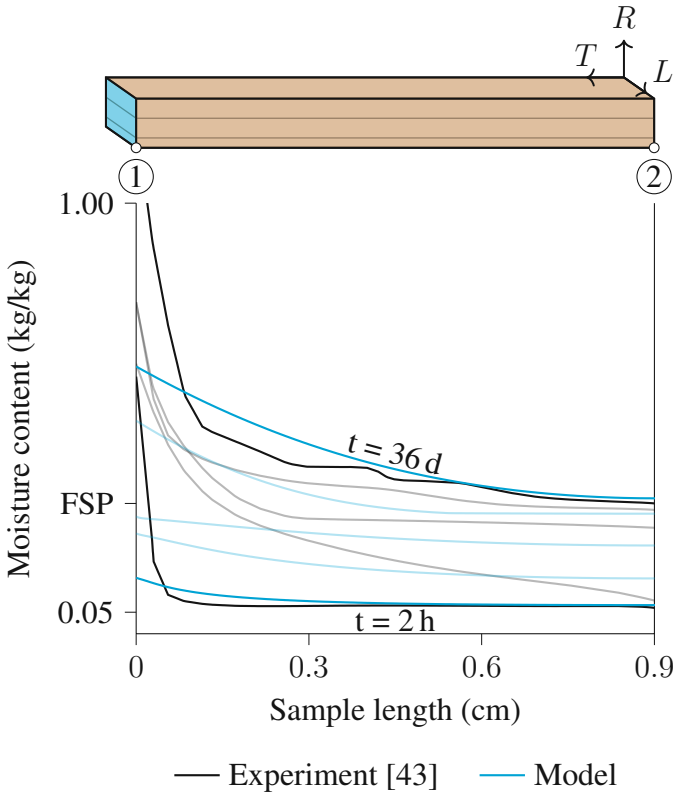

Figure 1.9: Moisture profiles for one-dimensional infiltration in tangential direction plotted after 2 h, 2 d, 7 d, 21 d and 36 d along the path from ① to ②. For the sake of clarity only profiles after 2 h and 36 d are plotted with full opacity. Initial conditions are 5.3 % MC and φ = 33 % at 22 °C. Boundary conditions are 160 % MC at 22 °C and are applied to the left surface shown in blue. Other surfaces were sealed. The FSP is at 30 % MC.

after 2 h, 2 d, 7 d, 21 d and 36 d. It can be seen that there is a fast increase of the MC values until the FSP is reached. In [43] also a relaxation analysis to determine the phases of water during the infiltration process was performed. Within the first days only bound

Die approbierte gedruckte Originalversion dieser Dissertation ist an der TU Wien Bibliothek verfügbar.
The approved original version of this doctoral thesis is available in print at TU Wien Bibliothek.
TU Bibliothek Your knowledge hub WIEN

water and the previously described behavior was observed. Free water is only present after the saturation of the cell walls with bound water. As described in the next section, an additional free water phase would be necessary to simulate the high MC gradients in the region close to the applied boundary condition, which arise due to the movement of free water into denser material.

1.3.7 Experiment Krabbenhoft and Damkilde [42]

In [42] different mathematical models were compared to experimental results of an infiltration in longitudinal direction. The material was fir sapwood with a dry density of 500 $\mathrm{kg\,m^{-3}}$. The fitted diffusivity for free water transport in the large vessels of the α-phase, which are quickly filling up, is used for the diffusivity of the model presented in this paper, reading

$$D_{c_w} = 39.2 \cdot 10^{-9} \exp(0.011 \cdot c_w). \tag{1.67}$$

The parameters for the sorption isotherm are set to: $f_1 = 1.804$, $f_2 = 13.630$ and $f_3 = -12.12$, taken from the adsorption isotherm in [56]. The film coefficient for the boundary condition for free water was determined as $k_{c_w} = 1.3 \cdot 10^{-5} \mathrm{m\,s^{-1}}$ and for heat transfer $k_T = 25\,\mathrm{W\,m^{-2}\,K^{-1}}$. No boundary condition for water vapor was applied. The simulation was modeled with 568 nodes and 141 elements ranging from 1 mm at the boundary to 5 mm with one element per cross section. 801 increments with a maximum time step of 3,600 s, respective 360 s during the phase change, were necessary to complete the wetting simulation with a CPU time of 925 s. In Figure 1.10, the moisture profiles after 6 d, 8 d, 15 d and 21 d are shown. Compared to the previously described infiltration experiment in [43], the MC plateau is not in the region of the fiber saturation point at about 30 %, instead it can be observed at an MC of about 45 %. To capture this behavior, the sorption isotherm was scaled to a FSP of 45 %, which defines the height of the plateau. The kink slightly below the FSP is due to the lower value of C_4 of the reaction function H_{bv} close to the FSP. The experimental results in this figure are taken in [42] from unpublished data, hence the exact experimental conditions are not known. The β-phase, as shown in [42], describes the infiltration into the smaller vessels and is responsible for the high MC values in the region close to the applied boundary condition. This is not included in the proposed model, which is thus not able to capture these effects after 15 and 21 days, respectively.

However, the basic moisture distribution as well as the evolution of the moisture profiles, which is characterized by a fast front propagation defined by the mechanisms below the FSP followed by a slower absorption defined by the mechanisms above the FSP can be depicted quite well with the proposed model.

Die approbierte gedruckte Originalversion dieser Dissertation ist an der TU Wien Bibliothek verfügbar.
The approved original version of this doctoral thesis is available in print at TU Wien Bibliothek.
TU Bibliothek Your knowledge hub WIEN

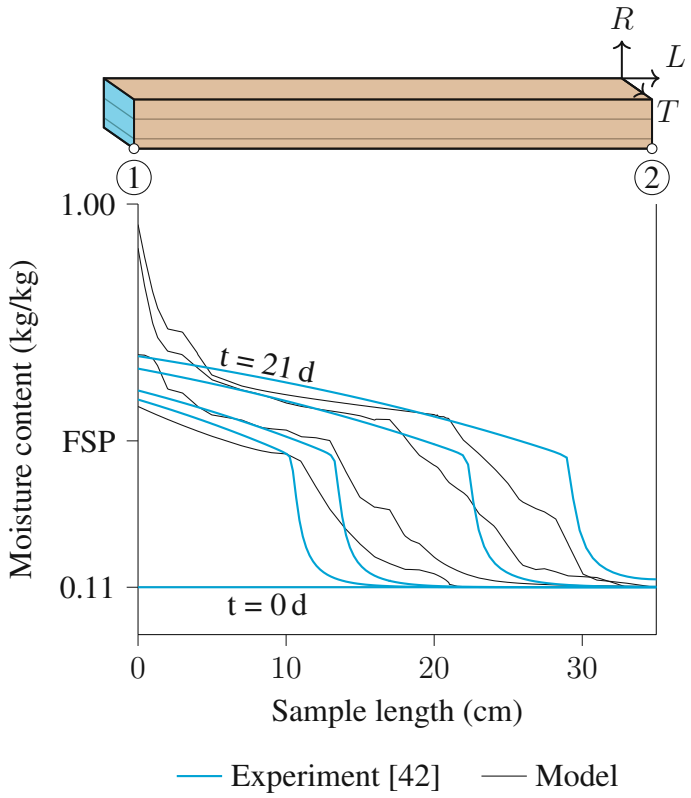

Figure 1.10: Moisture profiles for one-dimensional infiltration in longitudinal direction after 6 d, 8 d, 15 d and 21 d along the path from ① to ②. Initial conditions were 11 % MC and φ = 62 % at 23 °C. The boundary condition was applied on the left surface (blue) with 100 % MC at 23 °C. The mass transfer coefficient was fitted with $k_{c_w} = 1.3 \cdot 10^{-5} \mathrm{m\,s^{-1}}$ and the heat transfer coefficient with $k_T = 25\,\mathrm{W\,m^{-2}\,K^{-1}}$. All other surfaces were sealed. The FSP was set to 45 % to properly map the experimental behavior.

1.4 Parameter studies

To test the robustness and convergence behavior of the developed three-dimensional user element code, various parameters will be studied within this section. First, the influence of mesh size on the ability of the algorithm to correctly simulate critical situations, such as phase changes, is investigated. Then the choice of newly introduced and fixed parameters is examined with respect to their sensitivity.

1.4.1 Mesh study

Here, simulations based on the validation example of Section 1.3.2 were carried out. The sample is of cuboid shape with a length of 2 cm and a cross section of 0.5 by 0.5 cm which is affected by boundary conditions at one end. Material properties, initial and

Die approbierte gedruckte Originalversion dieser Dissertation ist an der TU Wien Bibliothek verfügbar.
The approved original version of this doctoral thesis is available in print at TU Wien Bibliothek.
TU Bibliothek Your knowledge hub WIEN

boundary conditions are defined according to Section 1.3.2. The six different mesh sizes with brick-type elements, linear shape functions and 8 nodes each, which were used in the study, are shown in Table 1.2.

Table 1.2: Mesh size study for 500 h of drying based on the validation example from Section 1.3.2

# elements	# nodes	element size [mm]	CPU time [s]	increments
4	20	5.0	634	5601
8	36	2.5	607	5451
20	84	1.0	705	5344
40	164	0.5	1188	5299
100	404	0.2	3008	5288
200	804	0.1	5358	5289

It should be noted that, when using an RVE, the minimum element size is related to the RVE size, which is defined on the level of many pores, as described earlier. This results in a minimum element size of about 0.2 mm, as the cell diameter of wood is about 30 µ m.

It can be seen in Figure 1.11, where the distributions of the different phases of water are depicted for the six different meshes, that a mesh refinement leads to a convergence of the solution. When the film boundary conditions are applied, the temperature first increases to the wet-bulb temperature of 306.97 K, where it stays until the free water concentration is reduced to a very low level, which is less than 0.5 % MC of free water, at the node at the boundary. During this first step, free water is moved to the boundary, where it evaporates. When the point at the boundary reaches these very low levels of free water the water vapor concentration (shown as relative humidity) and the coupled bound water concentration start to decrease as well. At the same time, the temperature starts to increase slowly to the level defined by the boundary condition, since the evaporation at the boundary decreases. Depending on the mesh size, this point occurs between 13.8 (for the mesh with 200 elements) and 17.8 h (for the mesh with 4 elements) after the start of the drying process. Also at the other observed points of Figure 1.11, which are located in the middle of the sample and at the opposite end of the boundary condition, the meshes tend to converge to the solution from the smallest element sizes. Between 45 h and 76.5 h the water vapor and bound water concentrations start to decrease in these points, again with a tendency at starting later for meshes with smaller elements. After about 500 h, the drying process has finished.

In Figure 1.12 profiles of the four different DOFs are shown after 10, 15, 30, 170 and 500 h of drying. As can be seen from Figure 1.12a, after 15 h for the fine mesh there is no more free water at the boundary. In case of the coarse mesh, this point is reached later, as was also shown in Figure 1.11. At 30 h, depending on the mesh size, the free water moisture content is between 3.2 % for the four element mesh and 8.4 % for the 200 element one. After 170 h of drying the free water is completely removed from the sample. The temperature profiles in Figure 1.12b show only a very slight gradient compared to the other profiles due to the thermal conductivities. As mentioned before, after the initial temperature of 298.15 K the temperature first increases to the wet-bulb tempera-

Die approbierte gedruckte Originalversion dieser Dissertation ist an der TU Wien Bibliothek verfügbar.
The approved original version of this doctoral thesis is available in print at TU Wien Bibliothek.
TU Bibliothek Your knowledge hub WIEN

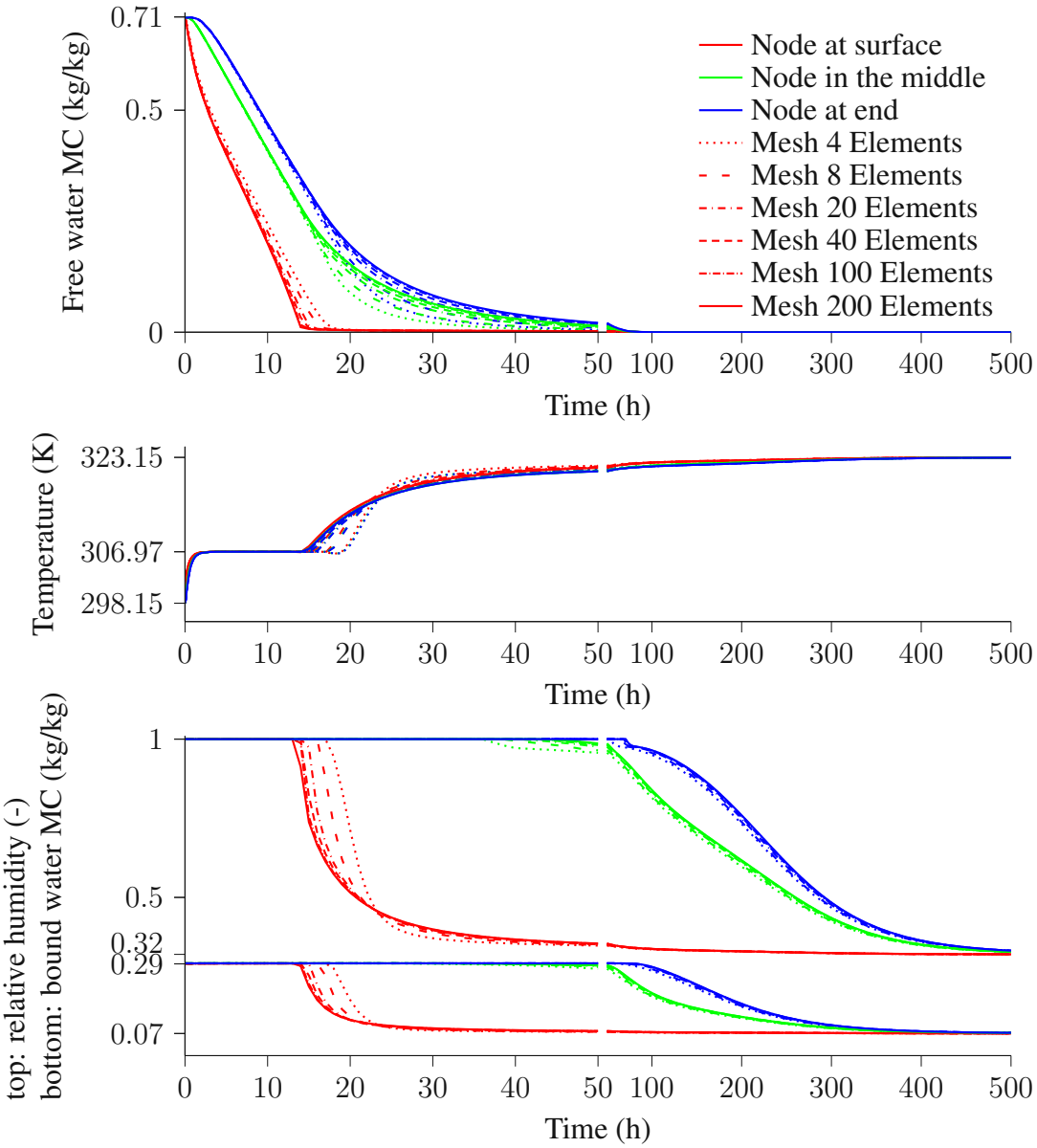

Figure 1.11: Comparison of six different meshes (4, 8, 20, 40, 100 and 200 elements) based on the conditions according to the example in Section 1.3.2. Distributions over simulation time up to 500 h of drying are shown for the four DOFs. Experimental conditions as well as material properties are shown in Section 1.3.2.

ture of 306.97 K. This temperature then stays constant for all investigated meshes until the free water is reduced to low values. Then the temperature starts to increase slowly to the boundary condition of 323 K. In Figure 1.12c and Figure 1.12d the bound water MC and the relative humidity, respectively, are shown. These two DOFs are connected by the time-dependent sorption rate. At 15 h, when the free water is removed for some of the mesh sizes, the profiles deviate from the initial value. The influence of the mesh

Die approbierte gedruckte Originalversion dieser Dissertation ist an der TU Wien Bibliothek verfügbar.
The approved original version of this doctoral thesis is available in print at TU Wien Bibliothek.
TU Bibliothek Your knowledge hub WIEN

size can also be observed after 30 h and 170 h, where for the coarse mesh the profile is defined by only five points along the specimen with linear interpolation inbetween. At the nodes, however, the values are not far from those of the smaller mesh sizes.

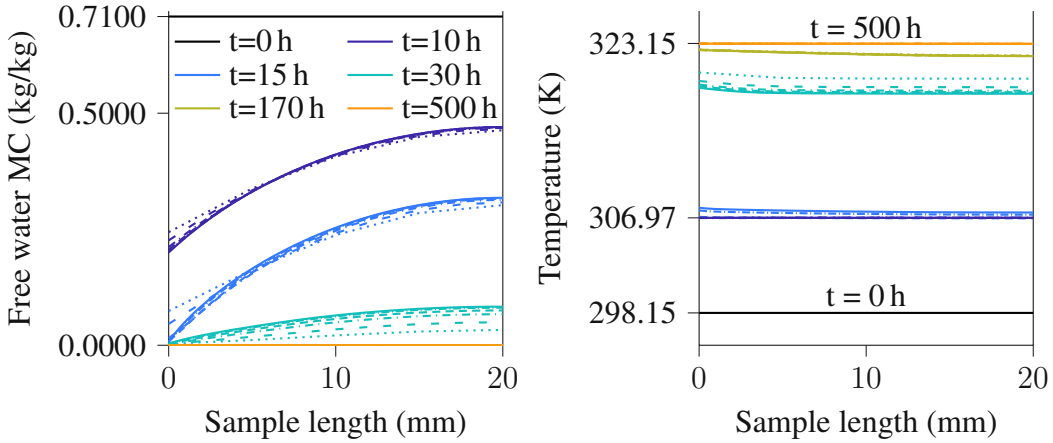

(a) Free water concentration, shown as free water MC c_w/ρ_d

(b) Temperature T

(c) Bound water concentration, shown as bound water MC c_b/ρ_d

(d) Water vapor concentration, shown as relative humidity

Figure 1.12: Comparison of six different meshes (4, 8, 20, 40, 100 and 200 elements) based on the conditions according to Section 1.3.2. Profiles along the specimen are shown for the four DOFs individually. Experimental conditions as well as material properties are given in Section 1.3.2

1.4.2 Parameters for reaction function H_{wv}

For the determination of reasonable parameter sets for $C_{wv,1}$ and $C_{wv,4}$, which are used in Equation (1.34) to determine H_{wv}, 9 different versions were compared, with $C_{wv,1}$ ranging from $10^3\,\mathrm{s}^{-1}$ to $10^7\,\mathrm{s}^{-1}$ and $C_{wv,4}$ from $1 \cdot C_{wv,1}$ to $10^{-5} \cdot C_{wv,1}$. Depending on the set, the computation time varied and the assumption that "if free water exists, the saturated water vapor concentration is reached quickly" was fulfilled to varying degrees. The geometry, material parameters and initial conditions were chosen as in the

Die approbierte gedruckte Originalversion dieser Dissertation ist an der TU Wien Bibliothek verfügbar.
The approved original version of this doctoral thesis is available in print at TU Wien Bibliothek.
TU Bibliothek Your knowledge hub WIEN

validation example of Section 1.3.2. The temperature was increased from 298.15 K to 323.15 K while two different heat transfer film boundary coefficients were tested with values of $50\,\mathrm{W\,m^{-2}\,K^{-1}}$ and $10\,\mathrm{W\,m^{-2}\,K^{-1}}$, respectively. The film boundary coefficient for mass transfer was set to zero, to keep the moisture inside the sample.

The lowest ratios of $c_v/c_{v_{sat}}$ at the boundary (point ① in Figure 1.5) during two hours of temperature increase with time increments of 1 s are presented in Table 1.3. To test the influence of the different sets in a real example, the experiment from Section 1.3.4 was simulated with all 9 sets, resulting in differences of less than 0.02 % MC for the film boundary heat transfer coefficient of $10\,\mathrm{W\,m^{-2}\,K^{-1}}$ and less than 0.8 % MC (except for Set 6 and 8, which are about 1 % off for some areas) for the heat transfer film boundary coefficient of $50\,\mathrm{W\,m^{-2}\,K^{-1}}$ but with differences in calculation time. The number of increments for these simulations are shown together with the CPU times in Table 1.3.

Table 1.3: Comparison of different parameter sets with k_T of $50\,\mathrm{W\,m^{-2}\,K^{-1}}$ and $10\,\mathrm{W\,m^{-2}\,K^{-1}}$ for H_{wv}. Minimum ratios of $c_v/c_{v_{sat}}$ for the case of increasing temperature of the sample. Number of increments and CPU time [s] for the experiment from Section 1.3.4 with the parameters given here. Set number 2 has been chosen for the model presented in this paper.

Set	1		2		3	
$C_{wv,1}$			10^7			
$C_{wv,4}$	10^7		10^4		10^2	
k_T	10	50	10	50	10	50
min $c_v/c_{v_{sat}}$	1.0	0.990	1.0	0.990	0.997	0.986
Increments	18733	16752	418	441	65	82
CPU time	7420	6837	216	222	38.8	47
Set	**4**		**5**		**6**	
$C_{wv,1}$			10^5			
$C_{wv,4}$	10^5		10^2		10^0	
k_T	10	50	10	50	10	50
min $c_v/c_{v_{sat}}$	1.0	0.990	0.997	0.986	0.985	0.976
Increments	1406	1515	53	74	92	75
CPU time	554	596	26	46	41	41
Set	**7**		**8**		**9**	
$C_{wv,1}$			10^3			
$C_{wv,4}$	10^3		10^0		10^{-2}	
k_T	10	50	10	50	10	50
min $c_v/c_{v_{sat}}$	0.999	0.989	0.976	0.966	0.974	0.965
Increments	104	154	46	50	47	58
CPU time	53	77	19	53	40	31

As can be seen from the comparison of Sets 1 and 2, the model with equal values for $C_{wv,1}$ and $C_{wv,4}$ needs more CPU time and increments. Also a version with a constant value of $10^7\mathrm{s}^{-1}$ for H_{wv} was tested, needing 17,049 increments and a CPU time of 6,661 s with a minimum ratio of $c_v/c_{v_{sat}}$ of 0.990. The version with a constant value of $10^5\mathrm{s}^{-1}$ led to 1,510 Increments with 715 seconds and the one with $10^3\mathrm{s}^{-1}$ to 144 In-

Die approbierte gedruckte Originalversion dieser Dissertation ist an der TU Wien Bibliothek verfügbar.
The approved original version of this doctoral thesis is available in print at TU Wien Bibliothek.
TU Bibliothek Your knowledge hub WIEN

crements with 70 s of CPU time, both with a minimum ratio of $c_v/c_{v_{sat}}$ of 0.990. When comparing these values for H_{wv} to the example from Section 1.3.4 with a heat transfer film boundary coefficient of 50 $\mathrm{W\,m^{-2}\,K^{-1}}$, differences of maximum 0.25 % MC were observed during the analysis when comparing Set 1 and the constant version with $10^7\mathrm{s}^{-1}$ (which differ by about 0.002 %) to Set 2. In case of the constant version with $10^3\mathrm{s}^{-1}$ the results differ by 0.5 %MC from the Set 1 and in case of $10^5\mathrm{s}^{-1}$ the differences were 0.2 %MC. The chosen Set 2 combines a short computation time with a high degree of confidence in the fulfilment of the mentioned assumption. In the next step, also the parameter $C_{wv,2}$ was varied as 10, 20 and 100 and $C_{wv,3}$ as 10, 50 and 100, resulting in no differences in case of the previous described modified example from Section 1.3.2. Thus, the previously used constants of $C_{wv,1} = 10^7\,\mathrm{s}^{-1}, C_{wv,2} = 20, C_{wv,3} = 50$ and $C_{wv,4} = 10^4\,\mathrm{s}^{-1}$ are justified. In [21] apples with a pore size of 25 µm were simulated, using a constant H_{wv} of $10^3\mathrm{s}^{-1}$. Since the non-equilibrium rate describes a evaporation zone with a thickness depending on the chosen parameter, the values of the chosen combination with values for H_{wv} between $10^3\mathrm{s}^{-1}$ of [21] and the maximum value in case of a sharp evaporation function, which would equal a value of infinity, seem to be reasonable.

1.4.3 Residual free water evaporation time t_{wv}

In a third parameter study, the value of t_{wv}, as described in Section 1.2.2.4, was investigated based on the previously shown mesh with 100 elements. As mentioned, a problem arises when $\dot{c}_{wv} \cdot \Delta t$ exceeds the free water content, which would lead to negative free water contents. In this case, $\dot{c}_{wv}$ is limited to c_w/t_{wv}. In Figure 1.13, the development of the water phases is shown for a t_{wv} of 36 s, 360 s, 3,600 s and 36,000 s. The smallest value of $t_{wv} = 36\,\mathrm{s}$, and thus the largest limit where the expression for $\dot{c}_{wv}$ from Equation (1.34) is not used any more, leads to a rapid decrease in the free water concentration, but also deviations of bound water content and relative humidity. The largest investigated t_{wv} of 36,000 s leads to a smooth transition, as it is depicted in the free water curves of Figure 1.13 and the bound water and relative humidity evolvement tend to converge to this solution, with little differences between 3,600 s and 36,000 s. Thus the value of t_{wv} of 36,000 s, which was chosen for all simulations, seems to be reasonable.

Die approbierte gedruckte Originalversion dieser Dissertation ist an der TU Wien Bibliothek verfügbar.
The approved original version of this doctoral thesis is available in print at TU Wien Bibliothek.
TU Bibliothek Your knowledge hub WIEN

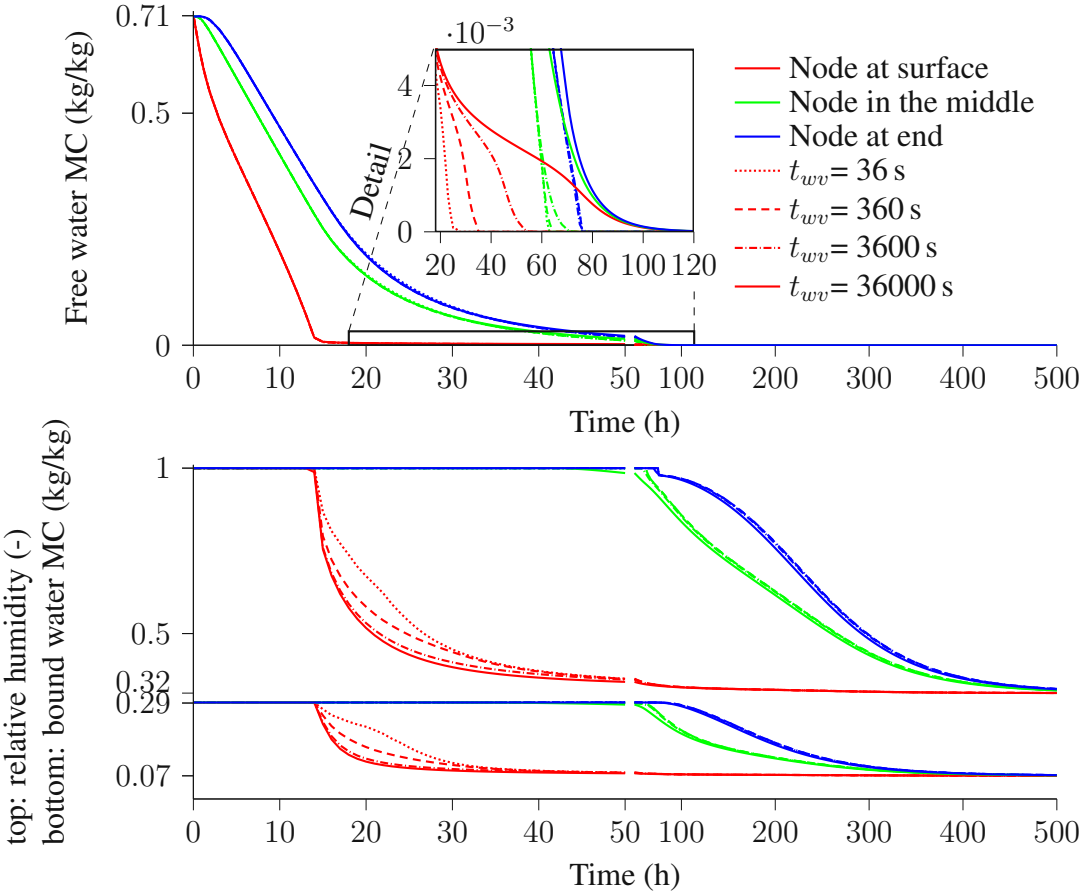

Figure 1.13: Comparison of four different values for t_{wv} including 36 s, 360 s, 3600 s and 36,000 s, based on the conditions according to Section 1.3.2. Distributions during the simulation between 0 and 50 h for free water MC and between 0 and 500 h for bound water MC and relative humidity. The evolvement of the free water MC in the point at the boundary is shown at very low levels (less than 0.5 %)

1.4.4 Maximum time increment size

For the fourth parameter study, the maximum time increment was set to 36 s, 360 s, 3,600 s and 36,000 s, respectively. The results for 360 s and 3,600 s show differences of 0.2 % RH and for 36 s and 360 s of 0.04 %. However, the simulations with a maximum increment size of 36,000 s show differences of up to 1.5 % RH after the phase-change (between 15 h and 80 h). Before and during the phase change, the time increment is automatically reduced by the FE software to smaller values, thus, the increment size is chosen based on the results after the phase change, leading to an optimal maximum increment size of either 360 s or 3,600 s for all simulations.

In addition to the parameter studies mentioned above, our simulation tool was tested for various different conditions, for which no numerical instabilities were observed. Here, cubic samples with a length of 2 cm were simulated under different conditions including drying from various initial values of free water concentration c_w (10, 15, 20, 30, 40, 50, 100, 200, 400 and 600$\mathrm{kg\,m^{-3}}$) and wetting from an initial level of 10 % MC.

Die approbierte gedruckte Originalversion dieser Dissertation ist an der TU Wien Bibliothek verfügbar.
The approved original version of this doctoral thesis is available in print at TU Wien Bibliothek.
TU Bibliothek Your knowledge hub WIEN

Additional studies were performed for isothermal conditions at 296.15 K and 333.15 K, heating from 296.15 K to 311.15 K and 333.15 K to 348.15 K and cooling from 296.15 K to 281.15 K and 333.15 K to 318.15 K, all with varying mesh sizes (64, 512, 1000 and 8000 nodes). The boundary conditions were also applied to different surfaces simultaneously to test two- and three-dimensional cases. For conditions below the FSP, the different meshes were tested with an increase of relative humidity from 54 % to 75 % as in Section 1.3.1.

1.5 Discussion

The performance of the proposed model was assessed by means of different drying and infiltration simulations and experiments from literature. The model was studied in detail regarding the mesh size and time increment as well as the newly defined phase change term which describes the evaporation rate time-dependent. By choosing the evaporation rate this way, adjusting material transport parameters by use of an adjusted Heaviside step function could be omitted leading to a numerical stable model, which was tested in various scenarios and also in seven different shown validation cases. The values of the four degrees of freedom could be predicted, including the temperature drop due to evaporation in case of drying shown in Section 1.3.2, which was achieved by the use of a smoothing function for applying the boundary condition to the proper DOF, as evaluated in Section 1.2.2.6, and also the slight increase of temperature during the sorption process, as shown in Section 1.3.1. Since the three different moisture transport processes are defined independently, processes like infiltration of free water into the cell wall can be described even though free water is already present.

For drying processes, simulations as well as experimental results could be reproduced quite well in most of the cases. Comparison with the simulation results in [22] gave a very good agreement, showing that moisture and temperature evolutions across the fiber saturation point can be reproduced with the proposed model quite well. Especially above the FSP the predictive capability of the model seems to be very good. Below the FSP the presented model is able to predict the results to a similar degree, as the comparison in Section 1.3.1 to the models presented in [8, 10] shows. In some of the validation experiments the results differ, because of the unknown material properties. With them adjusted, the multi-Fickian behavior of the proposed model is able to describe the experimental behavior below the FSP especially under conditions, as described in [8], which include for instance bodies thicker than a few millimeters and higher relative humidity levels, which is the case in the presented simulations. In case of the experiment of [41] the multi-Fickian moisture transport below the FSP leads to different MC distributions next to the boundary, when comparing the profiles shown here to the simulations of [41], which can also be seen in [8], where the single-phase diffusion was compared to the multi-Fickian modell below the FSP. The results of the model and experiment in [41] show that the use of S_w^2 instead of S_w^3 for the relative permeability give reasonably good results, which is also in agreement with the experiments in [22] and [38]. There was no change in the transport mechanisms made at the point of irreducible saturation S_{irr}, thus, free water transport in the pendular region is consid-

Die approbierte gedruckte Originalversion dieser Dissertation ist an der TU Wien Bibliothek verfügbar.
The approved original version of this doctoral thesis is available in print at TU Wien Bibliothek.
TU Bibliothek Your knowledge hub WIEN

ered. Beside the sorption isotherm, density and boundary conditions, for the first three drying validation examples from Section 1.3.2 to Section 1.3.4 the same set of material properties were used.

This means, good predictions could be achieved without individual calibration of model parameters, showing the overall stability of the prediction quality of the proposed model. However, the results of the drying example in [43] could not be described very well with the standard set of material parameters, as this experiment was performed on previously dried wood. Instead of using the capillary pressure as driving force the gradient of free water was used, as it was done for the infiltration experiments. The diffusivity was approximated by a linear expression, leading to a quite good prediction of the first 7 h of drying.

The infiltration experiment in [43] shows an increasing MC in the beginning up to the level of the FSP. After that, the infiltration increases the MC slowly. In the region close to the boundary, high experimental MCs exist. As it can be seen from the results of the infiltration in tangential direction from Section 1.3.6, the thickness of this zone is rather small (only about 1 mm after 36 d). For the description of the high MC values in the boundary region after more than one week of infiltration, the β-phase from [42] should be implemented in future versions of the proposed model. However, in many cases the infiltration takes place in radial or tangential direction, because the ends of the beams are sealed. Another reason to neglect this behavior is an infiltration time of less than a few days (rain, concrete hardening). However, the characteristic behavior, including an infiltration front up to a plateau followed by a slower absorption, could be predicted with the proposed model quite well.

During the simulation it could be noticed, that prior to and after the phase change the maximum increment size was reached, in some cases with two to three equilibrium iterations per increment. However, during the phase change of free water the time increment is reduced, depending on the simulation, to a minimum of 20 to 50 s with up to eleven equilibrium iterations.

In the parameter studies, first the mesh size was investigated showing, that the solution converges, when a smaller element size was chosen, but it has also to be considered, that the minimum element size should be more than 0.2 mm, as the cell diameter of wood is about 30 µ m and the RVE is defined on the level of many pores [10]. The results between the meshes with sizes of 0.2 mm and 0.1 mm showed only little differences, as can be seen in Figure 1.11, and is thus recommended. The parameters for the time dependent evaporation rate, based on the non-equilibrium approach, were fitted to deliver fast and accurate results, as shown in the validation examples. Beside the smoothed reaction function for the evaporation rate H_{wv}, also constant values as shown in [21] were tested with good results, thus this approach seems to be possible as well, but the numerical performance was not as good as with the shown smoothed reaction function. The third parameter investigated with a study was the residual free water evaporation time t_{wv}, which defines the maximum possible evaporation rate by $\dot{c}_{wv,max} = c_w/t_{wv}$, as with a higher rate the free water concentration would turn negative as the end of the time increment. Different values for t_{wv} were investigated, with bound water concentration and water vapor concentration curves converging to the curves, when a t_{wv} of 36,000 is chosen. Also the results of different chosen step times were tested, resulting in a chosen maximum time step of either 360 s or 3,600 s for the presented validation examples.

Die approbierte gedruckte Originalversion dieser Dissertation ist an der TU Wien Bibliothek verfügbar.
The approved original version of this doctoral thesis is available in print at TU Wien Bibliothek.
TU Bibliothek Your knowledge hub WIEN

1.6 Conclusion & Outlook

Existing numerical models for moisture transport mechanisms using the multi-Fickian approach are usually limited to conditions below the FSP. We present a unified moisture transport model for wood, which is able to describe both the multi-Fickian processes below as well as free water transport processes above the FSP. Implementation of the latter also includes the numerically challenging representation of the coupling mechanisms evaporation and condensation with their high gradients caused by capillary pressure. To overcome these numerical difficulties, techniques like upstreaming, mass lumping and a mixed formulation for the free water transport equation were implemented into a user element subroutine of the commercial finite element software *Abaqus*. The interaction between free water and water vapor was modeled with a time-dependent evaporation rate based on the non-equilibrium approach which has advantages in case of numerical implementation. The chosen set of material parameters was evaluated based on a parameter study and is able to model the evaporation rate well. The following points of this numerical implementation should be emphasized:

- The exchange processes between the three different water phases were defined explicitly.
- For the description of the evaporation or condensation rate, a new water vapor concentration-dependent reaction function was introduced.
- The time-dependent description of the evaporation rate does not require a smoothing of the material parameters with a Heaviside step function at the point of phase change.
- The numerical implementation of the processes in the user element is modular. For example, future improvements of infiltration models or better evaporation and condensation schemes can easily be implemented into the proposed model.
- The developed model was able to describe seven different validation experiments and simulations for both drying and infiltration situations quite well and numerically stable.
- The parameter studies to investigate the mesh size and the maximum time step showed a good convergence of the model. The choice of the fixed parameters for reaction function H_{wv} and residual free water evaporation time t_{wv} also proved to be reasonable.
- The wet-bulb temperature during the drying process could be predicted.

A lack of knowledge of moisture-related material properties made it necessary to tune some of the required parameters or to assume cross-species similarities. This means that, especially in the case of infiltration, there is a great need for additional identification experiments. Also the interaction between free and bound water needs closer experimental consideration.

Die approbierte gedruckte Originalversion dieser Dissertation ist an der TU Wien Bibliothek verfügbar.
The approved original version of this doctoral thesis is available in print at TU Wien Bibliothek.
TU Bibliothek Your knowledge hub WIEN

Possible extensions of the proposed model are the consideration of temperatures below the freezing point or the inclusion of the gaseous phase with an additional degree of freedom for handling high temperatures as well as fire [65]. Furthermore, it was shown that the prediction of near-surface moisture contents caused by direct surface contact with free water could benefit from the implementation of the so-called β-phase, described in [42].

With the developed model it is now possible to simulate all kinds of critical moisture situations of engineered wood products or timber constructions for various environmental conditions. By combining the resulting moisture fields with sophisticated simulation tools, capable of predicting local failure within wooden components, this approach can be used to investigate the moisture-dependent increased susceptibility of wood to cracking. Thus, the probability of failure due to moisture can be assessed already during the development and planning phase, and as a consequence reasonable design changes can be initiated in time.

Conflict of interest

None declared.

Acknowledgments

The funding from the Doka GmbH and the Austrian Research Promotion Agency (FFG, Project Number 857041) is gratefully acknowledged.

Die approbierte gedruckte Originalversion dieser Dissertation ist an der TU Wien Bibliothek verfügbar.
The approved original version of this doctoral thesis is available in print at TU Wien Bibliothek.
TU Bibliothek Your knowledge hub WIEN

Die approbierte gedruckte Originalversion dieser Dissertation ist an der TU Wien Bibliothek verfügbar.
The approved original version of this doctoral thesis is available in print at TU Wien Bibliothek.
TU Bibliothek Your knowledge hub WIEN

Publication 2

Numerical assessment of wood moisture content-based assignments to service classes in EC 5 and a prediction concept for moisture-induced stresses solely using relative humidity data [4]

Authored by Maximilian Autengruber, Markus Lukacevic, Christof Gröstlinger, Josef Eberhardsteiner and Josef Füssl

Submitted to *Construction and Building Materials*

Abstract: Moisture content (MC) fields in wood are in strong interplay with the surrounding climate, leading to dimensional changes in wooden elements as well as variation of their material behavior. In the European standard for the design of timber structures (EC 5) these effects are considered by assigning wood members to service classes which are solely based on environmental conditions, but independent of the cross-sectional dimensions. Moisture-induced stresses resulting from dimensional changes are not directly considered. In this paper, we compare the EC 5 assignment of service classes to an assignment based on the actual MCs, determined by simulations. Further, we present an approach to assign the service class for solid and glued laminated timber cross sections, depending on the dimensions of the cross section and based on realistic climate simulations for one location. With the proposed approach, the influence of moisture on serviceability design can be taken into account more appropriately, which is important when computing deflections and performing simulations based on 2nd order theory. In addition, a method to estimate MC distributions for larger cross sections solely based on relative humidities is proposed. With these, also moisture-induced stresses and dimensional changes can easily be considered in a static analysis.

2.1 Introduction

The recent advancement of computational methods makes it possible to design structures in a more cost and material efficient way, even for complex materials like wood. Wood is a naturally grown, inhomogeneous material based on a cellular structure which reacts to the surrounding climate as the hygroscopic cell walls tend to reach an equilibrium state. With the moisture content (MC) of the cell walls changing, also corresponding parameters like stiffness, strength, diffusivity, conductivity and density are influenced [35], which makes it difficult to describe mathematically. The growth direction defines the orthotropic material orientation of wood with the three characteristic directions longitudinal, radial and tangential, which have different hygro-expansion coefficients and lead to so-called moisture-induced stresses [66, 67], that can cause cracking or delamination.

When designing a wooden structure, these moisture-related effects have to be considered. In the current version of the European standard for the design of timber structures (EC 5) [7] a wooden cross section is assigned to a service class, depending on the surrounding climate (relative humidity, averaged MC) or its location, which can be outside, outside covered from rain and inside. With this service class assignment and the duration of loading, the parameter k_{mod} for the ultimate limit state (ULS) is defined, which acts as a reduction factor for the strength values. For the serviceability limit state (SLS), the parameter k_{def} is defined, considering moisture-influenced deflections based on the service class. In case of shear loads the parameter k_{cr} takes possible cracks into account and reduces the total width of the cross section. As stated in [68], moisture-induced stresses are not included directly in the current version of EC 5, thus, they are part of the material properties k_{mod}, k_{def} and k_{cr}. Also, moisture-related changes of stiffness values are not considered.

MC in wood is defined according to [55] as the mass of water in wood divided by the oven-dry mass of wood. When increasing the MC from an initial oven-dry sample, water first only exists in terms of water vapor in the lumen of the cell and as bound water in the cell wall. The amount of water held in the cell wall is limited by the so-called fiber saturation point (FSP). As the material property variations are related to the MC in the cell wall, they are generally also only influenced by conditions below the FSP. If an MC higher than the FSP exists, water is also stored in the lumen [35], but this is only the case when wood gets into contact with liquid water, which is normally omitted by the way wooden structures are designed. Thus, only conditions below the FSP are considered in this work.

Moisture in wood below the FSP is transferred by two different diffusion processes according to the multi-Fickian theory [9, 10] acting in-parallel which are transport of water vapor in the lumen and transport of bound water in the cell walls. These two processes are coupled via the sorption rate. Simulations of combined heat and multi-Fickian moisture transfer for conditions below the FSP were also investigated in [11, 12, 69, 70]. Possible extensions of this models are including an additional transport equation for free water transport for conditions above the FSP, as it was recently presented in [3], or a coupling with a mechanical material model as presented in [8]. For certain conditions as mentioned in [8], e.g. below a relative humidity of 65 %, a single Fickian equation is able to sufficiently describe the moisture transport, which is used in [66, 71].

Die approbierte gedruckte Originalversion dieser Dissertation ist an der TU Wien Bibliothek verfügbar.
The approved original version of this doctoral thesis is available in print at TU Wien Bibliothek.
TU Bibliothek Your knowledge hub WIEN

Based on the moisture field, moisture-induced stresses can be determined using the direction-dependent expansion coefficients. In [5] these stresses were used to evaluate a multisurface failure criterion from [31–34] in each integration point and calculate the so-called crack-prone volume, which is the sum of volumes associated with the integration points exceeding the tensile strength. This is done for each time increment. With this parameter, the critical points in time with the largest crack-prone volume during simulations can then be estimated considering also pith locations, elasticity tensor and expansion coefficients.

In [72, 73] MC distributions were determined based on in-situ measurements of [72, 74] and long-time data of the surrounding climate. This resulted in a guideline for Switzerland [75], which defines MC distributions for cross sections in certain types of buildings.

Changes of MC within wood were also investigated in [68], where the concept of penetration depth was introduced. By applying a harmonic variation of the relative humidity at the boundary, the MC fluctuations in certain depths from the boundary were investigated. The depth of penetration was defined as depth with less than 0.5 % MC fluctuation, which was about 10 mm for a time span of the harmonic function of at least five days. This led to the conclusion that only longer time spans are of interest for moisture-induced stresses.

MCs in certain depths were also investigated in [14], showing converging envelope curves (maximum/minimum MC value at each depth) towards the inside of the cross section which would lead to a penetration depth of more than 100 mm during the investigated time span of 20 months. In a depth of about 200 mm no MC fluctuations were observed and the MC stays constant.

In order to determine the influence of the surrounding climate on wood cross sections, this work analyzes 18 with different dimensions at the location of Linz, Austria, using a multi-Fickian hygrothermal transport model in a time span of 14 months after installation on site. The resulting MC distributions are compared at certain points in time, e.g. when maximum and minimum events occur. The assignment of the service class according to EC 5 based on the surrounding climate, relative humidity or numerically determined MC is then compared. Further, the envelope curves (max./min. MC values along a path) of the different cross sections are analyzed. We propose a method to estimate the MC at the boundary solely from the relative humidity of the surrounding climate, which is then used to approximate MC distributions in large cross sections also only based on the relative humidity. This approximation is then used to compute moisture-induced stresses for a glued laminated timber (GLT) cross section, which is then compared to the moisture-induced stress fields from the moisture simulations using the multi-Fickian transport model.

2.2 Materials and Methods

In this paper, the moisture transport model of [3] is used with the adjustments mentioned in [5] for conditions below the FSP, resulting in the model described subsequently. The cross sections are made of spruce (*Picea abies*) with a dry density of $420\,\mathrm{kg\,m^{-3}}$.

Die approbierte gedruckte Originalversion dieser Dissertation ist an der TU Wien Bibliothek verfügbar.
The approved original version of this doctoral thesis is available in print at TU Wien Bibliothek.
TU Bibliothek Your knowledge hub WIEN

2.2.1 Mathematical model for moisture transport in wood

The unknown degrees of freedom are the concentrations of water vapor c_v and bound water c_b as well as the temperature T. The model uses volume-averaged transport equations with the concentrations defined with respect to the whole volume in case of bound water c_b as well as the sorption rate $\dot{c}_{bv}$ and with respect to only the volume of the lumen, denoted by f_{lum}, in case of water vapor c_v. The set of governing equations can be noted as follows:

Conservation of bound water concentration:

$$\frac{\partial c_b}{\partial t} = \frac{\partial}{\partial \boldsymbol{x}} \cdot \boldsymbol{D_b} \cdot \frac{\partial c_b}{\partial \boldsymbol{x}} + \frac{\partial}{\partial \boldsymbol{x}} \cdot \boldsymbol{D_{bT}} \cdot \frac{\partial T}{\partial \boldsymbol{x}} + \dot{c}_{bv} \tag{2.1}$$

Conservation of water vapor concentration:

$$\frac{\partial c_v\, f_{lum}}{\partial t} = \frac{\partial}{\partial \boldsymbol{x}} \cdot \boldsymbol{D_v} \cdot \frac{\partial c_v}{\partial \boldsymbol{x}}\, f_{lum} - \dot{c}_{bv} \tag{2.2}$$

Conservation of energy:

$$\begin{aligned} \frac{\partial \rho\, h}{\partial t} = &+ \frac{\partial}{\partial \boldsymbol{x}} \cdot \boldsymbol{K} \cdot \frac{\partial T}{\partial \boldsymbol{x}} \\ &+ \frac{\partial}{\partial \boldsymbol{x}} \cdot \boldsymbol{D_b} \cdot \frac{\partial c_b}{\partial \boldsymbol{x}}\, \overline{h}_b + \frac{\partial}{\partial \boldsymbol{x}} \cdot \boldsymbol{D_{bT}} \cdot \frac{\partial T}{\partial \boldsymbol{x}}\, \overline{h}_b \\ &+ \frac{\partial}{\partial \boldsymbol{x}} \cdot \boldsymbol{D_v} \cdot \frac{\partial c_v}{\partial \boldsymbol{x}}\, h_v\, f_{lum} \\ &+ \dot{c}_{bv}\, (h_v - h_b) \end{aligned} \tag{2.3}$$

On the left-hand side of Equations (2.1) to (2.3) accumulation terms including the time derivative ∂t are located and on the right-hand side the transport mechanisms, which are defined by the diffusion tensors for bound water $\boldsymbol{D_b}$ and water vapor $\boldsymbol{D_v}$, respectively, and the phase change term, denoted as sorption rate $\dot{c}_{bv}$, are placed. In the energy conservation equation, thermal conduction $\boldsymbol{K}$ and the latent heat due to the phase change process are included as well as the mass transfer related components with their specific enthalpies h. The accumulation term of Equation (2.3) contains the enthalpy changes of the solid matrix as well as of the expressions related to the change of the concentrations during the time increment ∂t. Values for the parameters used in the Equations (2.1) to (2.3) are described in [5].

The system of governing equations is implemented with a user element subroutine in the finite element software *Abaqus* [59], where they are solved with the modified Newton method. Brick-type elements with linear interpolation functions are used for the discretization. To also include the cylindrical-orthotropic behavior of wood, the local material directions are defined in each integration point, depending on a chosen and cross-section-specific pith location.

Die approbierte gedruckte Originalversion dieser Dissertation ist an der TU Wien Bibliothek verfügbar.
The approved original version of this doctoral thesis is available in print at TU Wien Bibliothek.
TU Bibliothek Your knowledge hub WIEN

2.2.1.1 Initial conditions

The initial conditions are related to the climate of the production site, which is defined by a relative humidity of $\varphi_{ini} = 0.65$ at an initial temperature T_{ini} of 293.15 K. Based on these values, the initial water vapor concentration $c_{v,ini}$ can be determined with $0.011235\,\mathrm{kg\,m^{-3}}$. The initial bound water concentration $c_{b,ini}$ is defined with $49.25\,\mathrm{kg\,m^{-3}}$ based on the adsorption isotherm, which leads to an initial MC of 11.73 %.

2.2.1.2 Boundary conditions

The changes of the boundary conditions in the simulated time span of 14 months are applied with Neumann boundary conditions to all free surfaces except for the end-grain surfaces. As the moisture flux exists only in terms of water vapor concentration, only the flux ϕ_v is considered, i.e. $\phi_b = 0$. In addition to the moisture flux, also the energy flux ϕ_T with the contributions from conduction and enthalpy from mass exchange has to be considered. The resulting expressions for the boundary fluxes can be described as

$$\begin{aligned} \phi_v &= k_{c_v}\,(c_v - c_{v,0})\,f_{lum}, \\ \phi_T &= k_T\,(T - T_0) + k_{c_v}\,(c_v - c_{v,0})\,f_{lum}\;h_v, \\ k_{c_v} &= \mathrm{Sh}\,D_{air}/L. \end{aligned} \tag{2.4}$$

The coefficients k_{c_v} and k_T are the film boundary coefficients for mass and heat transfer, respectively. k_{c_v} can be described with the Sherwood number Sh, which is set to 1 and D_{air} being the diffusion coefficient of water vapor and L is set to 0.035 m. This definition of k_{c_v} was also used in [5, 11] and leads to values in the range of [14]. The heat transfer coefficient k_T was set to $25\,\mathrm{W m^{-2} K^{-1}}$.

The conditions of the surrounding climate during the time span are described with the water vapor concentration $c_{v,0}$ and the temperature T_0. These values are obtained from data available from [76] for the location of Linz, Austria, at a time interval of 6 h at 3 a.m., 9 a.m., 3 p.m. and 9 p.m. within the 14 simulated months from November 1, 2014, to January 1, 2016, as shown in [5].

2.2.2 Geometries

In this work eighteen commonly used cross sections are investigated. Six of type solid timber (ST) (6x8, 6x16, 6x24, 10x10, 10x20, 14x28, dimensions given in cm), eight of type GLT (6x16, 6x24, 6x32, 14x28, 20x20, 20x40, 20x80, 40x40) with a thickness of 4 cm of each lamella, three boards (BO) (6x1, 6x2, 20x4) and one pole (P) with a diameter of 6 cm which are described in detail in [5]. The pith is located in the middle of the left edge for the ST cross sections or in the middle of the bottom edge of the lamellas for the GLT and board cross sections. However, the pith location does not influence the moisture simulation results, as the directional components in radial and tangential direction are the same. In case of the GLT cross sections, the top lamellas are rotated by 180 degrees. The pith of the pole is located in its center.

The chosen thickness of the finite element models is 1 mm as the user element subroutine was developed for 3D conditions. In the in-plane directions the mesh has a minimum size of 2 mm each leading to 150 elements in case of the BT 6x1 cross section

Die approbierte gedruckte Originalversion dieser Dissertation ist an der TU Wien Bibliothek verfügbar.
The approved original version of this doctoral thesis is available in print at TU Wien Bibliothek.
TU Bibliothek Your knowledge hub WIEN

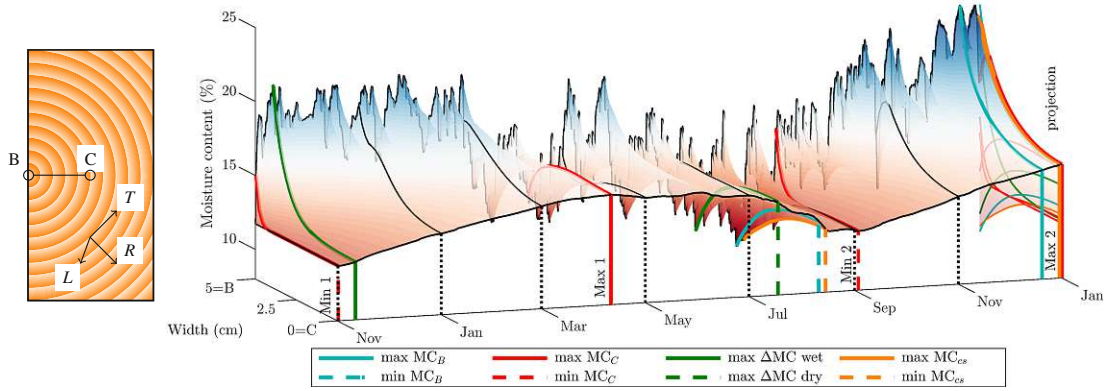

Figure 2.1: ST 10x20 cross section and MC distribution along the path from B (boundary) to C (center) over the simulated time span from November 1, 2014, to January 1, 2016. Specific points of the maximum and minimum MC values and MC differences occurring during this time span are highlighted. The projection on the right-hand side is shown in detail in Figure 2.2b in Section 2.3.2.

resulting in a total CPU time of 7,034 s for the simulated time span of 14 months. The ST 10x20 cross section consists of 5,000 elements, again with a constant element size of 2 mm, leading to a CPU time of 51 h and the largest cross section (GLT 40x40) consists of 9,600 elements with increasing element size from 2 mm close to the edge to 5 mm in the center with a CPU time of 66 h.

The glue line between the lamellas of the GLT cross sections are chosen to not influence the moisture transfer behavior, as also described in [5]. Experimental investigations of [77] with MUF-glued connections and solid timber as reference showed that glue lines have only little effect on diffusion behavior. In addition, the largest part of moisture transport is acting parallel to the glue line, as also mentioned in [73].

2.3 Results

With the presented numerical model, the MC distributions within the cross sections were computed. First the evolution of the MC values along a path from the middle of the left boundary (B) to the center (C) of the cross section is shown over the simulated time span of 14 months after installation on site between November 1, 2014, and January 1, 2016, is analyzed and specific events are defined using the ST 10x20 as an example. The MC distributions at similar events are then compared for four cross sections (ST 6x8, ST 10x20, GLT 20x40, GLT 40x40). Following notations are used: MC_B for the MC in (B), MC_C for the MC in (C), MC_{cs} for the MC averaged over the cross section (cs) and ΔMC for the difference between MC_B and MC_C.

Die approbierte gedruckte Originalversion dieser Dissertation ist an der TU Wien Bibliothek verfügbar.
The approved original version of this doctoral thesis is available in print at TU Wien Bibliothek.
TU Bibliothek Your knowledge hub WIEN

2.3.1 MC distributions over the simulation time

In Figure 2.1 the MC distribution is plotted along the path from the center of the cross section (C) to the closest point at the boundary (B), which is almost directly affected by the changing climatic conditions, with the film boundary condition and the time-dependent sorption rate reducing this influence. As during winter lower temperatures and higher relative humidities prevail, the MC values start to increase from the initial conditions which were defined based on the production process. As a result, the largest difference in MC during wetting is observed shortly after the start on November 11, 2014, with 9.11 %. In general, it can be seen that the greater the distance to the boundary, the less pronounced and delayed the MC changes. Between March and September, the temperatures are higher and relative humidities lower, thus, the MC is reduced first at the boundary in point (B) and then, after a local maximum for MC_C is reached on April 10, 2015, with 15.42 %, also inside the cross section. During summer the maximum difference in MC during the drying period is observed on July 17, 2015, with 4.75 % and MC_C starts to decrease faster due to the low relative humidities of the boundary condition, which lead to a minimum MC_B with 8.30 % on August 10, 2015. Shortly after that, on August 14, 2015, the minimum MC_{cs} is observed with 10.61 %. On September 3, 2015, the second minimum of MC_C is reached with 11.99 %. After this event, the MCs generally start to rise until the end of the year with the following maxima: MC_B on December 20, 2015, with 23.6 %, MC_{cs} on December 30, 2015, with 18.63 % and the global maximum of MC_C on December 31, 2015, with 15.69 %. When evaluating MC_B it can be seen that in general the MCs in the second winter are higher than in the first, which results from the boundary conditions as in the second winter higher relative humidities existed.

2.3.2 MC distributions at specific events

In Figure 2.2 MC distributions at specific events are depicted, which where determined from the MC distributions during the time span as shown, for example, in the projection on the right in Figure 2.1. These events are

- the maximum and minimum MC_B and MC_C,
- the critical point in time, where the crack-prone volume (sum of volumes associated with the integration points exceeding the brittle failure criterion) exhibits its maximum and minimum values during the drying and wetting period, respectively,
- the largest gradients during drying and wetting in a depth of 15 mm from the surface, as used by [72, 74],
- the maximum and minimum MC_{cs} as well as
- the maximum and minimum ΔMC.

For some cross sections the max./min. MC at the center shows two events each as the first minimum is often influenced by the initial condition (see e.g. Figure 2.1). Thus, a second minimum is defined after a first maximum is reached during spring. After this

Die approbierte gedruckte Originalversion dieser Dissertation ist an der TU Wien Bibliothek verfügbar.
The approved original version of this doctoral thesis is available in print at TU Wien Bibliothek.
TU Bibliothek Your knowledge hub WIEN

second minimum a second maximum is observed near or at the end of the simulated time span at the end of the year. If the second minimum is lower than the first, only one minimum is included. This is also done, when the first maximum during spring is greater than the maximum near the end of the year. All the mentioned distributions lie between the envelope curves, which define the maximum and minimum values at each point along the path during the simulated time span between November, 2014, and January, 2016, for Linz, Austria.

The influence of the sorption hysteresis leads to differences of up to about 4 % between the adsorption and desorption isotherm, which dampens the amplitude of the MC values. All the cross sections show their minimum of the MC_{cs} on August 14, 2015, as low relative humidities combined with higher temperatures prevail around this date. In case of the GLT 40x40 cross section a minimum would occur directly at the beginning of the time span and is, thus, an effect of the initial condition. To avoid this, the minimum MC was defined at the second minimum, occurring on August 14, 2015, with 11.96 % instead of 11.73 %.

From comparison of Figures 2.2a to 2.2d it can be seen that the envelope areas reach similar MCs at the boundaries, followed by a decrease towards the center depending on the point along the path. The MC distributions at the point of maximum and minimum MC_{cs} are in case of the two shown ST cross sections on top of the envelope boundaries,

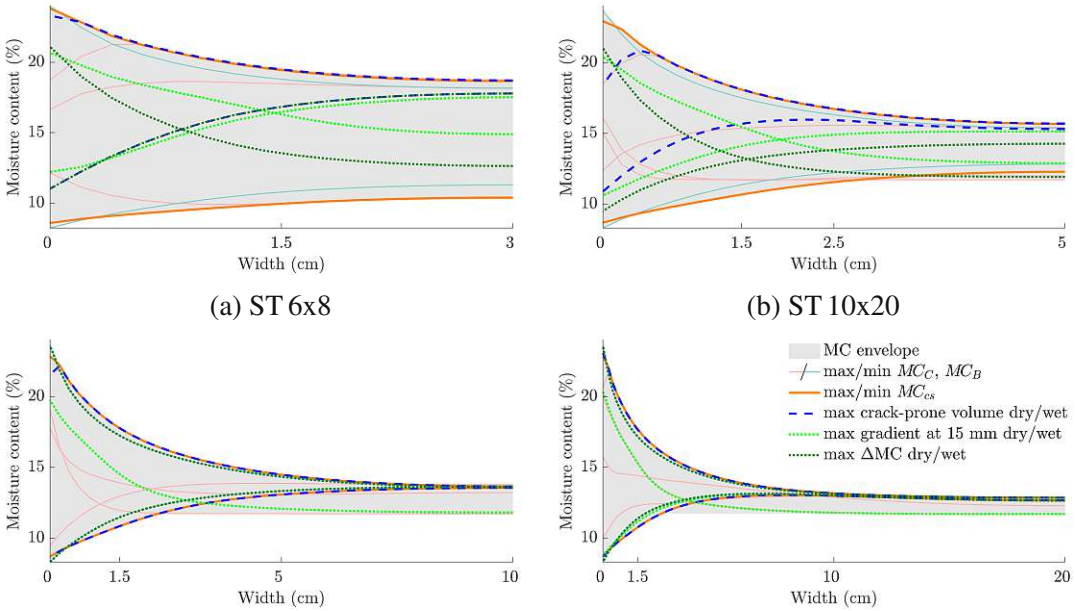

(a) ST 6x8 (b) ST 10x20

(c) GLT 20x40 (d) GLT 40x40

Figure 2.2: MC envelope, covering all possible MC states over the simulation period, and MC distributions for four different cross sections at specific events in the investigated time span based on the MC distributions along the path from B (boundary, width = 0) to C (center, width = max.) as shown for the example of the ST 10x20 cross section in Figure 2.1. For the ST 10x20 and the GLT cross sections the min. MC_{cs} refers to the previously mentioned second minimum. Drying curves show a concave and wetting curves a convex pattern.

Die approbierte gedruckte Originalversion dieser Dissertation ist an der TU Wien Bibliothek verfügbar.
The approved original version of this doctoral thesis is available in print at TU Wien Bibliothek.
TU Bibliothek Your knowledge hub WIEN

except close to a width of 0 cm, as shown in (a) and (b). Also in case of the maximum MC_{cs} curve of the GLT cross sections in (c) and (d) these two curves are congruent, however, for the minimum values the courses are different as the minimum MC_{cs} is defined excluding the initial phase, which is included in the envelope area. The curves of the maximum gradient, crack-prone volume and the maximum ΔMC occur at nearly the same point in time for the GLT and the ST 6x8 cross sections during the drying period. In case of the ST 10x20 cross section, these three distributions occur at three different points in time. While at the time of the maximum crack-prone volume ΔMC is 4.41 %, which is relatively close to the maximum of 4.75 %, the MC difference at the time of the maximum gradient at 15 mm from the boundary is only 2/3 of the maximum. For the wetting period, the distribution at the point in time of the crack-prone volume is close or congruent with the maximum envelope curve and the distribution of the maximum MC_{cs}. The maximum ΔMC is also quite close to the previously mentioned courses in case of the wide GLT cross sections as the MC in the center stays more or less constant during the simulated time span. In the smaller ST cross sections, due to the MC variation in the center, the maximum ΔMC distribution and maximum gradients in a depth of 15 mm from the boundary occur at different points in time.

2.4 Discussion

In the following, first, the results from the previously presented MC distributions during the time span are analyzed and compared to the definition of the service class thresholds from EC 5 and an assignment of the service class based on the simulated MC distributions is proposed. Second, the MC distributions within the cross sections are compared regarding the envelope curves. Then, third, based on these envelope curves MC distributions along the path from (B) to (C) are fitted for larger cross sections by only knowing the relative humidity of the surrounding relative humidity and temperature. With a similar examination in vertical direction, moisture-induced stresses in whole cross sections can easily be determined, as demonstrated by the example of the GLT 20x40.

2.4.1 Service Class

The service classes are defined in EC 5 based on the relative humidity, the MC_{cs} as well as the location of the wooden part with respect to the surrounding conditions. In general, the service classes are defined at a temperature level of 20 °C. For the relative humidity of the surrounding air in service class 1, the limit of 65 % may only be exceeded a few weeks per year. The threshold for service class 2 is a relative humidity of 85 %, which, again, only can be exceeded a few weeks per year. For the MC_{cs}, the value will not exceed 12 % and 20 % for service class 1 and 2, respectively. Additionally, in the Austrian annex to EC 5 [7], the climatic conditions are defined as indoor for service class 1, outdoor without contact with free water (rain, snow) for service class 2 and above for service class 3. Thus, according to this definition, the in this work shown cross sections have to be assigned to service class 2 due to the climatic conditions.

Die approbierte gedruckte Originalversion dieser Dissertation ist an der TU Wien Bibliothek verfügbar.
The approved original version of this doctoral thesis is available in print at TU Wien Bibliothek.
TU Bibliothek Your knowledge hub WIEN

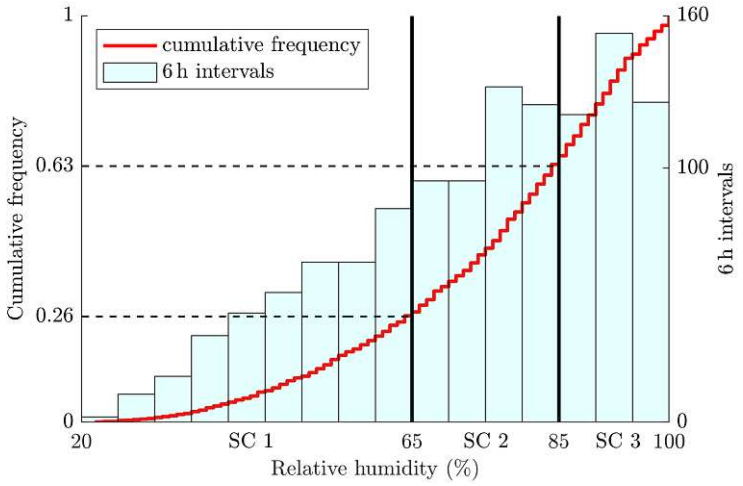

Figure 2.3: Histogram of relative humidity values between January 1, 2015, and January 1, 2016. The service class (SC) is defined based on the 65 % and 85 % thresholds.

In Figure 2.3 the histogram of the relative humidity of the surrounding air is shown. It can be seen that about 26 % of the time steps (6 h each) are in service class 1, 37 % in service class 2 and 37 % in service class 3. Even though the threshold of the chosen class can be exceeded "for a few weeks per year", the proportion in service class 3 is more than one third of the time steps, thus, an assignment to service class 2 based on the relative humidity appears to be questionable.

In Figure 2.4 the histogram of the MC_{cs} of the ST 6x8 as well as the GLT 20x40 are depicted. The averaged MCs based on the simulated moisture fields enable a definition of the cross sections according to the real climate. In case of the ST 6x8 cross section, only about 7 % of the time steps are in service class 1 and only 4 % are in class 3. The remaining 90 % are located in class 2. In case of the 20x40 GLT cross section only about 1 % of the time steps are in service class 1 and none in class 3. The remaining 99 % are in service class 2. However, the condition for exceeding the thresholds for a few weeks per year applies only to the relative humidity and, thus, service class 3 has to be assigned in case of the ST 6x8 cross section based on the EC 5 thresholds. The differences between the definitions based on the relative humidity and the MC_{cs} emerge due to the delayed reaction of the MC to the surrounding climate, which depends for instance on the size of the cross section, film boundary coefficient and sorption hysteresis, and dampens the reaction to the surrounding climate. Thus, only changes of the relative humidity for longer time spans have an effect on the averaged MCs of (larger) cross sections as mentioned in [68].

To consider the dimensions of the cross sections when assigning the service class, the maximum, minimum and averaged MC_{cs} for the year 2015 are related to the value of the cross-sectional area A by the perimeter P as it is used with the "notional size" in concrete engineering in a similar way when creep effects are determined [78]. This relation is depicted in Figure 2.5 and makes it possible to assign maximum, minimum and averaged MC values for the location Linz, Austria, for the year 2015. The relation

Die approbierte gedruckte Originalversion dieser Dissertation ist an der TU Wien Bibliothek verfügbar.
The approved original version of this doctoral thesis is available in print at TU Wien Bibliothek.
TU Bibliothek Your knowledge hub WIEN

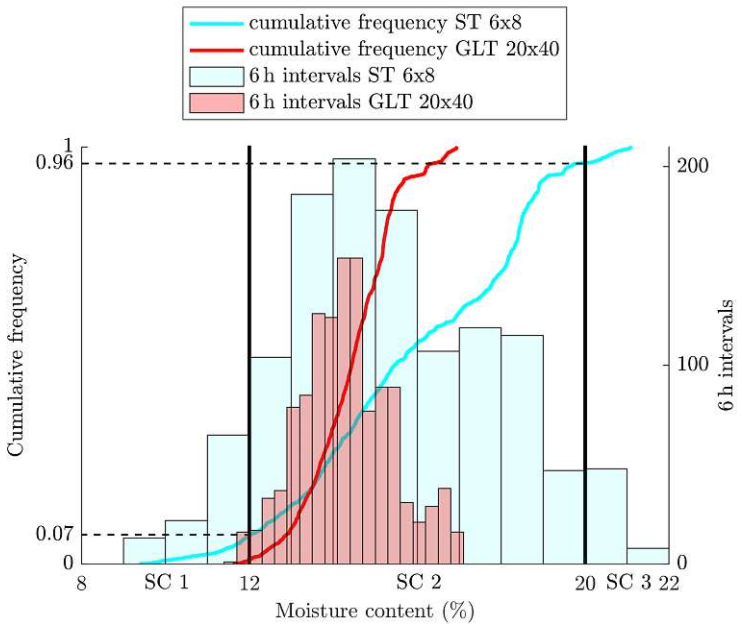

Figure 2.4: Histogram of the MC averaged over the cross section (MC_{cs}) between January 1, 2015, and January 1, 2016, determined by simulations. The service class is defined based on the 12 % and 20 % thresholds.

between the A/P ratio and the MC_{cs} can be described with the following expressions:

$$\begin{aligned} \max MC_{cs} &= 14.42 + 0.001021 \exp((x-30)^{0.65}), \\ \text{avg}\, MC_{cs} &= 14.42 + 4.174\text{E}{-5} \exp((x-30)^{0.7}) \text{ and} \\ \min MC_{cs} &= 14.42 - 0.02351 \exp((x-30)^{0.5}). \end{aligned} \tag{2.5}$$

The structure of Equation (2.5) is based on the later shown MC distributions along a path in Section 2.4.4 as the value at an A/P ratio of 0 is equal to the MC values at the boundary of 24.26 % and 8.91 % in case of wetting and drying, respectively. At "infinity", which is assumed at an A/P ratio of 30, the MC value is equal to the MC determined with the averaged RH of the whole year and the adsorption isotherm with 14.42 %, as shown in Section 2.4.3. The small BO cross sections are excluded from the fitting, as they react much faster to the surrounding climate, hence they are also excluded from the procedure in Section 2.4.3. The maximum values can be used for the definition of the service class based on the thresholds of 12 % and 20 % as well as for an estimation of the moisture-dependent stiffness behavior of wood under dry and wet conditions during the year when a moisture-dependent stiffness tensor is used. This could also be combined with the load duration class according to EC 5, i.e. the to the maximum and minimum MC_{cs} corresponding stiffness values could be used in the duration class short-term or medium-term, while the stiffness related to the over the time span averaged MC_{cs} can be used for the load duration class permanent.

Die approbierte gedruckte Originalversion dieser Dissertation ist an der TU Wien Bibliothek verfügbar.
The approved original version of this doctoral thesis is available in print at TU Wien Bibliothek.
TU Bibliothek Your knowledge hub WIEN

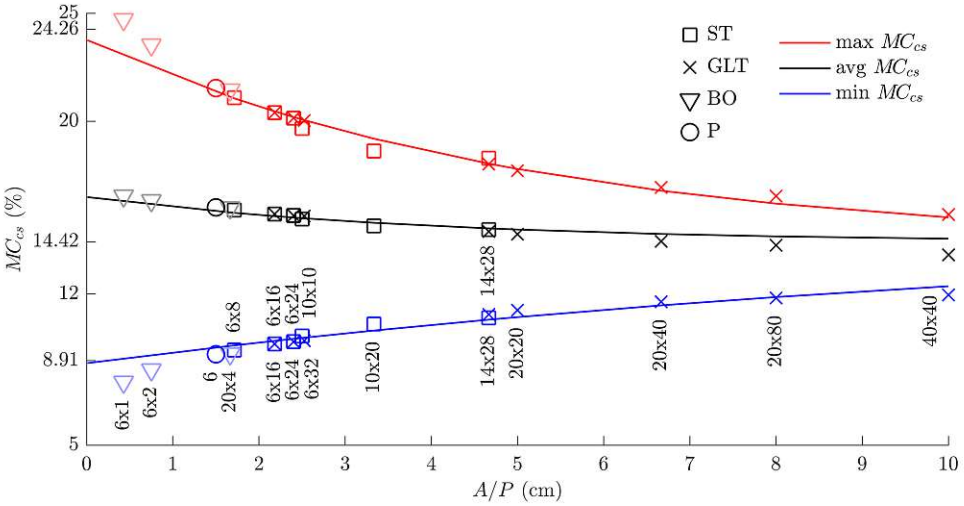

Figure 2.5: Comparison of maximum, minimum and average MC_{cs} for the year 2015 plotted against the ratio of the cross-sectional area by the perimeter (A/P). For the fitted relations, the BO cross sections are excluded as they react much faster to the boundary conditions.

Further, it can be seen that even though smaller cross sections up to a width of 6 cm had to be assigned to service class 2 based on the surrounding conditions (outside but sheltered), averaged MC values of more than 20 % occur during the time span, which would lead to conditions of service class 3, as also mentioned previously. Even when MC_{cs} is not exceeding 20 %, in some parts of the cross section MCs higher than 20 % can be observed (see Figure 2.7), which can be crucial in case of e.g. bending or torsion, where the largest stresses occur at the boundary.

2.4.2 Comparison of envelope curves

In Figure 2.6 the envelope curves of the cross sections ST 6x8, ST 10x20, ST 14x28 and GLT 20x40 are shown for the investigated time span from November 1, 2014, to January 1, 2016. The cross sections were selected such that each width is represented once, starting with a minimum value of 6 cm. While the top curve is defined by the maximum values reached during the whole simulation, the minimum values are defined after a first maximum is reached in point (C), as shown in Figure 2.1, to reduce the influence of the initial condition. The cross section GLT 40x40 is not included, as the MC in the center is always increasing during the investigated time span, thus, the final MC levels are not reached and a longer time span would be necessary to show meaningful envelope curves.

At the boundary, there is less than 0.5 % difference in MC between the different cross sections, as previously mentioned. It can be seen that the further the point is from the boundary, the smaller the distance between the envelope curves becomes. In the center of the widest shown cross section (GLT 20x40) the MC values are 13.78 % for the top and 13.21 % for the bottom curve leading to a difference of 0.57 %. The averaged

Die approbierte gedruckte Originalversion dieser Dissertation ist an der TU Wien Bibliothek verfügbar.
The approved original version of this doctoral thesis is available in print at TU Wien Bibliothek.
TU Bibliothek Your knowledge hub WIEN

relative humidity between January 1, 2015, and January 1, 2016, of the surrounding air is 75.06 % leading to an MC of 14.42 % in case of the adsorption isotherm. When comparing this value to the values of the envelope curves at the center, it is assumed that the MC of the largest cross sections might increase slightly in the following years, as can also be seen in Figure 2.1, where the MC in (C) on November 1, 2015, is 2.1 % larger than the initial value on November 1, 2014.

In [68] the concept of penetration depth was introduced. The penetration depth was defined as depth, where the difference in MC between the envelope curves is less than 0.5 % MC. Since the MC difference between the envelope curves at the center is 0.57 %, this criterion is slightly not fulfilled for the GLT 20x40 and, thus, results in a penetration depth of more than 10 cm for the location Linz, Austria, for the investigated time span. However, as the differences are generally decreasing, when the center is approached, it is assumed that the criterion would be fulfilled for the GLT 40x40 and, thus, the penetration depth is between 10 cm and 20 cm. This is in agreement with [14], where a simulation with weak paint (which is close to uncoated wood) still led to differences of also about 0.5 % MC in a depth of 10 cm. As the weak paint leads to damped maximum amplitudes compared to the uncoated sample, the MC differences are also slightly smaller compared to the here presented results.

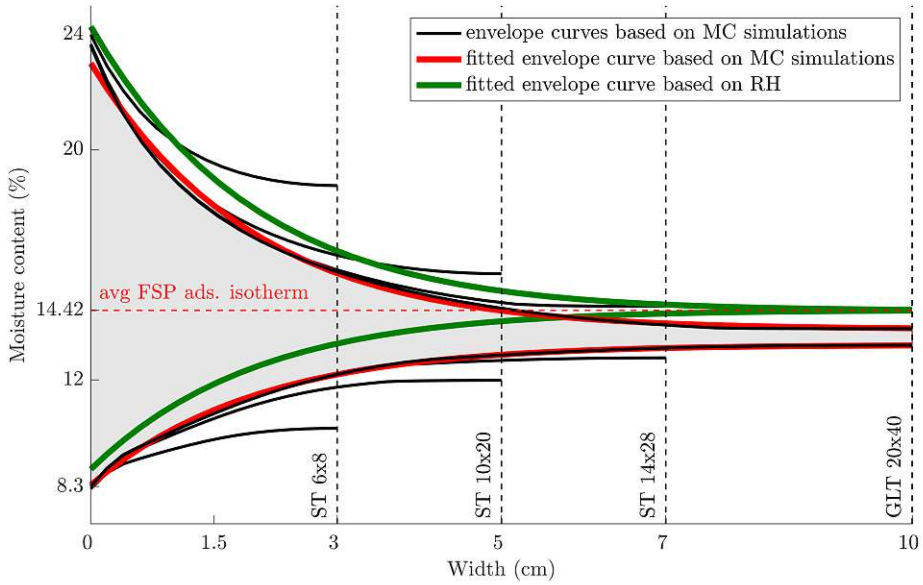

Figure 2.6: Comparison of envelope curves of selected cross sections ST 6x8, ST 10x20, ST 14x28 and GLT 20x40. Bottom curves are defined after a first maximum is reached in (C), shown in Figure 2.1, to reduce the influence of the initial MC. The horizontal dashed red line represents the MC value determined with the averaged relative humidity for the year 2015 and the adsorption isotherm. Fitted envelope curves based on the GLT 20x40 cross sections are added in red and envelope curves solely based on relative humidity in green from Section 2.4.4.

Die approbierte gedruckte Originalversion dieser Dissertation ist an der TU Wien Bibliothek verfügbar.
The approved original version of this doctoral thesis is available in print at TU Wien Bibliothek.
TU Bibliothek Your knowledge hub WIEN

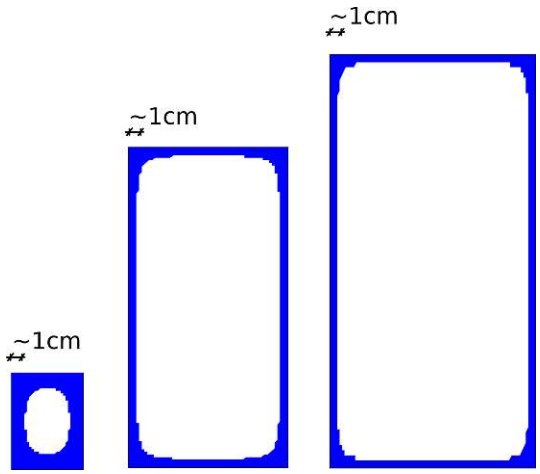

Figure 2.7: Zones, which exceed MC values of more than 20 % in case of the ST 6x8 (left), ST 14x28 (middle) and GLT 20x40 (right) cross sections during the simulated time span. The width of this zone is in all three cases about 1 cm and, thus, nearly independent of the size of the cross section.

The values at the boundary react fast to the surrounding climatic conditions, however, the values are still different from those determined with the sorption isotherm assuming an immediate equilibrium with the relative humidity by up to 10 % in MC during the investigated time span. These differences are resulting for instance from the time-dependent sorption rate as well as the film boundary coefficient. The differences are also evident when comparing the maximum MC at 0 cm from Figure 2.6 of about 24 % with the about 30 % that would result in the case of an instantaneous equilibrium to the relative humidity of 100 %. These results are in agreement with [69], where an uncoated wood cross section over a time span of 10 years was investigated, showing also maximum and minimum MC values at the boundary of 25 % and 9 %, respectively. The difference between the MC_B values determined by simulations and the calculated ones based on the relative humidity can be reduced, when an averaged MC is considered instead of using an instant equilibrium at the single point in time as described in Section 2.4.3.

Since the influence of the boundary condition is decreasing when approaching the center, only the first 0.7 cm to 1 cm next to the boundary are affected by MCs higher than 20 %. This is shown in Figure 2.7, where the areas exceeding an MC of 20 % are marked with blue. In every case the depth from the boundary is about 1 cm with larger values closer towards the edges.

2.4.3 Determination of MC values at the boundary based on relative humidities

In this section and the following sections, an approach to estimate 2D moisture fields based on the relative humidity of the surrounding climate is presented. In a first step, the MC values at the boundary are predicted in the following way: as the reaction of the MC values is dampened by the time-dependent sorption rate and the film boundary

Die approbierte gedruckte Originalversion dieser Dissertation ist an der TU Wien Bibliothek verfügbar.
The approved original version of this doctoral thesis is available in print at TU Wien Bibliothek.
TU Bibliothek Your knowledge hub WIEN

coefficient, instead of an instant equilibrium, a moving average of the relative humidity in a certain time span is used. While developing this approach, using a single time span was not sufficient to predict the maximum and minimum MC values, thus, one time span for the drying and one for the wetting case are proposed. After an optimization process based on the reduction of the error averaged over the investigated time span from November 1, 2014, to January 1, 2016, the minimum values can be predicted quite well, when a moving average with a time span of 24 h is used. The maximum values are overestimated with this simplified approach, which does not take into account both temperature effects and the time-dependent sorption rate, thus, a moving average over 24 d is used to determine the maximum values. Based on these averaged relative humidity values, the MC is calculated using the sorption hysteresis as given in [5]. The resulting MC values of the two criteria are then combined by a minimum function, leading to the "combined criterion" with results shown in Figure 2.8.

The proposed criterion leads to an averaged error of 1.19 % in MC over the entire time span. The maximum is predicted on December 17, 2015, with 24.26 % while the simulations showed a maximum value of 23.99 % (highest value of all cross sections with a width of min. 6 cm) on December 20, 2015. The minimum value is also predicted in a very good manner with 8.91 % on August 12, 2015. This is less than 0.7 % different in MC from the minimum of all the cross sections with a width of min. 6 cm, which is 8.23 % and reached on August 11, 2015. As can be seen from Figure 2.8, the proposed course is often congruent with the simulation results at the boundary, especially during the drying period. But, when using only the drying criterion, the values during the wetting period could not be predicted, as they would lead to far too high MC values. Thus, the wetting criterion is necessary to correctly predict the values during the wetting period, which can be seen in Figure 2.8 from the beginning until March and again at the end of the investigated time span.

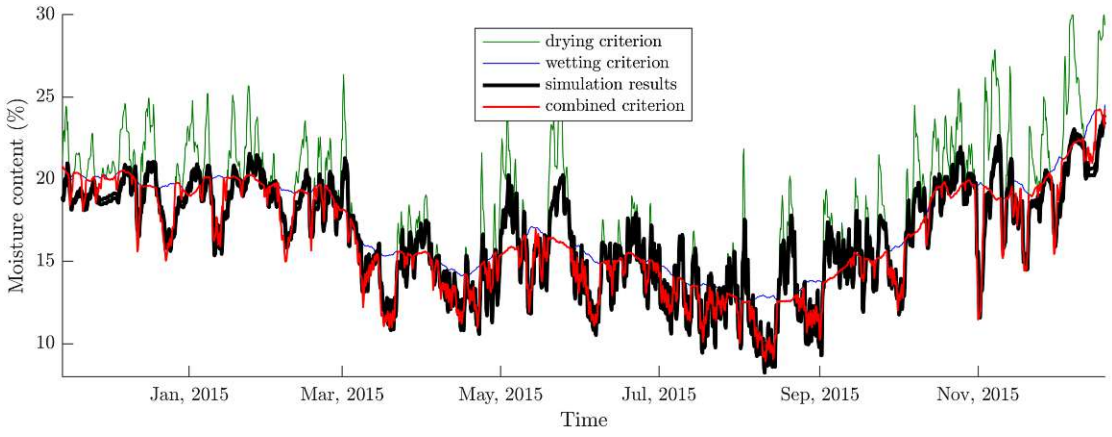

Figure 2.8: Comparison of the MC values at the boundary of all cross sections (black) with a minimum width of 6 cm to the proposed values based on the moving average of relative humidity values. For the drying and wetting criterion a time span of 24 h and 24 d is suggested, respectively.

Die approbierte gedruckte Originalversion dieser Dissertation ist an der TU Wien Bibliothek verfügbar.
The approved original version of this doctoral thesis is available in print at TU Wien Bibliothek.
TU Bibliothek Your knowledge hub WIEN

These MC values at the boundary can also be combined with results from [72–75], where MC values inside the cross sections were measured and also used to predict MC distributions, as described in the next subsection.

2.4.4 MC distributions along a path

In a second step, an MC distribution along a path using an exponential function is proposed based on Figure 2.6, where envelope curves, leading to critical MC distributions are shown for large cross sections (20 cm and more). The MC value in the center for such widths is changing only by about 0.5 % in MC during the investigated time span and, thus, can assumed to be constant. This is also in agreement with [14], where the wetting and drying envelope curves in a depth of 20 cm did not show differences. In between, an exponential fit seems to describe the values quite well. The following relations for the GLT 20x40 cross section can be determined for the upper and lower MC envelope curve based on the MC simulations with

$$\begin{aligned} upper\,MC_{sim} &= 13.78 + 0.01677\exp(x^{0.8}) \text{ and} \\ lower\,MC_{sim} &= 13.21 - 0.008837\exp(x^{0.8}). \end{aligned} \tag{2.6}$$

The expression includes the minimum and maximum values in the center, respectively.

If the MC values are not known by means of simulations, the ones in the center can be determined based on the adsorption isotherm and the averaged relative humidity during the time span. In case of the year 2015 this would lead to an averaged relative humidity of 75.06 % and an MC of 14.42 %, as also depicted in Figure 2.6. The boundary values can be estimated with the moving average, as proposed in Section 2.4.3. With the MC values at the boundary, the center and an exponential fit with an exponent of $x^{0.8}$, chosen similar to the previous approximation, the envelope curves can describe the MC distribution within the GLT 20x40 cross section with

$$\begin{aligned} upper\,MC_{RH} &= 14.42 + 0.01793\exp(x^{0.8}) \text{ and} \\ lower\,MC_{RH} &= 14.42 - 0.01004\exp(x^{0.8}). \end{aligned} \tag{2.7}$$

Both types of curves are shown in Figure 2.6. The difference between the curves based on the MC and the ones solely based on the relative humidity of the surrounding air is less than 1.3 % in MC.

As shown in Figure 2.2c, the envelope curves are quite close to the maximum curves of the crack-prone volume during the drying and wetting period.

For smaller cross sections, the difference of the envelope curves in the center is much larger as the small cross sections react much faster to changing boundary conditions, thus, the MC in the center cannot be estimated based on the averaged relative humidity of the surrounding air. However, larger cross sections are more likely to be of interest for load-bearing structures.

2.4.5 2D MC distributions within the GLT 20x40 cross section

In a third step, the function as described in Section 2.4.4 can not only be applied along the horizontal but also the vertical symmetry axis of the cross section. Both functions (in vertical and horizontal direction) are evaluated based on the following relation, where

Die approbierte gedruckte Originalversion dieser Dissertation ist an der TU Wien Bibliothek verfügbar.
The approved original version of this doctoral thesis is available in print at TU Wien Bibliothek.
TU Bibliothek Your knowledge hub WIEN

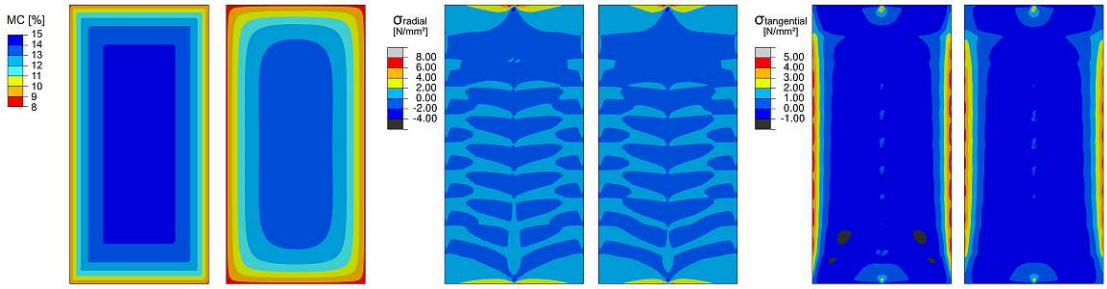

(a) Drying period - MC, radial and tangential normal stresses.

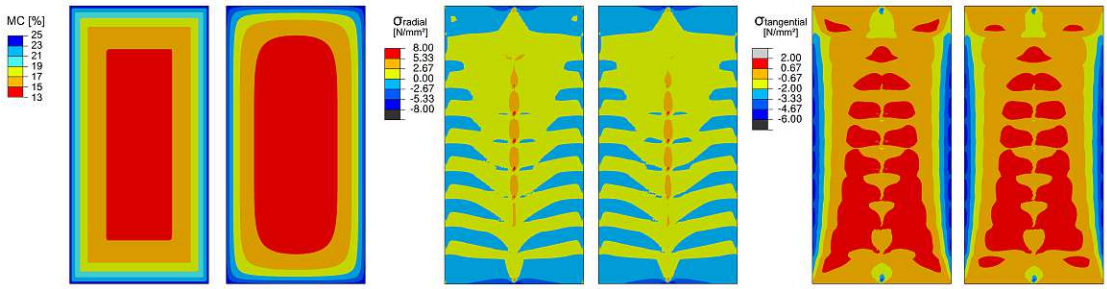

(b) Wetting period - MC, radial and tangential normal stresses.

Figure 2.9: Comparison of MCs as well as radial and tangential stresses of the simplified model solely based on relative humidities (left figures) with the complex multi-Fickian model (right figures) during the drying period (a) and wetting period (b) of the GLT 20x40.

the exponent of 0.8 for x is specific for the GLT 20x40:

$$\begin{aligned} upper\,MC_{RH} &= MC_C + F_{wet}\exp(x^{0.8}) \text{ and} \\ lower\,MC_{RH} &= MC_C - F_{dry}\exp(x^{0.8}), \end{aligned} \tag{2.8}$$

with the parameter MC_C as previously defined with an MC at the center of 14.42 % and the factor of the exponential part of the expression F determined by evaluation of the relations for the point at the boundary at x=10 cm along the width and x=20 cm along the height. The MC at the boundary is defined in Section 2.4.3 with 24.26 % for the wetting and 8.91 % for the drying case. The fields are then evaluated for both directions, which are along the width and height, and combined using the minimum value for the resulting moisture field during the drying period (and maximum for wetting). The resulting moisture field within the cross section is compared to the one determined with the multi-Fickian transport model in Figure 2.9. It can be seen that the MC values show generally a very good agreement and are only slightly underestimated towards the corners. The resulting stresses determined with the elasticity tensor and expansion coefficients given in [5] are shown by example of the normal stresses in radial and tangential directions in Figure 2.9 and depict a very good agreement. As the envelope curves of large cross sections are also congruent with the crack-prone volumes, the moisture-induced stresses leading to the largest potential of crack initiation can be determined solely based on relative humidities. In addition, the MC field can also be used for the assignment to the service class as shown in Section 2.4.1. Also, the A/P ratio for differently sized cross sections with a minimum width of 6 cm at one location can be determined solely

Die approbierte gedruckte Originalversion dieser Dissertation ist an der TU Wien Bibliothek verfügbar.
The approved original version of this doctoral thesis is available in print at TU Wien Bibliothek.
TU Bibliothek Your knowledge hub WIEN

on relative humidities as the maximum/minimum value at the boundary located at an A/P ratio of 0 are known with the procedure described in Section 2.4.3. The MC in the center of a very large cross section determined with the averaged relative humidity and the adsorption isotherm at an A/P of "infinity", which was chosen to be located at an A/P of 30, is defined according to Section 2.4.4. Then, with some points in between, determined with the procedure shown in this Section, a relation similar to Equation (2.5) can be established.

2.5 Conclusion & Outlook

To design a structural wood element according to the standard EC 5 an assignment to the service class is necessary. With the related modification factors moisture-related effects like strength and stiffness decrease at higher moisture levels as well as moisture-induced stresses are taken into account. Thus, moisture-induced stresses are not considered directly in the current code version [68]. The definition of the service class is independent of the geometry of the cross section and it is assigned based on the relative humidity of the surrounding air, the location of the wooden part with respect to the surrounding conditions or on the MC averaged over the cross section (MC_{cs}).

In this work 18 different, commonly used cross sections were investigated during 14 months after installation on site between November 1, 2014, to January 1, 2016, with a hygrothermal multi-Fickian transport model, to determine MC distributions within the cross sections exposed to a real climate condition at Linz, Austria. It is assumed that the structure is protected from rain, which is usually ensured by design methods. After the MC distributions of the 18 cross sections are simulated for the investigated time span, the following main findings can be concluded:

- When comparing the different thresholds of EC 5 it could be seen that the different criteria for assigning the service class would lead to different results. In contrast to the criteria for relative humidity or ambient conditions, the criterion for MC is influenced by the size of the cross section. However, since the MC under changing outdoor conditions can only be determined by simulations, this criterion is not easily applicable.

- A relationship between the minimum, maximum and averaged MC_{cs} for the year 2015 is presented based on the ratio of the area A by the perimeter P which can be used to assign the service class. Beside the assignment, maximum, minimum and average values of MC_{cs} can be used to include a moisture-dependent elasticity tensor, which could also be combined with the load duration classes i.e. the maximum and minimum values prevailing during short-term load duration class.

- The envelope curves of cross sections with a minimum width of 6 cm were compared, leading to similar curves, showing nearly the same maximum and minimum values at the boundary (with less than 0.5 % difference in MC) and converging towards the center of the largest cross sections. The envelope curves for large cross sections can be predicted with an exponential function in a very good manner.

Die approbierte gedruckte Originalversion dieser Dissertation ist an der TU Wien Bibliothek verfügbar.
The approved original version of this doctoral thesis is available in print at TU Wien Bibliothek.
TU Bibliothek Your knowledge hub WIEN

- The MC values at the boundary can be estimated with average differences during the simulated time span of 1.19 % with a moving average of the relative humidities of the surrounding climate. The maximum and minimum MC values at the boundary could also be predicted very well.
- With the previously described procedure an approach to predict 2D MC distributions within larger (more than 20 cm wide) cross sections solely based on relative humidities was proposed. Based on these, the same approach as before can now be used to obtain location-specific moisture-dependent stiffness values or moisture-induced stresses.

As the findings of this paper are related to the location of Linz, Austria, other locations should be investigated as well to check the reliability of the proposed methods. Also similarities between different locations should be examined which could lead to e.g. similar MC distributions of a specific climate zone. With these a "moisture load" map, like the existing maps for loads from wind, rain and snowfall, could be established to better consider moisture-related effects when designing a construction according to EC 5. The moisture fields determined by the proposed method can then also be combined with further developments in computational wood mechanics [29, 30], where also the possible presence of knots and fiber deviations can be considered. Thus, the study on wetting and drying cases can be extended to investigate the possible cracking or ductile failure of timber elements by applying wood-specific failure criteria [31–34, 79].

Conflict of interest

None declared.

Acknowledgements

The support from the Doka GmbH and the Austrian Research Promotion Agency (FFG, Project Number 857041) as well as the Austrian Science Fund (FWF) through the START project Y1093-N30 are gratefully acknowledged.

Die approbierte gedruckte Originalversion dieser Dissertation ist an der TU Wien Bibliothek verfügbar.
The approved original version of this doctoral thesis is available in print at TU Wien Bibliothek.
TU Bibliothek Your knowledge hub WIEN

Die approbierte gedruckte Originalversion dieser Dissertation ist an der TU Wien Bibliothek verfügbar.
The approved original version of this doctoral thesis is available in print at TU Wien Bibliothek.

Die approbierte gedruckte Originalversion dieser Dissertation ist an der TU Wien Bibliothek verfügbar.
The approved original version of this doctoral thesis is available in print at TU Wien Bibliothek.
TU Bibliothek Your knowledge hub WIEN

Publication 3

Finite-element-based prediction of moisture-induced crack patterns for cross sections of solid wood and glued laminated timber exposed to a realistic climate condition [5]

Authored by Maximilian Autengruber, Markus Lukacevic, Christof Gröstlinger and Josef Füssl

Published in *Construction and Building Materials*, 271 (2021), 121775

Abstract: Moisture may significantly influence the dimensions and behavior of wooden elements and, thus, it is important to consider within both serviceability as well as ultimate limit state designs. Dimensional changes, also called swelling (during wetting) and shrinkage (during drying), are non-uniform due to the direction-dependent expansion coefficients of wood and usually lead to eigenstresses. If these exceed certain strength values, cracking may occur, which reduces the resistance to external loads, especially to shear stresses. The current standard Eurocode 5 takes these circumstances very simplified into account, by so-called service classes, defined based on the surrounding climate and average moisture levels over the course of a year. Accordingly, reduction factors for strength values and cross section widths are assigned.

For a better understanding of the climate-induced changes in wooden beams, we exposed 18 different beams with varying cross sections to a representative climate of Linz, Austria, within the framework of a finite element simulation and investigated the resulting moisture fields and crack patterns. For this purpose, expansions and linear-elastic stresses were simulated by using the thermal and moisture fields obtained in the first simulation step and expansion coefficients. Using a multisurface failure criterion, two “critical points in time” were determined for each cross section, at which advanced

crack simulations were carried out using the extended finite element method. The resulting crack lengths showed that the Eurocode 5 assumption of a linear relationship between crack-free and total width could be verified for both drying and wetting cases.

In future, the obtained crack patterns might also be used to investigate the actual reduction of load-bearing capacities of such cross sections, since the position of a crack and, for example, the maximum shear stress may not coincide. For the first time in this work, a consistent concept is presented to estimate the resulting crack formation in a wooden element from any moisture load based on a mechanical well-founded simulation concept. For this reason, this work is intended to lay a basis for a more accurate consideration of climate-related loads on wooden elements up to timber constructions.

3.1 Introduction

Fracture in wood due to climate fluctuations over the year is an important issue for both the serviceability and the load-bearing capacity of timber structures. Wood is a naturally grown building material and consists of an inhomogeneous, cellular structure. The walls of these cells are hygroscopic, which leads to varying properties and dimensions depending on the moisture content (MC), e.g. resulting in density, stiffness and strength as well as thermal conductivity and diffusivity changes [35]. The MC is defined as the mass of water in wood divided by the oven-dry mass of wood [55]. The fraction of the MC, which is held in the cell wall, is limited by the so-called fiber saturation point (FSP). Thus, if the MC is lower than the FSP, it is assumed that water only exists as bound water in the cell wall and as water vapor in the lumen. If the MC is higher than the FSP, also free water in the lumen exists [35]. As the change of the stiffness and strength properties as well as the hygro-expansion behavior is related to the MC in the cell walls, the influence in MC on these properties is also limited by the FSP with only small additional changes when exceeding the FSP according to [35].

The change in dimensions is non-uniform due to the different hygro- and thermal expansion behavior in the three characteristic directions, namely longitudinal, radial and tangential. These differences in the orthotropic material orientations lead to stresses, which are called moisture-induced stresses [66], that can cause cracks or delamination if the corresponding strength values are exceeded.

To deal with these circumstances, the timber-related European structural design standard [7] (Eurocode 5, EC 5) offers different approaches with regard to the consideration of moisture-dependent material properties and cracks. For the former, EC 5 defines service classes depending on the surrounding climate on the basis of relative humidity and temperature. The location of the timber component is also taken into account and can be divided into: outside, outside covered from rain and inside. These conditions, together with the duration of loading, define the reduction factor for the strength k_{mod} for the ultimate limit state (ULS) and the stiffness k_{def} for the serviceability limit state (SLS), respectively. For the latter, cracks are considered for the design with regard to shear loading by introducing the parameter k_{cr} which reduces the total width of the cross section. Currently, moisture-induced stresses are not taken into account directly in EC 5, instead they are considered as material properties [68].

Die approbierte gedruckte Originalversion dieser Dissertation ist an der TU Wien Bibliothek verfügbar.
The approved original version of this doctoral thesis is available in print at TU Wien Bibliothek.
TU Bibliothek Your knowledge hub WIEN

Recent attempts to quantify these moisture-induced stresses were made in [75], where a guideline for Switzerland was proposed. Based on data of weather stations over a longer time span (average MCs and changes of MCs over the year for a total of 30 years) the MCs were calculated from relative humidities using the mathematical model of [80]. This results in a maximum and minimum MC value in the outer regions of the cross sections. In addition, measurements of [72, 74] on different types of wooden buildings over a period of one year were used to determine the MCs within the cross sections.

Moisture simulations of timber beams were also investigated in [12, 14, 68, 69], where wooden cross sections sheltered from rain, i.e. with moisture states below the FSP, were exposed to a climate and the moisture contents were calculated using a multi-Fickian model. In [8] a hygro-mechanical model was presented, which couples the multi-Fickian approach with a mechanical material model. It is also stated that a single-phase diffusion model must not be used for high MC gradients that occur in samples with a thickness of more than a few millimeters and relative humidities of more than 65 %. In [66], GLT beams were studied in different European climates. The authors concluded that northern European climates lead to higher stresses due to the greater changes in relative humidity. In [67], it is described that the tensile stresses are higher during drying than during wetting. Cracking would probably occur during drying from 90 % to 50 % relative humidity. During wetting from 50 % to 90 % relative humidity cracking is stated as less likely.

In [68] the concept of penetration depth was introduced, where a wooden sample was exposed to a harmonic variation of the relative humidity. Based on the chosen parameters of the sinusoidal function, which where amplitude, period and mean value of the relative humidity, it was concluded that the largest positive gradients (drying case) occur during a period chosen between 24 h and 48 h and are of interest when surface cracks are investigated. Also the influence of the period of the function was investigated and it was concluded that only longer time spans of more than a few days led to deeper penetration depths e.g. a period of five days with an amplitude of 50 % relative humidity starting from initially 65 % RH was necessary to reach a penetration depth of 10 mm.

The aim of this paper is to evaluate the assumptions in EC 5 regarding the crack lengths considered in case of shear loads. For this purpose, 18 uncoated cross sections with different dimensions made of solid timber (ST) and glued laminated timber (GLT) were simulation-wise exposed to a historical climate in Linz, Austria, for 14 months, to investigate the moisture behavior and resulting cracks during that time. Based on the external climate conditions, moisture and temperature fields were simulated for all cross sections. These fields were then used to determine the resulting stresses and strains within the cross sections, according to the previous literature. Based on these stresses, the following steps are also performed in the present paper:

1. A previously developed, moisture-independent, multisurface failure criterion [32] was used to investigate the cross sections' susceptibility to cracking.

2. Then, critical points in time were examined in more detail using the extended finite element method (XFEM) to simulate the initiation and propagation of moisture-induced cracking.

Die approbierte gedruckte Originalversion dieser Dissertation ist an der TU Wien Bibliothek verfügbar.
The approved original version of this doctoral thesis is available in print at TU Wien Bibliothek.
TU Bibliothek Your knowledge hub WIEN

3. The lengths of these cracks were then compared to the design rules in EC 5, which take into account the drying conditions. Additionally, similar suggestions for wetting cases were developed.

3.2 Materials and Methods

Wood is a naturally grown orthotropic material and changes in its moisture state lead to varying properties and dimensional changes. To describe the deformations caused by MC and temperature, first, the transport mechanisms within wood needs to be defined. Secondly, model and corresponding material properties are described, which are used to study the moisture-induced cracking behavior of timber cross sections.

3.2.1 Mathematical model for moisture transport in wood

Under normal service conditions, the MC of timber structures is always below the fiber saturation point (FSP), as such structures are designed to protect the wood from direct contact with liquid water. Thus, below the FSP, moisture transport can be modeled according to the multi-Fickian theory [8, 9, 11, 12, 14], considering diffusion in the lumens via water vapor (in terms of concentration c_v) from the boundary through open pits and in parallel diffusion of bound water (in terms of concentration c_b) within the cell walls. These two diffusion processes are coupled via sorption, that can be described by including a hysteresis effect, and the related sorption rate is denoted by $\dot{c}_{bv}$. The variation of the bound water concentration then leads to the dimensional changes.

While c_v is defined with respect to the lumen, which has the volume proportion f_{lum}, c_b and $\dot{c}_{bv}$ are defined with respect to the whole volume of the representative volume element (RVE).

In this paper, the moisture transport model of [3] was used, but without free water transport mechanisms and their corresponding phase change terms.

This leads to the following set of governing equations:

Conservation of bound water concentration:

$$\frac{\partial c_b}{\partial t} = \frac{\partial}{\partial \boldsymbol{x}} \cdot \boldsymbol{D_b} \cdot \frac{\partial c_b}{\partial \boldsymbol{x}} + \frac{\partial}{\partial \boldsymbol{x}} \cdot \boldsymbol{D_{bT}} \cdot \frac{\partial T}{\partial \boldsymbol{x}} + \dot{c}_{bv} \tag{3.1}$$

Conservation of water vapor concentration:

$$\frac{\partial c_v\, f_{lum}}{\partial t} = \frac{\partial}{\partial \boldsymbol{x}} \cdot \boldsymbol{D_v} \cdot \frac{\partial c_v}{\partial \boldsymbol{x}}\, f_{lum} - \dot{c}_{bv} \tag{3.2}$$

Conservation of energy:

$$\begin{aligned} \frac{\partial \rho\, h}{\partial t} = &+ \frac{\partial}{\partial \boldsymbol{x}} \cdot \boldsymbol{K} \cdot \frac{\partial T}{\partial \boldsymbol{x}} \\ &+ \frac{\partial}{\partial \boldsymbol{x}} \cdot \boldsymbol{D_b} \cdot \frac{\partial c_b}{\partial \boldsymbol{x}}\, \overline{h}_b + \frac{\partial}{\partial \boldsymbol{x}} \cdot \boldsymbol{D_{bT}} \cdot \frac{\partial T}{\partial \boldsymbol{x}}\, \overline{h}_b \\ &+ \frac{\partial}{\partial \boldsymbol{x}} \cdot \boldsymbol{D_v} \cdot \frac{\partial c_v}{\partial \boldsymbol{x}}\, h_v\, f_{lum} \\ &+ \dot{c}_{bv}\, (h_v - h_b) \end{aligned} \tag{3.3}$$

Die approbierte gedruckte Originalversion dieser Dissertation ist an der TU Wien Bibliothek verfügbar.
The approved original version of this doctoral thesis is available in print at TU Wien Bibliothek.
TU Bibliothek Your knowledge hub WIEN

The term on the left-hand side of Equations (3.1) to (3.3) accounts for the change of the concentration/energy over time ∂t, which can be described as accumulation. The diffusion processes are described by the transport tensors for bound water $\boldsymbol{D_b}$ and water vapor $\boldsymbol{D_v}$, respectively. Thermal conduction is denoted with $\boldsymbol{K}$.

In (3.3), $\overline{h}_b$ and h_b are the averaged and specific enthalpy of bound water, respectively, and h_v is the specific enthalpy of water vapor. The numerator of the term describing the change of the internal energy over time increment Δt from Equation (3.3) can be described as

$$\begin{aligned}(\rho\, h)_{t+\Delta t} - (\rho\, h)_t = {} & \rho_d\, c_{p_s}\, (T_{t+\Delta t} - T_t) \\ & + c_{b_{t+\Delta t}}\, \overline{h}_{b_{t+\Delta t}} - c_{b_t}\, \overline{h}_{b_t} \\ & + c_{v_{t+\Delta t}}\, h_{v_{t+\Delta t}}\, f_{lum_{t+\Delta t}} - c_{v_t}\, h_{v_t}\, f_{lum_t}.\end{aligned} \tag{3.4}$$

The mathematical descriptions of these terms as well as the transport tensors are defined in Tables 3.A.1 and 3.A.2 in Section 3.A.

Equations (3.1) to (3.3) are implemented with a user element subroutine in the finite element software *Abaqus* [59], where they are solved with the modified Newton method. The used elements are brick-type with linear interpolation functions. The material orientations are considered to be cylindrical-orthotropic and defined in each integration point, depending on a chosen and cross-section-specific pith location.

The hysteresis was chosen to be isothermal as shown in [12] and described in Section 3.B. Values for a temperature-dependent hysteresis were recently presented in [14] and could be implemented into a future model. However, for the two temperature-dependent adsorption isotherms for 273.15 K and 303.15 K, the difference in moisture content is always less than 2 % when considering the RH range from 0 % to 90 %. Since high values of temperatures correspond to lower relative humidities, the resulting effect is even smaller. Similarly, the differences between the desorption isotherm of [12] and the desorption isotherm for 273.15 K and 303.15 K, respectively, are less than 2.5 % MC for relative humidities below 85 %. Thus, it seems to be acceptable to use an isothermal hysteresis function for this work.

3.2.1.1 Initial conditions

The initial temperature, denoted by T_{ini}, and the initial water vapor concentration, denoted by $c_{v,ini}$ and based on the relative humidity φ_{ini}, define the initial bound water concentration $c_{b,ini}$, which is chosen to be in equilibrium via the adsorption isotherm.

3.2.1.2 Boundary conditions

The fluxes through exchange surfaces, which are affected by climate changes, are described with Neumann boundary conditions. The water vapor concentration flux ϕ_v across the boundary is defined as

$$\begin{aligned}\phi_v &= k_{c_v}\, (c_v - c_{v,0})\, f_{lum}, \\ k_{c_v} &= \mathrm{Sh}\, D_{air}/L\end{aligned} \tag{3.5}$$

Die approbierte gedruckte Originalversion dieser Dissertation ist an der TU Wien Bibliothek verfügbar.
The approved original version of this doctoral thesis is available in print at TU Wien Bibliothek.
TU Bibliothek Your knowledge hub WIEN

with k_{c_v} as the film boundary coefficient, which considers air flow and convection depending on air speed as well as potential coatings. $c_{v,0}$ is the water vapor concentration of the surrounding climate and f_{lum} accounts for the lumen part of the volume, where the exchange takes place. The film boundary coefficient is chosen as in [11] with the Sherwood number Sh of 1 and D_{air} the diffusion coefficient of water vapor in air from Table 3.A.1 with $\boldsymbol{\xi}$ of 1 and L of 0.035 m. This leads to k_{c_v} values in the range of [14].

The energy flux ϕ_T across the exchange surface is described by

$$\phi_T = k_T \left(T - T_0\right) + k_{c_v} \left(c_v - c_{v,0}\right) f_{lum}\ h_v, \tag{3.6}$$

with the heat transfer coefficient k_T and the temperature of distant air T_0. The heat transfer coefficient was set to $25\,\mathrm{W m^{-2} K^{-1}}$.

3.2.1.3 Glue lines

For the GLT cross sections it is assumed that the adhesive is based on melamine. [77] showed that wood with glued connections of this type (MUF) has no or only very little difference in diffusion behavior compared to a reference specimen of solid timber with the same geometry. Thus, it is assumed that water vapor and bound water penetrate through the glue line without further resistance. The effect of glue lines was also investigated in [81].

3.2.2 Finite-element-based model for fracture in wood

In this paper, the model of [32] was used to investigate the moisture-induced cracking behavior of timber cross sections. Based on the moisture fields (see Figure 3.1a), the cross sections' expansion due to swelling and shrinkage was determined with linear elastic simulations, i.e. viscoelastic effects and mechanosorption as well as plastifications are not included. In each integration point and for all simulation increments the multisurface failure criterion from [32] was evaluated (see Figure 3.1b). For each integration point violating this criterion, the corresponding volume was added up, resulting in a "crack-prone volume" per time point, thus, the crack-prone volume is the volume, where the moisture-induced stress violates one of the crack initiation surfaces of the multisurface failure criterion. This results in a graph of this volume over the simulation time (see Figure 3.1c). At two distinct peaks of this graph, one for the drying period (MC at the boundary is higher than at the center) and one for the wetting period (MC at the boundary is lower than at the center), simulations with the XFEM were performed (see Figure 3.1d) to find the most critical moisture-induced stress situations, which would result in multiple cracks. These two distinct points are further called "critical points in time". For some cross sections, crack-prone volumes exist only during the drying period.

3.2.2.1 Material properties

The moisture-dependent elastic material properties were determined using the continuum micromechanics model of [82]. Input parameters are a clear wood dry density of $420\,\mathrm{kg\,m^{-3}}$ and the chemical composition of spruce. With these parameters, the

Die approbierte gedruckte Originalversion dieser Dissertation ist an der TU Wien Bibliothek verfügbar.
The approved original version of this doctoral thesis is available in print at TU Wien Bibliothek.
TU Bibliothek Your knowledge hub WIEN

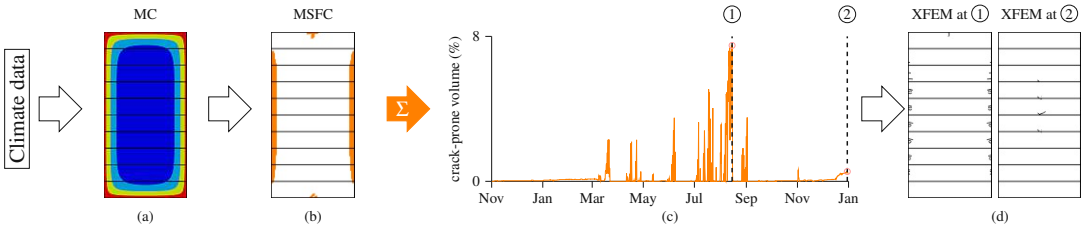

Figure 3.1: Schematic description for the identification of crack-prone regions and critical points in time. Based on climate data, for various cross sections (a) moisture fields and resulting stress states were simulated. Next, (b) a multisurface failure criterion (MSFC) was evaluated in each integration point to identify crack-prone regions. (c) The corresponding *crack-prone volumes* were then added up and plotted versus the time domain. At specific peaks, ① for the drying and ② for the wetting period, (d) XFEM simulations were performed to determine crack patterns.

Table 3.1: Expansion coefficients α for temperature [84] and β for moisture [83]

	α [1/K]	β [%/%]
L	3.15 E-6	0.015
R	23.8 E-6	0.19
T	32.3 E-6	0.36

moisture-dependent micromechanical model is pre-evaluated for MC levels from 3 % to 30 % at 1 % increments. The resulting material properties serve as a database in tabular form and are then interpolated by Abaqus for the specific MC. The components for the elasticity tensor are given in Table 3.C.1 in Section 3.C.

The coefficients of moisture [83] and thermal [84] expansion are defined according to Table 3.1.

3.2.2.2 Multisurface failure criterion

Since wood is naturally grown, the resulting irregular structure makes it challenging to describe its failure behavior. An approach to describe the failure behavior at the level of annual rings has been studied on a unit cell in [32], using previous results from single wood cell simulations [31, 34, 85]. Various load combinations were numerically tested and, thus, the main failure characteristics could be characterized. Based on these, a multisurface failure criterion was developed, which is able to describe ductile (plastic) and brittle (cracking) failure mechanisms. The failure criterion is described in terms of multiple Tsai-Wu failure surfaces [86] at the clear wood level as follows:

Die approbierte gedruckte Originalversion dieser Dissertation ist an der TU Wien Bibliothek verfügbar.
The approved original version of this doctoral thesis is available in print at TU Wien Bibliothek.
TU Bibliothek Your knowledge hub WIEN

$$
\begin{aligned}
f_i^{cw}(\sigma) = \; & a_{LL,i} \cdot \sigma_{LL} + a_{RR,i} \cdot \sigma_{RR} + a_{TT,i} \cdot \sigma_{TT} \\
& + b_{LLLL,i} \cdot \sigma_{LL}^2 + b_{RRRR,i} \cdot \sigma_{RRRR}^2 \\
& + b_{TTTT,i} \cdot \sigma_{TT}^2 + 2\, b_{RRTT,i} \cdot \sigma_{RR} \cdot \sigma_{TT} \\
& + 4\, b_{RTRT,i} \cdot \tau_{RT}^2 + 4\, b_{TLTL,i} \cdot \tau_{TL}^2 \leqslant 1
\end{aligned}
\tag{3.7}
$$

The Tsai-Wu tensor components $a_{LL,i}$, $a_{RR,i}$, $a_{TT,i}$, $b_{LLLL,i}$, $b_{RRRR,i}$, $b_{TTTT,i}$, $b_{RRTT,i}$, $b_{RTRT,i}$ and $b_{TLTL,i}$ are defined according to [32] for all 8 failure surfaces, which are depicted in Figure 3.2. It can be seen that the strength in longitudinal direction is much higher than in transversal direction, with the perpendicular-to-grain tensile strengths being approximately 5 MPa in radial direction and 2 MPa in the tangential one. For this

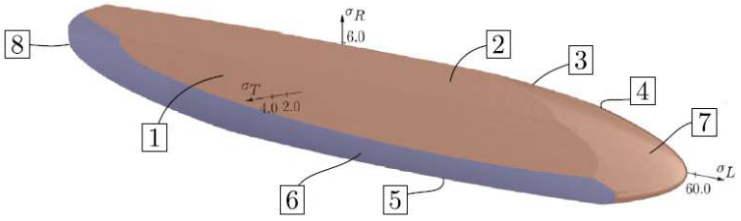

Figure 3.2: Multisurface failure criterion shown in the σ_L–σ_R–σ_T-space from [32].

study, the failure surfaces are kept constant with respect to moisture and temperature changes.

3.2.3 Geometries

Eighteen commonly used cross sections are investigated in this paper: six of type solid timber (ST) with a rectangular cross section, eight of type glued laminated timber (GLT), three boards (BO) and one pole (P). The dimensions are given in Table 3.2 for solid timber and the boards, respectively. The GLT beam dimensions and configurations as well as the pole are described in Table 3.3. The bond lines are considered as tied connections and, thus, cracks do not occur at the bond line but possibly next to them, as it is oftentimes the case as described in [1].

For the solid timber cross sections, the pith is located in the middle of the left edge and for the GLT cross sections in the middle of the width of the lamellas (see Figure 3.3), with the lamella heights being 4 cm. The top lamellas of the GLT beams are flipped according to usual GLT setups.

The pith of the pole is located in the center point and the pith of the boards in the middle of the bottom edge in analogy to the lamellas of the GLT cross sections.

The discretization is done by brick-type elements with linear shape functions for both the hygrothermal and the stress simulations. The chosen thickness of the models is 1 mm, which leads to pseudo-3D conditions, so that the simulation program could easily be extended to more complex 3D geometries.

Die approbierte gedruckte Originalversion dieser Dissertation ist an der TU Wien Bibliothek verfügbar.
The approved original version of this doctoral thesis is available in print at TU Wien Bibliothek.
TU Bibliothek Your knowledge hub WIEN

Table 3.2: Solid timber (ST) and board (BO) dimensions

	ST						BO		
	6x8	6x16	6x24	10x10	10x20	14x28	6x1	6x2	20x4
Width (cm)	6	6	6	10	10	10	6	6	20
Height (cm)	8	16	24	10	20	28	1	2	4
Element size (mm)	2	2	2	2	2	5	2	2	2
# of finite elements	1200	2400	3600	2500	5000	3600	150	300	2000

Table 3.3: Glued laminated timber (GLT) and pole (P) dimensions

	6x16	6x24	6x32	14x28	20x20	20x40	20x80	40x40	P 6
Width (cm)	6	6	6	14	20	20	20	40	6
Height (cm)	16	24	32	28	20	40	80	40	-
Element size (mm)	2	2	2	2-5	2-5	2-5	2-5	2-5	2
# of finite elements	1200	2400	4800	2464	2400	4800	9600	9600	942
# of lamellas	4	6	8	7	5	10	20	2x10	-

The boundary conditions are a hinged support in the center point and a roller support in the middle of the vertical edge on the right hand side of the cross section, as shown in Figure 3.3. Plane strain conditions define the out-of-plane boundary conditions. It is assumed that at the initial state no moisture-induced eigenstresses are present.

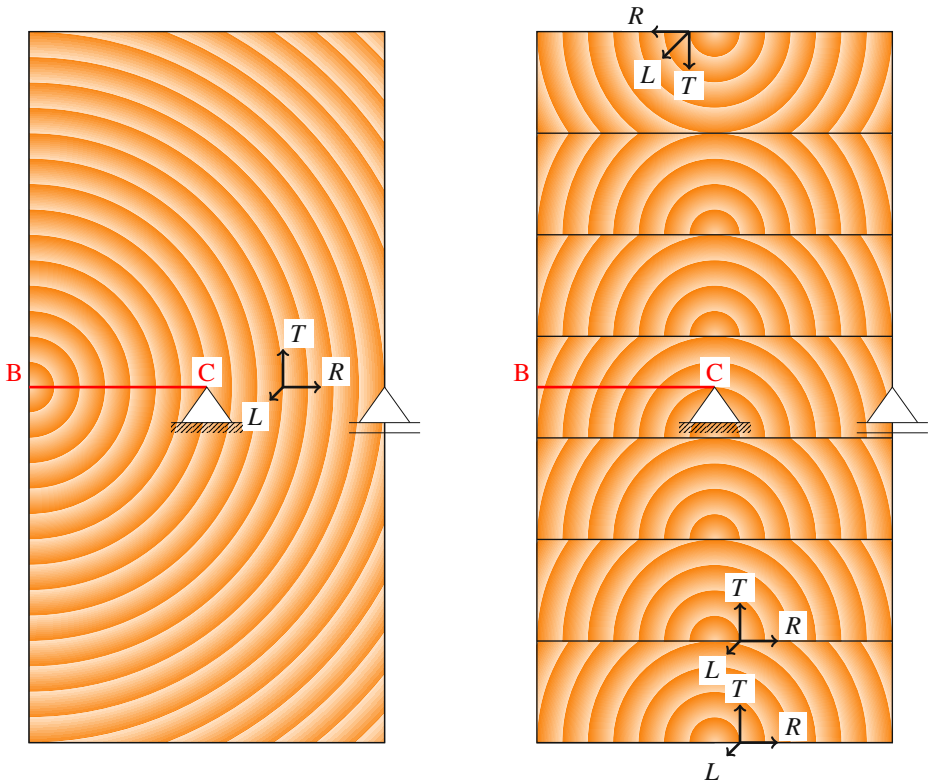

(a) ST 14x28 (b) GLT 14x28

Figure 3.3: Boundary conditions, pith locations and definition of local coordinate systems for (a) ST and (b) GLT cross sections.

Die approbierte gedruckte Originalversion dieser Dissertation ist an der TU Wien Bibliothek verfügbar.
The approved original version of this doctoral thesis is available in print at TU Wien Bibliothek.
TU Bibliothek Your knowledge hub WIEN

3.2.4 Climate data

For the evaluation of the moisture fields at the location of Linz, Austria, the values for temperature and relative humidity are based on data available from [76] at a time interval of 6 h. Figure 3.4 shows the time course of these boundary conditions for a total of 14 months (November 1, 2014, to January 1, 2016). The time span was chosen based on a comparison to long term climate measurements, as the year 2015 showed drier and slightly warmer conditions, except in May where the relative humidity was higher compared to the average between 1971 and 2000. It can be seen that low temperatures and high relative humidities prevail in the wetting period during winter, while higher temperatures and larger changes in relative humidity occur in the drying period during summer. The boundary conditions are applied to all four sides of the cross sections, i.e. no boundary conditions are applied to the front and back, thus assuming infinitely long or end sealed beams. The maximum value of 100 % relative humidity is reached a few times during the year, while the minimum value of 22 % occurs in the drying period. The maximum temperature is 36 °C and the lowest is -9 °C. As mentioned, it is assumed that the cross sections are prevented from coming into contact with liquid water, e.g. from rain.

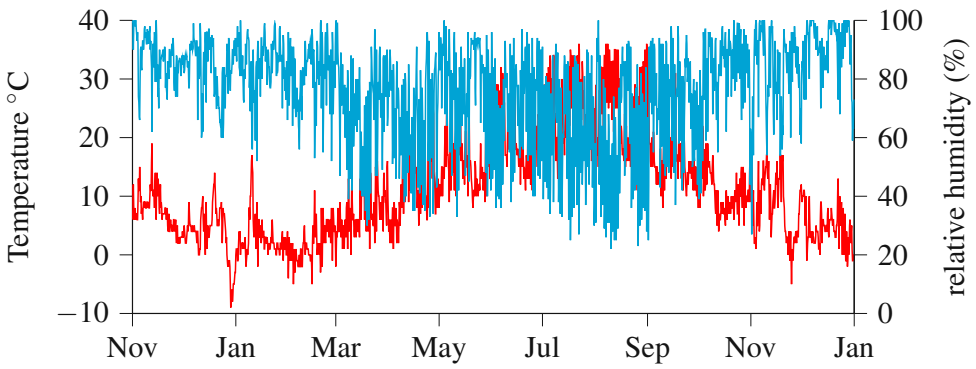

Figure 3.4: Relative humidity (blue) and temperature (red) for the simulated period from November 1, 2014, to January 1, 2016, in Linz, Austria (Location: Linz Airport, 298 m AMSL).

The initial conditions are set to a relative humidity of $\varphi_{ini} = 0.65$ at a temperature of 293.15 K. This results in an initial water vapor concentration of $0.011235\,\mathrm{kg\,m^{-3}}$ and an initial bound water concentration of $49.25\,\mathrm{kg\,m^{-3}}$, respectively.

3.3 Results

In the following section, first the results of the moisture field simulations are presented and then the results of the linear elastic stress simulations are shown, using the moisture and temperature fields from the first step as loads. A multisurface failure criterion is used to identify "crack-prone regions" in the cross sections, on the basis of which critical points in time are defined. In the last step, results from XFEM simulations are presented for the identified critical time points.

Die approbierte gedruckte Originalversion dieser Dissertation ist an der TU Wien Bibliothek verfügbar.
The approved original version of this doctoral thesis is available in print at TU Wien Bibliothek.
TU Bibliothek Your knowledge hub WIEN

3.3.1 Moisture fields

The boundary conditions for the moisture fields are based on data available from [76] as described above. Although data exists for every 30 minutes, an interval of 6 h is selected for the boundary conditions to reduce computational effort with an acceptable loss of accuracy. Even longer intervals could lead to a loss of extreme values and were therefore avoided. The selected times are 3 a.m., 9 a.m., 3 p.m. and 9 p.m., since the lowest daily temperatures (with the correspondingly highest relative humidities) occur in the night before sunrise and the highest (with the lowest relative humidities) in the afternoon, so that the peaks of the daily fluctuations are covered. Two representative moisture distributions over time, obtained with the proposed simulation approach, are shown in Figure 3.5 for the ST 6x8 cross section and in Figure 3.6 for the GLT 20x40 cross section along a path from the boundary (B) to the center (C) of the cross section (depicted in Figure 3.3) for the entire simulation period. It can be seen that regions close to the boundary are affected by strongly varying MCs. The further the observed point moves towards the center (C), the smaller and more delayed the changes in MC become.

The simulation period begins on November 1, 2014, and high relative humidities occur in the following winter. As a result, the MC values increase in the area close to the boundary and, with a time lag, also in the center. The smaller cross section (see Figure 3.5) reacts quite quickly to the climate changes and reaches up to 18 % MC in the center in March, followed by a decreasing trend until September, while the 20x40 cross section (see Figure 3.6) reacts much more delayed in the center due to the larger width and does not reach more than 14 % MC until July. After that, the values fall slightly until October. Thus, it can be noticed that the width of the cross section influences the occurrence of the maximum differences between the boundary and the center in the course of the year. At the boundary there is less than 0.5 % difference in MC between these two cross sections.

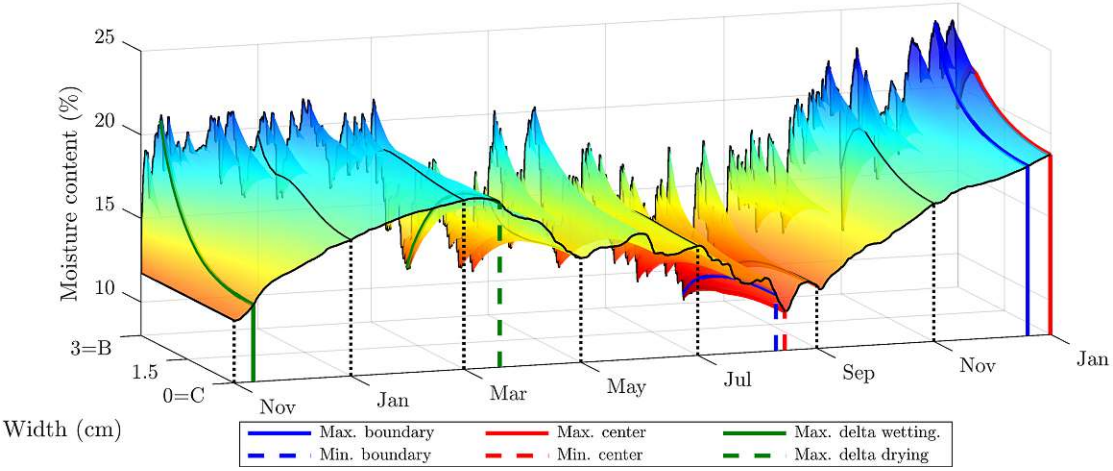

Figure 3.5: Time history of MC along the path from B (boundary) to C (center) from November 1, 2014, to January 1, 2016, for the ST 6x8 cross section. Also depicted are the points in time for maximum and minimum values at B and C, as well as for the maximum differences between B and C.

Die approbierte gedruckte Originalversion dieser Dissertation ist an der TU Wien Bibliothek verfügbar.
The approved original version of this doctoral thesis is available in print at TU Wien Bibliothek.
TU Bibliothek Your knowledge hub WIEN

For the ST 6x8 cross section the maximum value at the boundary (B) is reached on December 20, 2015, with 24 % and the minimum value on August 10, 2015, with 8.2 %, while in the center (C), the maximum MC is reached on December 31, 2015, with 18.8 % and the minimum on August 15, 2015, with 10.3 %. The largest differences can be determined on November 10, 2014, with a difference of 8.5 % for the wetting and on March 19, 2015, with a difference of 6.8 % for the drying period as shown in Figure 3.5.

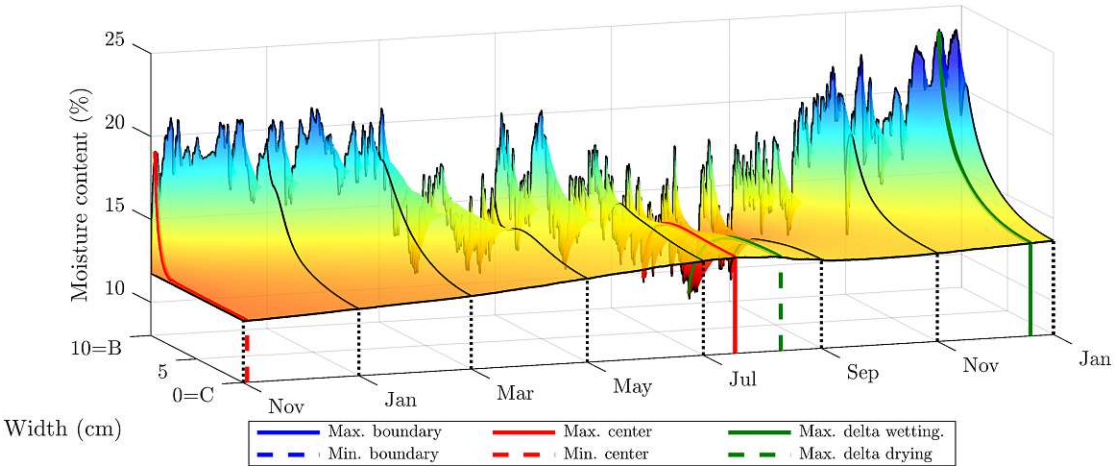

Figure 3.6: Time history of MC along the path from B (boundary) to C (center) from November 1, 2014, to January 1, 2016, for the GLT 20x40 cross section. Also depicted are the points in time for maximum and minimum values at B and C, as well as the maximum differences between B and C.

The GLT 20x40 cross section reaches the maximum value at the boundary (B) on December 20, 2015, with 23.6 % and the minimum value also on August 10, 2015, with 8.3 %, while in the center (C), the maximum MC is reached on July 17, 2015, with 13.8 % and the minimum on November 1, 2014, with 11.7 %. The largest differences can be determined on December 20, 2015, with a difference of 10.0 % for the wetting and on August 10, 2015, with a difference of 5.3 % for the drying period as shown in Figure 3.6.

3.3.2 Critical points in time

Figure 3.7 shows MC distributions over time at two points (one at the boundary and one at the center) of two cross sections (ST 6x8 and GLT 20x40). For the “critical points in time” (for the wetting and drying period for each cross section) additional figures show the increase of the crack-prone volume in detail. As previously mentioned, the points at the boundary react quite fast to changes of the relative humidity and the difference in MC at the boundary between the two samples is less than 0.5 %. The center point reacts, depending on the distance to the surface, slower.

While during the wetting period, when MCs at the surface are higher than at the center, cracks may occur near the center of the cross section, during the drying period, when the MCs at the boundaries are lower than at the center, cracks would be initiated at

Die approbierte gedruckte Originalversion dieser Dissertation ist an der TU Wien Bibliothek verfügbar.
The approved original version of this doctoral thesis is available in print at TU Wien Bibliothek.
TU Bibliothek Your knowledge hub WIEN

the boundaries. The crack-prone volume of ST 6x8 reaches its maximum on March 19, 2015, with 6.00 % of the cross section near the boundary as can be seen in Figure 3.8(a), whereas the crack-prone volume during the wetting period is non-existent and, thus, no cracks occur during this time span. The GLT 20x40 reaches the values on August 14, 2015, with 7.53 % near the boundary and December 30, 2015, with 0.54 % near the center, as also depicted in Figure 3.8(b). During the wetting period, this cross section shows a continuous curve of the crack-prone volume, which begins in December and reaching the critical points in time at the end of December as shown in Figure 3.7 for the "GLT-wetting" case, but with much smaller values (0.54 %) than during the drying period.

There is a clear correlation between the moisture differences and the crack-prone volume during the drying period. In case of the ST 6x8 the largest difference of MC occurs at the same time as the largest crack-prone volume exists. For the GLT 20x40 cross section, the crack-prone volume reaches a high level when the largest MC difference exists on August 10, 2015, but the critical point in time occurs a few days later on August 14, 2015 as can be seen in Figure 3.7.

For the drying period, the crack-prone volumes are located close to the boundaries of all edges of the cross sections since perpendicular-to-grain tension due to drying prevails in these areas (see Figure 3.8). The main cause for fulfilling the failure criterion is a combination of tangential normal stress σ_T with in-plane shear stress τ_{RT}. The crack-prone volume also depends on the pith location, e.g. for solid timber, especially at the edge opposite the pith, large volumes exist.

During the wetting period the boundary region experiences higher MCs than the center. This leads to compression in the boundary region and tension in the center zone. As a result, the crack-prone volumes are located in the center of the GLT 20x40 as can be seen in Figure 3.8. In the GLT 20x40 cross section, the crack-prone regions are located close to the pith of each lamella, except for the second lamella from the bottom, as tension σ_R exceeds the corresponding strength.

In the next section, crack patterns are investigated at the previously identified critical points in time, for both the wetting and drying period.

3.3.3 Crack patterns at critical points in time

Instead of only checking for violations of the failure criterion in linear-elastic simulations, the previously presented multisurface failure criterion (see Section 3.2.2.2) is now used to determine the initiation of cracks in an XFEM simulation. In the used FE software *Abaqus*, during such an XFEM simulation, only a single crack can appear per predefined so-called enrichment region. An exception is the violation of the failure criterion in multiple elements within the same time increment. In this case, multiple cracks can be initiated. Thus, the definition of these enrichment regions, i.e. the models subdivision, is crucial to obtain realistic simulation results. To ensure that the enrichment regions are chosen properly, the failure criterion was evaluated in all integration points during the analysis. In Figure 3.9, three different configurations of these enrichment regions are shown. With the "3x3" configuration, large crack-prone volumes (i.e. regions where the failure criterion is violated, but no cracks can be initiated due to the above-mentioned software implementation) still exist, while a finer subdivision reduces these

Die approbierte gedruckte Originalversion dieser Dissertation ist an der TU Wien Bibliothek verfügbar.
The approved original version of this doctoral thesis is available in print at TU Wien Bibliothek.
TU Bibliothek Your knowledge hub WIEN

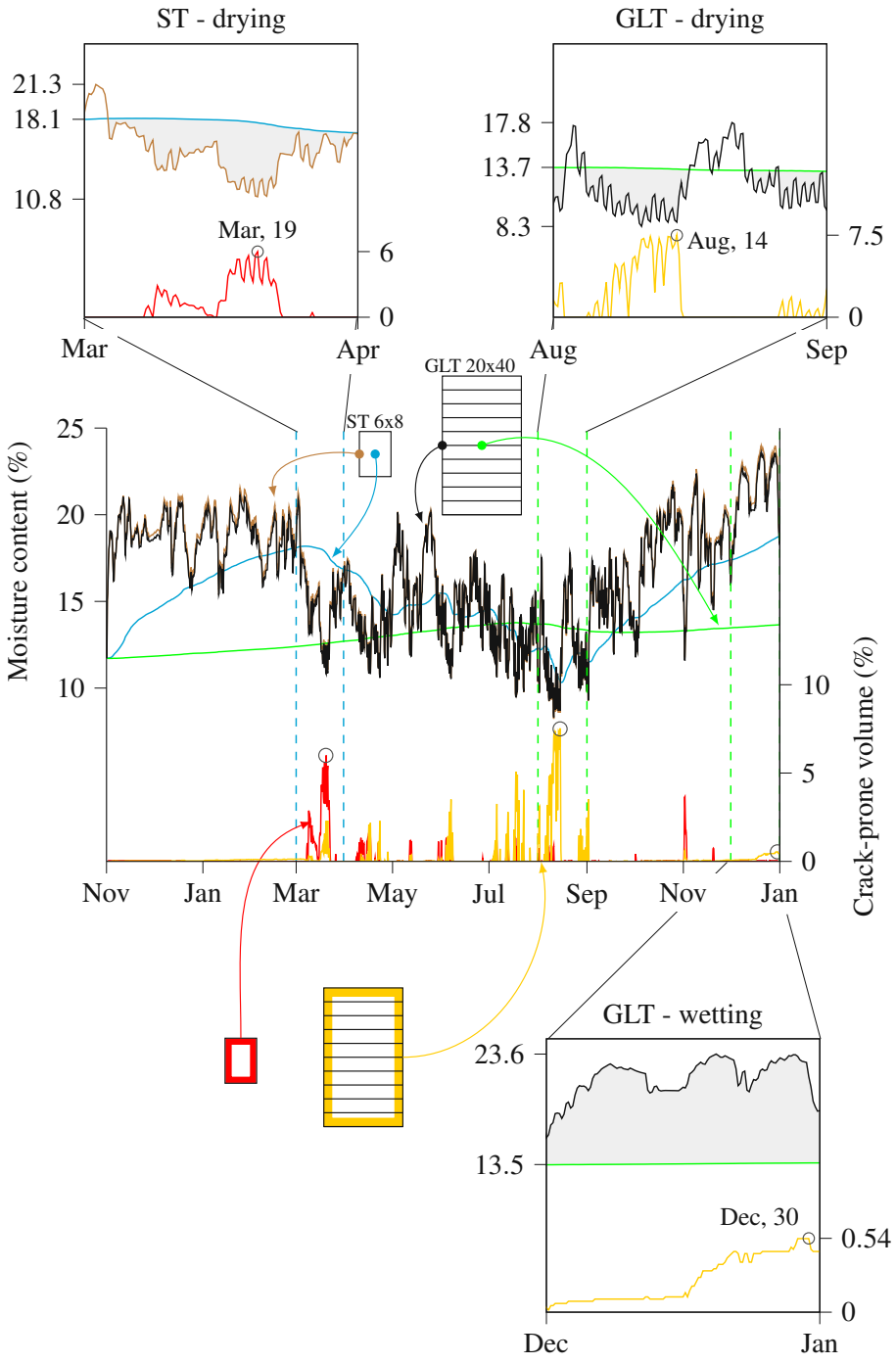

Figure 3.7: Course of moisture contents at boundary and center for ST 6x8 (shown in brown, blue) and GLT 20x40 (black, green), and ratio of the crack-prone volume by total volume plotted for the entire simulation time (red for ST, orange for GLT). For the drying period the critical point in time for ST 6x8 is on March 19, 2015, and for GLT 20x40 on August 14, 2015, and for the wetting period December 30, 2015, respectively (see detail plots). A critical point in time for the wetting period of the ST 6x8 does not exist i.e. no cracks are to be expected during this time span. The gray shading depicts the difference between the MC at boundary and center for the drying and wetting periods, leading to moisture-induced stresses and crack-prone volumes.

Die approbierte gedruckte Originalversion dieser Dissertation ist an der TU Wien Bibliothek verfügbar.
The approved original version of this doctoral thesis is available in print at TU Wien Bibliothek.
TU Bibliothek Your knowledge hub WIEN

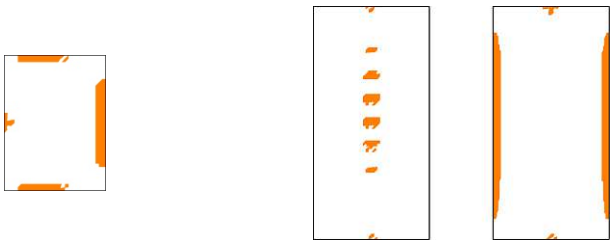

Mar 19, 2015 Dec 30, 2015 Aug 14, 2015

(a) ST 6x8 (b) GLT 20x40

Figure 3.8: Crack-prone volumes for ST 6x8 and GLT 20x40 cross sections at the critical points in time during wetting and drying periods. ST 6x8 shows crack-prone volumes only during the drying period.

volumes, as can be seen in the case of the "3x9" and "3x11 refined" (final configuration, used in Figure 3.11) configuration. However, for all configurations the average crack lengths as well as the basic crack pattern changes only slightly. For this reason, the influence of the configuration and number of enrichment regions on the overall result is manageable.

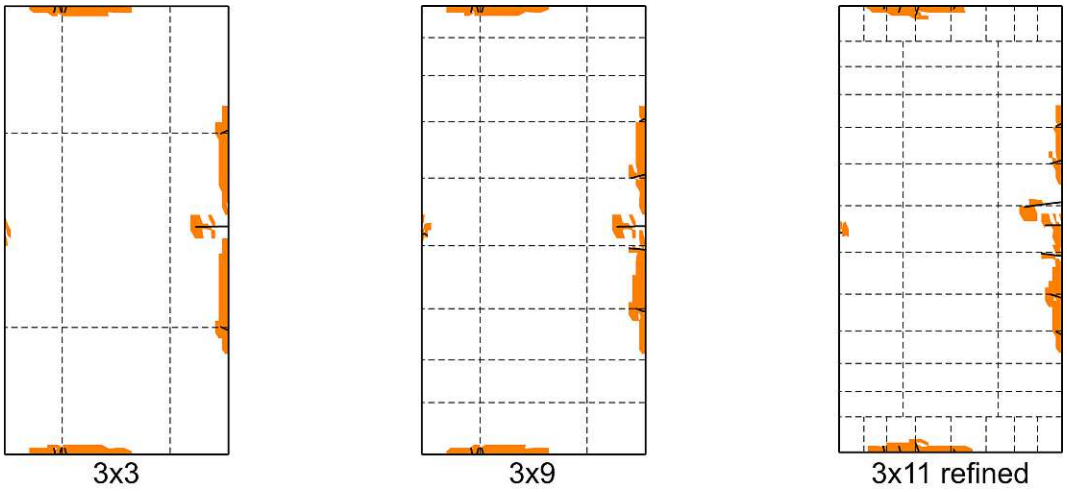

Figure 3.9: Different configurations of enrichment regions in case of the ST 14x28 cross section reduce the remaining crack-prone volumes (shown in orange)

The pith location is usually defined during the manufacturing process, where structural timber is sawn out of the tree trunk. Thus, in a next step, crack patterns for different pith locations, as shown on the left of Figure 3.10, were compared at the critical point in time for the drying period of the ST 6x8 cross section. Since the radial and tangential components of the transport tensors for bound water as well as water vapor are equal, a change in the position of the pith only affects the XFEM simulation. As can be seen in Figure 3.10, different crack patterns occur depending on the pith location. In general, the cracks are located close to the boundary, in the middle of the edges and are pointing towards the pith location. For example in (c), where the pith is set to the center, cracks are evenly distributed along the edges with an additional crack at the pith location. In

Die approbierte gedruckte Originalversion dieser Dissertation ist an der TU Wien Bibliothek verfügbar.
The approved original version of this doctoral thesis is available in print at TU Wien Bibliothek.
TU Bibliothek Your knowledge hub WIEN

(j), also a crack at the pith location emerges together with up to 4 mm long cracks at the bottom and right edge. When the pith is located at (e), there is no crack at the pith location but only at the bottom and right edge showing up. The remaining two pith locations at the boundary of the cross section (b) and (f) show small cracks at the pith location and cracks on the opposite edge. In case of (b), one crack opposite to the pith is 2 cm long. In (a) and (i), where the pith is outside the cross section but aligned with the center, cracks up to 4 mm in length can be observed at the edges tangential to the growth rings. Small cracks up to 4 mm are also showing up when the pith is located at (d), (g) or (h), where only cracks on the right edge (d) or bottom edge (g) emerge, whereas in case of (h) cracks on the bottom edge and one crack on the top edge can be observed.

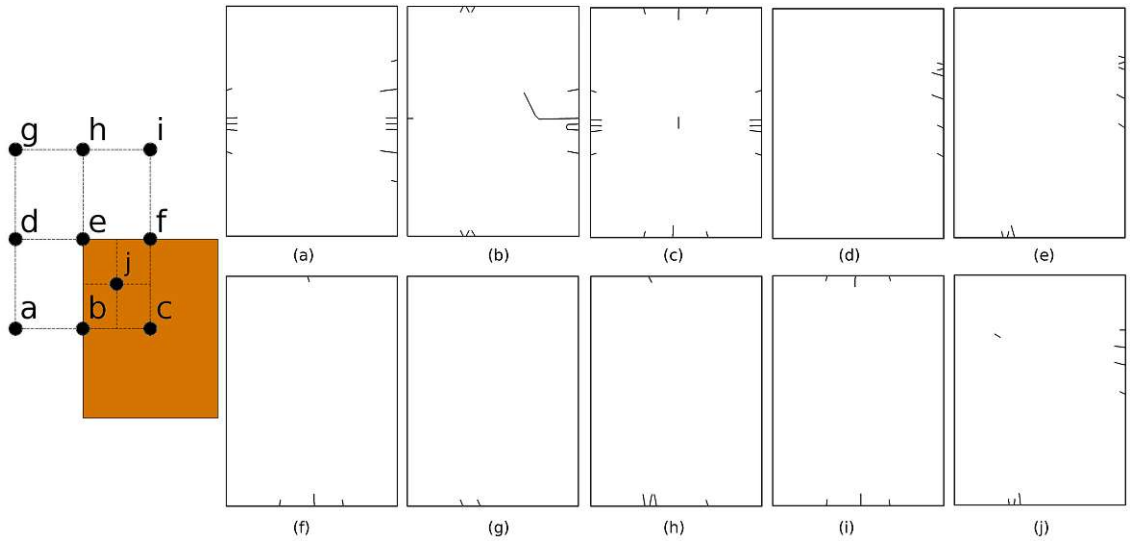

Figure 3.10: Investigated pith locations (a-j) of the ST 6x8 cross section and resulting crack patterns for the drying period.

Figure 3.11a depicts the crack patterns of all 18 investigated cross sections for the drying period. While for the 6 cm wide cross sections the critical points in time are during March, for the ones with 14 cm and more they occur during August, since the larger width leads to a slower reaction to moisture changes of the center. Cracks in the solid timber cross sections occur in the boundary areas. On the side where the pith is located, only one crack is initiated in some of the cross sections, starting from the pith location. GLT cross sections show a symmetrical crack pattern with one or two cracks per side of each lamella next to the glue line, which could lead to delamination. In contrast, in the top and bottom lamellas cracks were initiated next to the pith.

In Figure 3.11b the crack patterns for the wetting period are shown. The cracks occur inside the GLT cross sections and the pole due to the perpendicular-to-grain tension in these middle section, while compression takes place in the boundary zones. Compared to the cracks during the drying period, these are less in numbers. The cracks occur due to failure in tangential direction and are, thus, orientated towards the pith in case of the pole cross sections. GLT cross sections show cracks in the area of the glue line towards the pith, which could again lead to delamination. The ST and BO cross sections do not show cracks during this period, as can be concluded from Figure 3.7.

Die approbierte gedruckte Originalversion dieser Dissertation ist an der TU Wien Bibliothek verfügbar.
The approved original version of this doctoral thesis is available in print at TU Wien Bibliothek.
TU Bibliothek Your knowledge hub WIEN

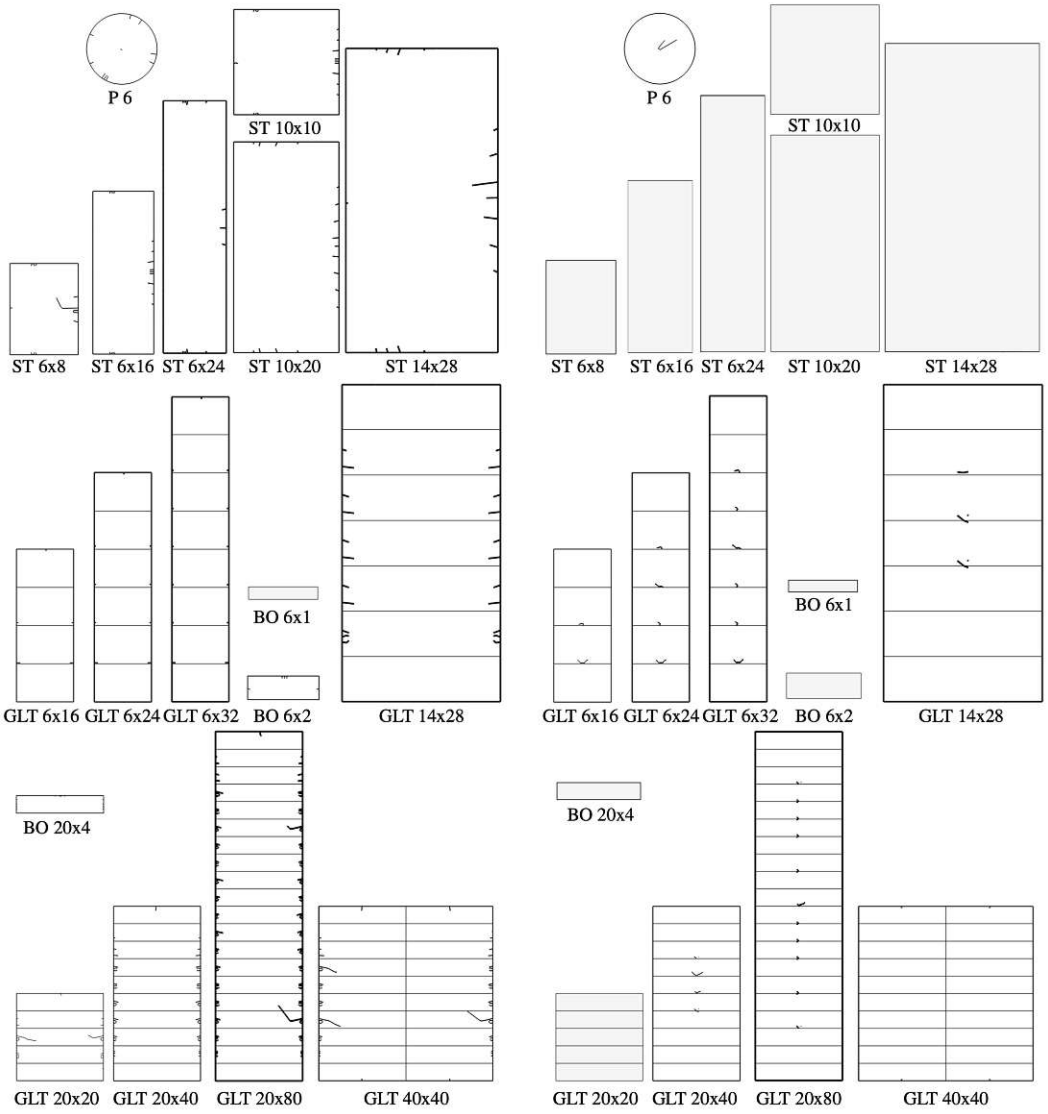

(a) Drying period (b) Wetting period

Figure 3.11: Crack patterns for the 18 investigated cross sections for the critical points in time for the (a) drying and (b) wetting period. Solid gray cross sections do not show cracks.

Die approbierte gedruckte Originalversion dieser Dissertation ist an der TU Wien Bibliothek verfügbar.
The approved original version of this doctoral thesis is available in print at TU Wien Bibliothek.

3.4 Discussion

The results show that at both critical points in time, which are during the drying and wetting period, respectively, cracks occur, with the former period being more critical. From Figure 3.7 it also can be seen that the MCs at the critical point in time for solid timber are 12.2 % at the boundary and 17.8 % at the center. For GLT they are 8.7 % at the boundary and 13.6 % in the center. Thus, the crack-prone volumes are in regions where the MC is close to 12 %, which was the reference MC for the failure criterion, i.e. it is safe to neglect a moisture-dependent decrease in tensile strength for this study. For the wetting period, the MC of the GLT is 21.6 % at the boundary and 13.7 % in the center. Since the cracks are initiated near the center of the cross section, the strength values are again close to the reference MC of 12 %. The solid timber (ST) and board (BO) cross sections do not crack during the wetting period. However, for the GLT cross sections and the pole cracks are predicted by the model, which are currently not considered by EC 5. Depending on the time of installation of the timber structure in the course of the year, either cracks due to drying at the boundary or cracks due to wetting inside the cross section occur first.

The crack-prone volume during the drying period is related to the difference between the MC at the boundary and the center and reacts to daily changes, as can be seen from Figure 3.7, where volumes are depicted in a time interval of 6 h. The critical point in time is chosen at the largest crack-prone volume, which corresponds to the largest differences in MC between the boundary and the center in case of the ST 6x8 cross section. The shown GLT cross section reaches its maximum volume at August 14, 2015, while the largest differences in MC are occurring on August 10, 2015, leading to a only slightly smaller crack-prone volume.

During the wetting period, the crack-prone volume reacts much slower to the MC differences, as shown in case of the GLT cross section in Figure 3.7, where the volume increases slowly during the whole month, with a steeper increase in the middle of December. Thus, critical points in time occur after longer periods with constant high moisture differences as the MC needs time to penetrate into the cross section and form critical MC distributions which do not correspond to the largest differences in MC between the boundary and the center. The crack-prone volume is also much smaller (0.54 %) than during the drying period (up to 7.5 %), hence resulting cracks are also shorter, as can be seen from Figure 3.11. Since the crack-prone volume during the wetting period is slowly changing in comparison to the drying period, the underlying moisture-induced stress levels are also present over a longer time span meaning effects like mechanosorption and viscoelastic creep could actually reduce these stresses and the cracks during this time. Thus, the results can be considered as an upper limit of moisture-induced cracks under the given climatic conditions. An estimation of the crack-prone volume based on the MC distribution does not seem to be easily possible, as the crack-prone volume includes also information on the elasticity tensor, expansion coefficients and pith location.

In [74] moisture gradients and distributions were defined based on values in a depth of 15 mm from the surface to omit single events which do effect the moisture contents only little. In this work the time interval was chosen with 6 h, which also leads to a smoothing of the boundary conditions. Further simulations showed that if the relative

Die approbierte gedruckte Originalversion dieser Dissertation ist an der TU Wien Bibliothek verfügbar.
The approved original version of this doctoral thesis is available in print at TU Wien Bibliothek.
TU Bibliothek Your knowledge hub WIEN

humidity of the boundary condition is changed from 40 % to 7 %, it takes about 6 h to affect the MC at a depth of 12-14 mm. A change of the relative humidity of such a magnitude (about 30 %) occurs at the critical point in time for the ST (which is also the point in time of the maximum MC difference between the boundary and the center) as well as at the critical point in time of the GLT cross section during the drying period.

In general, for the chosen real climate as boundary condition, higher compressive stresses were observed during the wetting period in case of the ST cross sections, which are located at the boundary. As can be seen from Figure 3.7, no crack-prone volumes occur during the wetting period for the ST cross sections. For the GLT cross sections, compressive and tensile stresses are of the same magnitude during the simulated time span. This difference, which is caused by the different pith locations, seems to be the reason, why only GLT cross sections show cracks during the wetting period as they show much higher and larger zones of radial stresses next to the pith location. These stresses are also building up over longer time spans, as can also be seen from the resulting crack-prone volume in Figure 3.7, meaning they could be lower if mechanosorption, viscoelastic creep and plastifications are included, as already mentioned.

During the drying period, the difference of the stress levels between both types of cross sections is not significant, thus, for both cracks occur during this period and are of the same magnitude. Higher tensile stresses in tangential direction were observed during the drying period, which is in agreement with [67].

While the EC 5 service classes reduce the strength parameters via the factor k_{mod} and stiffness properties via k_{def}, the factor k_{cr} defines the crack-free width of the cross section, which is crucial in case of shear loads. According to EC 5 this factor is equal to 0.67. In the national annex for Austria the width of the cross section is not reduced, but instead the maximum shear strength is lowered. This corresponds to a k_{cr} of 0.575 for solid timber and 0.625 for GLT for strength class C24.

The crack-free widths of the cross sections are plotted versus the total widths for the critical points in time for both the drying (see Figure 3.12) and the wetting period (see Figure 3.13). In these Figures the crack free widths beside individual large cracks are depicted. It can be seen that the relationship between crack-free and total width is quite linear for both periods. A linear regression results in a value of $k_{cr,Sim} = 0.923$ with a coefficient of determination of 0.999 for the drying period. A linear relationship between the width of the cross section and the crack length is also used in EC 5, but with a lower k_{cr} value. Thus, it must be concluded that, at least for the investigated location (Linz, Austria), the code values are on the conservative side. However, if we include individual large cracks, the value of $k_{cr,Sim}$ is reduced to 0.756 with a determination coefficient of 0.984.

For the wetting case, also a linear regression was made. The value of $k_{cr,Sim}$ results in 0.963 with a coefficient of determination of 0.996. Only GLT cross sections and the pole showed cracks. Although, again the EC 5 assumption is on the conservative side and our simulated and fitted k_{cr} tends towards 1.0, i.e. almost completely crack-free cross sections, some of the cross sections (e.g. $k_{cr,Sim}$ for P 6 is 0.683) are still critically cracked for the investigated climate conditions. If we only include the cracked cross sections in the linear regression, $k_{cr,Sim}$ results in a value of 0.880 with a coefficient of determination of 0.998.

Die approbierte gedruckte Originalversion dieser Dissertation ist an der TU Wien Bibliothek verfügbar.
The approved original version of this doctoral thesis is available in print at TU Wien Bibliothek.
TU Bibliothek Your knowledge hub WIEN

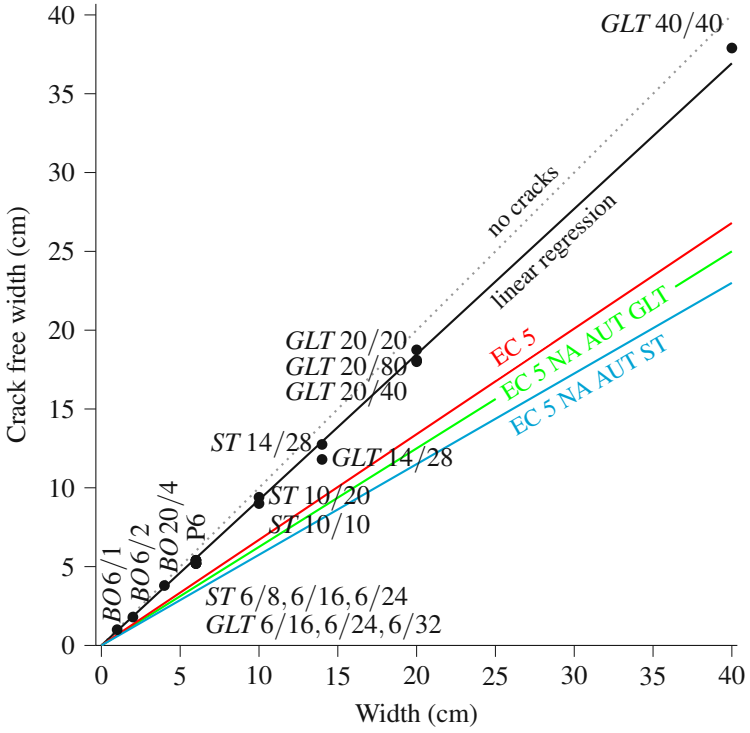

Figure 3.12: Comparison of numerically obtained crack-free/total width ratios for the drying period (cracks in the boundary area) to the linear relationships of EC 5 and the national annex of Austria (NA AUT) for strength class C24.

During the simulations of the drying period also cracks at the top and bottom boundaries appeared. These do not affect the mechanisms for shear, but could influence the cross section's resistance to torsion. The resulting crack-free height from the linear regression is 98.1 % of the total height with a coefficient of determination of 0.999.

Die approbierte gedruckte Originalversion dieser Dissertation ist an der TU Wien Bibliothek verfügbar.
The approved original version of this doctoral thesis is available in print at TU Wien Bibliothek.
TU Bibliothek Your knowledge hub WIEN

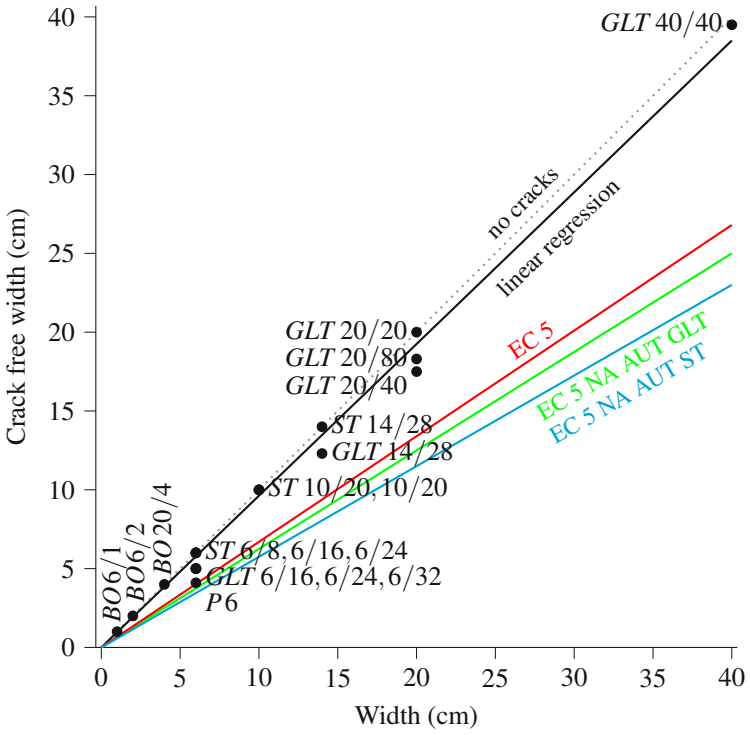

Figure 3.13: Comparison of numerically obtained crack-free/total width ratios for the wetting period (cracks close to cross section centers) to the linear relationships of EC 5 and the national annex of Austria (NA AUT) for strength class C24. Only GLT cross sections and the pole showed cracks during this period.

3.5 Conclusion & Outlook

In this work, 18 typical wooden cross sections were numerically investigated by subjecting them to a real historic climate in Linz, Austria, and studying the resulting crack patterns. It was assumed that the cross sections were prevented from getting into contact with liquid water, from e.g. rain. The results were then compared to the Eurocode 5 parameter k_{cr}, which considers cracks in case of shear loads and reduces the cross sectional widths.

To determine the crack patterns, first the moisture and temperature fields were computed, by applying a multi-Fickian model with consideration of a sorption hysteresis. In a second step, these fields were used in a linear-elastic stress simulation to identify critical points in time by evaluating a previously developed multisurface failure criterion [32] and using moisture-dependent stiffness values by means of a multiscale material model [82]. In the third step, an XFEM simulation was performed with the moisture fields as load at the identified critical points in time. The main findings can be summarized as follows:

- The linear elastic stress simulations have shown that stresses, which could lead to cracks, occur during the investigated 14 months. The XFEM simulations at the critical points in time show cracks starting at the edges for the drying period and inside the cross section for the wetting period. The linear relationship between

Die approbierte gedruckte Originalversion dieser Dissertation ist an der TU Wien Bibliothek verfügbar.
The approved original version of this doctoral thesis is available in print at TU Wien Bibliothek.
TU Bibliothek Your knowledge hub WIEN

crack-free width and total width of the cross section, as suggested in EC 5, is verified with the results. For the drying case, the crack-free width is about 92.3 % of the total width for the investigated time span.

- While EC 5 considers only cracks in the boundary area, results of crack patterns of the wetting period showed that for some cross section types cracks inside the cross sections could arise with a linear relationship between crack-free width and total width of the cross section of 96.3 %. However, the simulations did not consider mechanosorptive effects and viscoelastic creep as well as plastifications. Thus, the stresses, especially during wetting at higher MCs, are assumed to be overestimated as well as the resulting real crack lengths. In the next step, such a material model should be implemented. Furthermore, GLT and pole cross sections are more prone to cracking in the wetting period, leading to a $k_{cr,sim}$ of 0.880 when only considering these cross section types.

- For the GLT cross sections, cracks occur next to the glue lines, which could lead to delamination effects.

- The influence of different pith locations during the drying state was also investigated. No major dependency could be identified. In almost all cases, the cracks were initiated at the boundary.

- The used failure criterion is not moisture-dependent, but the MCs in the elements where cracks initially occur were close to the reference MC of 12 %. Thus, the influence of a moisture-dependent, brittle failure criterion is assumed to be negligible.

When designing a structure according to EC 5, the ultimate and serviceability limit states must be fulfilled. Changing climatic conditions and, thus, resulting moisture-induced stresses are not taken into account in the current version of this standard, instead they are treated as material properties [68]. In comparison to other loads like wind and snow, no similar site-specific data are given. Therefore, simulations such as those performed in this paper could be a starting point to determine the location-specific moisture-induced eigenstresses and crack patterns resulting from MC changes for different cross sections, which could lead to a better understanding of the associated uncertainties and, thus, a better and more efficient design of timber structures. In further simulation efforts, the presence of realistically modeled knots [29, 30, 87] should also be taken into account, as these definitely influence the initiation of cracks and subsequent crack patterns.

Conflict of interest

None declared.

Die approbierte gedruckte Originalversion dieser Dissertation ist an der TU Wien Bibliothek verfügbar.
The approved original version of this doctoral thesis is available in print at TU Wien Bibliothek.
TU Bibliothek Your knowledge hub WIEN

Acknowledgements

The funding from the Doka GmbH and the Austrian Research Promotion Agency (FFG, Project Number 857041) is gratefully acknowledged.

Appendices

3.A Constitutive equations and material parameters for heat and moisture transport

Table 3.A.1: Constitutive equations and material parameters used in the model.

Property	Value/Expression	Ref.
Dry density	$\rho_d = 420\,\mathrm{kg\,m^{-3}}$	
Moisture content	$X = \frac{c_b}{\rho_d}$	
Bound water diffusion tensor	$\boldsymbol{D_b} = \boldsymbol{D_0}\,\exp\left(\frac{-E_b}{RT}\right)$	[47]
Bound water diffusion tensor (Soret Effect)	$\boldsymbol{D_{bT}} = \boldsymbol{D_0}\,\frac{c_b\,E_b}{RT^2}\,\exp\left(\frac{-E_b}{RT}\right)$	[47]
Activation energy of bound water	$E_b = 38500 - 29000\,X$	[35]
Universal gas constant	$R = 8.314\,\mathrm{J\,mol^{-1}\,K^{-1}}$	
Water vapor diffusion tensor	$\boldsymbol{D_v} = \boldsymbol{\xi}\left(2.31\cdot 10^{-5}\,\frac{p_{atm}}{p_{atm}+p_{v_{air}}}\,\left(\frac{T}{273}\right)^{1.81}\right)$	[9, 10, 48]
Water vapor pressure	$p_{v_{air}} = c_v\,\frac{RT}{M_{H_2O}}$	
Molar mass of water	$M_{H_2O} = 18.015\,\mathrm{g\,mol^{-1}}$	
Moist density of wood	$\rho_{moist} = \rho_d\,\frac{1+X}{1+0.84\,c_b}$	[53]
Volume proportion of the lumen	$f_{lum} = 1 - \frac{\rho_{moist}}{\rho_{cwm}}$	
Density (pure cell wall)	$\rho_{cwm} = 1530\,\mathrm{kg\,m^{-3}}$	[11, 35]
Conduction tensor	$\boldsymbol{K} = \boldsymbol{K_0}\,(0.142 + 0.46\,X)$	[15]
Heat capacity (pure cell wall)	$c_{p_s} = -0.60453 + 0.006714\,T$	[54]
Enthalpy of water vapor	$h_v = 2060.5 + 1.3798\,T + 0.84808\cdot 10^{-4}\,T^2$	[49]
Specific enthalpy of bound water	$h_b = 4.185\,(T - 273.15\,\mathrm{K}) - 1146.4\,\exp\left(-14.48\,X\right)$	[49, 55]
Average enthalpy of bound water	$\overline{h}_b = -1143.1 + 4.185\,T - \frac{79.172\,\rho_d\,(1-\exp(-14.48\,X))}{c_b}$	[23, 24, 49]

The reference state for the expressions to determine the thermodynamic properties for specific isobaric heat capacities c_p and enthalpies h is set to 273.15 K and 101,325 Pa.

Table 3.A.2: Diagonal components of the material parameter tensors

Parameter	Component L	Component R	Component T	Ref.
$\boldsymbol{D_0}$	$2.5\cdot 7\cdot 10^{-6}$	$7\cdot 10^{-6}$	$7\cdot 10^{-6}$	[12]
$\boldsymbol{\xi}$	0.9	0.11	0.11	[62]
$\boldsymbol{K_0}$	2	1	1	[63]

Die approbierte gedruckte Originalversion dieser Dissertation ist an der TU Wien Bibliothek verfügbar.
The approved original version of this doctoral thesis is available in print at TU Wien Bibliothek.
TU Bibliothek Your knowledge hub WIEN

3.B Interaction between bound water and water vapor

The model of [9, 12, 56] is used for the determination of the sorption rate. A certain relative humidity φ is connected to an EMC denoted by $X_{\alpha,eq}$ with a sorption isotherm. Here the definition by [57] for the isotherms is used to determine the boundary curves, which define the zone of possible EMCs in case of a sorption hysteresis and is given as

$$X_{\alpha,eq} = \frac{\varphi}{f_{1,\alpha} + f_{2,\alpha}\,\varphi + f_{3,\alpha}\,\varphi^2}. \tag{3.B.1}$$

The shape factors were determined from experimental results in [56] with $f_{1,a} = 1.804$, $f_{2,a} = 13.63$, $f_{3,a} = -12.12$ for adsorption ($\alpha = a$) and $f_{1,d} = 1,886$, $f_{2,d} = 7.884$, $f_{3,d} = -6.526$ for desorption ($\alpha = d$). The relationship between c_v and φ is $c_v = \varphi\, c_{v_{sat}}$.

For the definition of the hysteresis dependent equilibrium bound water concentration at the end of the increment $c_{b,eq}$, first, the initial state s_0 at the beginning of the time increment between the two boundary curves is defined as $s_0 = (X_0 - X_{0,a,eq})/(X_{0,d,eq} - X_{0,a,eq})$. In addition to s_0, also the parameters $\varphi_{0,a}$ and $\varphi_{0,d}$, which define the origins of the scanning curves on the adsorption and desorption boundary curve, respectively, have to be determined as

$$\begin{aligned}
\varphi_{0,a} =& \varphi_0 \cdot (d_2 \cdot \varphi_0)^{q_1} \text{ and} \\
\varphi_{0,d} =& 1 - (1 - \varphi_0) \cdot (d_2 \cdot (1 - \varphi_0))^{q_2} \text{ with} \\
q_1 =& -\frac{\ln(\ln(2)) - \ln(\ln(2 - s_0))}{\ln(\ln(2)) - \ln(\ln(2 - s_0)) - d_1} \text{ and} \\
q_2 =& -\frac{\ln(\ln(2)) - \ln(\ln(1 + s_0))}{\ln(\ln(2)) - \ln(\ln(1 + s_0)) - d_1},
\end{aligned} \tag{3.B.2}$$

where d_1 and d_2 are constants with -1.3 and 0.88, respectively, as obtained in [56]. The current value of s can then be calculated based on the current relative humidity φ as

$$s = \begin{cases}
-1 + 2^{\left(\frac{1-\varphi}{1-\varphi_{0,d}}\right)^{\left(\frac{d_1}{\ln\left[d_2\left(1-\varphi_{0,d}\right)\right]}\right)}} & \text{if } \varphi > \varphi_0 \;\&\; s > 0, \\
0 & \text{if } \varphi > \varphi_0 \;\&\; s = 0, \\
2 - 2^{\left(\frac{\varphi}{\varphi_{0,a}}\right)^{\left(\frac{d_1}{\ln[d_2 \cdot \varphi_{0,a}]}\right)}} & \text{if } \varphi < \varphi_0 \;\&\; s < 1, \\
1 & \text{if } \varphi < \varphi_0 \;\&\; s = 1.
\end{cases} \tag{3.B.3}$$

After the determination of s, the equilibrium bound water concentration at the end of the increment can be estimated as $c_{b,eq} = (X_{d,eq} \cdot s + X_{a,eq} \cdot (1 - s)) \cdot \rho_0$. The sorption rate, which is the amount of water per time that changes phase, is then calculated with the moisture-dependent reaction function H_{bv} and reads as $\dot{c}_{bv} = H_{bv}\,(c_{b,eq} - c_b)$. Depending on whether there is adsorption or desorption the parameter H_{bv} can be cal-

Die approbierte gedruckte Originalversion dieser Dissertation ist an der TU Wien Bibliothek verfügbar.
The approved original version of this doctoral thesis is available in print at TU Wien Bibliothek.
TU Bibliothek Your knowledge hub WIEN

culated as:

$$H_{bv} = \begin{cases} \text{if } c_b < c_{b,eq} \text{ adsorption:} \\ C_{bv,1} \exp\left(-C_{bv,2}\left(\frac{c_b}{c_{b,eq}}\right)^{C_{bv,3}}\right) + C_{bv,4} \\ \text{if } c_b > c_{b,eq} \text{ desorption:} \\ C_{bv,1} \exp\left(-C_{bv,2}\left(2 - \frac{c_b}{c_{b,eq}}\right)^{C_{bv,3}}\right) + C_{bv,4}. \end{cases} \tag{3.B.4}$$

Values for $C_{bv,1}$, $C_{bv,3}$ and $C_{bv,4}$ are constant and taken from [62] as $C_{bv,1} = 3.8 \cdot 10^{-4}\,\mathrm{s}^{-1}, C_{bv,3} = 80, C_{bv,4} = 5.94 \cdot 10^{-7}\,\mathrm{s}^{-1}$, whereas $C_{bv,2}$ depends on relative humidity and is given as $C_{bv,2} = c_{21}\exp(c_{22}\,\varphi) + c_{23}\exp(c_{24}\,\varphi)$, with $c_{21} = 3.58, c_{22} = 2.21, c_{23} = 1.59 \cdot 10^{-3}$ and $c_{24} = 14.98$, also from [62].

3.C Elasticity tensor for spruce

Table 3.C.1: $\boldsymbol{C}$ entries in MPa for spruce (ρ_d = 420 kg m^{-3}) at 293.15 K.

MC (%)	C_{LLLL}	C_{RRRR}	C_{TTTT}	C_{LLRR}	C_{RRTT}	C_{TTLL}	C_{LRLR}	C_{LTLT}	C_{RTRT}
3	13981.39	1127.15	755.30	343.76	272.01	520.26	396.68	389.40	53.70
4	13824.31	1094.04	733.20	337.33	266.94	504.70	385.64	378.57	52.23
5	13669.80	1061.40	711.42	330.88	261.87	489.33	374.67	367.80	50.79
6	13517.80	1029.22	689.96	324.41	256.78	474.16	363.78	357.11	49.37
7	13368.23	997.51	668.82	317.92	251.67	459.21	352.97	346.49	47.97
8	13221.06	966.26	647.98	311.40	246.55	444.47	342.25	335.97	46.60
9	13076.22	935.48	627.46	304.86	241.40	429.95	331.63	325.55	45.24
10	12933.66	905.17	607.25	298.29	236.23	415.66	321.12	315.23	43.91
11	12793.34	875.33	587.34	291.68	231.03	401.60	310.72	305.02	42.59
12	12655.21	845.95	567.74	285.04	225.80	387.77	300.45	294.94	41.29
13	12519.23	817.05	548.45	278.37	220.55	374.19	290.31	284.99	40.00
14	12385.35	788.61	529.47	271.66	215.27	360.84	280.32	275.18	38.73
15	12253.54	760.65	510.79	264.92	209.95	347.74	270.47	265.51	37.47
16	12123.75	733.16	492.42	258.14	204.61	334.88	260.78	256.00	36.23
17	11995.96	706.15	474.35	251.33	199.24	322.26	251.25	246.64	35.01
18	11870.13	679.60	456.59	244.48	193.84	309.90	241.89	237.46	33.79
19	11746.22	653.53	439.14	237.61	188.41	297.77	232.71	228.44	32.60
20	11624.20	627.93	421.99	230.71	182.96	285.89	223.70	219.60	31.41
21	11504.05	602.80	405.15	223.78	177.49	274.26	214.88	210.94	30.24
22	11385.74	578.14	388.62	216.82	171.99	262.86	206.25	202.47	29.08
23	11269.23	553.95	372.39	209.85	166.48	251.71	197.81	194.18	27.94
24	11154.50	530.22	356.46	202.86	160.95	240.79	189.56	186.09	26.81
25	11041.52	506.95	340.83	195.86	155.41	230.11	181.51	178.18	25.70
26	10930.28	484.14	325.51	188.86	149.86	219.66	173.66	170.47	24.60
27	10820.74	461.80	310.49	181.85	144.30	209.44	166.00	162.96	23.52
28	10712.87	439.90	295.77	174.84	138.75	199.44	158.55	155.64	22.45
29	10606.66	418.46	281.35	167.84	133.20	189.67	151.29	148.52	21.40
30	10502.09	397.46	267.22	160.84	127.65	180.11	144.23	141.59	20.36

Die approbierte gedruckte Originalversion dieser Dissertation ist an der TU Wien Bibliothek verfügbar.
The approved original version of this doctoral thesis is available in print at TU Wien Bibliothek.
TU Bibliothek Your knowledge hub WIEN

Die approbierte gedruckte Originalversion dieser Dissertation ist an der TU Wien Bibliothek verfügbar.
The approved original version of this doctoral thesis is available in print at TU Wien Bibliothek.

Publication 4

Finite-element-based concept to predict stiffness, strength, and failure of wood composite I-joist beams under various loads and climatic conditions [6]

Authored by Maximilian Autengruber, Markus Lukacevic, Gregor Wenighofer, Raimund Mauritz and Josef Füssl

Submitted to *Engineering Structures (currently under review)*

Abstract: Formwork support constructions are an indispensable part of almost all reinforced concrete structures. The main supporting system usually consists of wood-based composites, where solid timber, plywood and, more recently, aluminum profiles are combined to form I-beams. These beams have to go through a very complex test program, to ensure that they withstand all mechanical and moisture-related stresses during their service life. To better understand the mechanisms leading to mechanical failure as well as to support a targeted optimization of new cross section types, we developed a finite-element-based simulation concept. Moisture-related effects occurring during the service life are considered with an advanced moisture transport model and a multisurface failure criterion is implemented for modeling the plastic and brittle failure mechanisms in wood, resulting in a very good prediction of stiffness values, load capacities and failure behavior of the experimentally investigated beams. The performance of the modeling approach is shown by simulation of three different experiments, representing different mechanical loading situations at three different moisture levels.

Die approbierte gedruckte Originalversion dieser Dissertation ist an der TU Wien Bibliothek verfügbar.
The approved original version of this doctoral thesis is available in print at TU Wien Bibliothek.
TU Bibliothek Your knowledge hub WIEN

4.1 Introduction

The development of new wood products is a challenging task due to the natural grown structure of wood and its moisture-dependent material properties. Thus, a new wood product has to be tested in different climatic conditions, which may occur during its service life. About 46 % of damage cases of large span timber constructions can be related to moisture events according to [1]. For wooden beams used in concrete scaffold constructions, environmental conditions during loading as well as storing have to be considered. Since these beams are re-used on different construction sites, they are also exposed to different climate conditions. In this work, two different types of beams are studied, a new development called *I tec pro* and a conventional formwork beam called *H20 top P*. In this work, the beams that have so far only been investigated experimentally, are analyzed numerically by simulating bending, shear and bearing resistance tests according to the standard EN 13377 [88], under dry conditions as well as after three (only in case of the *I tec pro*) and 60 days of exposure to wet conditions (defined as 100 % relative humidity at 293.15 K). The cross sections of these two wood composite beams with an I-joist shape are made of different materials. The flange consists of spruce solid timber, the web of a special high density particle board and the *I tec pro* incorporates an aluminum profile in the region of the flange. A unified set of material parameters (at each moisture level) is used for both beams in all three tests for the numerical analysis.

To determine the moisture state after three and 60 days of exposing the beam to wet conditions, a multi-Fickian transport model as presented in [3, 11, 12, 14, 68, 69] was used. This model is able to appropriately describe high moisture content (MC) gradients that occur in samples with a thickness of more than a few millimeters and relative humidities of more than 65 % according to [8]. Moisture transport in the particle board is assumed to take place in a similar way to softwood, as the particles work as cell walls and the lumen are partially filled with adhesive, reducing the water vapor diffusivity. Diffusion coefficients of particle boards were investigated in [89, 90] and are used to determine the bound water and water vapor diffusion coefficients for the multi-Fickian model. In contrast to solid wood, the directional behavior of the particle board is different, as the two characteristic directions are in-plane and out-of-plane. Since the particles are made of spruce, the same sorption mechanism is assumed to take place. With these assumptions, the multi-Fickian transport model could be used for the whole cross section.

In a subsequent mechanical analysis step, first the determined moisture fields are applied as loading and then external loads via the realistically modeled load transmission construction. This sequence is similar to that in the experiments, where the beams are also conditioned prior to the resistance tests. The failure behavior of spruce is defined by a multisurface criterion based on [31–34, 85], which was also used in [5] to determine crack patterns in wooden cross sections under changing climate loading, leading to brittle or plastic failure modes. Von Mises plasticity is assumed for the particle board as well as for the aluminum profile, with material parameters calibrated by modeling a tensile test of an aluminum sample.

The main objective of this work is to present an advanced simulation concept for predicting the stiffness and strength of wood composite I-joist beams at different moisture states, and the same time the validation of this tool on the basis of several experiments.

Die approbierte gedruckte Originalversion dieser Dissertation ist an der TU Wien Bibliothek verfügbar.
The approved original version of this doctoral thesis is available in print at TU Wien Bibliothek.
TU Bibliothek Your knowledge hub WIEN

For this purpose, after the definition of the material properties and the description of the test setups, the resulting moisture fields after the exposure to wet conditions are presented. Since the same numerical model (including material definitions and properties) should be used for all the experiments of a certain moisture level and the full set of material parameters is not available from experiments (e.g. friction coefficients, elasticity tensors of the particle board and load transmission construction) a sensitivity analysis is used to determine the missing elastic material parameters for the mechanical finite element simulation. The results of these simulations are then presented for each of the three investigated setups for the two beams under different moisture conditions and compared to experimental results.

4.2 Materials and Methods

To determine the maximum load capacity of the beams by means of numerical simulations under different moisture conditions, the necessary material parameters and numerical methods are presented in this section. Moisture leads to dimensional changes of the wooden parts and also variations in the material properties. Therefore, a hygrothermal multi-Fickian transport model is evaluated first and the resulting moisture and temperature fields are then applied in a second mechanical analysis, where also the external loads according to EN 13377 are applied, to determine the load-displacement behavior and the maximum load capacity.

4.2.1 Cross sections

In this work two different types of beams of the P20 class according to EN 13377 with a total height of 20 cm, a flange width of 8 cm and flange height of 4 cm are presented. The *H20 top P* cross section in Figure 4.1a consists of two flanges made of spruce solid timber and a web made of a 22 mm thick particle board. The newly developed *I tec pro* beam in Figure 4.1b has two additional aluminum profiles placed in the flanges to increase the strength while the remaining geometry is similar to the *H20 top P*.

4.2.2 Moisture transport simulations

For conditions below the fiber saturation point (FSP), moisture transport in wood can be modeled with the multi-Fickian theory as described in [3, 8, 9, 11, 12, 14], where two diffusion processes, one for water vapor in the lumen of the cell and one for bound water in the cell wall, act in parallel and are coupled via the sorption rate. An energy conservation equation completes the system of equations, considering the enthalpy changes due to the transport processes and also the thermal conduction process. The model is based on the theory of drying in porous media from [44], where volume averaging of the parameters was used. While the bound water concentration degree of freedom (c_b) and the sorption rate ($\dot{c}_{bv}$) are defined over the whole representative volume element (RVE), the water vapor concentration degree of freedom (c_v) refers only to the lumen part of the volume, which is defined with the volume proportion f_{lum}. The third degree of freedom is the temperature T, also defined over the whole RVE. The moisture content (MC) is defined as the bound water concentration by the dry density of wood (c_b/ρ_d).

Die approbierte gedruckte Originalversion dieser Dissertation ist an der TU Wien Bibliothek verfügbar.
The approved original version of this doctoral thesis is available in print at TU Wien Bibliothek.
TU Bibliothek Your knowledge hub WIEN

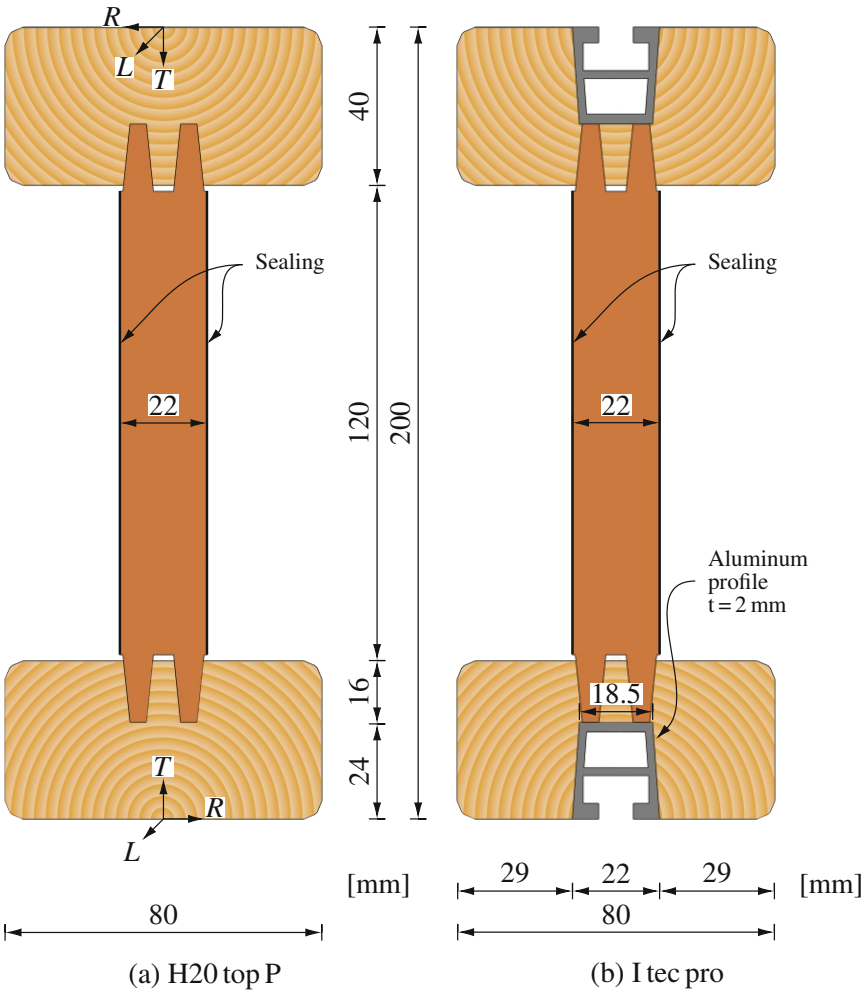

(a) H20 top P (b) I tec pro

Figure 4.1: Investigated cross sections of P20 class. The flanges with a cross section of 4x8 cm are made of solid timber with the pith located in the middle of the top and bottom edge, respectively, and the web is made of a 22 mm thick particle board, which is sealed. In case of the *I tec pro* an aluminum profile is placed in the flanges as can be seen in (b).

In the present paper, the model of [3, 5] was used, without the free water conservation equation since no free water is present, resulting in the following set of governing equations:

Conservation of bound water concentration:

$$\frac{\partial c_b}{\partial t} = \frac{\partial}{\partial \boldsymbol{x}} \cdot \boldsymbol{D_b} \cdot \frac{\partial c_b}{\partial \boldsymbol{x}} + \frac{\partial}{\partial \boldsymbol{x}} \cdot \boldsymbol{D_{bT}} \cdot \frac{\partial T}{\partial \boldsymbol{x}} + \dot{c}_{bv} \tag{4.1}$$

Conservation of water vapor concentration:

$$\frac{\partial c_v\, f_{lum}}{\partial t} = \frac{\partial}{\partial \boldsymbol{x}} \cdot \boldsymbol{D_v} \cdot \frac{\partial c_v}{\partial \boldsymbol{x}}\, f_{lum} - \dot{c}_{bv} \tag{4.2}$$

Die approbierte gedruckte Originalversion dieser Dissertation ist an der TU Wien Bibliothek verfügbar.
The approved original version of this doctoral thesis is available in print at TU Wien Bibliothek.
TU Bibliothek Your knowledge hub WIEN

Conservation of energy:

$$\begin{aligned}\frac{\partial \rho\, h}{\partial t} = &+ \frac{\partial}{\partial \boldsymbol{x}} \cdot \boldsymbol{K} \cdot \frac{\partial T}{\partial \boldsymbol{x}} \\ &+ \frac{\partial}{\partial \boldsymbol{x}} \cdot \boldsymbol{D_b} \cdot \frac{\partial c_b}{\partial \boldsymbol{x}}\, \overline{h}_b + \frac{\partial}{\partial \boldsymbol{x}} \cdot \boldsymbol{D_{bT}} \cdot \frac{\partial T}{\partial \boldsymbol{x}}\, \overline{h}_b \\ &+ \frac{\partial}{\partial \boldsymbol{x}} \cdot \boldsymbol{D_v} \cdot \frac{\partial c_v}{\partial \boldsymbol{x}}\, h_v\, f_{lum} \\ &+ \dot{c}_{bv}\,(h_v - h_b)\end{aligned} \tag{4.3}$$

Where the left hand side shows the accumulation expression, which accounts for the change of the concentration/energy over time ∂t, and the right hand side the diffusion processes with transport tensors for bound water $\boldsymbol{D_b}$ and water vapor $\boldsymbol{D_v}$ as well as the phase change between the two states of water, which is denoted with the sorption rate $\dot{c}_{bv}$. In Equation (4.3), the thermal conduction $\boldsymbol{K}$ is considered together with the enthalpy changes due to the transport processes, which are considered with $\overline{h}_b$ as the averaged enthalpy of bound water and h_v as the specific enthalpy of water vapor. The phase change, based on the sorption rate, is considered with the enthalpy difference between h_v and h_b, where h_b is the specific enthalpy of bound water. The constitutive equations are given in Section 4.A.

The system of Equations (4.1) to (4.3) is implemented with a user element subroutine in the finite element software *Abaqus* [59] with brick-type elements using linear interpolation functions for the discretization and solved by using the modified Newton method, according to [3].

4.2.2.1 Material properties for moisture transport

As the User Element Subroutine was used in the whole cross sections, the moisture and temperature transport are modeled with the same multi-Fickian transport model, as previously described, in all three materials. Thus, the particle board and also the aluminum profile have to be used with properties fitting into this model as described in the following paragraphs.

4.2.2.1.1 Solid timber (spruce)

The material parameters for spruce are defined according to [5], but with a dry density of 405 $\mathrm{kg\,m^{-3}}$ and a cylindrical-orthotropic material orientation was used. The material orientation is then defined in each integration point, depending on the pith location in the lower and upper flange, by means of a user subroutine. A sorption hysteresis was also included to define the sorption rate $\dot{c}_{bv}$ under the isothermal experimental conditions. The material properties are given in Tables 4.A.1 and 4.A.2 in Section 4.A.

4.2.2.1.2 Particle board

The moisture transport in the particle board was considered to be similar to solid wood, hence the wood particles act as cell walls, but the glue decreases the diffusivities of the lumen, thus, the moisture transport in the particle board was also modeled using the multi-Fickian approach.

Die approbierte gedruckte Originalversion dieser Dissertation ist an der TU Wien Bibliothek verfügbar.
The approved original version of this doctoral thesis is available in print at TU Wien Bibliothek.
TU Bibliothek Your knowledge hub WIEN

For the moisture diffusivities, a value for μ of 20 for wet particle boards and 50 for dry ones is given in [91]. Since the standard does not distinguish between the two water phases, it is assumed, that the dry value represents the water vapor diffusion property and the other part of the moisture transport process is considered with bound water diffusion. The reduction tensor for water vapor diffusion $\boldsymbol{\xi}$ is determined based on the reciprocal value of μ, which results in 0.02 for the out-of-plane direction. Based on [89] the in-plane diffusivity of particle boards is about 15 times larger than the one in out-of-plane direction, thus, the in-plane value is set to 0.3. For the bound water diffusivity, the coefficients were scaled from solid timber of the previous section. In [91], the same μ values are given for a particle board and solid timber and, thus, for the diffusivity in the out-of-plane direction the value from the radial direction (which is equal to the tangential direction) of solid timber was chosen. However, for the longitudinal direction, the bound water transport in solid timber is 2.5 times larger than in the other directions. For the water vapor diffusivity, this factor is about 20 in case of solid timber (see on Table 4.A.2), when comparing the longitudinal and tangential directions, and 15, as previously mentioned, for the particle board. Thus, the factor for the longitudinal component of the bound water diffusivity is set to 1.875. The specific heat capacity is set to $1700\,\mathrm{J\,kg^{-1}\,K^{-1}}$ according to [91] and the thermal conductivity is interpolated from the data given in [91] with $0.167\,\mathrm{W\,m^{-1}\,K^{-1}}$.

The sorption process was modeled with the same hysteresis model as used for solid timber, hence the particle board is based on solid timber particles, but the isotherms were adjusted to the dry density of the particle board by scaling with the relation of the dry densities ($\rho_{d,sp}/\rho_{d,pb}$). As the particles consist of the same solid wood material, also the specific and averaged bound water enthalpy expressions from solid timber were used for the particle board.

The particle board is sealed as shown in Figure 4.1 and the coating has an s_d-value of 2.

4.2.2.1.3 Aluminum

The multi-Fickian model was also used for the aluminum profile, but with the diffusion coefficients set to zero, leaving only thermal conduction active in this material. The density of aluminum is set to $2700\,\mathrm{kg\,m^{-3}}$, the heat capacity to $897\,\mathrm{J\,kg^{-1}\,K^{-1}}$ and the thermal conductivity to $235\,\mathrm{W\,m^{-1}\,K^{-1}}$.

4.2.2.2 Glue lines and interaction between parts

The components of the cross sections are combined with an adhesive of type 1C-PUR, which has a higher diffusion resistance than e.g. MUF. This was investigated in [77], where two wooden samples glued together had a twice as high resistance during the dry cup test and a 3.6 times higher resistance in case of the wet cup test compared to a continuous sample. During the simulation it is considered that water vapor and heat penetrate through the glue line without further resistance, while bound water is prevented from transferring through the glue line.

Die approbierte gedruckte Originalversion dieser Dissertation ist an der TU Wien Bibliothek verfügbar.
The approved original version of this doctoral thesis is available in print at TU Wien Bibliothek.
TU Bibliothek Your knowledge hub WIEN

4.2.2.3 Initial conditions

The initial conditions are a temperature T_{ini} of 293.15 K and an initial water vapor concentration $c_{v,ini}$ of 11.2 $\mathrm{g\,m^{-3}}$, which is determined from the initial relative humidity φ_{ini} of 65 %. Based on the initial water vapor concentration the initial bound water concentration $c_{b,ini}$ can be defined from the adsorption isotherm with 47.5 $\mathrm{kg\,m^{-3}}$.

4.2.2.4 Boundary conditions

Exchange with the surrounding climate occurs only in terms of water vapor and energy, which can be described with Neumann boundary conditions. In terms of the water vapor concentration, the flux ϕ_v across the boundary is described as

$$\begin{aligned} \phi_v &= k_{c_v}\left(c_v - c_{v,0}\right) f_{lum}, \\ k_{c_v} &= \frac{1}{\frac{1}{k_{c_v,surf}} + \frac{1}{k_{c_v,coat}}} \\ k_{c_v,coat} &= D_{air}/s_d \end{aligned} \tag{4.4}$$

with the film boundary coefficient $k_{c_v,surf}$, which is set to 1 $\mathrm{m\,s^{-1}}$ and the water vapor concentration of the surrounding climate $c_{v,0}$, which is based on a relative humidity of 100 %. This is in agreement with [92], where rain-exposed samples were also modeled with a relative humidity of 100 % and a "high" value (compared to the value of 1.4E-7 $\mathrm{m\,s^{-1}}$, which was used when no rain was present) for the film boundary coefficient. The coating is considered according to [14] with Equation (4.4). D_{air} denotes the diffusivity of air, as defined in Table 4.A.1 with a value for $\boldsymbol{\xi}$ of 1 and s_d is the water vapor diffusion-equivalent air layer thickness, according to [91]. The front and back ends of the beams, i.e. the end grain surfaces, are sealed.

In addition to the mass transfer, also the energy flux ϕ_T across the exchange surface has to be considered with contributions from thermal and mass transfer effects due to enthalpy changes and is described by

$$\phi_T = k_T\left(T - T_0\right) + k_{c_v}\left(c_v - c_{v,0}\right) f_{lum}\, h_v, \tag{4.5}$$

with the heat transfer coefficient k_T of 25 $\mathrm{W\,m^{-2}\,K^{-1}}$ and the temperature of distant air T_0 of 293.15 K.

4.2.3 Resistance tests

In the following section, the material parameters for the resistance tests are described. In order to correctly model the behavior of the moist and wet beams, not only dry material parameters are presented, but also the moisture dependence has to be considered. Additionally, the interactions between the parts of the cross section are also described as well as the test setups.

Die approbierte gedruckte Originalversion dieser Dissertation ist an der TU Wien Bibliothek verfügbar.
The approved original version of this doctoral thesis is available in print at TU Wien Bibliothek.
TU Bibliothek Your knowledge hub WIEN

Table 4.1: Entries for elasticity tensor $\boldsymbol{C}$ at 12% MC and 293.15 K in MPa for a dry density of 405 $\mathrm{kg\,m^{-3}}$.

C_{LLLL}	C_{RRRR}	C_{TTTT}	C_{LLRR}	C_{RRTT}	C_{TTLL}	C_{LRLR}	C_{LTLT}	C_{RTRT}
12204.7	798.8	531.8	274.3	376.1	216.3	566.9	577.5	73.2

4.2.3.1 Solid timber (spruce)

As described in [5], the material parameters for the elasticity tensor for the wooden flange made of spruce are determined with the continuum micromechanics model of [82], where the necessary input parameters are a clear wood density of 405 $\mathrm{kg\,m^{-3}}$ and the chemical composition of spruce as well as the moisture content. The model is pre-evaluated for MC levels from 3 % to 30 % at 1 % increments and with the information on the moisture distribution from the previous simulation it is now possible to consider moisture-dependent stiffness properties in each integration point individually. The exemplary elasticity tensor components at 12% MC and 293.15 K are given in Table 4.1. A cylindrical-orthotropic coordinate system is considered, which is defined with the pith locations in the lower and upper flange, respectively, as shown in Figure 4.1.

For moist and wet beams, the coefficients of moisture expansion are defined according to [83] with 0.015 %/% in longitudinal, 0.19 %/% in radial and 0.36 %/% in tangential direction.

For modeling the failure behavior of spruce, a multisurface failure criterion was included.

4.2.3.1.1 Multisurface failure criterion

Since wood is naturally grown, the resulting irregular structure makes it challenging to describe its failure behavior. An approach to describe the failure behavior at the level of both single cells and the level of annual rings has been studied on a unit cell in [31, 32]. Various load combinations were numerically tested and, the main failure characteristics could be characterized. Based on these, a multisurface failure criterion was developed, which is able to describe ductile (plastic) and brittle (cracking) failure mechanisms. The failure criterion is described in terms of multiple Tsai-Wu failure surfaces [86] at the clear wood level as follows:

$$\begin{aligned} f_i^{cw}(\sigma) = \; & a_{LL,i} \cdot \sigma_{LL} + a_{RR,i} \cdot \sigma_{RR} + a_{TT,i} \cdot \sigma_{TT} \\ & + b_{LLLL,i} \cdot \sigma_{LL}^2 + b_{RRRR,i} \cdot \sigma_{RRRR}^2 \\ & + b_{TTTT,i} \cdot \sigma_{TT}^2 + 2\, b_{RRTT,i} \cdot \sigma_{RR} \cdot \sigma_{TT} \\ & + 4\, b_{RTRT,i} \cdot \tau_{RT}^2 + 4\, b_{TLTL,i} \cdot \tau_{TL}^2 \leqslant 1 \end{aligned} \tag{4.6}$$

The Tsai-Wu tensor components $a_{LL,i}$, $a_{RR,i}$, $a_{TT,i}$, $b_{LLLL,i}$, $b_{RRRR,i}$, $b_{TTTT,i}$, $b_{RRTT,i}$, $b_{RTRT,i}$ and $b_{TLTL,i}$ are defined according to [32] for all eight failure surfaces, which are depicted in Figure 4.2. It can be seen that the strength in longitudinal direction is much higher than in transversal direction, with the perpendicular-to-grain tensile strengths being approximately 5 MPa in radial direction and 2 MPa in the tangential one.

Die approbierte gedruckte Originalversion dieser Dissertation ist an der TU Wien Bibliothek verfügbar.
The approved original version of this doctoral thesis is available in print at TU Wien Bibliothek.
TU Bibliothek Your knowledge hub WIEN

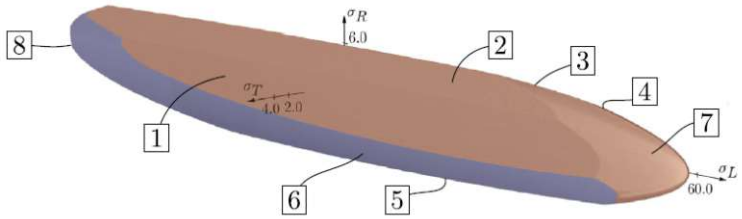

Figure 4.2: Multisurface failure criterion shown in the σ_L–σ_R–σ_T-space from [32].

As the criterion was developed for dry conditions, the stress values during the evaluation of the multisurface failure criterion in case of the wet beam computations are multiplied with a factor of 2, which is corresponding to a reduction in strength compared to the dry level by 50 % to account for the moisture-related strength decrease. For brittle failure in case of the tests for bending resistance, the maximum strength values are calibrated for each moisture level, to reach the experimental load capacities, leading to a maximum tensile strength for spruce of 35 MPa in case of the dry beams, 25 MPa for the moist beams and 20 MPa in case of the wet beams.

4.2.3.2 Particle Board

The webs of the cross sections are made of a special particle board with higher resin content and density compared to other commercial boards of type P7 (heavy duty load-bearing boards for use in humid conditions) according to EN 312 [93]. The material parameters were determined with ultrasonic tests according to [94] under dry conditions and are given in Table 4.2. For the moist and wet simulations, the elasticity tensor was scaled by calibrating it to the experimental load-displacement curves of the resistance tests, since the other components were either not moisture-dependent (aluminum profile, load transmission construction) or already determined (spruce). As the goal was to predict the test results in all test setups with the same stiffness reduction factors, the values in Table 4.2 were chosen. As can be seen, the values do not differ between the moist and wet state, which is a consequence of the bending tests, where the moist and wet beam show only little differences and also the center part of the web has the same MC due to the sealing, as can be seen from Figure 4.7. However, MC values in the critical joint between the flange and the web change from the moist to the wet state and thus, the values for the yield criterion are adjusted from 32.5 MPa for the dry, to 23.7 MPa for the moist and 14.6 MPa for the wet state. These values were fitted based on the test for shear resistance for the *I tec pro* and then used in all other simulations. From [95] it can be concluded that the strength can be reduced to about 50 % of the dry value in case of the bending strength, thus the chosen values seem to be reasonable. A von Mieses yield stress of 32.5 MPa corresponds to a shear stress (in case of pure shear) of 18.76 MPa. This value is similar to a fiber board with a density of 800 $\mathrm{kg\,m^{-3}}$ which has a characteristic shear strength in the out-of-plane direction of 16 MPa according to EN 12369-1 [96].

The moisture-related expansion coefficients are chosen also according to [97] with 0.035 %/% MC for the in-plane and 0.93 %/% MC for the out-of-plane direction.

Die approbierte gedruckte Originalversion dieser Dissertation ist an der TU Wien Bibliothek verfügbar.
The approved original version of this doctoral thesis is available in print at TU Wien Bibliothek.
TU Bibliothek Your knowledge hub WIEN

Table 4.2: Entries for the elasticity tensor C for the particle board in MPa. Directions 1 and 2 are in-plane.

conditions	C_{1111}	C_{1122}	C_{2222}	C_{1133}	C_{2233}	C_{3333}	C_{1212}	C_{1313}	C_{2323}
dry	7597.4	5797.2	7597.4	1863.1	1863.1	667.9	900.5	47.7	47.7
moist/wet	3038.9	2318.9	3038.9	745.3	745.3	267.2	360.2	19.1	19.1

4.2.3.3 Aluminum

For the profile in the *I tec pro* flange, aluminum of type AW 6060 T66 was used. A tensile experiment with an aluminum sample led to the stress-strain relationship depicted in Figure 4.3. This test was also used to calibrate the material parameters to represent this stress-strain relationship by means of finite elements for the resistance tests. Thus, simulations with an element size of 2 mm (as in the resistance tests) were performed to define the plastic material behavior based on the Abaqus metal plasticity model as shown in Table 4.3. The modulus of elasticity was determined experimentally with 64 GPa and the yield strength with about 220 MPa.

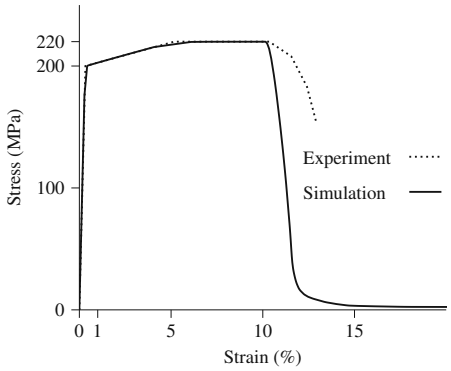

Figure 4.3: Stress-strain relationship for aluminum of type AW 6060 T66 used for the profile in the *I tec pro* beam. Calibrated simulation results shown in comparison to the experimental results.

Table 4.3: Definition of the plastic material behavior of aluminum

yield stress	plastic strain
200	0
220	0.0484
220	0.1500
1	0.4000

4.2.3.4 Interactions between components

During the dry and moist states, the flanges, the web and the aluminum profiles are connected by tie interactions. This is also the case for the wet tests for bending resistance. However, for the wet tests for shear and bearing resistance, the contact interactions were

Die approbierte gedruckte Originalversion dieser Dissertation ist an der TU Wien Bibliothek verfügbar.
The approved original version of this doctoral thesis is available in print at TU Wien Bibliothek.
TU Bibliothek Your knowledge hub WIEN

adjusted, since during the experiments a delamination process had taken place between the aluminum profile and the flange as a result of the moistening process. Thus, the tied condition was changed to contact in normal and frictionless in tangential direction in case of the interaction between the flange and the aluminum profile for the *I tec pro*. In the joint between the aluminum profile and the web, an interaction with a friction coefficient of 0.5, which was determined by a parameter study, was applied. In case of the test for bearing resistance this was applied for the whole beam, while for the shear resistance test these conditions were applied to the section of the beam between the load and the support plate, also according to a parameter study. For the second beam type *H20 top P* a similar behavior was observed, which is a relative displacement of flange and web. Thus, a contact interaction with a friction coefficient of 0.5 was applied in the joint between the flange and the web in the same sections as in case of the *I tec pro*.

4.2.3.5 Load transmission construction

With the load transmission construction the forces are applied displacement-controlled onto the investigated beam as prescribed in EN 13377 and shown in Figures 4.4 to 4.6. In the experiment it consisted of metal beams with hinges on both ends. One construction was used for the test for bearing and bending resistance and another for the test for shear resistance. The beams of the constructions were modeled with a rectangular cross section of 10x4 cm and the modulus of elasticity was calibrated such that the beam's deflection corresponds to the experimental one, which leads to an MOE of 85,585,800 MPa and a Poisson's ratio of 0.3. The mesh consists of one brick-type element with linear shape functions per cross section to reduce the number of DOF and a length of 4 cm in longitudinal direction.

The plates for the load distribution on the top of the beam and also at the supports are modeled each with 20 cm long, 2 cm thick and 10 cm wide plates, made of steel with a modulus of elasticity of 210,000 MPa and a Poisson's ratio of 0.3. According to EN 13377, the top plates for load distribution consist of wooden blocks with at least 4 cm thickness. However, during the computations also steel plates, as previously described, were used, but with an adjusted friction coefficient of 0.15 between the plate and the beam instead of the 0.10 between the beam and the support plates. For the mesh of the plates, brick-type elements with a length of 1 cm per direction and linear shape functions were chosen.

4.2.3.6 Test setup for the bending resistance of EN 13377

According to EN 13377, for testing the bending resistance, a 3.3 m long beam was loaded with eight single forces, which are applied via a load transmission construction as shown in Figure 4.4. To reduce the degrees of freedom in the finite element model, only a quarter of the beam was computed during the analysis. In case of this test, the maximum bending moment is expected in the middle of the beam, with the largest shear forces in the area of the supports. The used mesh for the whole model uses 13,023 elements of brick type with linear shape functions in case of the *I tec pro* and 10,307 elements in case of the *H20 top P*. The element size in longitudinal direction is reduced in the region of the maximum bending moment from 4.5 cm to 0.6 cm. The dimensions of the elements within the cross section are between 0.2 and 0.7 cm.

Die approbierte gedruckte Originalversion dieser Dissertation ist an der TU Wien Bibliothek verfügbar.
The approved original version of this doctoral thesis is available in print at TU Wien Bibliothek.
TU Bibliothek Your knowledge hub WIEN

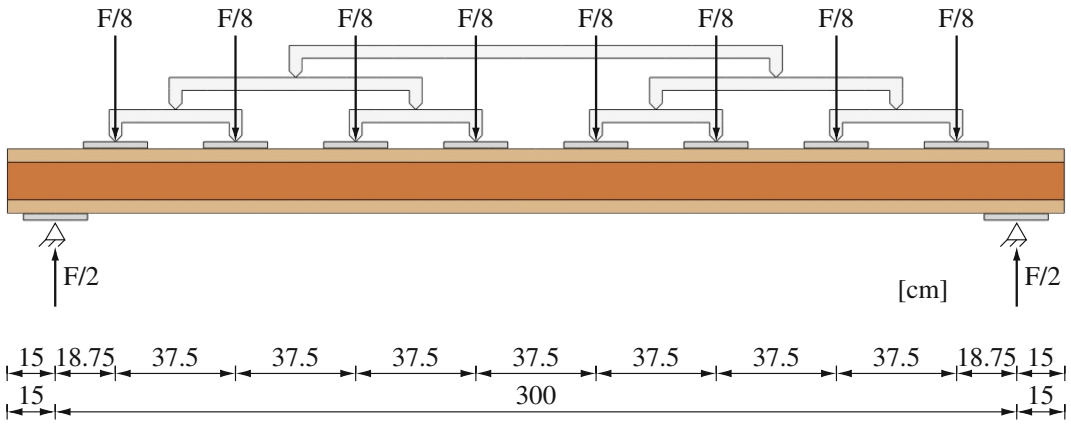

Figure 4.4: Test for bending resistance according to EN 13377. The 3.30 m long beam is loaded with eight single forces and supported at two locations at the end of the beam.

4.2.3.7 Test setup for the bearing resistance of EN 13377

The test for bearing resistance has nearly the same setup as the previously described test, but the supports are placed towards the middle of the beam as depicted in Figure 4.5. This leads to large shear forces next to the support and also to negative bending moments in this zone. By utilizing the beam's symmetry, also only a quarter model was computed during the FE Analysis. The mesh for the whole model uses 12,067 elements of brick type with linear shape functions in case of the *I tec pro* and 14,187 elements in case of the *H20 top P*. The element size in longitudinal direction is reduced in the region of the support from 4.5 cm to 2.4 cm in case of the *I tec pro* and to 1 cm in case of the *H20 top P*. The dimensions of the elements within the cross section are between 0.2 and 0.7 cm.

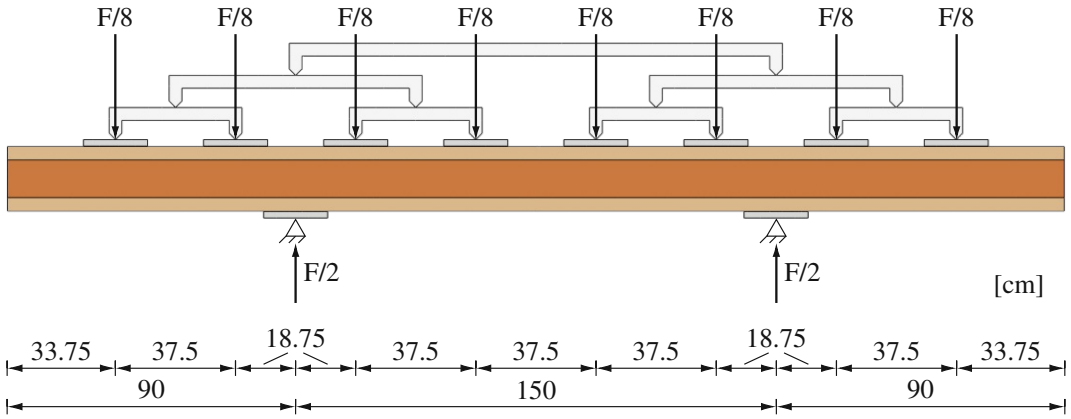

Figure 4.5: Test for bearing resistance according to EN 13377. The 3.30 m long beam is loaded with eight single forces and supported at two locations of the beam.

Die approbierte gedruckte Originalversion dieser Dissertation ist an der TU Wien Bibliothek verfügbar.
The approved original version of this doctoral thesis is available in print at TU Wien Bibliothek.
TU Bibliothek Your knowledge hub WIEN

4.2.3.8 Test setup for the shear resistance of EN 13377

For the test for shear resistance, a 1.50 m long beam was investigated with two single loads applied, as shown in Figure 4.6. The setup leads to high shear forces in the section of the beam between the support and the load plate and also a bending moment in the middle of the beam. Again, only a quarter model was analyzed to save computational time. The mesh for the whole model uses 9,729 elements of brick type with linear shape functions in case of the *I tec pro* and 13,530 elements in case of the *H20 top P*. The element size in longitudinal direction is about 2.5 cm and reduced next to the support to 1.8 cm and 1 cm in case of the *I tec pro* and *H20 top P*, respectively. The dimensions of the elements within the cross section are between 0.2 and 0.7 cm.

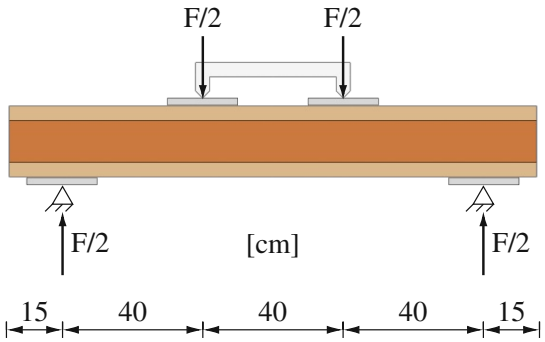

Figure 4.6: Test for shear resistance according to EN 13377. The 1.50 m long beam is loaded with two single forces and supported at two locations at the end of the beam.

4.3 Results

In this section the results of the computed resistance tests are presented. A sensitivity analysis is made first to determine the influence of the single parameters on the overall tests and to find a unique set of parameters, which predict the results of the different experiments at a certain moisture level. After this, the moisture fields determined with the multi-Fickian transport model are presented followed by a detailed description of the three different tests of the two investigated beams at various moisture levels. All the resistance tests were displacement-controlled.

4.3.1 Sensitivity analysis

To determine a unique set of stiffness parameters for the entire set of experiments (for each moisture state), a sensitivity analysis was performed.

As Table 4.4 shows, the various parameters influence the tests in certain directions relative to a reference configuration. A change of the stiffness tensor of the flange material by scaling the tensor by +10 % leads to a load capacity increase of 6.25 % at the same displacement in case of the bending resistance test. Another way to investigate the influence of the spruce material is to change the density, which leads also to different stiffness properties according to the continuum micromechanics model of [82]. The

Die approbierte gedruckte Originalversion dieser Dissertation ist an der TU Wien Bibliothek verfügbar.
The approved original version of this doctoral thesis is available in print at TU Wien Bibliothek.
TU Bibliothek Your knowledge hub WIEN

Table 4.4: Variation of parameters and their influence on beam stiffness in case of *I tec pro* relative to a reference configuration.

Parameter	Bearing test	Shear test	Bending test
Flange/Spruce elasticity tensor ±10 %	±2.84 %	±4.10 %	±6.25 %
Flange/Spruce density 405 ±55 $\mathrm{kg\,m^{-3}}$	±7.27 %	±7.58 %	±8.10 %
Web/Particle board elasticity tensor ±10 %	±5.98 %	±5.72 %	±2.02 %
Friction at top load plates ±0.1	±6.24 %	±1.11 %	±5.16 %
Friction at bottom load plates ±0.1	±0.9 %	±2.03 %	±2.09 %

change from the initial density of 405 $\mathrm{kg\,m^{-3}}$ to 460 $\mathrm{kg\,m^{-3}}$ and 350 $\mathrm{kg\,m^{-3}}$ (range according to measurements), respectively, leads to an average stiffness change of 7.27 % in case of the test for bearing, 7.58 % for shear and 8.10 % for bending resistance. These results are in agreement with the previous method, where the stiffness tensor was scaled by 10 %, since the influence on the bearing test was the smallest and on the bending test the largest. In addition to the flange stiffness, also the friction of the top and bottom plates have a large influence on the overall system stiffness. In case of the test for bearing resistance, the stiffness of the web and also the friction between the beam and the top load plates influence the system stiffness significantly. In the test for shear resistance, the stiffness of both flange and web have a large influence, whereas the top load plates have only a small influence on the system stiffness. Based on these studies, one set of material parameters for all investigated experiments of each moisture level was chosen (see Section 4.2.3).

4.3.2 Moisture fields

To determine the stiffness and strength of the moist and wet beams, moisture simulations with the multi-Fickian transport model, described in Section 4.2.2, were made. In Figure 4.7 the results of the different beams at the two investigated points in time after 3 and 60 days of exposing the beam to 100 % relative humidity are shown. Experimental results of the *H20 top N* beam after three days of exposure were investigated in [98] and are shown in Figure 4.7a. This beams shares the same geometry of the flange as the *H20 top P*, but with a different material and dimension of the web. As can be seen when comparing the results after three days of the *H20 top N* and the *I tec pro*, as shown in Figures 4.7a and 4.7b, respectively, the model is able to predict the results from the experiment in the flanges quite well. After 60 days of exposure, the moisture fields in the spruce parts of both of the modeled cross sections (*I tec pro* in Figure 4.7c and *H20 top P* in Figure 4.7d) are close to uniform with less than 2 % variation in MC within the fields. In contrast to the spruce in the flange, the particle board in the web is sealed and, thus, the reaction to the moistening process is much slower. In the top and bottom zone of the particle board, where the web is connected with a finger joint to the flange, the moisture content increases due to the contact with the spruce material.

Die approbierte gedruckte Originalversion dieser Dissertation ist an der TU Wien Bibliothek verfügbar.
The approved original version of this doctoral thesis is available in print at TU Wien Bibliothek.
TU Bibliothek Your knowledge hub WIEN

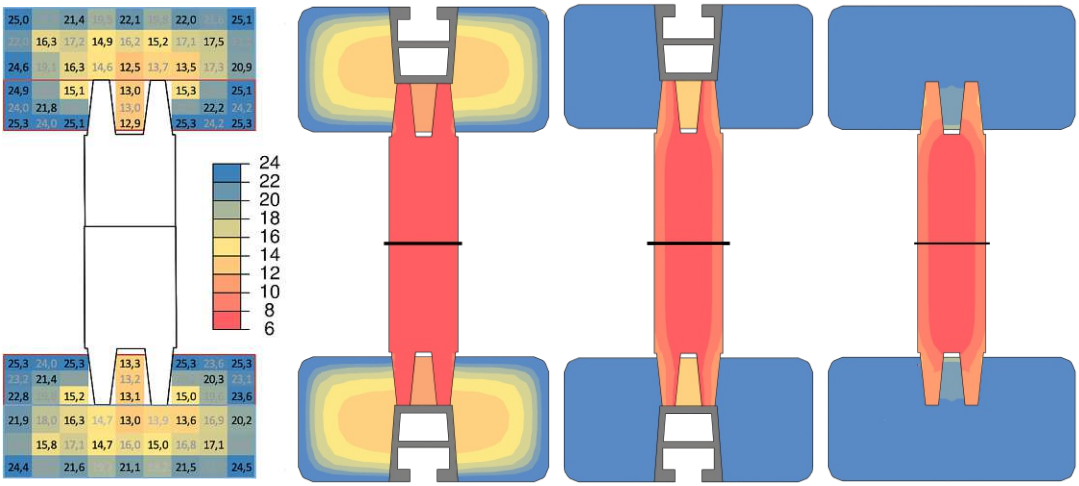

(a) H20 top N - 3d Experimental [98]

(b) I tec pro - 3d moist

(c) I tec pro - 60d wet

(d) H20 top P - 60d wet

Figure 4.7: (a) Experimental and (b-d) computed moisture content fields after 3 d and 60 d of exposure of the cross sections to 100 % relative humidity at 20 °C. The discontinuity between MCs of the spruce in the flange and the web is a result of the different dry densities. The web is sealed, which leads to smaller changes of the MC, compared to the flange region.

4.3.3 Test for bending resistance

In this section, the results of the test for bending resistance of the two investigated beam types are described. In addition to the dry case, the *I tec pro* beam was also tested under moist and wet conditions and the *H20 top P* beam under wet conditions. For both beam types, the failure mechanism in case of this test was observed to be related to the tensile strength of spruce in longitudinal direction. The calculation time was between 1 h and 4 h.

4.3.3.1 I tec pro

The load-displacement curve of the *I tec pro* test for bending resistance, as shown in Figure 4.8, begins with linear-elastic behavior and ends with brittle failure due to exceeding of longitudinal tensile stresses, with a crack starting at the lower edge of the bottom flange. The computed dry beam fails at a displacement of 25 mm with a maximum load of 62.95 kN which is close to the experiment, failing at 61.61 kN and 24.13 mm, respectively. The computed moist beam reaches 51.41 kN at 25.7 mm, while the experiment fails at 48.78 kN and a displacement of 25.21 mm, showing also a good agreement. Under wet conditions the computation reached 50.06 kN at 28.5 mm, which is again close to the experimental value of 47.2 kN at a displacement of 30.8 mm. The difference in stiffness and strength between the moist and wet beam is small, compared to the dry beam, as can be seen in Figure 4.8.

Die approbierte gedruckte Originalversion dieser Dissertation ist an der TU Wien Bibliothek verfügbar.
The approved original version of this doctoral thesis is available in print at TU Wien Bibliothek.

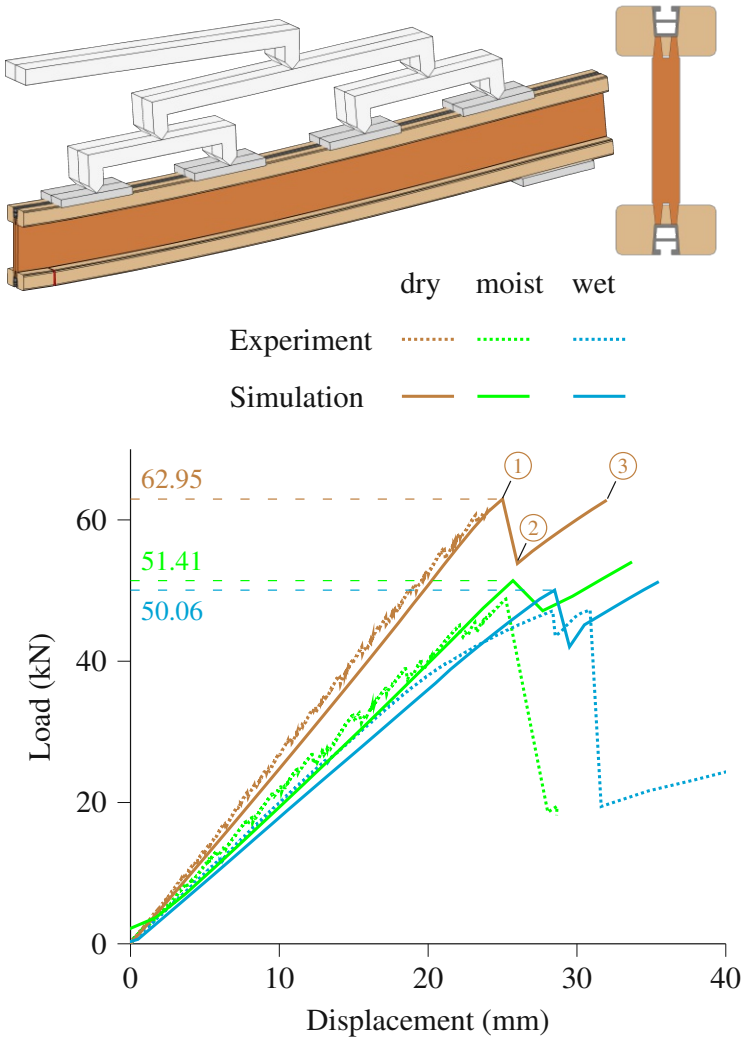

Figure 4.8: Load-displacement curves for dry, moist and wet bending resistance tests of the *I tec pro* beam. Failure is initiated by a crack due to exceeding the longitudinal tensile strength of spruce when the maximum load is reached. Detailed description of the marked states of the different materials is shown in Figure 4.9. The top left image shows the dry simulation at ③ with a deformation scale factor of 2.

Cracking starts at the marked point ① at the location shown in Figure 4.9a and continues until the spruce part of the flange is fully cracked, which is depicted in Figure 4.9c for point ③. To predict the measured loads from the experiment, the maximum tensile stress for spruce was reduced from 56 MPa in case of clear wood from the model of [32] to 35 MPa to take into account the structure of wood, which is non-homogeneous due to knots and the finger joints of the flange and the web, which have to be located in the critical middle section of the beam, according to EN 13377. As soon as the crack initiates, the aluminum profile also shows plastic zones, as shown in Figure 4.9a. With the growth of the crack, also the plastic zones get larger (Figure 4.9b) until the flange is fully cracked in Figure 4.9c. The material behavior of the aluminum profile does not allow for brittle failure, instead the stresses at larger strains are reduced to small values,

Die approbierte gedruckte Originalversion dieser Dissertation ist an der TU Wien Bibliothek verfügbar.
The approved original version of this doctoral thesis is available in print at TU Wien Bibliothek.
TU Bibliothek Your knowledge hub WIEN

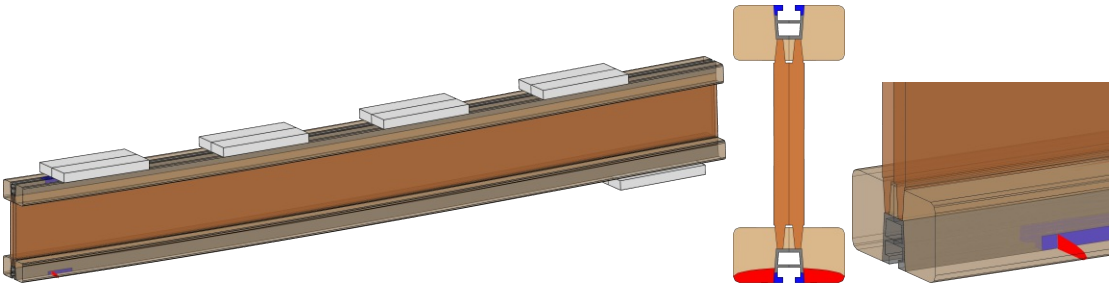

(a) Deformations, plastic zones and crack growth at ① (25 mm displacement)

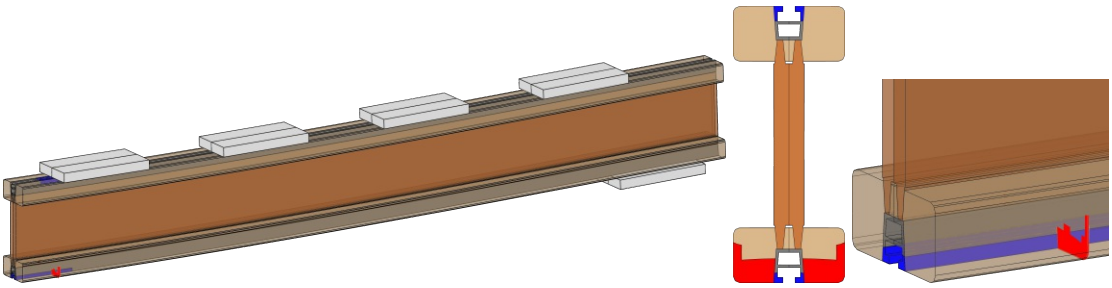

(b) Deformations, plastic zones and crack growth at ② (26 mm displacement)

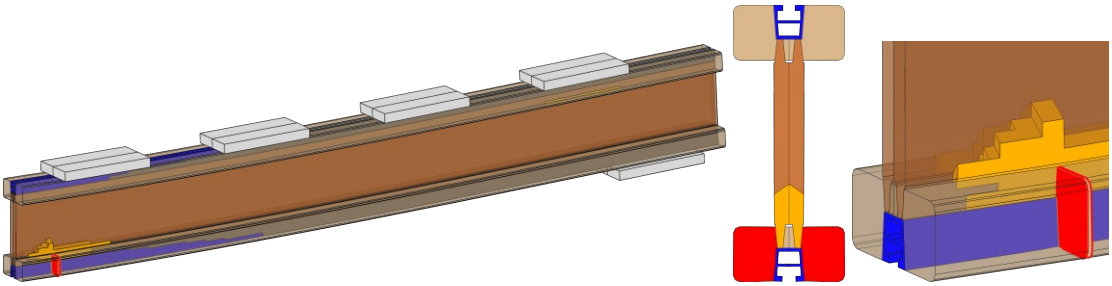

(c) Deformations, plastic zones and crack growth at ③ (32 mm displacement)

Figure 4.9: States of plastic zones in the aluminum profile (blue) and particle board web (orange) as well as crack growth (red) in the flange made of spruce at three different displacements of the load transmission construction (shown in Figure 4.8) for the bending resistance test of the dry *I tec pro* beam. In each row, the entire model is depicted on the left hand side, followed by a cross section cut at the the crack in the middle and a detail of crack region on the right hand side

as shown in Figure 4.3. This is the reason for the remaining stiffness in the computation after failure at a displacement of 25 mm. In the experiments, both, the flange and the aluminum profile, showed cracks as depicted in Figure 4.10.

For the moist and wet beams, the same model was used, but with different moisture fields, which reduce the stiffness parameters of the flange and the web accordingly. The experiments and also the computations show a similar stiffness for both the moist and the wet state, as depicted in Figure 4.8. In the experiment, the failure is located in the finger joints as shown in Figure 4.11. This is considered during the computation with the reduced tensile strength, which was set to 25 MPa for the moist and to 20 MPa for the wet beam, based on the experimental results. The strength values in the plastic failure criterion for the particle board were also reduced according to Table 4.2. Again, failure

Die approbierte gedruckte Originalversion dieser Dissertation ist an der TU Wien Bibliothek verfügbar.
The approved original version of this doctoral thesis is available in print at TU Wien Bibliothek.
TU Bibliothek Your knowledge hub WIEN

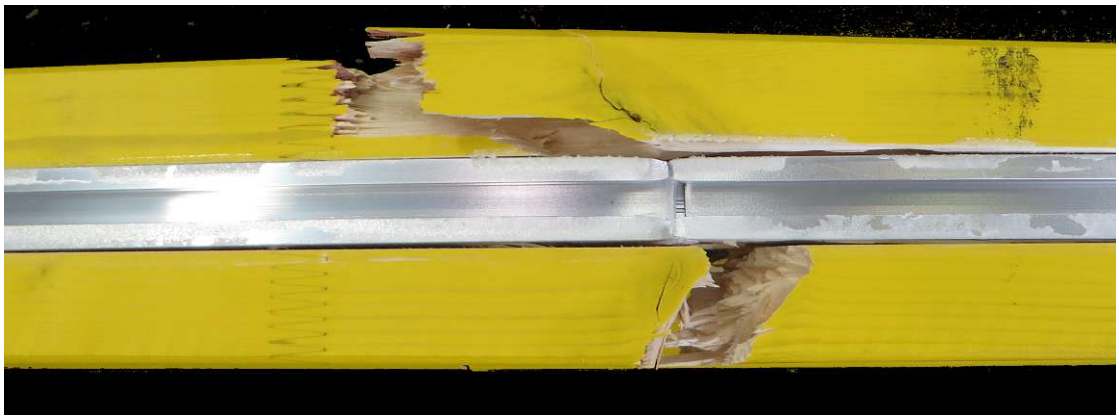

Figure 4.10: Failure of the dry *I tec pro* beam in case of the bending resistance test. Both, the aluminum profile and the spruce in the flange show a crack. In the spruce, this crack is related to a knot and the finger joint.

occurs due to exceeding the longitudinal tensile stresses at roughly the same load level for both moisture states, which is caused by the maximum bending stress at the bottom edge of the flange where the values of the moisture contents are quite similar for both cases as can be seen by comparing Figures 4.7b and 4.7c.

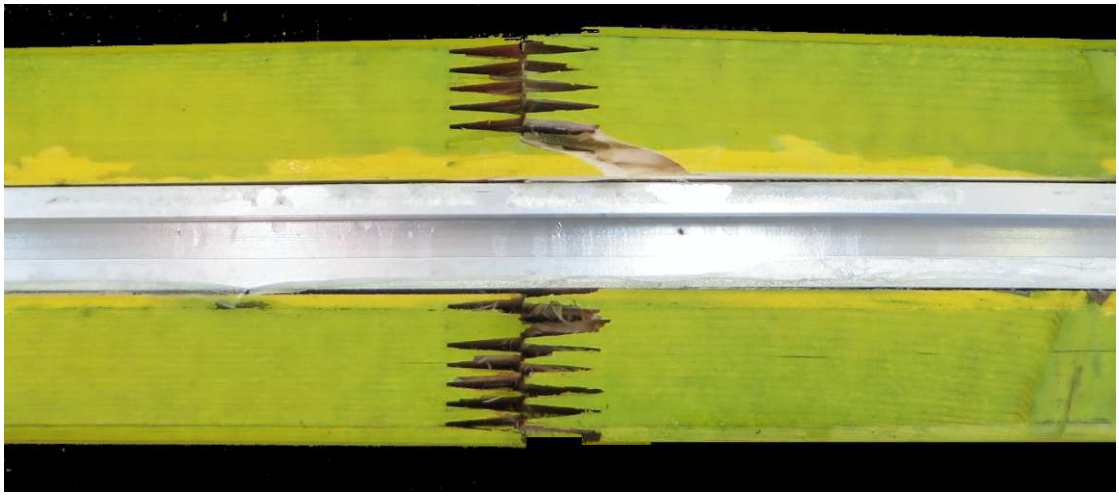

Figure 4.11: Failure in the finger joint of the wet *I tec pro* beam in case of the bending resistance test. The aluminum profile did not show a crack in this experiment. In the simulation, the reduced tensile strength accounts for the failure in the finger joint.

4.3.3.2 H20 top P

The *H20 top P* beam also shows a linear-elastic behavior until brittle failure takes place at a displacement of 21 mm and a maximum load capacity of 48.37 kN at ① (see Figure 4.12) in case of the dry beam computation. This is close to the experimental result, which is 47.76 kN at a displacement of 23.07 mm. Compared to the *I tec pro* beam with

Die approbierte gedruckte Originalversion dieser Dissertation ist an der TU Wien Bibliothek verfügbar.
The approved original version of this doctoral thesis is available in print at TU Wien Bibliothek.
TU Bibliothek Your knowledge hub WIEN

the aluminum profile in the flange, the maximum load at time of cracking is lower. As in case of the *I tec pro*, the maximum longitudinal tensile stress was reduced to 35 MPa. The wet beam fails at 20 mm and 28.86 kN as can be seen in Figure 4.12 with a maximum longitudinal tensile stress of 20 MPa. This is again in good agreement with the experimental result of 18.95 kN at 25.42 mm.

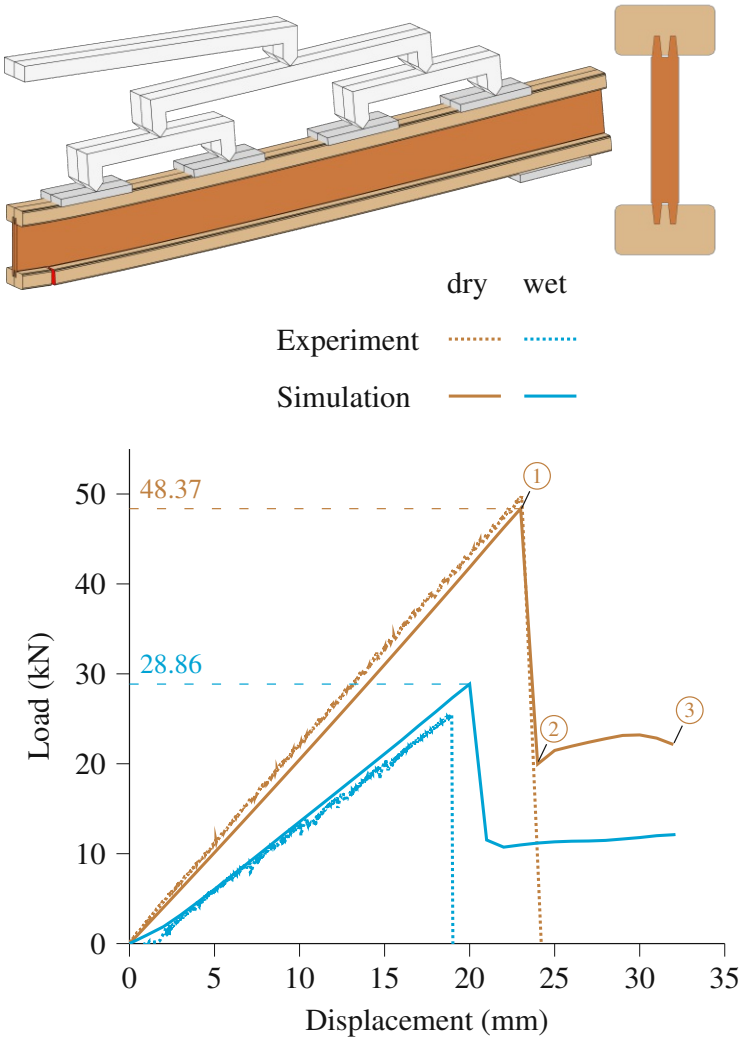

Figure 4.12: Load-displacement curves for dry and wet bending resistance tests of the *H20 top P* beam. Failure is initiated by a crack due to exceeding the longitudinal tensile strength of spruce when the maximum load is reached. Detailed description of the states of the different materials is shown in Figure 4.13. The top left image shows the dry simulation at point ③ with a deformation scale factor of 2.

In case of the dry *H20 top P* beam, the crack is initiated due to longitudinal tensile stresses and is located in the middle section of the beam next to the loading plate and begins to emerge from the bottom of the lower flange. At ①, the web shows no plastic behavior as can be seen in Figure 4.13a. This is the case until the crack reaches the finger joint in the flange as depicted in Figure 4.13b at ②. After that, the web starts to

Die approbierte gedruckte Originalversion dieser Dissertation ist an der TU Wien Bibliothek verfügbar.
The approved original version of this doctoral thesis is available in print at TU Wien Bibliothek.
TU Bibliothek Your knowledge hub WIEN

show plastic zones, which increase until the end of the computation at ③, shown in Figure 4.13c. This change can also be seen in the load-displacement curve in Figure 4.12, where a plateau is reached after the steep drop between ① (21 mm displacement) and ② (23 mm displacement).

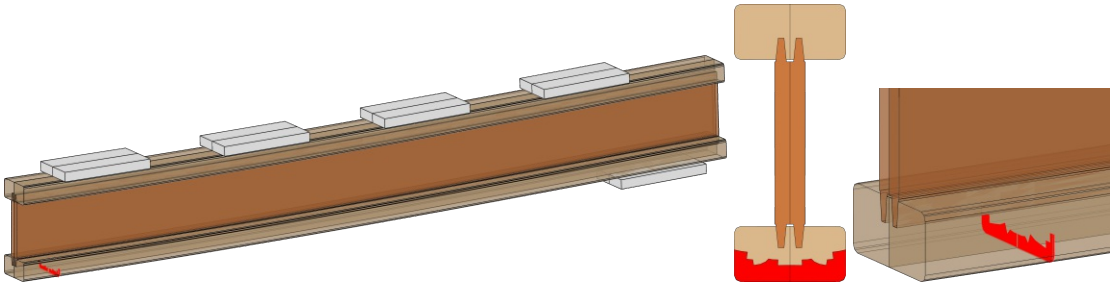

(a) Deformations, plastic zones and crack growth at ① (21 mm displacement)

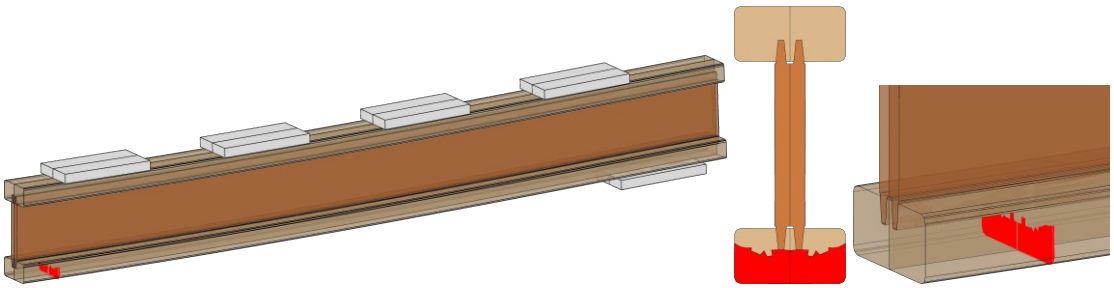

(b) Deformations, plastic zones and crack growth at ② (23 mm displacement)

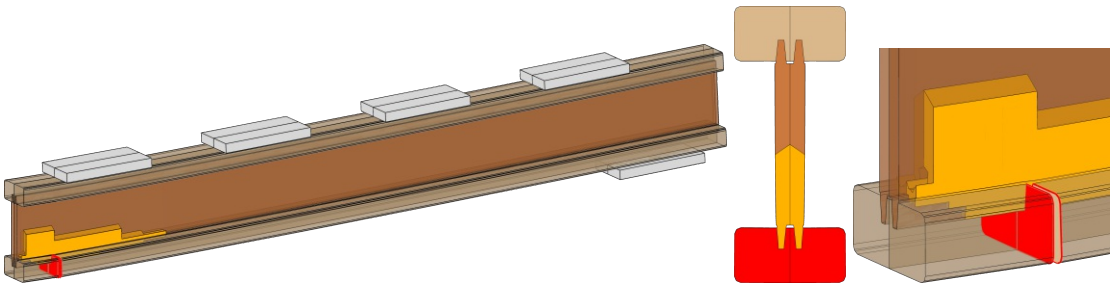

(c) Deformations, plastic zones and crack growth at ③ (32 mm displacement)

Figure 4.13: States of plastic zones in the particle board (orange) as well as crack growth (red) in the flange made of spruce at three different displacements (shown in Figure 4.12) for the bending resistance test of the dry *H20 top P* beam. In each row, the entire model is depicted on the left hand side, followed by a cross section cut at the crack location in the middle and a detail of the crack region on the right hand side.

For the wet *H20 top P* beam, the same model as in the dry computation was used, but with the reduced stiffness values for the flange and the web based on the moisture field. The failure behavior is similar to the dry beam.

Die approbierte gedruckte Originalversion dieser Dissertation ist an der TU Wien Bibliothek verfügbar.
The approved original version of this doctoral thesis is available in print at TU Wien Bibliothek.
TU Bibliothek Your knowledge hub WIEN

4.3.4 Test for shear resistance

In the following section, the results of the test for shear resistance of the two beams under different moisture conditions are presented. The *I tec pro* beam is, again, simulated under dry, moist and wet conditions, while the *H20 top P* was investigated under dry and wet conditions. Collapse is characterized by the plastic failure of the web next to the joint between the lower flange and the web. The calculation time was between 3 h and 40 h.

4.3.4.1 I tec pro

The test for shear resistance leads to high forces in the joint between the web and the flange. In the experiments, the web material plasticizes next to the joint and a relative displacement of the web and the lower flange leads to failure. The dry and the moist beam share the same geometric model, whereas the wet beam also includes a failed glue line between the aluminum profile and the flange material due to the deformations based on the moisture field, which leads to delamination at very low load levels. This behavior could also be observed during the experiments and is depicted in Figure 4.16. The maximum load capacity is reached in the simulation under dry conditions at 100.19 kN with a yield strength in the particle board of 32.5 MPa, under moist conditions a maximum capacity of 74.10 kN is obtained with a yield strength of 23.7 MPa and under wet conditions, the capacity is 46.19 kN with a yield strength of 14.6 MPa according to Table 4.2. During the experiment, the maximum load capacities were 99.75 kN in case of the dry, 71.49 kN for the moist and 43.4 kN in case of the wet beam, as shown in Figure 4.14.

Under dry conditions, the plastic zones in the web in the area of the joint is growing until the point of failure at ②, as can be seen in Figure 4.17. In Figure 4.17a, showing point ① at a displacement of 6 mm, plastic strains in the web and also the upper flange arise in the horizontal section of the beam between the top and bottom plates. At ② in Figure 4.17b, when the maximum load capacity is reached at a displacement of 9.5 mm, also the aluminum profile shows plastic zones appearing in the middle of the beam, where tensile stresses due to bending arise. After reaching the maximum load capacity, the plastic zones are growing along the joint between the web and the flange in the particle board until the end of the beam next to the support is reached at ③ at a displacement of 9.61 mm as shown in Figure 4.17c. A relative displacement of the flange and the web caused by plastic failure of the web, as can be seen in Figure 4.15, leads to a drop in the load-displacement curve between ② and ③.

In case of the moist beam, the failure mechanisms are similar to the dry beam. However, the wet beam undergoes some significant changes due to the elevated moisture level, leading to moisture-induced deformations in the spruce cross section in the flange zones. After applying the external loads, the spruce and aluminum profile show delamination and thus, the resistance of the cross section is seriously affected, as shown in Figure 4.16. In the model, this delamination effect was considered as described in Section 4.2.3.4 and able to predict the behavior of the wet beam, as can be seen in Figure 4.14. In addition to the delamination, the failure behavior is the same as described for the two other moisture states with plastic failure of the web leading to a drop in the load-displacement curve, after the maximum load capacity of 46.19 kN is reached.

Die approbierte gedruckte Originalversion dieser Dissertation ist an der TU Wien Bibliothek verfügbar.
The approved original version of this doctoral thesis is available in print at TU Wien Bibliothek.
TU Bibliothek Your knowledge hub WIEN

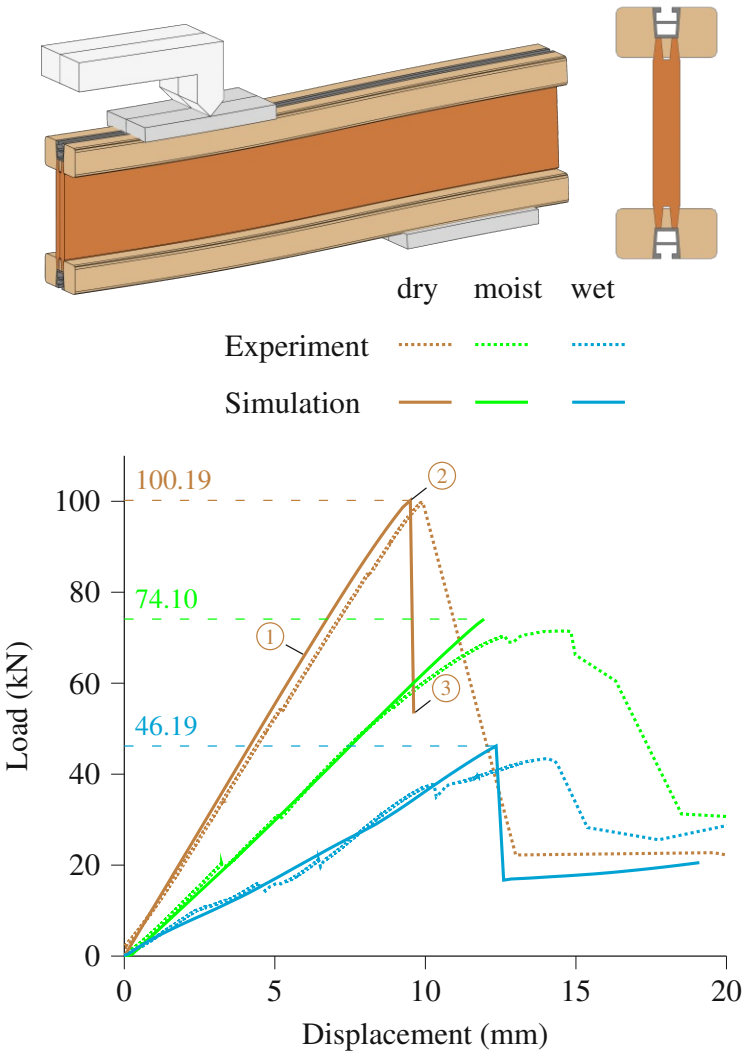

Figure 4.14: Load-displacement curves for dry, moist and wet shear resistance tests of the *I tec pro* beam. Failure is initiated by a plastic failure in the web next to the joint between the web and the lower flange, when the maximum load capacity is reached. Detailed description of the states of the different materials is shown in Figure 4.17. The top left image shows the dry simulation at ③ with a deformation scale factor of 2.

Die approbierte gedruckte Originalversion dieser Dissertation ist an der TU Wien Bibliothek verfügbar.
The approved original version of this doctoral thesis is available in print at TU Wien Bibliothek.
TU Bibliothek Your knowledge hub WIEN

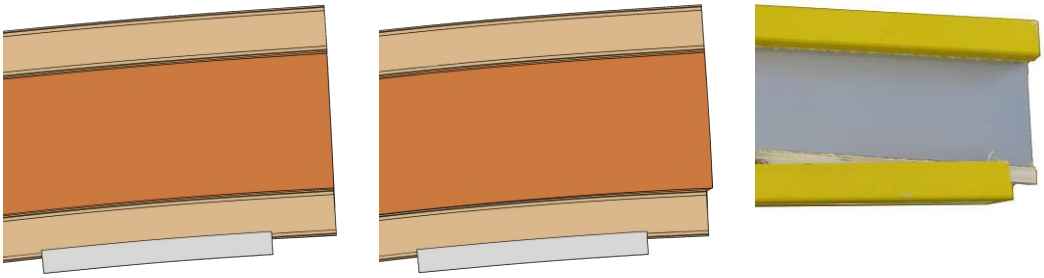

(a) Deformations before failure at ②

(b) Deformations after failure at ③

(c) Experimental failure at the end of the experiment

Figure 4.15: Modeled and experimental failure modes in case of the test for shear resistance of the dry *I tec pro* beam with a deformation scale factor of 4 at ② and ③ as shown in Figure 4.14. Failure is plastic and results in a relative displacement of the web and the flange.

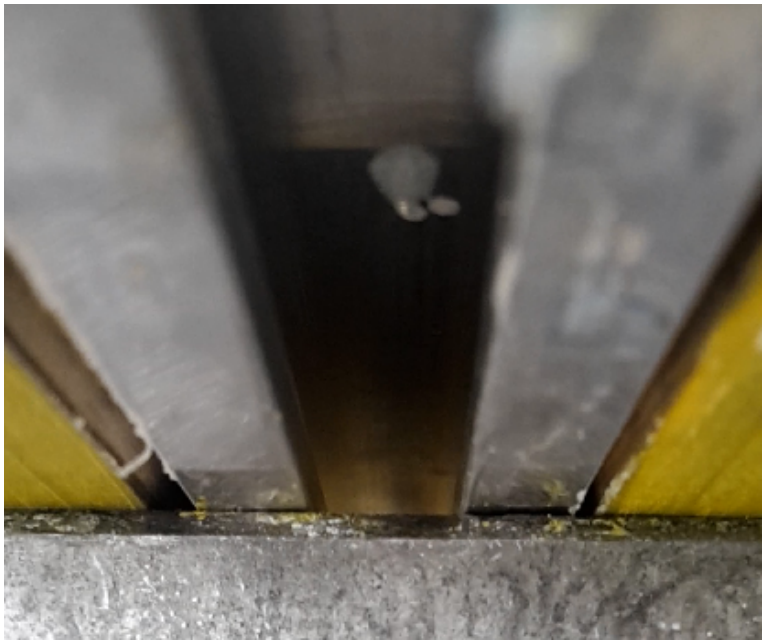

Figure 4.16: Delamination of the aluminum profile after loading in case of the wet *I tec pro* beam.

Die approbierte gedruckte Originalversion dieser Dissertation ist an der TU Wien Bibliothek verfügbar.
The approved original version of this doctoral thesis is available in print at TU Wien Bibliothek.
TU Bibliothek Your knowledge hub WIEN

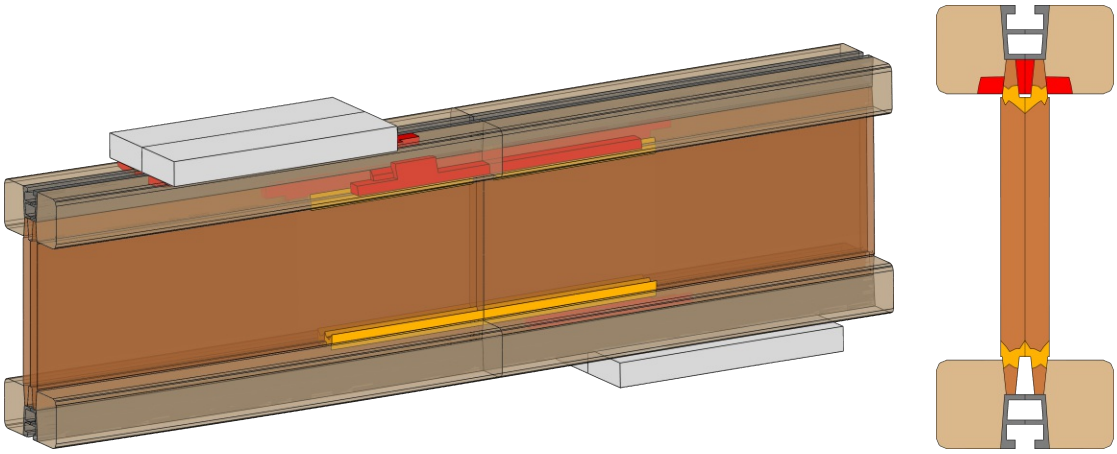

(a) Deformations and plastic zones at ① (6.0 mm displacement)

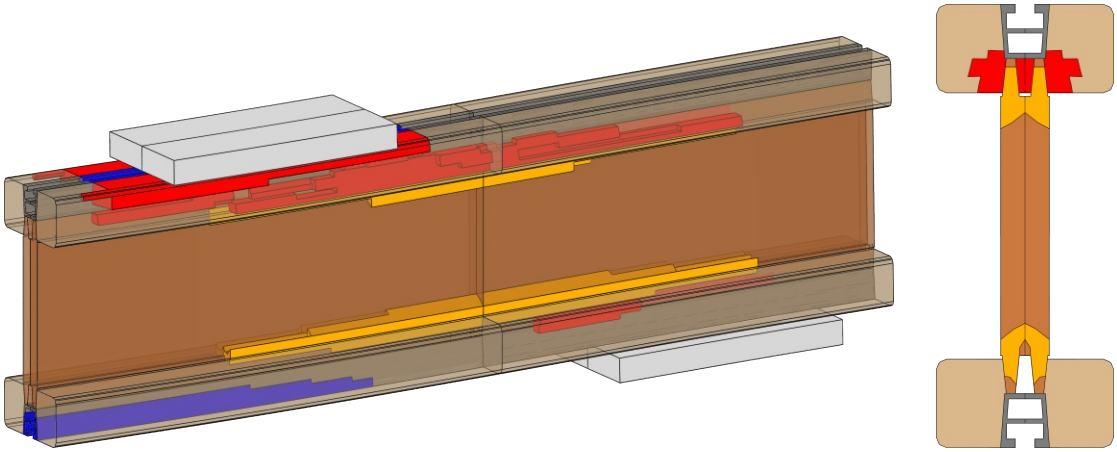

(b) Deformations and plastic zones at ② (9.5 mm displacement)

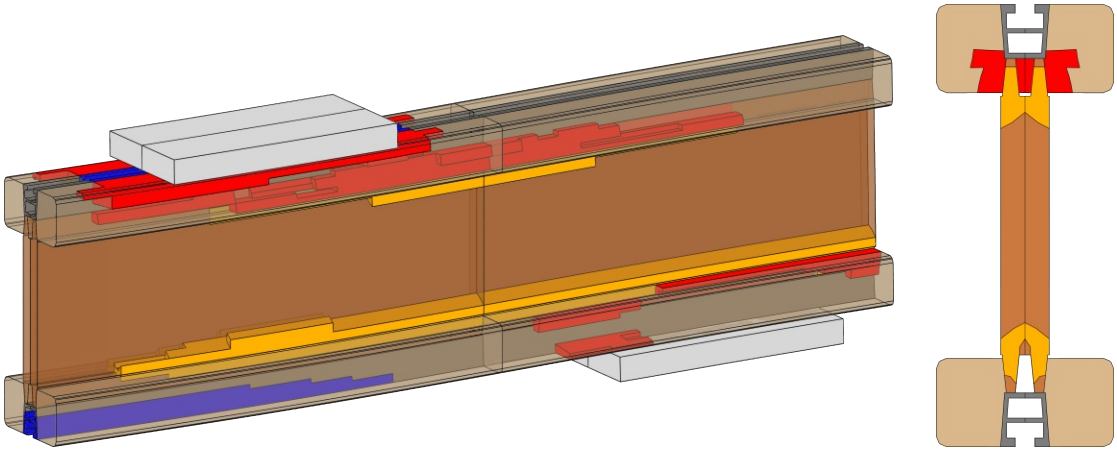

(c) Deformations and plastic zones at ③ (9.61 mm displacement)

Figure 4.17: Growth of plastic zones of the aluminum profile (blue), web (orange) and flange (red) at different displacements of the load transmission construction as shown in Figure 4.14 during the test for shear resistance of the dry *I tec pro* beam. The cross sections are located in the middle of the model.

Die approbierte gedruckte Originalversion dieser Dissertation ist an der TU Wien Bibliothek verfügbar.
The approved original version of this doctoral thesis is available in print at TU Wien Bibliothek.
TU Bibliothek Your knowledge hub WIEN

4.3.4.2 H20 top P

The *H20 top P* beam, without the aluminum profile, shows the load-displacement behavior depicted in Figure 4.18. The dry beam reaches a maximum load capacity of 78.41 kN at a displacement of 8.9 mm, whereas the computed beam reaches 90.27 kN at a displacement of 15.6 mm. The experimental and the computational failure are both plastic due to the particle board and result in a relative displacement between the web and the lower flange. This is shown in Figure 4.15 for the dry *I tec pro* beam and this is also the failure mode in case of the wet *H20 top P* beam, but with a highly reduced stiffness due to the increased moisture contents and the interaction between the flange and the web, which is defined with a friction coefficient of 0.5 in the section of the beam between the load and support plates. The wet beam in the experiment reaches a maximum load capacity of 40.47 kN at a displacement of 15 mm. The computation is able to predict the maximum load capacity with 39.8 kN at a displacement of 11.4 mm.

In Figure 4.19 the failure behavior of the dry *H20 top P* beam is shown at three characteristic steps. The plastic zones start to emerge at a displacement of 5.2 mm next to the joint of the flange and the web. They increase with ongoing displacement of the load transmission construction as can be seen in Figure 4.19a, where the load-displacement curve starts to deviate from the linear-elastic behavior at ①. The maximum load capacity is reached at a displacement of 15.6 mm at ② with large plastic zones in the flanges next to the support and the loading plate as well as in the joint between the web and the flange, as shown in Figure 4.19b. As in case of the *I tec pro* beam, the plastic zone in the web next to the joint to the lower flange further grows when the displacement is increased and the beam fails, when the plastic zone reaches the end of the beam next to the support, as shown in Figure 4.19a at ③ after the steep drop in the load-displacement curve.

For the wet beam, the stiffness is much lower in comparison to the dry beam. This can not be explained by the reduced stiffness values for the flange and web based on the moisture field alone. The investigation of different definitions of the joint between flange and web has shown that the stiffness could be reached if the joint is modeled with a contact definition with a friction coefficient of 0.5 for the region between the load and the support plates, as described in Section 4.2.3.4. The main failure mechanism is the plastic failure of the web, which leads to a relative displacement of the web and the lower flange.

Die approbierte gedruckte Originalversion dieser Dissertation ist an der TU Wien Bibliothek verfügbar.
The approved original version of this doctoral thesis is available in print at TU Wien Bibliothek.
TU Bibliothek Your knowledge hub WIEN

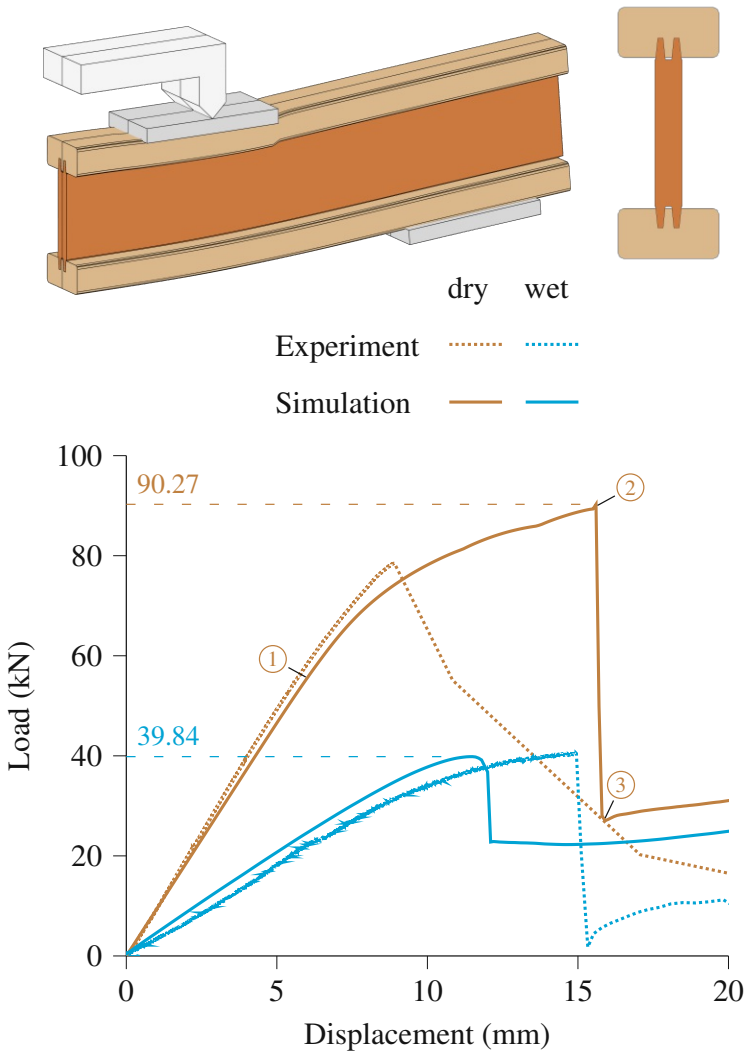

Figure 4.18: Load-displacement curves for dry and wet shear resistance tests of the *H20 top P* beam. Failure is initiated by plastic failure in the web next to the joint between the web and the lower flange, when the maximum load capacity is reached. Details of the states of the different materials are shown in Figure 4.19. The top left image shows the dry simulation at ③ with a deformation scale factor of 2.

Die approbierte gedruckte Originalversion dieser Dissertation ist an der TU Wien Bibliothek verfügbar.
The approved original version of this doctoral thesis is available in print at TU Wien Bibliothek.
TU Bibliothek Your knowledge hub WIEN

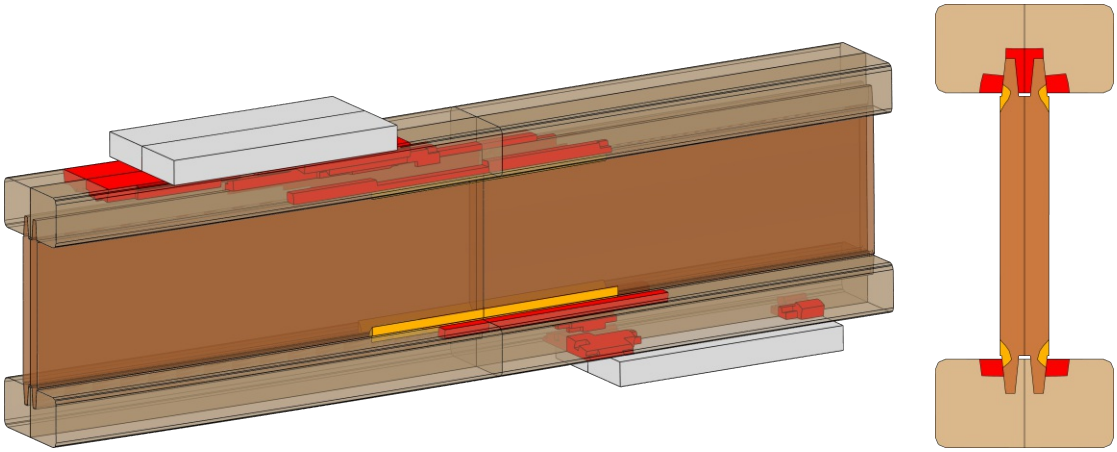

(a) Deformations and plastic zones at ① (6.0 mm displacement)

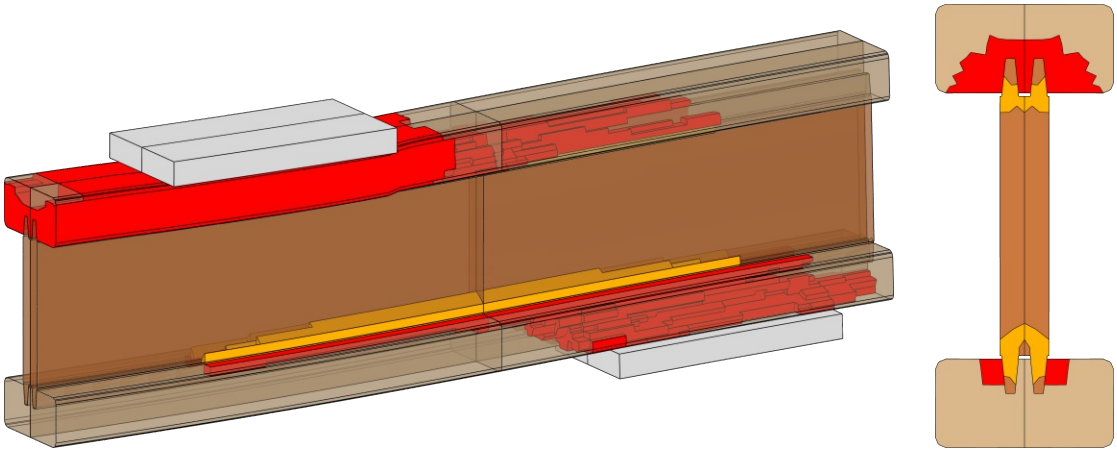

(b) Deformations and plastic zones at ② (15.6 mm displacement)

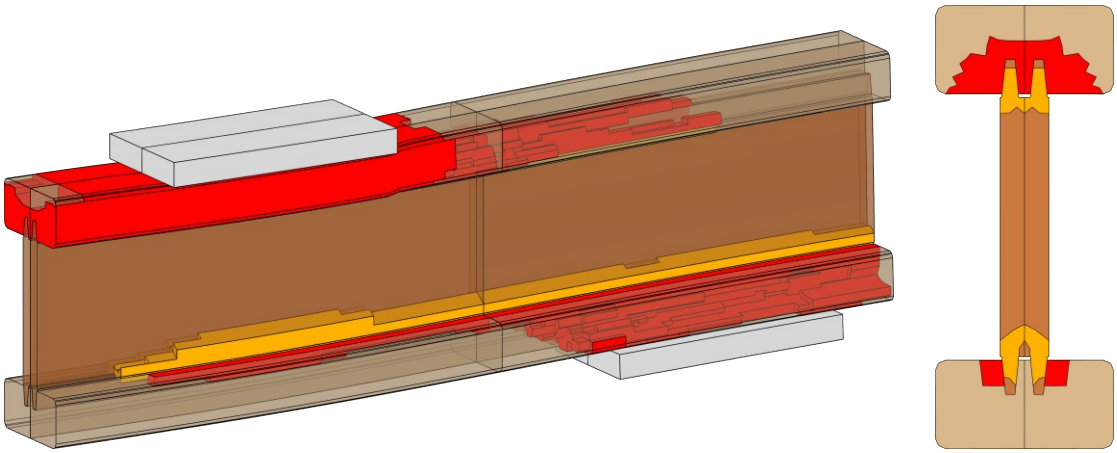

(c) Deformations and plastic zones at ③ (15.7 mm displacement)

Figure 4.19: Growth of plastic zones of the web (orange) and flange (red) at different displacements of the load transmission construction as shown in Figure 4.18 during the test for shear resistance of the dry *H20 top P* beam. The cross sections are located in the middle of the model.

Die approbierte gedruckte Originalversion dieser Dissertation ist an der TU Wien Bibliothek verfügbar.
The approved original version of this doctoral thesis is available in print at TU Wien Bibliothek.
TU Bibliothek Your knowledge hub WIEN

4.3.5 Test for bearing resistance

In this section, the results of the test for bearing resistance are presented. The *I tec pro* beam is investigated under dry, moist and wet conditions and the *H20 top P* is tested under dry and wet conditions, with the moisture fields shown in Figure 4.7. Collapse is characterized by the plastic failure of the web next to the joint between the lower flange and the web. The calculation time was between 1 day and 4 days.

4.3.5.1 I tec pro

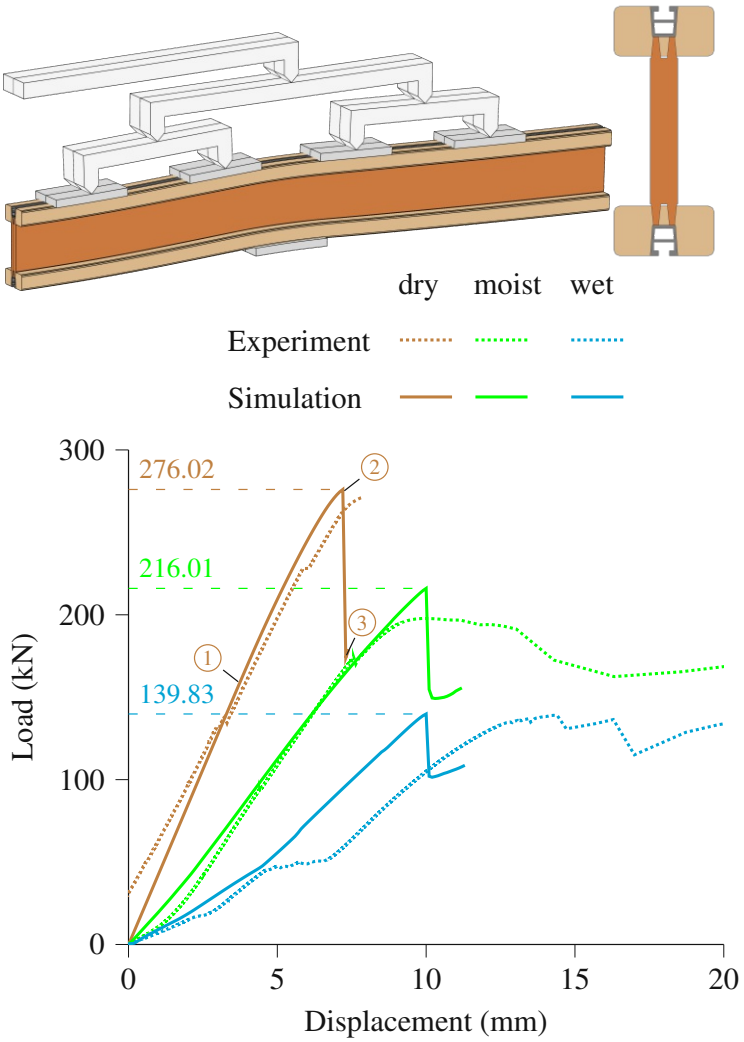

Figure 4.20: Load-displacement curves for dry, moist and wet bearing resistance tests of the *I tec pro* beam. Failure is initiated by a plastic failure in the web next to the joint between the web and the upper flange, when the maximum load capacity is reached. Detailed description of the states of the different materials is shown in Figure 4.21. The top left image shows the dry simulation at ③ with a deformation scale factor of 2.

Die approbierte gedruckte Originalversion dieser Dissertation ist an der TU Wien Bibliothek verfügbar.
The approved original version of this doctoral thesis is available in print at TU Wien Bibliothek.
TU Bibliothek Your knowledge hub WIEN

The load-displacement curves begin with a linear-elastic region and end with failure at ②, as can be seen in Figure 4.20. The dry *I tec pro* reaches the maximum load capacity of 276 kN at 7.2 mm. In case of the moist beam the maximum load capacity is 216 kN at a displacement of 10 mm and the wet beam fails at 139.8 kN and also 10 mm. The maximum load capacities are in good agreement with the experimental values, which are 271.1 kN for the dry, 197.8 kN for the moist and 139 kN for the wet beam. During the wetting process of the wet beam, non-uniform swelling of the spruce parts occur. As a result, the aluminum profile is not in contact with the support plate at the start of loading. Load application moves the aluminum profile back towards the support plate until the aluminum profile is back in contact with the support plate at a displacement of approximately 4.6 mm and after which stiffness increases. At this point, also delamination, as shown in Figure 4.16, occurs, which is considered during the simulation with contact in normal direction and frictionless in tangential direction between the aluminum profile and the spruce as well as a friction coefficient of 0.5 instead of the tie condition between the web and the aluminum profile, as described in Section 4.2.3.4.

In case of the dry beam, after the linear-elastic region, first, the flange starts to plasticize at 2.6 mm. Shortly after that, at 3.5 mm, the web and at 3.7 mm also the aluminum profile show plastic zones, as depicted in Figure 4.21a at ① in the region of the support, where the largest vertical loads are to be expected. At the point of failure at ② (7.2 mm displacement), large parts of the spruce and the aluminum profile in both flanges as well as the web show plastic zones next to the support, as can be seen in Figure 4.21b. While the plastic zones in the lower flange occur because of vertical loads, in the upper flange also tension due to the negative bending moment can be observed. The forces are transferred from the load plate via the aluminum profile to the web and further via the aluminum profile into the load plate, as can be seen from the depicted plastic zones in the cross sections. At ③ (73 mm displacement) the plastic zones in the web next to the finger joint between the upper flange and the web are growing rapidly towards the middle of the beam, which leads to the drop in the load-displacement curve, as can be seen when comparing Figure 4.21b at ② with Figure 4.21c at ③.

For the moist beam the same model as for the dry one was used, but with a reduced stiffness for the spruce in the flanges and the particle board in the web. The strength for the moist web was reduced from 32.5 MPa in case of the dry beam to 23.7 MPa according to Table 4.2. The main failure mechanism in the joint between web and flange, is similar as observed for the dry beam.

In case of the wet beam, the moisture field leads to a deformation of the cross section, as previously described, with only the top and bottom edges of the spruce touching the load and support plates, respectively. After 4.6 mm of displacement, the beam is compressed thus far that the aluminum profile touches the load plates and forces can be transferred directly into the support plate. This point is marked with the mentioned kink in the load-displacement curve in Figure 4.20. In addition to the different moisture field, also the interaction between the aluminum profile and the surrounding materials was changed, as described in Section 4.2.3.4. In the particle board the maximum stress for the failure mechanism was reduced to 14.6 MPa, as in the previous examples. To

Die approbierte gedruckte Originalversion dieser Dissertation ist an der TU Wien Bibliothek verfügbar.
The approved original version of this doctoral thesis is available in print at TU Wien Bibliothek.
TU Bibliothek Your knowledge hub WIEN

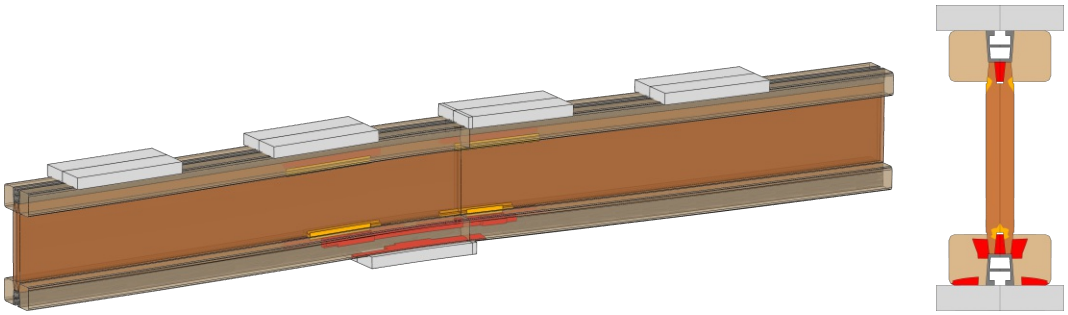

(a) Deformations and plastic zones at ① (3.7 mm displacement)

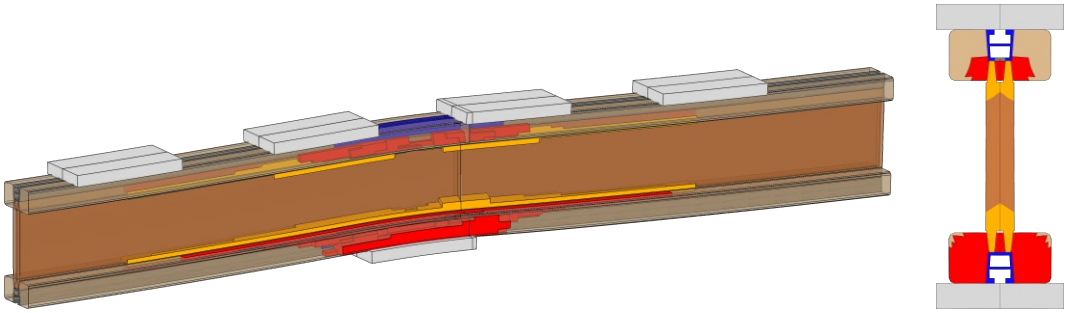

(b) Deformations and plastic zones at ② (7.2 mm displacement)

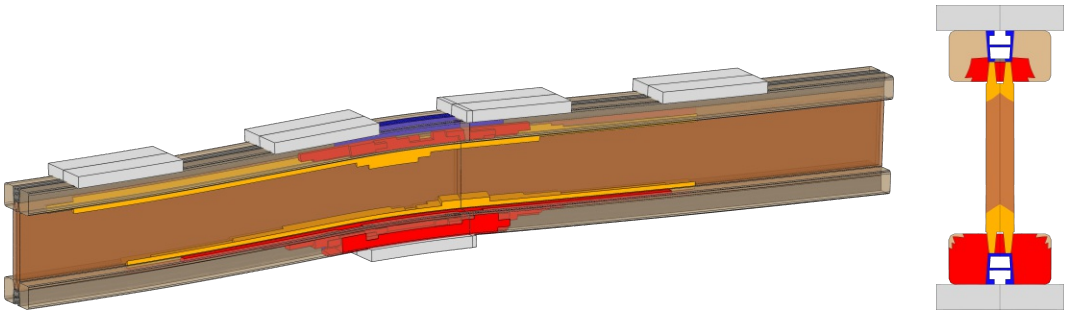

(c) Deformations and plastic zones at ③ (7.3 mm displacement)

Figure 4.21: Growth of plastic zones of the aluminum profile (blue), web (orange) and flange (red) at different displacements of the load transmission construction as shown in Figure 4.20 during the test for bearing resistance of the dry *I tec pro* beam. The cross sections are located next to the end of the support plate.

account for the different plastic behavior of moist wood, the plastic yield stress was reduced by 50 % according to Section 4.2.3.1. The resulting failure mechanism is then similar to the dry and moist computation.

Die approbierte gedruckte Originalversion dieser Dissertation ist an der TU Wien Bibliothek verfügbar.
The approved original version of this doctoral thesis is available in print at TU Wien Bibliothek.
TU Bibliothek Your knowledge hub WIEN

4.3.5.2 H20 top P

In case of the *H20 top P* beam, the low stiffness of wood perpendicular to the grain direction reduces the overall stiffness of the beam in comparison to the *I tec pro*, where the load was transferred via the, in comparison stiffer, aluminum profiles. The maximum load capacity in case of the dry simulation is reached with 140 kN at a displacement of 15.9 mm and in case of the wet beam 84.92 kN at 45.6 mm, as shown in Figure 4.22. While the dry beam shows a drop in the load-displacement curve at 25.3 mm, the wet beam exhibits a yield plateau until failure occurs. The experimental results show a plateau beginning after a first peak with a load capacity of 116.7 kN at a displacement of 7.3 mm and reach the highest values at 129 kN at a displacement of 27.6 mm in the dry case. The wet experiment shows a very good agreement to the computations until 30 mm of displacement and reaches the maximum load capacity after an increase after 30 mm at 106.8 kN at a displacement of 38.8 mm.

The load-displacement curves of the dry beam show a decrease in stiffness as the spruce in the lower flange starts to plasticize at a displacement of about 1.1 mm until at ① (8.5 mm displacement) nearly the whole cross section of the lower flange shows plastic behavior in the region around the support plate, as can be seen in Figure 4.23a. Also a crack starts to emerge in the upper flange together with plastic regions next to the load plates. At ② (15.9 mm displacement) the maximum load capacity of 140 kN is reached. The web shows plastic zones only in the joint above the support and the crack has further increased, as can be seen in Figure 4.23b. The upper flange is fully cracked at ③ at a displacement of 16.1 mm, leading to a drop in the load-displacement curve. Plastic zones are now also showing up in the web next to the crack, as depicted in Figure 4.23c. The load capacity increases slightly after the drop and reaches 90.43 kN at ④ (20.7 mm displacement) while the plastic zones in the web increase and stay constant in the web, as shown in Figure 4.23d. At ⑤ at a displacement of 23.7 mm the plastic regions in the web cover nearly the full height, while those of the flanges stay about the same (see Figure 4.23e).

In case of the wet beam the stiffness is smaller due to the reduced stiffness of the spruce in the flange and the web. Also the joint between the flange and the web is modeled with contact and friction properties instead of a tie constraint. After a short sequence of linear-elastic behavior, the web starts to plasticize and also the spruce shows plastic behavior next to the support, as can be seen in Figure 4.24a at ① (9.6 mm displacement). Further increase of the displacement of the load transmission construction leads to extending plastic zones in both materials around the support. After ②, at a displacement of 25.6 mm with the plastic zones depicted in Figure 4.24b, the load level is only slightly increasing. The web now also shows large plastic zones in the area of the support. This plastic behavior continues until ③, where the maximum load capacity is reached at a displacement of 45.6 mm with 84.92 kN. The corresponding plastic zones (shown in Figure 4.24c) are now enlarged, especially in the web in the area around the support, where almost a plastic hinge is established. Also the lower flange is moving away from the rest of the cross section at the free end of the beam, which is only connected by frictionless contact to the rest of the beam. At ④, the plastic hinge is fully established, as can be seen in Figure 4.24d at a displacement of 50.6 mm.

Die approbierte gedruckte Originalversion dieser Dissertation ist an der TU Wien Bibliothek verfügbar.
The approved original version of this doctoral thesis is available in print at TU Wien Bibliothek.
TU Bibliothek Your knowledge hub WIEN

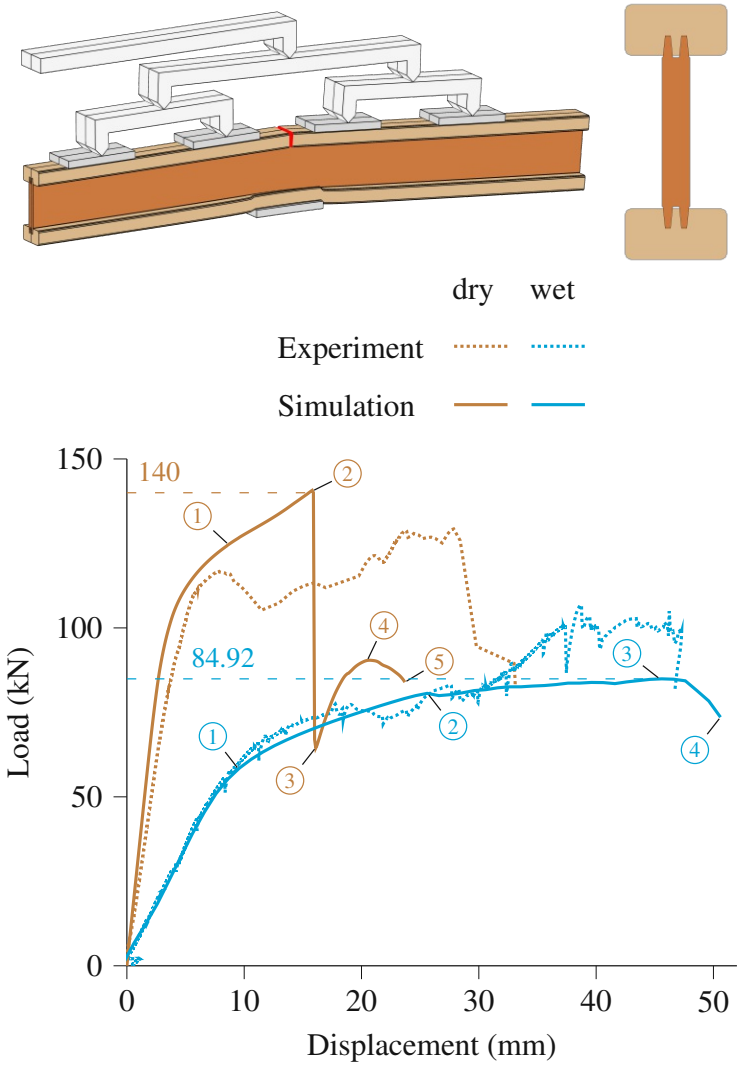

Figure 4.22: Load-displacement curves for dry and wet bearing resistance tests of the *H20 top P* beam. Failure is initiated by a plastic failure in the web next to the joint between the web and the lower flange, when the maximum load capacity is reached. Detailed description of the states of the different materials is shown in Figure 4.23 and Figure 4.24, respectively. The top left image shows the dry simulation at ⑤ with a deformation scale factor of 1.

Die approbierte gedruckte Originalversion dieser Dissertation ist an der TU Wien Bibliothek verfügbar.
The approved original version of this doctoral thesis is available in print at TU Wien Bibliothek.
TU Bibliothek Your knowledge hub WIEN

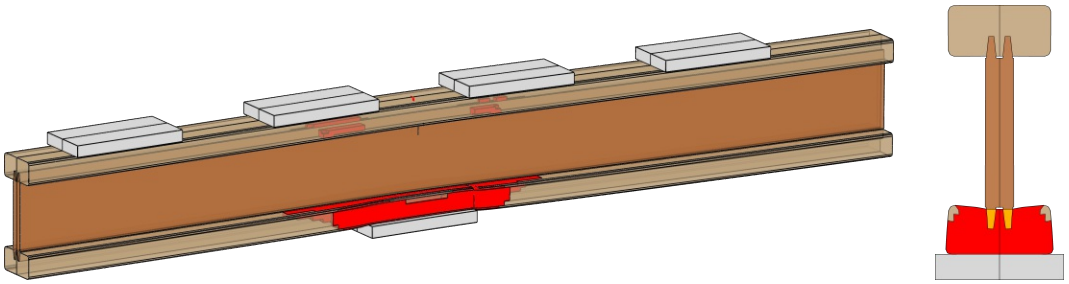

(a) Deformations and plastic zones at ① (8.5 mm displacement)

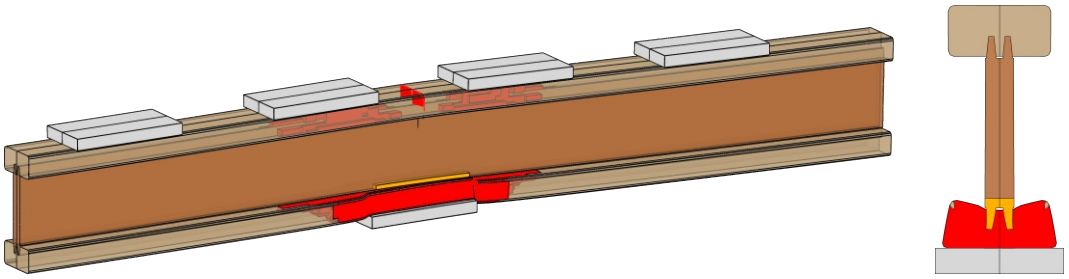

(b) Deformations and plastic zones at ② (15.9 mm displacement)

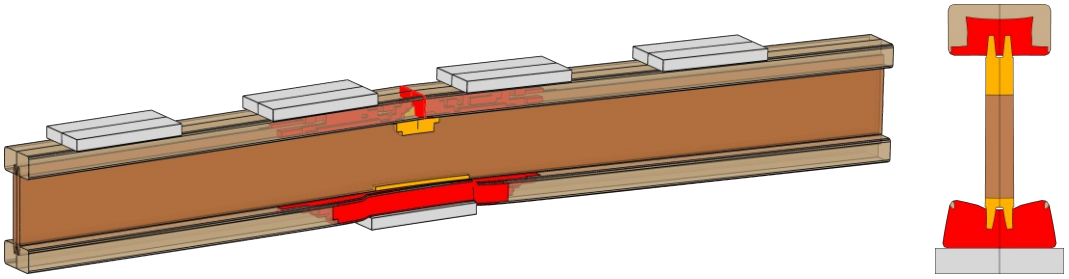

(c) Deformations and plastic zones at ③ (16.1 mm displacement)

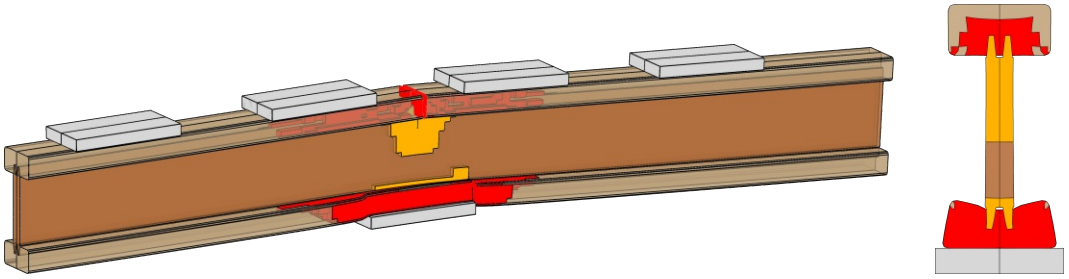

(d) Deformations and plastic zones at ④ (20.7 mm displacement)

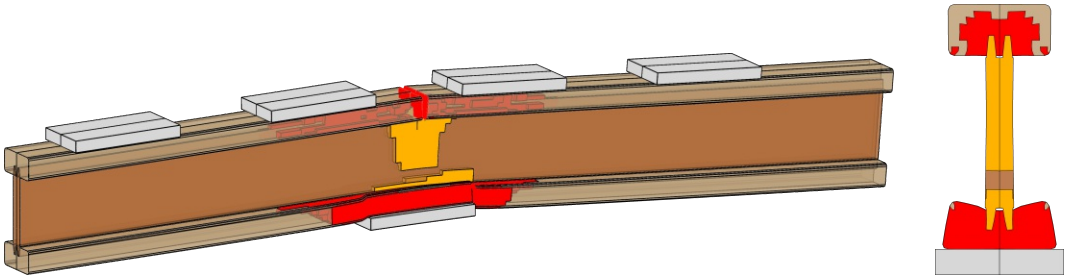

(e) Deformations and plastic zones at ⑤ (23.7 mm displacement)

Figure 4.23: Growth of plastic zones of the web (orange) and flange (red) at different displacements of the load transmission construction as shown in Figure 4.22 during the test for bearing resistance of the dry *H20 top P* beam. A crack emerges in the upper flange in the region of the support. The cross sections are located in the middle of the support plate, next to the crack location.

Die approbierte gedruckte Originalversion dieser Dissertation ist an der TU Wien Bibliothek verfügbar.
The approved original version of this doctoral thesis is available in print at TU Wien Bibliothek.
TU Bibliothek Your knowledge hub WIEN

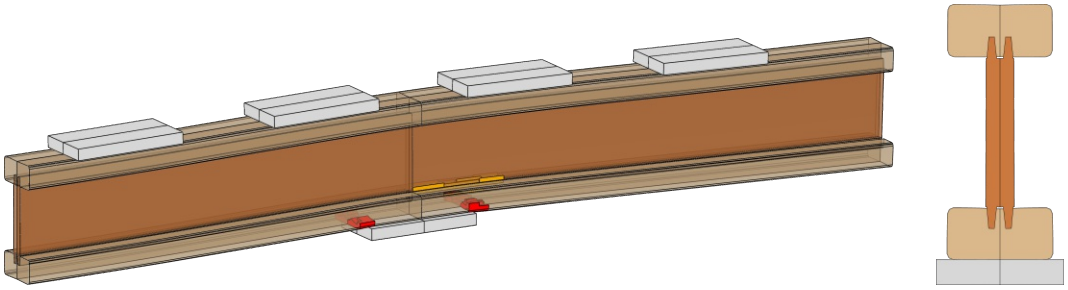

(a) Deformations and plastic zones at ① (9.6 mm displacement)

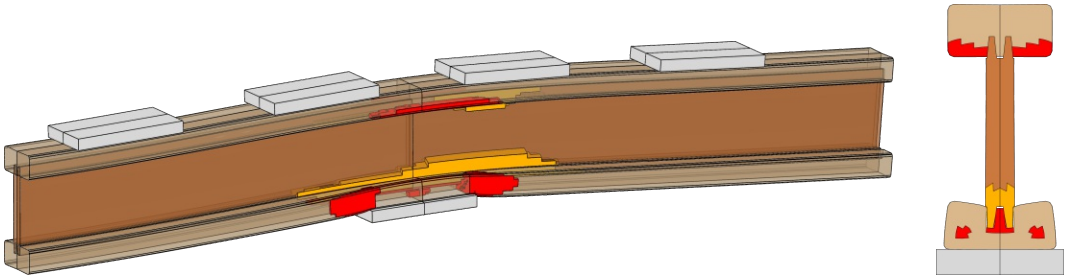

(b) Deformations and plastic zones at ② (25.6 mm displacement)

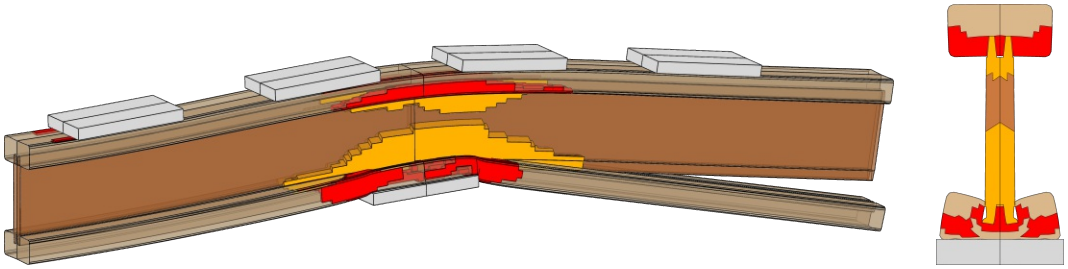

(c) Deformations and plastic zones at ③ (45.6 mm displacement)

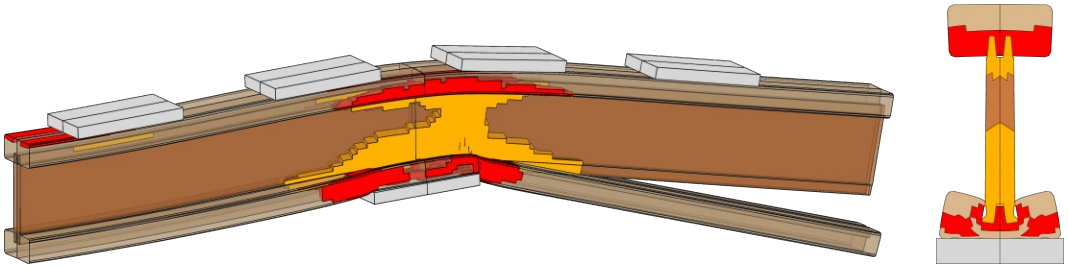

(d) Deformations and plastic zones at ④ (50.6 mm displacement)

Figure 4.24: Growth of plastic zones of the web (orange) and flange (red) at different displacements of the load transmission construction as shown in Figure 4.22 during the test for bearing resistance of the wet *H20 top P* beam. The cross sections are located in the middle of the support plate.

Die approbierte gedruckte Originalversion dieser Dissertation ist an der TU Wien Bibliothek verfügbar.
The approved original version of this doctoral thesis is available in print at TU Wien Bibliothek.
TU Bibliothek Your knowledge hub WIEN

4.4 Discussion

The moisture field simulations, shown in Figure 4.7, gave good results compared to the experimentally determined moisture fields. In the web, no experimental data was available and the values had to be calibrated. The decrease of the moisture-dependent stiffness parameters of the web and flange could well describe the overall stiffness of the investigated beams in the three different test setups. In case of the wet test for bearing resistance of the *I tec pro* beam, the point at about 4.6 mm of displacement, where the aluminum profile gets back in contact with the support plate and the stiffness increases, could be reproduced.

In Figure 4.25, the experimental and numerical results of all investigated beams are shown using box and whisker plots. As can be seen, the chosen sets of material parameters and geometric conditions are able to predict the experimental results in a very good manner for all the 15 different settings. During the experiments, the finger joints in the flange and also the web have to be placed in the critical sections. To account for this, the strength values for spruce during the simulation for bending resistance and for the web were adjusted accordingly. In case of the test for bearing resistance of the wet *H20 top P* beam, the results are slightly off the experimental ranges. However, as can be seen from Figure 4.22, the load-displacement curve can be reproduced in a very good way up to 30 mm of displacement. In the last section of the experiment, the beam shows a slight increase in the load capacity, which could not be reproduced in the simulations and, thus, the shown results depict smaller values than observed during the experiments.

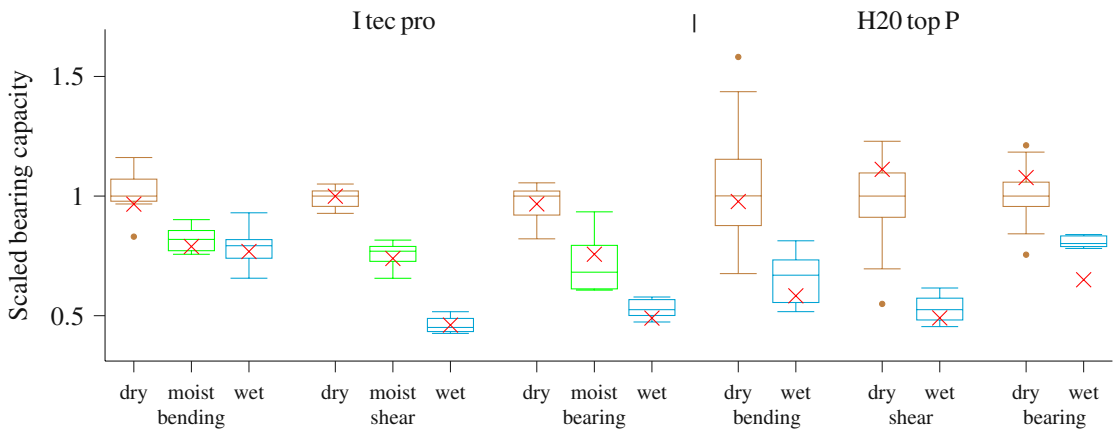

Figure 4.25: Comparison of maximum, median and minimum load bearing capacities from experimental tests with the results from the computations (marked with a red x). In case of the *I tec pro* ten beams for each moisture state were experimentally tested and in case of the *H20 top P* beam 56 samples for the bending and bearing as well as 61 beams for the shear resistance test were analyzed for dry conditions and six beams each for wet conditions. The values are scaled to the median of the respective dry experiments.

Die approbierte gedruckte Originalversion dieser Dissertation ist an der TU Wien Bibliothek verfügbar.
The approved original version of this doctoral thesis is available in print at TU Wien Bibliothek.

Comparing the *I tec pro* with the *H20 top P* beam during the test for bending resistance, both beams show the same failure characteristics, which are based on exceeding the longitudinal tensile strength of wood. The aluminum profile of the *I tec pro* leads to a larger stiffness in the linear-elastic region. For the *I tec pro* beam, the results under moist and wet conditions differ only slightly, compared to the dry beam, as shown in Figure 4.8. This is caused by the moisture fields, which show similar MC values in the zone close to the boundary, where the crack initiates, according to Figure 4.7. This is also the reason why the stiffness tensor for the web from Table 4.2 under moist and wet conditions was chosen to be equal. Experimentally, the moist and wet beams show failure in the finger joints in the area of the flange, according to Figure 4.11, which is accounted for with a reduction in tensile strength for spruce. Also, only in case of the dry beam, the aluminum profile showed cracks.

The test for shear resistance was used to calibrate the yield criterion of the particle board in the web, which was then also used in all other simulations. The chosen strength was able to predict the failure modes of the test for shear and bearing resistance. While the moist model used the same geometry as the dry version, for the wet beam, additional adjustments to reach the stiffness of the experimental beam had to be made. Since the wet beam shows a delamination behavior between the aluminum profile and the web, when an external load is applied, as shown in Figure 4.16, this was incorporated by removing the tied interaction between these two materials in the region between the load and support plate. In the region, where the web and the aluminum profile adjoin each other, a friction coefficient of 0.5 was introduced based on a parameter study. With this adjustment, the stiffness could be well reproduced, as can be seen in Figure 4.14. This concept was also used in case of the wet *H20 top P*, where contact in normal direction and the friction coefficient in tangential direction were included between the web and the flange, leading again to good results, as shown in Figure 4.18.

The stiffness in the linear-elastic region of the dry test for bearing resistance of the two investigated beams show a very similar behavior. This changes in case of the *H20 top P* at about 100 kN of loading, as the wooden flange starts to show plastic behavior, as the wood gets compressed due to the perpendicular to the grain loading. This effect is much smaller in case of the *I tec pro* beam, since the forces get transferred from the particle board via the aluminum profile into the support plate, thus the failure mode of this beam shows less plastic behavior, as can be seen when comparing Figure 4.20 with Figure 4.22. While for the moist simulation the dry model was used, for the wet beams the previously described adjustments from the test for shear resistance were also made, but in this case not only in a specific section of the beam, instead the interaction between the aluminum profile and the flange, respective between the web and the aluminum profile, were applied to the whole beam. Thus, the models were able to predict the stiffness and maximum load capacity of the wet beams, as can be seen from Figures 4.20 and 4.22, respectively.

Die approbierte gedruckte Originalversion dieser Dissertation ist an der TU Wien Bibliothek verfügbar.
The approved original version of this doctoral thesis is available in print at TU Wien Bibliothek.
TU Bibliothek Your knowledge hub WIEN

4.5 Conclusion & Outlook

When developing a new wood composite beam, various experiments must be performed, which are complex and time consuming. In case of prefabricated timber formwork beams these experiments are defined in EN 13377. In addition to a test under dry conditions, also different moisture states must be considered to evaluate the behavior of the beams. In this work, a numerical concept is proposed, able to support this complex experimental program and to significantly reduce it in the medium term. Moisture fields are determined based on a hygrothermal multi-Fickian transport model, which includes heat and mass transfer within spruce, particle board and also aluminum. The interactions between these materials were also taken into account. In a second step, different resistance tests, as specified in EN 13377, were performed numerically. Different failure mechanisms, in some cases also dependent on the moisture state, could be described appropriately. Especially in case of wet beams, which were exposed for 60 d to a climate of 100 % relative humidity, the delamination between the aluminum profile and the wooden flange showing up during the loading process, which is crucial for the beam stiffness under such conditions, could be simulated realistically. The main findings are emphasized as follows:

- By means of the determined moisture fields, the stiffness decrease and the deformations of the cross sections, as well as the moisture-related delamination effects in case of the tests for shear and bearing resistance could be predicted accurately.
- The stiffness and maximum load capacity of the two wood composite beams could be estimated in a very good manner for all three test setups.
- The failure modes could be predicted, both brittle modes by using the extended finite element method (XFEM) and plastic effects in the area of the joint between the flange and the web by simulating plastic flow.
- With the proposed methods, concepts and the few calibrated parameters it is possible to numerically evaluate wood composite beams according to EN 13377 under different moisture conditions,
- and, thus, the approach is able to complement the experimental tests in order to further improve the beam geometries as well as to include new materials under various climatic conditions.

Conflict of interest

None declared.

Acknowledgments

The funding from the Doka GmbH and the Austrian Research Promotion Agency (FFG, Project Number 857041) is gratefully acknowledged.

Die approbierte gedruckte Originalversion dieser Dissertation ist an der TU Wien Bibliothek verfügbar.
The approved original version of this doctoral thesis is available in print at TU Wien Bibliothek.
TU Bibliothek Your knowledge hub WIEN

Appendix

4.A Constitutive equations and material parameters

Table 4.A.1: Constitutive equations and material parameters used in the model.

Property	Value/Expression	Ref.
Spruce dry density	$\rho_{d,sp} = 405\,\mathrm{kg\,m^{-3}}$	
Particle board dry density () (spruce fibers)	$\rho_{d,pb} = 797\,\mathrm{kg\,m^{-3}}$	
Moisture content	$X = \frac{c_b}{\rho_d}$	
Bound water diffusion tensor	$\boldsymbol{D_b} = \boldsymbol{D_0}\,\exp\left(\frac{-E_b}{RT}\right)$	[47]
Bound water diffusion tensor (Soret Effect)	$\boldsymbol{D_{bT}} = \boldsymbol{D_0}\,\frac{c_b\,E_b}{RT^2}\,\exp\left(\frac{-E_b}{RT}\right)$	[47]
Activation energy of bound water	$E_b = 38500 - 29000\,X$	[35]
Universal gas constant	$R = 8.314\,\mathrm{J\,mol^{-1}\,K^{-1}}$	
Water vapor diffusion tensor	$\boldsymbol{D_v} = \boldsymbol{\xi}\left(2.31\cdot10^{-5}\,\frac{p_{atm}}{p_{atm}+p_{v_{air}}}\,\left(\frac{T}{273}\right)^{1.81}\right)$	[9, 10, 48]
Water vapor pressure	$p_{v_{air}} = c_v\,\frac{RT}{M_{H_2O}}$	
Molar mass of water	$M_{H_2O} = 18.015\,\mathrm{g\,mol^{-1}}$	
Moist density of wood	$\rho_{moist} = \rho_d\,\frac{1+X}{1+0.84\,c_b}$	[53]
Volume proportion of the cell lumen	$f_{lum} = 1 - \frac{\rho_{moist}}{\rho_{cwm}}$	
Density (pure cell wall)	$\rho_{cwm} = 1530\,\mathrm{kg\,m^{-3}}$	[11, 35]
Spruce conduction tensor	$\boldsymbol{K} = \boldsymbol{K_0}\,(0.142 + 0.46\,X)$	[15]
Heat capacity (pure cell wall)	$c_{p_s} = -0.60453 + 0.006714\,T$	[54]
Enthalpy of water vapor	$h_v = 2060.5 + 1.3798\,T + 0.84808\cdot10^{-4}\,T^2$	[49]
Specific enthalpy of bound water	$h_b = 4.185\,(T - 273.15\,\mathrm{K}) - 1146.4\,\exp\left(-14.48\,X\right)$	[49, 55]
Average enthalpy of bound water	$\overline{h}_b = -1143.1 + 4.185\,T - \frac{79.172\,\rho_d\,(1-\exp(-14.48\,X))}{c_b}$	[23, 24, 49]

The reference state for the expressions to determine the thermodynamic properties for specific isobaric heat capacities c_p and enthalpies h is set to 273.15 K and 101,325 Pa.

Table 4.A.2: Diagonal components of the material parameter tensors. For the particle board the components 1 and 3 are the in-plane directions and 2 is the perpendicular-to-the-plane direction

Parameter	Component L/1	Component R/2	Component T/3	Ref.
Spruce $\boldsymbol{D_0}$	$2.5\cdot7\cdot10^{-6}$	$7\cdot10^{-6}$	$7\cdot10^{-6}$	[12]
Spruce $\boldsymbol{\xi}$	0.98	0.07	0.05	[11]
Spruce $\boldsymbol{K_0}$	2	1	1	[63]
Particle board $\boldsymbol{D_0}$	$1.875\cdot7\cdot10^{-6}$	$7\cdot10^{-6}$	$1.875\cdot7\cdot10^{-6}$	
Particle board $\boldsymbol{\xi}$	0.3	0.02	0.3	
Particle board $\boldsymbol{K}$	0.167	0.167	0.167	[91]

Die approbierte gedruckte Originalversion dieser Dissertation ist an der TU Wien Bibliothek verfügbar.
The approved original version of this doctoral thesis is available in print at TU Wien Bibliothek.
TU Bibliothek Your knowledge hub WIEN

Conclusions and Outlook

The key findings of Publications 1-4 are presented below, followed by suggestions for possible next steps in future research studies.

Key Findings

In **Publication 1**, the existing multi-Fickian transport model for moisture contents (MCs) in wood below the fiber saturation point (FSP) is extended for conditions above with the introduction of an additional transport equation for free water and the corresponding interaction terms. Based on the existing description of the sorption rate, a new time-dependent evaporation/ condensation rate was developed and validated by several examples from the literature (experiments and simulations). In addition to several experiments, different mesh sizes and the sensitivity of newly introduced parameters were also tested, resulting in a reliable tool to describe the drying process of wood from the green state far above the FSP very well. The wet-bulb temperature, characteristic for the drying process, could also be predicted. Reliable results could also be determined for the reverse case of infiltration, but further experimental studies on the infiltration behavior of wood need to be conducted to determine the appropriate material parameters. Since the model is implemented in the finite element software *Abaqus*, the resulting MC fields can easily be used for accompanying mechanical simulations.

In **Publication 2** and **Publication 3**, the moisture transport model for wood presented in Publication 1 was used to analyze the climatic behavior of 18 cross sections of different sizes at the location of Linz, Austria, during the time span from November 1, 2014, to January 1, 2016. While in Publication 2 the focus lies on the resulting 2D MC fields during this time span, in Publication 3 the emphasis is placed on the resulting mechanical behavior and possible cracking mechanisms.

In **Publication 2**, the results are compared with respect to the MC. In the European standard Eurocode 5 moisture-induced stresses are currently not directly considered, as stated in [68], and the categorization for the effect of the surrounding conditions (service classes) is independent of the dimensions of the cross sections. A categorization based on MC averaged over the cross section to account for cross-sectional dimensions and a relation based on area to perimeter ratio is established. For larger cross sections (wider than 20 cm), a method for determining 2D MC fields solely on the relative humidity of ambient conditions is also developed to allow moisture-induced stresses and moisture-dependent elasticity tensors to be considered in mechanical calculations for more detailed and improved design of wooden structures.

Die approbierte gedruckte Originalversion dieser Dissertation ist an der TU Wien Bibliothek verfügbar.
The approved original version of this doctoral thesis is available in print at TU Wien Bibliothek.
TU Bibliothek Your knowledge hub WIEN

In **Publication 3**, critical points in time were determined by evaluating a multisurface failure criterion with respect to brittle failure in the integration points. Each integration point represents a partial volume of an element and the sum of this volumes over the model leads to a newly developed "crack-prone volume". The development of this sum over time can then be used to define critical points in time. Simulations with the extended finite element method at these critical points in time resulted in crack patterns for certain cross sections with lengths dependent on the cross-sectional size, as also assumed by the European standard for timber structures Eurocode 5. However, this standard only considers cracks during the drying period, whereas the simulations performed in Publication 3 also showed cracks inside the cross sections during the wetting period. In glued laminated timber cross sections, cracks were also observed next to glue lines, which can lead to delamination.

In **Publication 4**, the moisture transport model is applied to three-dimensional formwork beam structures to numerically predict the load-deflection behavior of bending, shear and bearing resistance tests of EN 13377 including failure. The beams are of I-shape and consist of spruce in the flanges (one beam also contains an additional aluminum profile in this area) and a web made of a special particle board. These tests are computed under dry, moist and wet conditions and the stiffness, maximum load capacities as well as failure mechanisms could be well reproduced with the same set of material parameters for both investigated beam-types in all three test setups within one MC level. While brittle failure occurs during bending, plastic effects are more pronounced during shear and bearing resistance tests, with the joint between the flange and web of the I-beams playing a key role in particular. With the proposed numerical simulation model, it is possible to accompany and reduce the expensive and time-consuming experiments for newly developed or improved beams.

Perspectives and Future Research Studies

As the numerical model for moisture transport in wood from **Publication 1** was developed for temperature levels between 0 and 50°C, possible extensions could be outside this range by including, for example, freezing of free water as well as higher temperatures, which would also include the dry air transport equation to account for changes in pressure within the wood sample and convective mass transport, which becomes significant at such conditions. For the case of infiltration, a better understanding of the behavior when the wood is in contact with water needs to be found to simulate the high MC values next to the boundary and also the boundary conditions when in contact with free water.

The methods presented in **Publication 2** and **Publication 3** are only applied to the location of Linz, Austria, and the year 2015. In a next step, these models should be applied to different locations in a region or country to get a realistic impression of the influence of the surrounding climate on timber structures. This could also discover similarities between different sites in a climatic region. The cracks observed inside the cross sections occur during the wetting period, which is characterized by higher MC values for longer periods (several months). Under such conditions, the long-term behavior of wood should also be considered. Thus, especially for cracks inside the

Die approbierte gedruckte Originalversion dieser Dissertation ist an der TU Wien Bibliothek verfügbar.
The approved original version of this doctoral thesis is available in print at TU Wien Bibliothek.
TU Bibliothek Your knowledge hub WIEN

cross sections, the observed crack length could be shorter to non-existent under real conditions. Therefore, the development of a viscoelastic material model that works in conjunction with the moisture transport model could be one of the next steps.

The approach to simulate wood composite beams from **Publication 4** can be used to accompany beam experiments to understand the failure mechanisms in greater detail and to further improve such beams. Possible extensions would be the inclusion of a failure mechanism directly in the glue line by cohesive surfaces and the addition of a more advanced failure criterion in the web, which needs to be developed through material testing. Since long-term behavior is not of great importance due to the short periods of use under load for the beams studied, the associated material long-term behavior was not of significant relevance to these types of simulations. However, viscoelastic effects should be taken into account when wood composite beams are used with loads over longer periods of time.

Die approbierte gedruckte Originalversion dieser Dissertation ist an der TU Wien Bibliothek verfügbar.
The approved original version of this doctoral thesis is available in print at TU Wien Bibliothek.
TU Bibliothek Your knowledge hub WIEN

Die approbierte gedruckte Originalversion dieser Dissertation ist an der TU Wien Bibliothek verfügbar.
The approved original version of this doctoral thesis is available in print at TU Wien Bibliothek.

Bibliography

[1] P. Dietsch and T. Tannert, "Assessing the integrity of glued-laminated timber elements," *Construction and Building Materials*, vol. 101, pp. 1259–1270, 2015.

[2] M. Lukacevic, *Numerical simulation of wooden boards considering morphological characteristics and complex failure processes*. PhD thesis, Wien, Techn. Univ., Diss., 2014, 2014.

[3] M. Autengruber, M. Lukacevic, and J. Füssl, "Finite-element-based moisture transport model for wood including free water above the fiber saturation point," *International Journal of Heat and Mass Transfer*, vol. 161, p. 120228, 2020.

[4] M. Autengruber, M. Lukacevic, C. Gröstlinger, J. Füssl, and J. Eberhardsteiner, "Numerical assessment of wood moisture content-based assignment to service classes in EC 5 and prediction concept for moisture-induced stresses solely using relative humidity data," *prepared for submission*, 2021.

[5] M. Autengruber, M. Lukacevic, C. Gröstlinger, and J. Füssl, "Finite-element-based prediction of moisture-induced crack patterns for cross sections of solid wood and glued laminated timber exposed to a realistic climate condition," *Construction and Building Materials*, vol. 271, p. 121775, 2021.

[6] M. Autengruber, M. Lukacevic, G. Wenighofer, R. Mauritz, and J. Füssl, "Finite-element-based concept to predict stiffness, strength, and failure of wood composite I-joist beams under various loads and climatic conditions," *Engineering Structures (under review)*, 2021.

[7] Austrian Standards Institute, "ÖNORM EN B 1995-1-1:2015-06, Eurocode 5: Design of timber structures – Part 1-1: General — Common rules and rules for buildings – National specifications for the implementation of ÖNORM EN 1995-1-1, national comments and national supplements," 6 2015.

[8] D. Konopka and M. Kaliske, "Transient multi-fickian hygro-mechanical analysis of wood," *Computers & Structures*, vol. 197, pp. 12–27, Feb. 2018.

[9] K. Krabbenhøft and L. Damkilde, "A model for non-Fickian moisture transfer in wood," *Materials and Structures*, vol. 37, no. 9, pp. 615–622, 2004.

[10] H. L. Frandsen, L. Damkilde, and S. Svensson, "A revised multi-Fickian moisture transport model to describe non-Fickian effects in wood," *Holzforschung*, vol. 61, pp. 563–572, 2007.

Die approbierte gedruckte Originalversion dieser Dissertation ist an der TU Wien Bibliothek verfügbar.
The approved original version of this doctoral thesis is available in print at TU Wien Bibliothek.
TU Bibliothek Your knowledge hub WIEN

[11] J. Eitelberger, K. Hofstetter, and S. Dvinskikh, "A multi-scale approach for simulation of transient moisture transport processes in wood below the fiber saturation point," *Composites Science and Technology*, vol. 71, pp. 1727–1738, Oct. 2011.

[12] S. Fortino, A. Genoese, A. Genoese, L. Nunes, and P. Palma, "Numerical modelling of the hygro-thermal response of timber bridges during their service life: A monitoring case-study," *Construction and Building Materials*, vol. 47, pp. 1225–1234, Oct. 2013.

[13] C. Gebhardt, D. Konopka, A. Börner, M. Mäder, and M. Kaliske, "Hygro-mechanical numerical investigations of a wooden panel painting from "Katharinenaltar" by Lucas Cranach the Elder," *Journal of Cultural Heritage*, vol. 29, pp. 1–9, Jan. 2018.

[14] S. Fortino, P. Hradil, A. Genoese, A. Genoese, and A. Pousette, "Numerical hygro-thermal analysis of coated wooden bridge members exposed to northern european climates," *Construction and Building Materials*, vol. 208, pp. 492–505, May 2019.

[15] P. Perré and I. W. Turner, "A 3-d version of transpore: a comprehensive heat and mass transfer computational model for simulating the drying of porous media," *International Journal of Heat and Mass Transfer*, vol. 42, pp. 4501–4521, Dec. 1999.

[16] D. Gawin, C. E. Majorana, and B. A. Schrefler, "Numerical analysis of hygro-thermal behaviour and damage of concrete at high temperature," *Mech. Cohes.-Frict. Mater.*, vol. 4, pp. 37–74, Jan. 1999.

[17] F. Pesavento, B. A. Schrefler, and G. Sciumè, "Multiphase flow in deforming porous media: A review," *Archives of Computational Methods in Engineering*, vol. 24, no. 2, pp. 423–448, 2017.

[18] S.-L. Su, "Modeling of multi-phase moisture transfer and induced stress in drying clay bricks," *Applied Clay Science*, vol. 12, no. 3, pp. 189–207, 1997.

[19] A. Halder, A. Dhall, and A. K. Datta, "An improved, easily implementable, porous media based model for deep-fat frying: Part i: Model development and input parameters," *Food and Bioproducts Processing*, vol. 85, no. 3, pp. 209–219, 2007.

[20] A. Halder, A. Dhall, and A. K. Datta, "Modeling transport in porous media with phase change: Applications to food processing," *J. Heat Transfer*, vol. 133, p. 031010, Nov. 2010.

[21] C. Kumar, M. U. H. Joardder, T. W. Farrell, G. J. Millar, and A. Karim, "A porous media transport model for apple drying," *Biosystems Engineering*, vol. 176, pp. 12–25, 2018.

[22] P. Perré, "The proper use of mass diffusion equations in drying modeling: Introducing the drying intensity number," *Drying Technology*, vol. 33, pp. 1949–1962, Nov. 2015.

Die approbierte gedruckte Originalversion dieser Dissertation ist an der TU Wien Bibliothek verfügbar.
The approved original version of this doctoral thesis is available in print at TU Wien Bibliothek.
TU Bibliothek Your knowledge hub WIEN

[23] M. A. Stanish, G. S. Schajer, and F. Kayihan, "A mathematical model of drying for hygroscopic porous media," *AIChE J.*, vol. 32, pp. 1301–1311, Aug. 1986.

[24] I. W. Turner, "A two-dimensional orthotropic model for simulating wood drying processes," *Applied Mathematical Modelling*, vol. 20, pp. 60–81, Jan. 1996.

[25] R. P. Ramachandran, M. Akbarzadeh, J. Paliwal, and S. Cenkowski, "Computational fluid dynamics in drying process modelling–a technical review," *Food and Bioprocess Technology*, vol. 11, no. 2, pp. 271–292, 2018.

[26] K. Krabbenhøft, *Moisture Transport in Wood - A Study of Physical-Mathematical Models and their Numerical Implementation*. PhD thesis, Technical University of Denmark, 2003.

[27] P. A. Forsyth and M. C. Kropinski, "Monotonicity considerations for saturated–unsaturated subsurface flow," *SIAM Journal on Scientific Computing*, vol. 18, no. 5, pp. 1328–1354, 1997.

[28] M. A. Celia, E. T. Bouloutas, and R. L. Zarba, "A general mass-conservative numerical solution for the unsaturated flow equation," *Water Resour. Res.*, vol. 26, pp. 1483–1496, Aug. 1990.

[29] M. Lukacevic and J. Füssl, "Numerical simulation tool for wooden boards with a physically based approach to identify structural failure," *European Journal of Wood and Wood Products*, vol. 72, pp. 497–508, July 2014.

[30] M. Lukacevic, G. Kandler, M. Hu, A. Olsson, and J. Füssl, "A 3d model for knots and related fiber deviations in sawn timber for prediction of mechanical properties of boards," *Materials & Design*, vol. 166, p. 107617, Mar. 2019.

[31] M. Lukacevic, J. Füssl, and R. Lampert, "Failure mechanisms of clear wood identified at wood cell level by an approach based on the extended finite element method," *Engineering Fracture Mechanics*, vol. 144, pp. 158–175, Aug. 2015.

[32] M. Lukacevic, W. Lederer, and J. Füssl, "A microstructure-based multisurface failure criterion for the description of brittle and ductile failure mechanisms of clear-wood," *Engineering Fracture Mechanics*, vol. 176, pp. 83–99, May 2017.

[33] J. Füssl, M. Li, M. Lukacevic, J. Eberhardsteiner, and C. M. Martin, "Comparison of unit cell-based computational methods for predicting the strength of wood," *Engineering Structures*, vol. 141, pp. 427–443, June 2017.

[34] M. Li, J. Füssl, M. Lukacevic, J. Eberhardsteiner, and C. M. Martin, "Strength predictions of clear wood at multiple scales using numerical limit analysis approaches," *Computers & Structures*, vol. 196, pp. 200–216, Feb. 2018.

[35] J. Siau, *Transport Processes in Wood*. Springer-Verlag Berlin Heidelberg New York Tokyo, 1984.

[36] R. Thomas and K. Kringstad, "The role of hydrogen bonding in pit aspiration," *Holzforschung*, vol. 25, no. 5, pp. 143–149, 1971.

Die approbierte gedruckte Originalversion dieser Dissertation ist an der TU Wien Bibliothek verfügbar.
The approved original version of this doctoral thesis is available in print at TU Wien Bibliothek.
TU Bibliothek Your knowledge hub WIEN

[37] J. J. Nijdam, T. A. G. Langrish, and R. B. Keey, "A high-temperature drying model for softwood timber," *Chemical Engineering Science*, vol. 55, pp. 3585–3598, Sept. 2000.

[38] J. Eriksson, H. Johansson, and J. Danvind, "A mass transport model for drying wood under isothermal conditions," *Drying Technology*, vol. 25, pp. 433–439, Mar. 2007.

[39] S. Florisson, S. Ormarsson, and J. Vessby, "A numerical study of the effect of green-state moisture content on stress development in timber boards during drying," *Wood and Fiber Science*, vol. 51, pp. 41–57, Jan. 2019.

[40] P. Wiberg and T. J. Morén, "Moisture flux determination in wood during drying above fibre saturation point using CT-scanning and digital image processing," *Holz als Roh- und Werkstoff*, vol. 57, pp. 137–144, Apr. 1999.

[41] S. Sandoval-Torres, A. Pérez-Santiago, and E. Hernández-Bautista, "Drying model for softwood and moisture patterns measured by magnetic resonance imaging," *Drying Technology*, vol. 37, pp. 458–467, Mar. 2019.

[42] K. Krabbenhøft and L. Damkilde, "Double porosity models for the description of water infiltration in wood," *Wood Science and Technology*, vol. 38, no. 8, pp. 641–659, 2004.

[43] O. Gezici-Koç, S. J. F. Erich, H. P. Huinink, L. G. J. van der Ven, and O. C. G. Adan, "Bound and free water distribution in wood during water uptake and drying as measured by 1d magnetic resonance imaging," *Cellulose*, vol. 24, pp. 535–553, Feb. 2017.

[44] S. Whitaker, J. P. Hartnett, and T. F. Irvine, "Simultaneous heat, mass, and momentum transfer in porous media: A theory of drying," in *Advances in Heat Transfer*, vol. 13, pp. 119–203, Elsevier, 1977.

[45] N. Ouelhazi, G. Arnaud, and J. P. Fohr, "A two-dimensional study of wood plank drying. the effect of gaseous pressure below boiling point," *Transport in Porous Media*, vol. 7, pp. 39–61, Jan. 1992.

[46] S. Pang, "Relative importance of vapour diffusion and convecttve flow in modelling of softwood drying," *Drying Technology*, vol. 16, pp. 271–281, Jan. 1998.

[47] H. L. Frandsen, *Selected Constitutive Models for Simulating the Hygromechanical Response of Wood*. PhD thesis, Aalborg University, 2007.

[48] R. Schirmer, "Die Diffusionszahl von Wasserdampf-Luft-Gemischen und die Verdampfungsgeschwnidigkeit," *VDI Beiheft Verfahrenstechnik*, vol. 1938, no. 6, pp. 170–177, 1938.

[49] J. Eitelberger, *A multiscale material description for wood below the fiber saturation point with particular emphasis on wood-water interactions*. PhD thesis, Wien, Techn. Univ., Diss., 2011, 2011.

Die approbierte gedruckte Originalversion dieser Dissertation ist an der TU Wien Bibliothek verfügbar.
The approved original version of this doctoral thesis is available in print at TU Wien Bibliothek.
TU Bibliothek Your knowledge hub WIEN

[50] E. Schmidt, *Properties of Water and Steam in SI-Units.* Springer Verlag, Berlin, 4 ed., 1989.

[51] Y. Touloukian, S. Saxena, and P. Hestermans, "Thermophysical Properties of Matter-the TPRC Data Series. Volume 11. Viscosity," tech. rep., Thermophysical and Electronic Properties Information Center, 1975.

[52] G. A. Spolek and O. A. Plumb, "Capillary pressure in softwoods," *Wood Science and Technology*, vol. 15, pp. 189–199, Sept. 1981.

[53] F. Kollmann, *Technologie des Holzes und der Holzwerkstoffe - Band 1.* Springer-Verlag Berlin Heidelberg, 1951.

[54] Q.-x. Yang, "Study on the specific heat of wood by statistical mechanics," *Journal of Forestry Research*, vol. 11, pp. 265–268, Dec. 2000.

[55] C. Skaar, *Wood-Water Relations*. Springer-Verlag Berlin Heidelberg, 1988.

[56] H. L. Frandsen, L. Damkilde, and S. Svensson, "A hysteresis model suitable for numerical simulation of moisture content in wood," *Holzforschung*, vol. 61, pp. 175–181, 2007.

[57] A. J. Hailwood and S. Horrobin, "Absorption of water by polymers: analysis in terms of a simple model," *Trans. Faraday Soc.*, vol. 42, pp. B084–B092, 1946.

[58] H. L. Frandsen, L. Damkilde, and S. Svensson, "Implementation of sorption hysteresis in multi-fickian moisture transport," *Holzforschung*, vol. 61, pp. 693–701, 2007.

[59] Abaqus Documentation, *Abaqus Online Documentation*. Dassault Systemes Simulia Corporation, Providence, RI, USA, 2016.

[60] H.-J. G. Diersch and P. Perrochet, "On the primary variable switching technique for simulating unsaturated-saturated flows," *Advances in Water Resources*, vol. 23, pp. 271–301, Nov. 1999.

[61] L. A. Richards, "Capillary conduction of liquids through porous mediums," *Physics*, vol. 1, pp. 318–333, Sept. 1931.

[62] S. V. Dvinskikh, M. Henriksson, A. L. Mendicino, S. Fortino, and T. Toratti, "Nmr imaging study and multi-Fickian numerical simulation of moisture transfer in norway spruce samples," *Engineering Structures*, vol. 33, pp. 3079–3086, Nov. 2011.

[63] P. Perré, M. Moser, and M. Martin, "Advances in transport phenomena during convective drying with superheated steam and moist air," *International Journal of Heat and Mass Transfer*, vol. 36, pp. 2725–2746, July 1993.

[64] S. Sandoval-Torres, E. Hernández-Bautista, J. Rodríguez-Ramírez, and A. Carrillo Parra, "Numerical simulation of warm-air drying of mexican softwood (pinus pseudostrobus): An empirical and mechanistic approach," *Chemical and Biochemical Engineering Quarterly*, vol. 28, no. 1, pp. 125–133, 2014.

Die approbierte gedruckte Originalversion dieser Dissertation ist an der TU Wien Bibliothek verfügbar.
The approved original version of this doctoral thesis is available in print at TU Wien Bibliothek.
TU Bibliothek Your knowledge hub WIEN

[65] R. Pečenko, S. Svensson, and T. Hozjan, "Modelling heat and moisture transfer in timber exposed to fire," *International Journal of Heat and Mass Transfer*, vol. 87, pp. 598–605, 2015.

[66] M. Fragiacomo, S. Fortino, D. Tononi, I. Usardi, and T. Toratti, "Moisture-induced stresses perpendicular to grain in cross-sections of timber members exposed to different climates," *Engineering Structures*, vol. 33, pp. 3071–3078, Nov. 2011.

[67] S. Huč, S. Svensson, and T. Hozjan, "Numerical analysis of moisture-induced strains and stresses in glued-laminated timber," *Holzforschung*, vol. 74, no. 5, pp. 445–457, 2019.

[68] S. Svensson, G. Turk, and T. Hozjan, "Predicting moisture state of timber members in a continuously varying climate," *Engineering Structures*, vol. 33, pp. 3064–3070, Nov. 2011.

[69] S. Fortino, P. Hradil, and G. Metelli, "Moisture-induced stresses in large glulam beams. case study: Vihantasalmi bridge," *Wood Material Science & Engineering*, vol. 14, pp. 366–380, Sept. 2019.

[70] S. Fortino, P. Hradil, K. Koski, A. Korkealaakso, L. Fülöp, H. Burkart, and T. Tirkkonen, "Health monitoring of stress-laminated timber bridges assisted by a hygro-thermal model for wood material," *Applied Sciences*, vol. 11, no. 1, 2021.

[71] S. Florisson, J. Vessby, W. Mmari, and S. Ormarsson, "Three-dimensional orthotropic nonlinear transient moisture simulation for wood: analysis on the effect of scanning curves and nonlinearity," *Wood Science and Technology*, vol. 54, no. 5, pp. 1197–1222, 2020.

[72] A. Gamper, P. Dietsch, M. Merk, and S. Winter, "Gebäudeklima - Langzeitmessung zur Bestimmung der Auswirkungen auf Feuchtegradienten in Holzbauteilen," *Bautechnik*, vol. 90, pp. 508–519, Mar. 2013.

[73] B. Franke, S. Franke, M. Schiere, and A. Müller, "Moisture content and moisture-induced stresses of large glulam members: laboratory tests, in-situ measurements and modelling," *Wood Material Science & Engineering*, vol. 14, pp. 243–252, July 2019.

[74] B. Franke, S. Franke, M. Schiere, and A. Müller, "Quality assurance of timber structures," tech. rep., Bern University of Applied Sciences, Institute for Timber Constructions, Structures and Architecture, 2019.

[75] B. Franke, S. Franke, M. Schiere, and A. Müller, "Praxisleitfaden Beurteilung der Holzfeuchte für Tragwerke und Brücken für die Planung, Errichtung und Nutzung," tech. rep., Berner Fachhochschule, 2019.

[76] timeanddate.com, 2017. [Online; visited October 19, 2017].

[77] T. Volkmer, J.-A. Schmidt, K. Kranitz, and P. Niemz, "Untersuchungen zum Einfluss der Klebstoffart auf den Diffusionswiderstand von Holzverklebungen," *Bauphysik*, vol. 34, pp. 55–60, Apr. 2012.

Die approbierte gedruckte Originalversion dieser Dissertation ist an der TU Wien Bibliothek verfügbar.
The approved original version of this doctoral thesis is available in print at TU Wien Bibliothek.
TU Bibliothek Your knowledge hub WIEN

[78] Austrian Standards Institute, "ÖNORM EN 1992-1-1:2015-02, Eurocode 2: Design of concrete structures – Part 1-1: General rules and rules for buildings," 2 2015.

[79] S. Pech, M. Lukacevic, and J. Füssl, "A robust multisurface return-mapping algorithm and its implementation in abaqus," *Finite Elements in Analysis and Design*, vol. 190, p. 103531, 2021.

[80] W. T. Simpson, "Prediciting equilibrium moisture content of wood by mathematical models," *Wood and Fiber*, vol. 5, no. 1, pp. 41–49, 1973.

[81] M. M. Hassani, *Adhesive Bonding of Structural Hardwood Elements*. PhD thesis, ETH-Zürich, 2015.

[82] K. Hofstetter, C. Hellmich, and J. Eberhardsteiner, "Development and experimental validation of a continuum micromechanics model for the elasticity of wood," *European Journal of Mechanics - A/Solids*, vol. 24, no. 6, pp. 1030–1053, 2005.

[83] S. Gloimüller, K. De Borst, T. Bader, and J. Eberhardsteiner, "Determination of the linear elastic stiffness and hygroexpansion of softwood by a multilayered unit cell using poromechanics," *Interaction and multiscale mechanics*, vol. 5, no. 3, pp. 229–265, 2012.

[84] R. C. Weatherwax and A. J. Stamm, "The coefficients of thermal expansion of wood and wood products," Tech. Rep. 1487, US Forest Products Laboratory, March 1956.

[85] M. Lukacevic and J. Füssl, "Application of a multisurface discrete crack model for clear wood taking into account the inherent microstructural characteristics of wood cells.," *Holzforschung*, vol. 70, no. 9, pp. 845–853, 2016.

[86] S. W. Tsai and E. M. Wu, "A general theory of strength for anisotropic materials," *Journal of Composite Materials*, vol. 5, pp. 58–80, Feb. 1971.

[87] G. Kandler, M. Lukacevic, and J. Füssl, "An algorithm for the geometric reconstruction of knots within timber boards based on fibre angle measurements.," *Construction and Building Materials*, vol. 124, pp. 945–960, 2016.

[88] DIN Deutsches Institut für Normung e.V.EN, "EN 13377:2002 (D), Prefabricated timber formwork beams – Requirements, classification and assessment; German version," 2002.

[89] D. Fangtian, C. Lipin, and Z. Shufen, "Determination of static and dynamic diffusion coefficients of moisture in particleboards," *Journal of Northeast Forestry University*, vol. 4, no. 2, pp. 87–92, 1993.

[90] W. Sonderegger and P. Niemz, "Thermal conductivity and water vapour transmission properties of wood-based materials," *European Journal of Wood and Wood Products*, vol. 67, no. 3, pp. 313–321, 2009.

Die approbierte gedruckte Originalversion dieser Dissertation ist an der TU Wien Bibliothek verfügbar.
The approved original version of this doctoral thesis is available in print at TU Wien Bibliothek.
TU Bibliothek Your knowledge hub WIEN

[91] DIN Deutsches Institut für Normung e.V., "DIN EN ISO 10456:2010-05, Building materials and products – Hygrothermal properties – Tabulated design values and procedures for determining declared and design thermal values; German version," 5 2010.

[92] J. Niklewski, M. Fredriksson, and T. Isaksson, "Moisture content prediction of rain-exposed wood: Test and evaluation of a simple numerical model for durability applications," *Building and Environment*, vol. 97, pp. 126–136, Feb. 2016.

[93] DIN Deutsches Institut für Normung e.V., "DIN EN 312:2010-12, Particleboards – Specifications; German version," 12 2010.

[94] T. K. Bader, F. Dastoorian, G. Ebrahimi, G. Unger, O. Lahayne, C. Hellmich, and B. Pichler, "Combined ultrasonic-mechanical characterization of orthotropic elastic properties of an unrefined bagasse fiber-polypropylene composite," *Composites Part B: Engineering*, vol. 95, pp. 96–104, June 2016.

[95] A. Pavlekovics, P. Niemz, W. Sonderegger, and S. Molnar, "Studies on the influence of wood moisture content on selected properties of particle boards and MDF," *Holz als Roh- und Werkstoff*, vol. 66, no. 2, pp. 99–105, 2008.

[96] DIN Deutsches Institut für Normung e.V., "DIN EN 12369-1:2001-04, Wood-based panels – Characteristic values for structural design – Part 1: OSB, particleboards and fibreboards; German version," 4 2001.

[97] W. Sonderegger and P. Niemz, "Investigation of swelling and thermal expansion of fibreboard, particleboard and plywood," *Holz als Roh- und Werkstoff*, vol. 64, no. 1, pp. 11–20, 2005.

[98] Holzforschung-Austria, "Radikale Schalungsinnovationen Projektteil SSTH – Stärkerer Systemträger Holz Pilzresistenz und Feuchteverhalten," tech. rep., Holzforschung-Austria, 2010.

Die approbierte gedruckte Originalversion dieser Dissertation ist an der TU Wien Bibliothek verfügbar.
The approved original version of this doctoral thesis is available in print at TU Wien Bibliothek.
TU Bibliothek Your knowledge hub WIEN

Publications and Conference Contributions

Publications

M. Autengruber, M. Lukacevic, J. Füssl:
Finite-element-based moisture transport model for wood including free water above the fiber saturation point,
International Journal of Heat and Mass Transfer, 161 (2020), 120228.

M. Autengruber, M. Lukacevic, C. Gröstlinger, J. Füssl:
Finite-element-based prediction of moisture-induced crack patterns for cross sections of solid wood and glued laminated timber exposed to a realistic climate condition,
Construction and Building Materials, 271 (2021), 121775.

Conference Proceedings

M. Autengruber, M. Lukacevic, J. Eberhardsteiner, J. Füssl:
A Numerical Simulation Tool for Coupled Heat and Mass Transfer in Wood,
In: *Programme & Book of Abstracts on Computational Methods in Wood Mechanics - from Material Properties to Timber Structures (CompWood 2017)*, TU Verlag, Wien, 2017.

M. Autengruber, M. Lukacevic, J. Eberhardsteiner, J. Füssl:
A Numerical Simulation Tool for Coupled Heat and Mass Transfer in Wood,
In: *Book of Abstracts of the XXIst. Inter-Institute Seminar for Young Researchers*, Department of Structural Mechanics, Budapest University of Technology and Economics, 2017, S. 6.

M. Autengruber, M. Lukacevic, J. Füssl:
Heat and Mass Transfer Model for Wood Under Real Climate Conditions,
In: *Book of Abstracts of the International Conference on Computational Methods in Wood Mechanics - from Material Properties to Timber Structures (CompWood 2019)*, Linnaeus University, 2019.

Die approbierte gedruckte Originalversion dieser Dissertation ist an der TU Wien Bibliothek verfügbar.
The approved original version of this doctoral thesis is available in print at TU Wien Bibliothek.
TU Bibliothek Your knowledge hub WIEN

Conference Presentations

M. Autengruber, M. Lukacevic, J. Eberhardsteiner, J. Füssl:
A Numerical Simulation Tool for Coupled Heat and Mass Transfer in Wood,
Conference on Computaional Methods in Wood Mechanics - From Material Properties to Timber Structures (CompWood 2017),
Wien, Austria, 06/07/2017 – 06/09/2017.

M. Autengruber, M. Lukacevic, J. Eberhardsteiner, J. Füssl:
A Numerical Simulation Tool for Coupled Heat and Mass Transfer in Wood,
XXIst. Inter-Institute Seminar for Young Researchers,
Budapest, Hungary, 10/06/2017 – 10/08/2017.

M. Autengruber, M. Lukacevic, J. Füssl:
Numerical Simulation of Moisture Induced Cracking Behaviour in Wood Cross Sections Under Real Climate Conditions,
Engineering Mechanics Institute Conference 2018 (EMI 2018),
Cambridge, Massachusetts, USA, 05/29/2018 – 06/01/2018.

M. Autengruber, M. Lukacevic, J. Füssl:
Numerical Simulation of Moisture Induced Cracking Behaviour in Wood Cross Sections Under Real Climate Conditions,
6th European Conference on Computational Fluid Dynamics (ECCM - ECFD 2018),
Glasgow, United Kingdom, 06/11/2018 – 06/15/2018.

M. Autengruber, M. Lukacevic, J. Füssl:
Heat and Mass Transfer Model for Wood Under Real Climate Conditions,
International Conference on Computational Methods in Wood Mechanics - From Material Properties to Timber Structures (CompWood 2019),
Växjo, Sweden, 06/17/2019 – 06/19/2019.

M. Autengruber, M. Lukacevic, J. Füssl:
Heat and Mass Transfer Model for Wood Under Real Climate Conditions,
XV. International Conference on Computational Plasticity - Fundamentals and Applications (COMPLAS 2019),
Barcelona, Spain, 09/03/2019 – 09/05/2019.

M. Autengruber, M. Lukacevic, J. Füssl:
Numerical Simulation of Moisture Transport in Wood Including Free Water Transport,
14th Virtual Congress WCCM & ECCOMAS 2020,
Paris, France (virtual), 01/11/2021 – 01/15/2021.

Die approbierte gedruckte Originalversion dieser Dissertation ist an der TU Wien Bibliothek verfügbar.
The approved original version of this doctoral thesis is available in print at TU Wien Bibliothek.
TU Bibliothek Your knowledge hub WIEN

Master's Thesis (own and supervised)

M. Autengruber:
Modellierung und numerische Simulation des Feuchte- und Temperaturverhaltens von Holz-Aluminium-Verbundträgern,
Supervised by M. Lukacevic, J. Füssl, J. Eberhardsteiner, TU Wien, 2016.

C. Gröstlinger:
Numerical simulation of moisture induced cracking behaviour in wood cross sections under real climate conditions,
Supervised by M. Autengruber, M. Lukacevic, J. Füssl, TU Wien, 2018.

T. Raimer:
The effect of fresh concrete application on the moisture distribution in timber-concrete composite floors with notched connections, investigated by means of numerical simulation,
Supervised by M. Autengruber, M. Lukacevic, J. Füssl, TU Wien, 2020.

F. Brandstätter:
Numerical simulation concept to determine moisture loading and the resulting crack behaviour of different timber cross sections depending on the location in Austria,
Supervised by M. Autengruber, M. Lukacevic, J. Füssl, TU Wien, 2020.

Die approbierte gedruckte Originalversion dieser Dissertation ist an der TU Wien Bibliothek verfügbar.
The approved original version of this doctoral thesis is available in print at TU Wien Bibliothek.
TU Bibliothek Your knowledge hub WIEN

Die approbierte gedruckte Originalversion dieser Dissertation ist an der TU Wien Bibliothek verfügbar.
The approved original version of this doctoral thesis is available in print at TU Wien Bibliothek.

Curriculum Vitae

Personal Data

Name:	Dipl.-Ing. **Maximilian AUTENGRUBER**, BSc
Date of Birth:	April 13, 1991
Place of Birth:	Wien, Austria
Nationality:	Austria
Current address:	Schönbrunner Straße 217/1/35, 1120 Wien, Austria

Education

since 07/2016	Doctoral program in Civil Engineering at TU Wien, Austria
11/2014 – 06/2016	Master program in Civil Engineering at TU Wien, Austria with distinction
10/2011 – 11/2014	Bachelor program in Civil Engineering and Management Infrastructure at TU Wien, Austria with distinction
09/2005 – 06/2010	College of Construction Engineering Specialising in Civil Engineering at HTL Mödling, Austria with distinction
09/2001 – 06/2005	High school student at BRG Perchtoldsdorf, Austria

Awards

2016	Award for excellent Master's Thesis, granted by Stadt Wien
2016	FCP Innovation Prize, category Master's Thesis, granted by FCP
2016 – 2012	Awards for excellent performance as a student, granted by the Faculty of Civil Engineering of TU Wien
2010	Awards for excellent performance as a student, granted by HTL Mödling

Work experience

since 07/2016	Research assistant at the Institute for Mechanics of Materials and Structures, TU Wien, Austria
03/2014 – 06/2016	Student assistant at the Civil Engineering Computer Laboratory, TU Wien, Austria
10/2012 – 02/2014	Tutor at the Civil Engineering Computer Laboratory, TU Wien, Austria

Die approbierte gedruckte Originalversion dieser Dissertation ist an der TU Wien Bibliothek verfügbar.
The approved original version of this doctoral thesis is available in print at TU Wien Bibliothek.
TU Bibliothek Your knowledge hub WIEN